Inversion for Local Stress Field Inhomogeneities

Dissertation

zur Erlangung des Doktorgrades der Naturwissenschaften
im Department
Geowissenschaften der Universität Hamburg

vorgelegt von

Jörg Reinhardt

aus

Heide

Hamburg

2007

Als Dissertation angenommen vom Department Geowissenschaften der Universität Hamburg

auf Grund der Gutachten von Prof. Dr. Torsten Dahm
und Dr. Thomas Plenefisch

Hamburg, den _____

Professor Dr. Kay-Christian Emeis
Leiter des Departments Geowissenschaften

Für Karen

Abstract

In this thesis, the 1997 Vogtland/NW-Bohemia swarm has been selected for the analysis of inhomogeneities in the stress field because two predominant nearly perpendicular flat zones of seismicity are visible in the hypocentre distribution implying inhomogeneities in the stress field. This is unusual compared to other swarms originating from this area. An existing dataset of waveform data, P- and S-phase picks, and master event locations has been analysed regarding similarity of waveforms, location refinement, and estimation of relative moment tensors. The latter are used together with a regional dataset of 50 single focal mechanisms and 125 focal mechanisms from the 2000 hydraulic fracturing experiment at the KTB for an estimate of the regional homogeneous and the locally inhomogeneous stress field.

An automated processing procedure consisting of coherence analysis, precise relocation, relative moment tensor inversion, and stress trajectory determination has been set up. The coherence analysis has been successfully applied using a new method that uses three component seismograms. 457 events are separated into 13 multiplets of similar waveforms of at least size 8. Another result are precise relative arrival time measurements which are fed into the precise relocation program `hypoDD`. Two nearly perpendicular structures are found in the hypocentre distribution. 352 moment tensors are estimated using a relative moment tensor inversion. Three different algorithms to distinguish between fault plane and auxiliary plane are successfully applied to them. A regional homogeneous stress inversion using the focal mechanisms of the single events and selected events from the other datasets has been applied yielding (azimuth/plunge) $\sigma_1 = (147^o/9^o)$, $\sigma_2 = (10^o/78^o)$, and $\sigma_3 = (238^o/8^o)$. The dense population of moment tensors for the 1997 swarm inside a volume of aproximately $1km^3$ has been systematically subdivided using a moving box technique. A locally homogeneous stress inversion has been applied to each subset that consists of at least 10 measurements. The resulting deviatoric stress tensors are arranged on a regular grid and their components are smoothed using Non Uniform Rational B-Splines (NURBS) depending on three spatial parameters. The resulting σ_1 and σ_3 trajectories are visualised by projecting part of them into the plane.

The plane structures derived from the hypocentre distribution are consistent with the fault planes that have been selected from moment tensors and with the patterns found in the stress trajectories. Neutral points regarding the maximum and minimum horizontal stresses, σ_H and σ_h, respectively, are identified. The results of this work support the model of fluid induced seismicity and migrating fluids.

Contents

Chapter 1

Introduction

The continents on the Earth's surface are moving permanently. They collide at convergent, divergent, and transform boundaries. According to the theory of plate tectonics, which has been set up in the early 1960's, the plates are driven by forces generated in the Earth's interior. This causes forces to act on the edges of the plates, resulting in stresses inside the plates. For example, the African plate pushes some micro-plates northwards against Europe, piling up the Alps and adjoining mountain ranges. The related compressional stresses are present all inside the Eurasian plate. Because mountain building is a very common event in the history of the European continent, many tectonic features like remains of old rock masses with folds and fractures, wide graben structures, gaps, and faults are present. Therefore many of the rocks are very disturbed and full of zones of weakness which may show brittle failure, if the stress inside the rock generates forces that overcome the frictional resistance on the surface of the according fault plane. A common assumption is that the direction of the resulting slip is governed by the stress field and the orientation of the fault plane, in that way that slip occurs in the direction of maximum shear stress on the fault, which is the component of traction parallel to the fault.

If forces are acting on a body, stress is present everywhere inside its interior. There are two basic types of forces acting on a volume element, namely body forces (with the unit *force per volume element*) like gravity or fluid pressure and surface forces (with the unit *force per surface element*) like forces at the edge of a rock body, e.g. the relative movement of a tectonic plate against another plate or the torque caused by rocks at the edge of a cliff. In many cases the resulting stress field can be said to be homogeneous. However, there are tectonic settings that lead to inhomogeneities in the stress field, such as volcanic activity, enlarged pore pressure, and faults or fault zones. The main goal of this work is to develop techniques to describe stress trajectories, i.e. traces of the direction of the principal axes of stress, to quantitatively estimate stress inhomogeneities.

1.1   Outline of the thesis

In this work, several aims have been followed from which the estimation and visualisation of stress inhomogeneities is the main goal. Starting from event related seismograms which are available with the appropriate P- and S-phase picks several processing steps that finally lead to the determination of the deviatoric stress tensor in space have been developed and applied. This first chapter gives an overview of topics related to stress manifestiation in the form of stress indicators and the inversion of the state of stress from them. In the second chapter, the methods that are needed for the different processing steps are presented and, if necessary, developed from scratch. The third chapter deals with the application of the previously described methods to a dataset of focal mechanisms from the Vogtland/NW-Bohemia
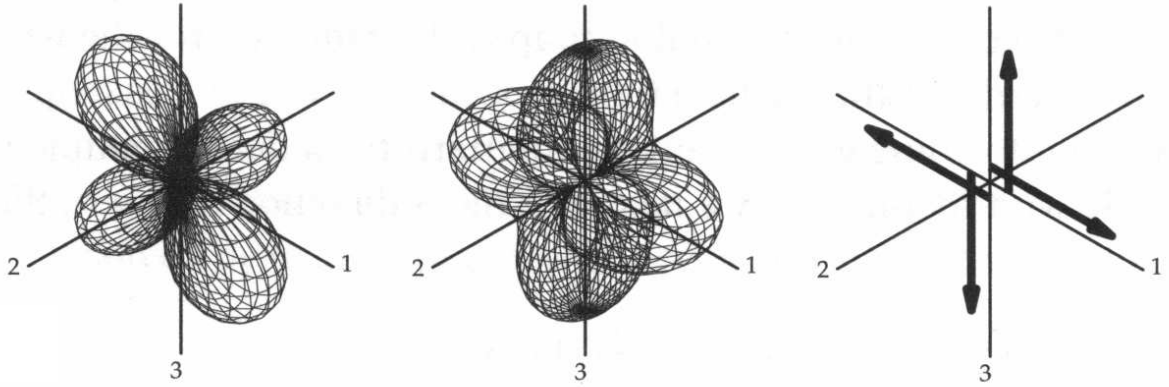
Figure 1.1: Radiation pattern of a double couple point source in a uniform medium; numbers $1-3$ are indicating the direction of the cartesian coordinates (Kennett, 2001, fig. 11-4, p. 203) shows the orientation of the forces of the double couple together with the radiation pattern of the emitted pressure and shear waves.

swarm earthquake region, the KTB, and their regional vicinity. Finally, in chapter four, the results are discussed controversely.

1.2 Basic concepts and tools

This section covers basic concepts of seismology and structural geology that will be used throughout the entire work. The most fundamental idea covered here is the concept of the moment tensor as a representation of a seismic source and derived values.

1.2.1 The moment tensor and its decompositions

A seismic source emitting energy in the form of elastic waves can be modeled by the concept of directional moments acting on a certain point in space. These moments of this so called point source can be summarised in the second rank symmetric moment tensor consisting of six independent components (Aki and Richards, 1980, fig. 3-7, p. 51). Jost and Hermann (1989) describe the concept of decomposing the full moment tensor into elementary tensors like the most common standard decomposition into an isotropic (unit tensor times $1/3 \sum_{i=1}^{3} M_{ii}$) and a deviatoric tensor (isotropic tensor substracted). The latter can be decomposed in several different ways from which the decomposition into a best double couple (DC) and a compensated linear vector dipole (CLVD) are used in this work.

1.2.2 The double couple component

After decomposing the full moment tensor into isotropic, CLVD, and DC part the latter can be treated as a focal mechansim. It has been invented to model the radiation pattern of an earthquake by the simple approximation of a system of four single forces that build two force couples which are perpendicular to each other - the double couple. It is a good approximation of an earthquakes assuming a point source and shear cracking on a fault plane (fig. 1.1). However, it can not describe crack opening or explosive sources (which is the main motivation for the development of the moment tensor concept).

2

Focal mechanism projection

For later use, the term *dihedron* is introduced here. It refers to a quarter of space which is limited by two arbitrarily oriented perpendicular planes (similar to a tetrahedron, which is limited by four planes whose edges enclose the same angle to the neighboring plane at each of its three edges). From a point source, seismic waves are emitted in a specific manner dependent on the kind of source model which applies (radiation pattern). For a double-couple point source, the sign of first motion for waves that are emitted from two opposite dihedra is identical (see fig. 1.1). This fact motivates a quite simple representation for the DC radiation pattern. Imagine a unit sphere around the centre of the DC. Now paint all areas for which the appropriate emission vectors indicate positive first motion black. All areas with negative first motion are painted white. Two planes are left uncolored for which the DC indicates that no energy is radiated. These planes are called nodal planes and with their introduction, the biggest problem of the point source approximation becomes obvious. As illustrated in fig. 1.2, the orientation of fault normal and slip vector may be switched and negated without changing the focal mechanism which makes the fault plane ambiguous. The nodal plane in which slip occurs is called fault plane while the other is called auxiliary plane. The last step is the visualisation which is done by simply projecting the sense of motion from the lower hemisphere of the focal sphere into the horizontal plane as shown in fig. 1.3.

1.3 Stress indicators

There is no way to measure the components of the stress tensor inside a body directly. However, it is possible to gain a general idea of how the stress tensor looks like. Depending highly on material properties and temperature, five reactions of rock on stress are possible: equilibrium, elastic deformation, ductile (non-reversible) deformation, brittle failure, and metamorphosis. The first and second do not change the body at all, but the latter three can result in tectonic features, like folds, earthquakes, faults, joints, cracks, or reorganisation of minerals. All theses features will be called stress indicators, since their measurement can be used to calculate the appropriate stress tensor or at least some part of it.

1.3.1 Geological stress indicators

From a geological point of view, all manifestations of stress that are visible on the Earth's surface, like cracks, faults and folds, are of interest. Furthermore faults often show secondary features where slip has occured, like lineations on a fault's surface or Riedel shear cracks. Folds also are a clear sign for stress acting on rock. Throughout the next few paragraphs the most common features will be examined in more detail.

Principal crack propagation modes

The displacement field of cracks can be categorised into three modes (see e.g. Scholz, 1990, fig. 1.5 and fig. 1.4). Mode I is the tensile, or opening, mode in which the crack wall displacements are normal to the crack. There are two shear modes: in-plane shear, Mode II, in which the displacements are in the plane of the crack and normal to the crack edge; and antiplane shear, Mode III, in which the displacements are in the plane of the crack and parallel to the edge. A schematic diagram of the interaction of cracks with different Modes is shown in fig. 1.5. More complex cracks, like an opening
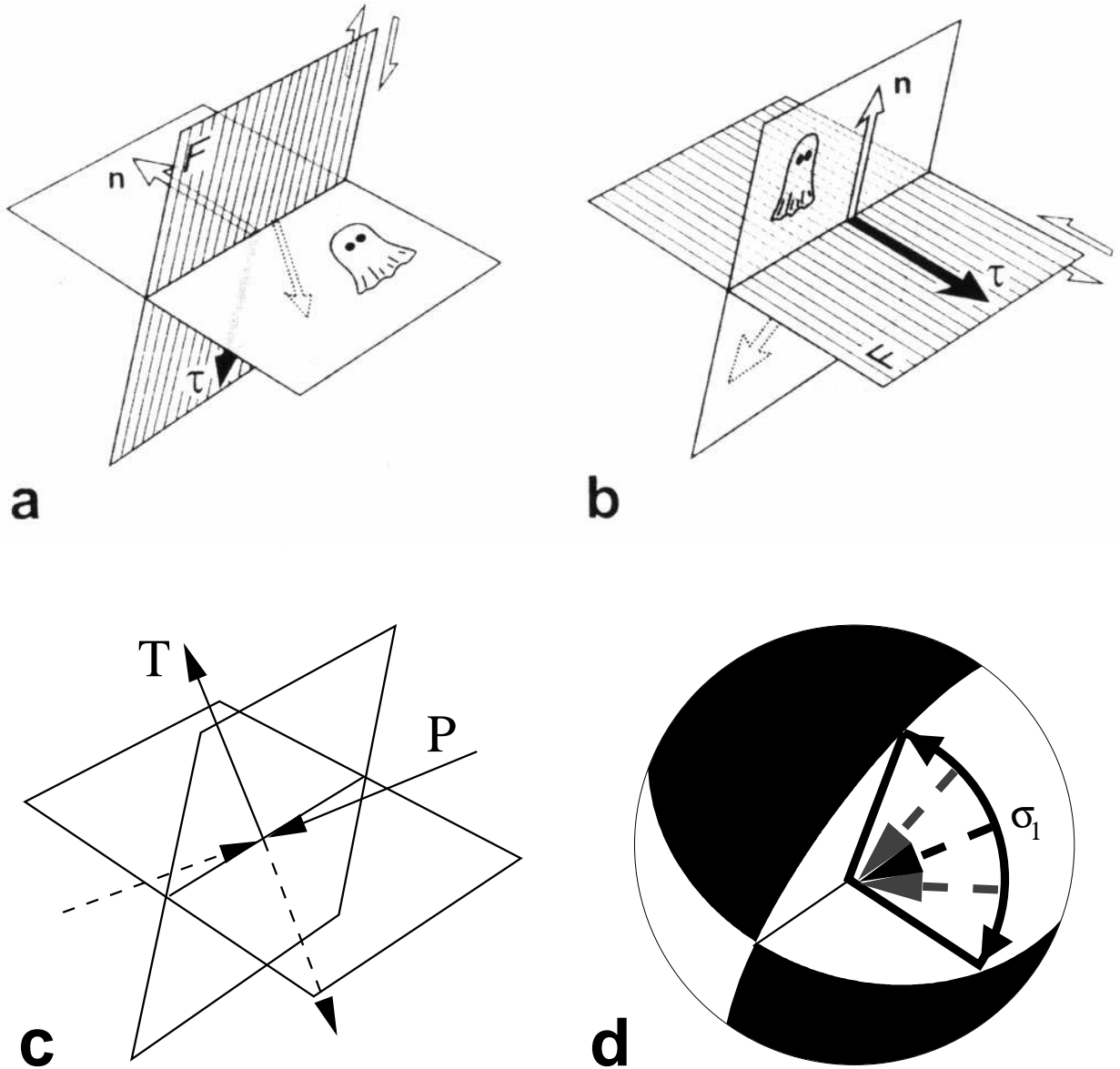
Figure 1.2: Nodal planes for the double-couple representation of an earthquake: $\mathbf{n}$ is the normal, τ is the slip direction (Angelier, 2002, fig. 3); the ambiguity in correct nodal plane selection is illustrated (both cases lead to the same radiation pattern): a) F is the fault plane and the ghost denotes the auxiliary plane; b) the opposite is the case; c) directions of tension- ($\mathbf{T}$) and pressure- ($\mathbf{P}$) axes as bisecting lines of the compressional (positive first motion) and dillatational (negative first motion) dihedra for this fault geometry; d) focal mechanism in upper hemisphere projection: range of reasonable σ_1-directions inside one dillatational dihedron (axis lies also in opposite dihedron)
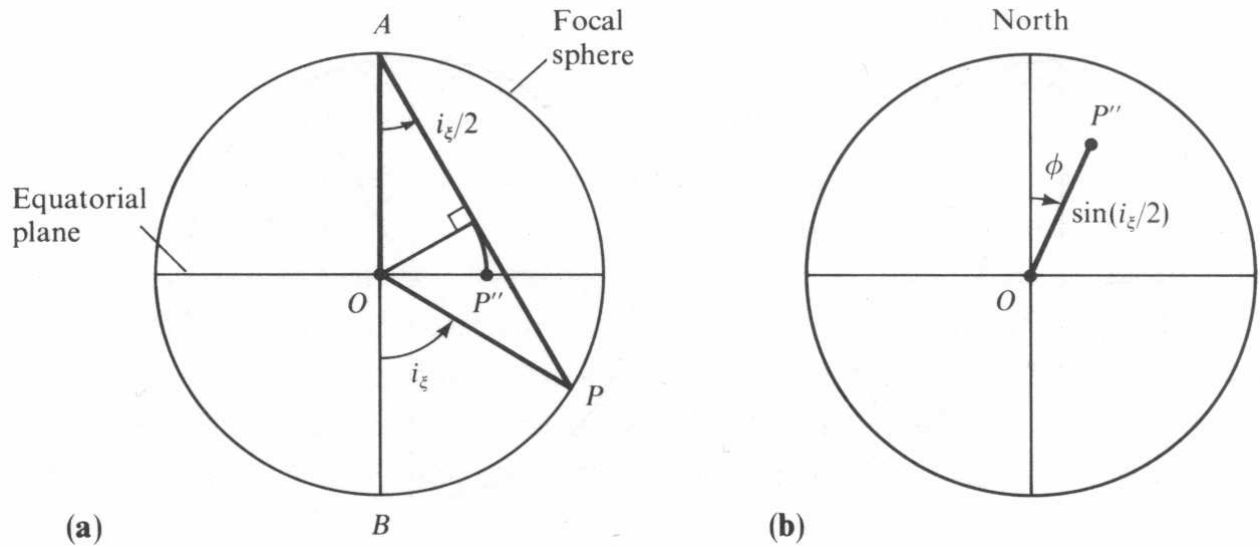
Figure 1.3: Projection of the focal sphere into the horizontal plane using the equal-area projection: a) vertical section where P is projected to P''; b) top view (Aki and Richards, 1980, fig. 4-16 and 4-17, pp. 109)
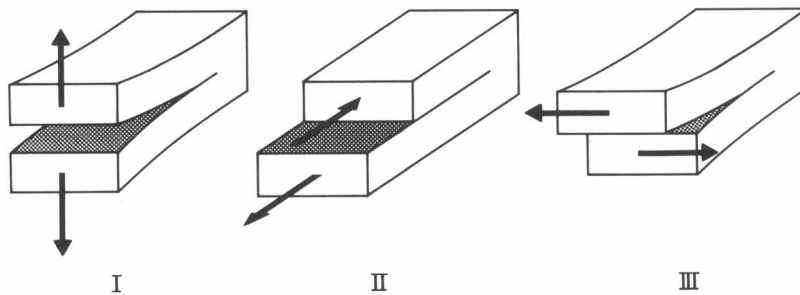
Figure 1.4: The three crack propagation modes (Scholz, 1990, fig 1.5, p. 9)

crack with some amount of slip parallel to the opening plane, can be represented by a superposition of these principal crack modes.

Faults

Faults, as a consequence of brittle failure due to the presence of a sufficient stress load, are very common indicators of stress. Some famous faults are shown in fig. 1.6. Two angles, strike and dip, which are defined in fig. 1.7 are sufficient to define the orientation of a fault. The following paragraphs deal with tectonic features that form during fault development or reactivation by slip due to sufficient stress load.

Mineral fibres are the filling of mode I cracks that have been developed as a consequence of a certain tectonic event. They preserve the appropriate stress field and need to be dated correctly. The type of information about the stress field is given by the type of crack that is preserved, usually mode-I (opening) cracks. Typical minerals that can be found in fibres are calcite, kaolinite, and quartz, which are all soluble in water. Examples are found in fig. 1.8 c, fig. 1.9, and fig. 1.13.

5
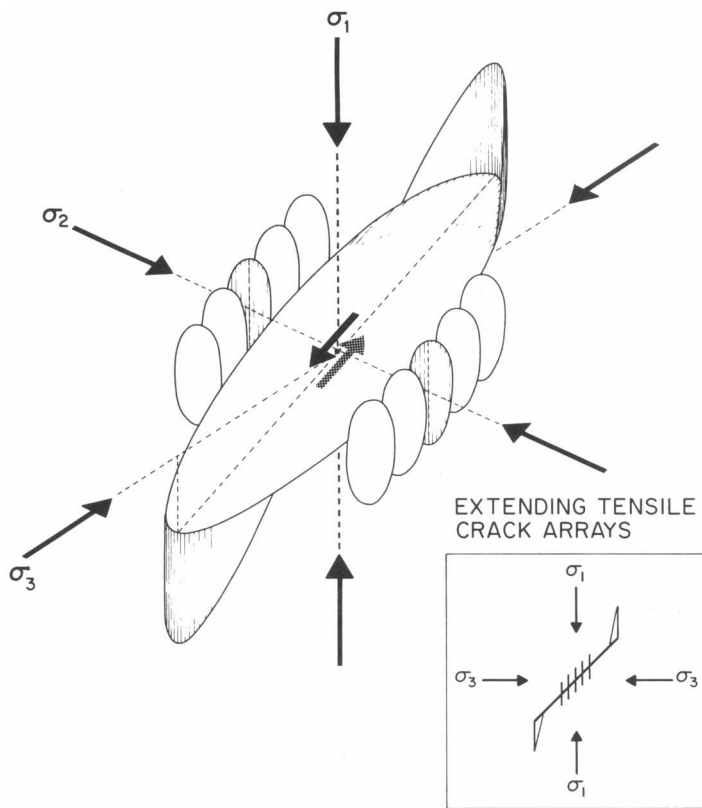
Figure 1.5: Schematic diagram showing the propagation of tensile cracks from the edges of a shear crack in a brittle material; the patterns at the Mode II and Mode III edges are quite different (Scholz, 1990, fig 1.5, p. 27)

a)
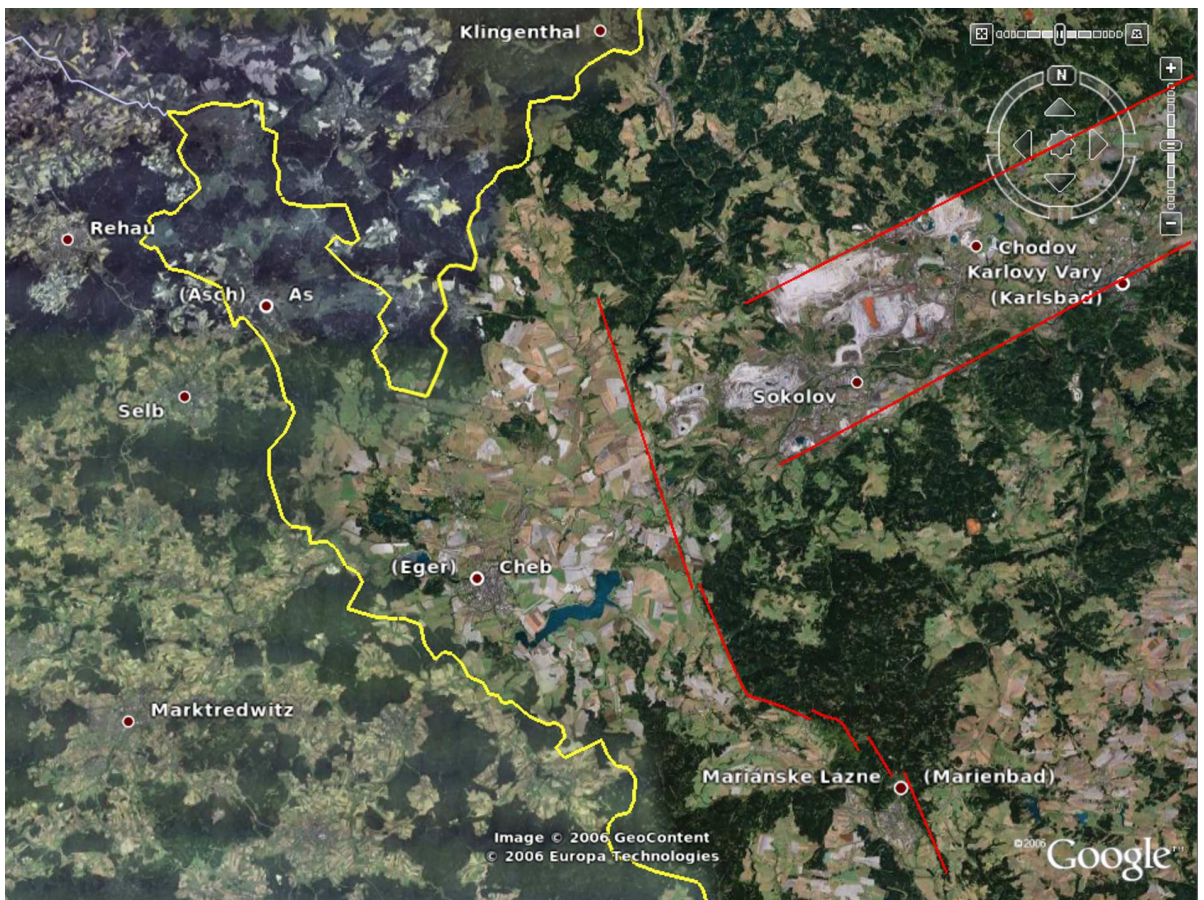
b)

c)

Figure 1.6: Examples of famous faults; a) Czechia, Mariánské Lázně Fault and Eger Graben in NW-Bohemia (Google-earth, 2006); b) U.S.A., San Andreas Fault on the West Coast (USGS, 1999); c) New Zealand, Alpine Fault on South Island (Lund, Björn, 2003)
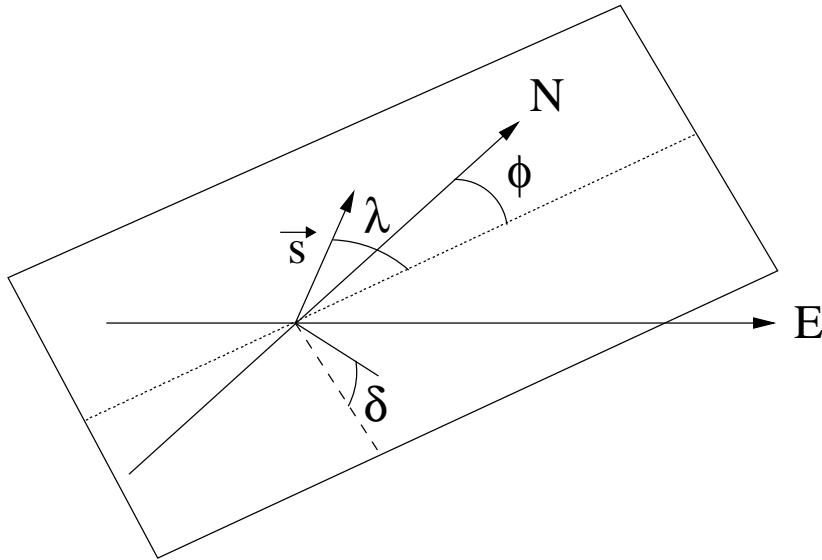
Figure 1.7: Definition of a relationgiven slip vector $\vec{s}$ by the three angles strike (ϕ), dip (δ), and rake (λ)

Fault planes themselves yield only information about the stress field at the time of their development, but active faults exist over extremely long periods of sometimes several million years. Over such long time spans, the stress field is very likely to change a lot. Therefore by knowing only the fault plane no qualitative information about the stress field can be obtained. However, sometimes it is possible to tell the sense of slip (i.e. normal vs. reverse faulting or sinistral vs. dextral fault movement) by identifying the offset of planar markers, such as beds matched in the footwall and hanging wall (see e.g. Twiss and Moores, 1992) or by evaluating other secondary faulting features.

Fault surface lineations indicate the ambiguous slip direction on a fault. Sometimes also the sense of slip can be determined and together with the orientation of the fault, the slip vector is known. Fig. 1.8 shows examples for different types of lineations that may form on the surface between two blocks of rock. Another example of slickenfibre lineations in conjunction with calcite fibres is shown in fig. 1.9.

Second-order faults are also indicating the sense of slip on a major fault. Their development is not restricted to shear zones but may occur due to any type of faulting. Riedel, W. (1929) described such secondary features during horizontal faulting experiments with clay. His main finding is that shear cracks as well as tension cracks develop during a shear process (see fig. 1.10). There is not only one type of secondary crack like Riedel, W. originally found. Fig. 1.11 shows R- (Riedel), R'- (Anti-Riedel), and P-shear-crack orientations found in a sample clay block under sinistral simple shear induced by shearing the substrate of the clay.

An example of real Riedel shear cracks is shown in fig. 1.12. Interpretation of such features with respect to stress distribution has been developed later by e.g. Anderson (1951) who found that as a result of the formation of a major fault, the stress distribution in the rocks immediately adjacent to the fault plane become altered. If the redistributed stresses along the sides of the fault surface attain sufficiently large values, the rock may fail again on surfaces which are at 30° to the modified principal compressive strength (e.g. Ramsay, 1967). Identifying such cracks lets the observer determine the sense of slip on a fault.

Another feature typically found in shear zones are tension gashes. Fig. 1.13 shows an example of gashes that have been filled up with quartz crystals. Tension gashes commonly develop as a result of
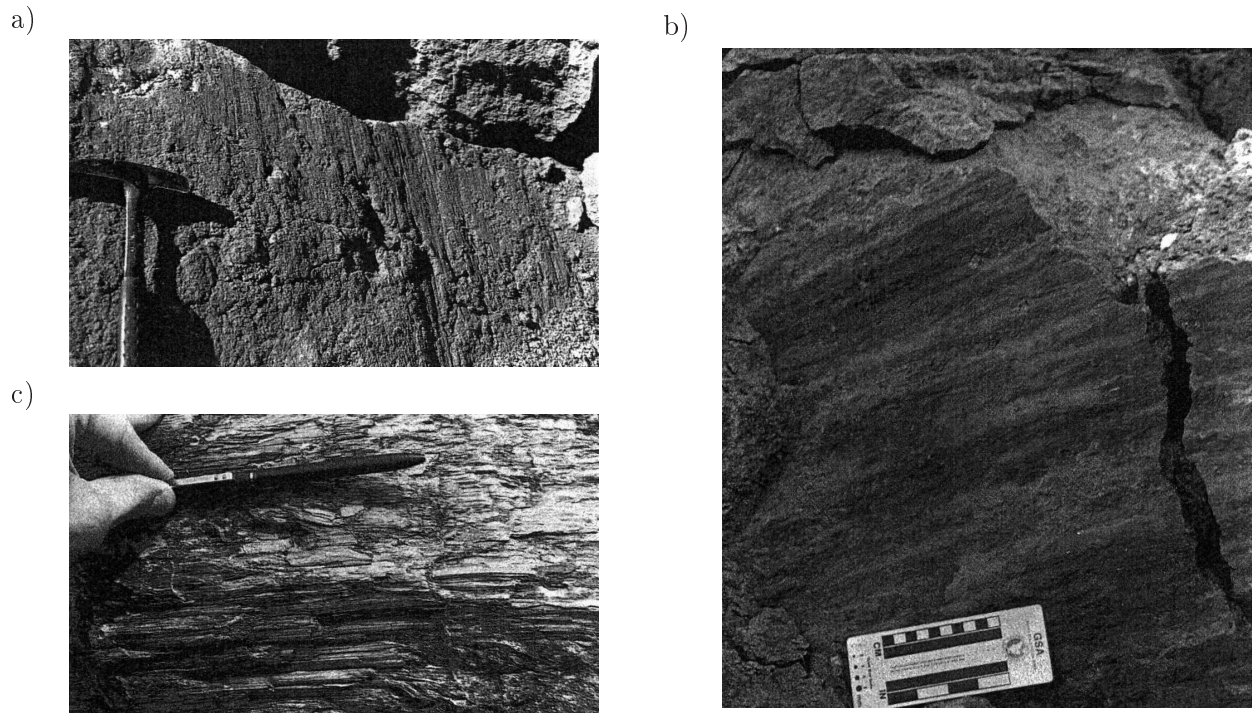
Figure 1.8: Lineations on fault surfaces formed during fault slip (Twiss and Moores, 1992, fig. 4.8, p. 57); a) Lineations formed by scratching and gouging of the fault surface; b) Ridge-in-groove lineations, or fault mulions; c) Serpentine slickenfiber lineations

the presence of water during the shear process (Sherbon Hills, 1972, p. 100). As Riedel shears do, they also form an acute angle with the shear planes, indicating the sense of relative movement of blocks. Also pinnate fractures are forming in the same manner as Riedel shears next to major faults (Twiss and Moores, 1992, fig.3.7, p. 41).

Joints

A joint is a fracture of geological origin along which no appreciable shear displacement has occurred. A group of parallel or sub-parallel joints as shown in fig. 1.14 is called a joint set and where differently orientd sets cross, like in fig. 1.15, they form a joint system. The tip of a growing joint is always perpendicular to σ_3 at the joint tip during propagation. Therefore temporal and/or spatial variations in the orientation of σ_3 during joint growth are indicated if curved joints are observed. More on joint development can be found in Price (1966).

Stylolites

Stylolites are one of several tectonic and/or diagenetic features considered to be formed by the process of "pressure solution". A comprehensive overview of stylolites and pressure solution is given by Guzzetta (1984). Important for palaeostress analysis is that stylolites form perpendicular to σ_1 (e.g. Ramsay and Huber, 1987, pp. 627). Fig. 1.16 shows examples of stylolite surfaces.

Figure 1.9: A steeply dipping fault surface at Ogmore-by-Sea, south Wales. The slickenfibre lineations provide information on the direction of fault slip; the stepped geometry of the calcite fibres indicates a sinistral sense of movement; such data on the orientations of fault planes and of the associated lineations permit the estimation of plaeostresses (Ramsay and Lisle, 2000, fig. 32.1, p. 786)
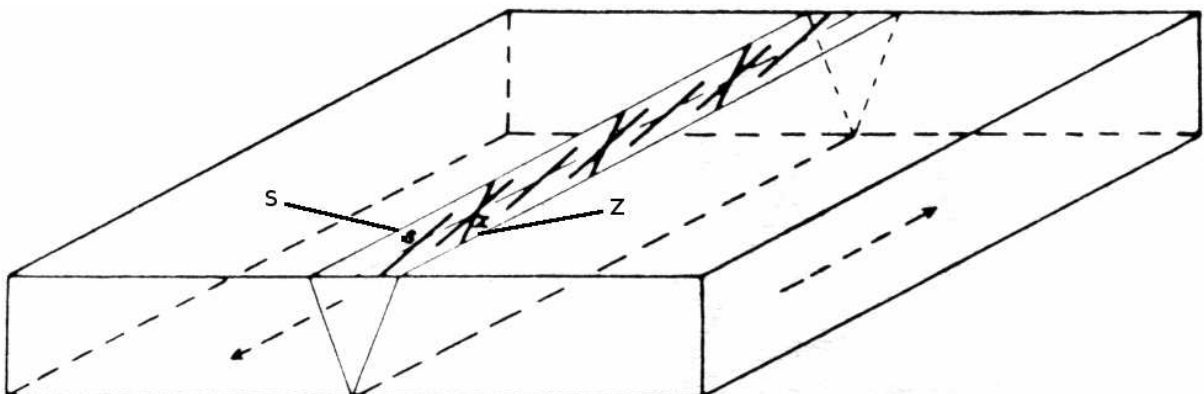
Figure 1.10: Development of secondary tension cracks (Z) during a shear process that causes shear cracks (S) (Riedel, W., 1929, fig. 9)
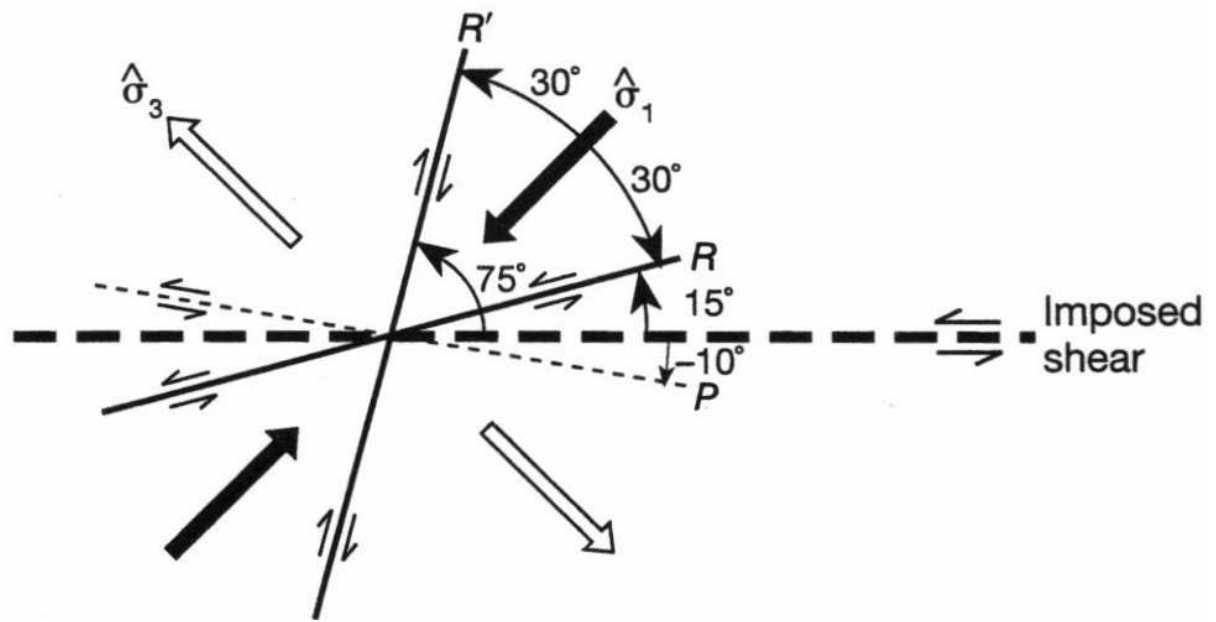
Figure 1.11: Example of the interpretation of R, R', and P-shears in terms of the Coulomb fracture criterion (Twiss and Moores, 1992, fig. 9.8 c., p. 174)
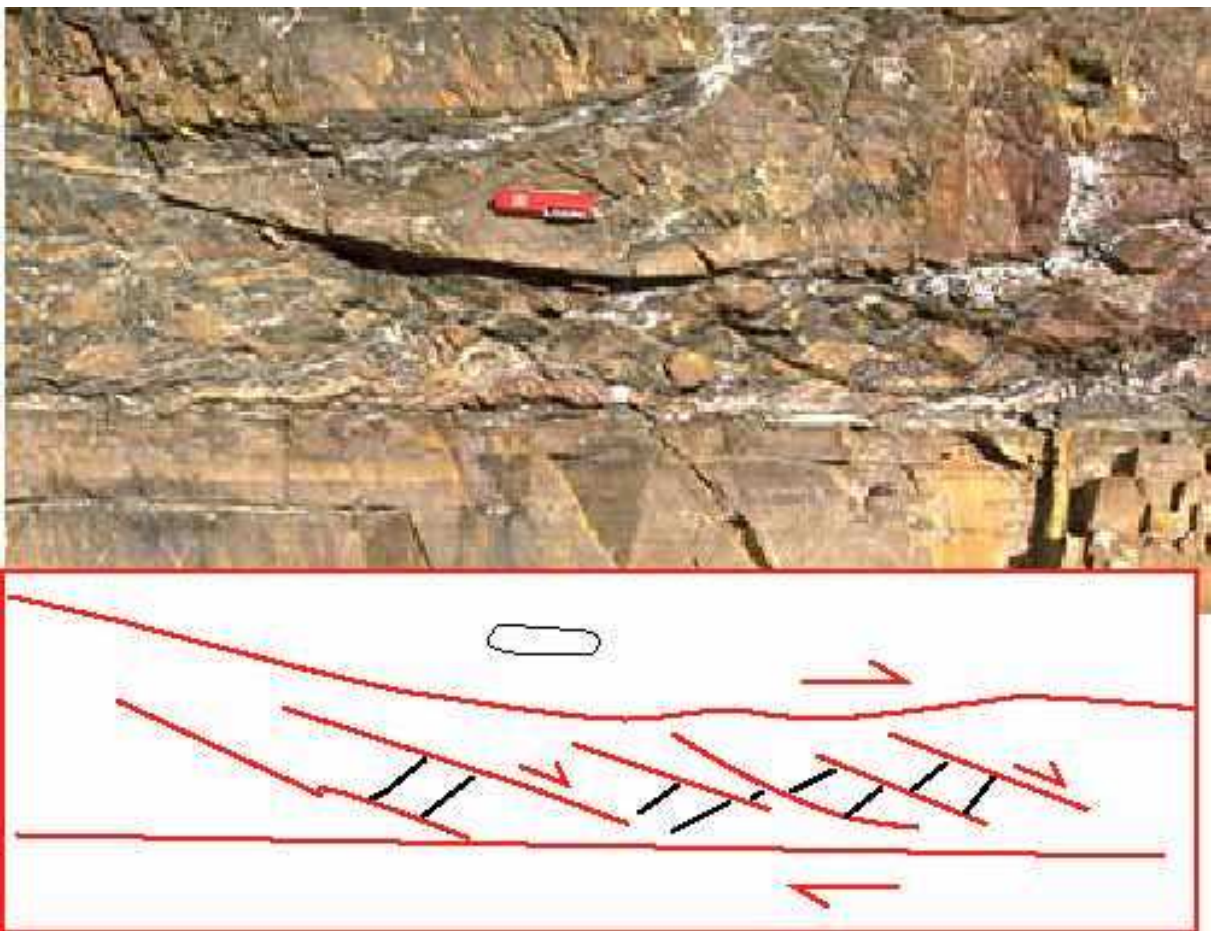
Figure 1.12: This photo is looking straight down onto a fault zone; the Riedel shears (also called R shears) are the small right-lateral faults which are gently inclined to the strike of the main fault; their presence suggests overall right-lateral motion on the zone (Miller, 2006)

Figure 1.13: Gash fractures (white veins) are extenstion fractures that commonly develop in a shear zone; they are aligned along differently oriented planar shear zones that make an angle of approximately 50° with each other; the ends of the fractures tend to bisect the angle between these shear zones (Twiss and Moores, 1992, fig. 3.8, p. 41)
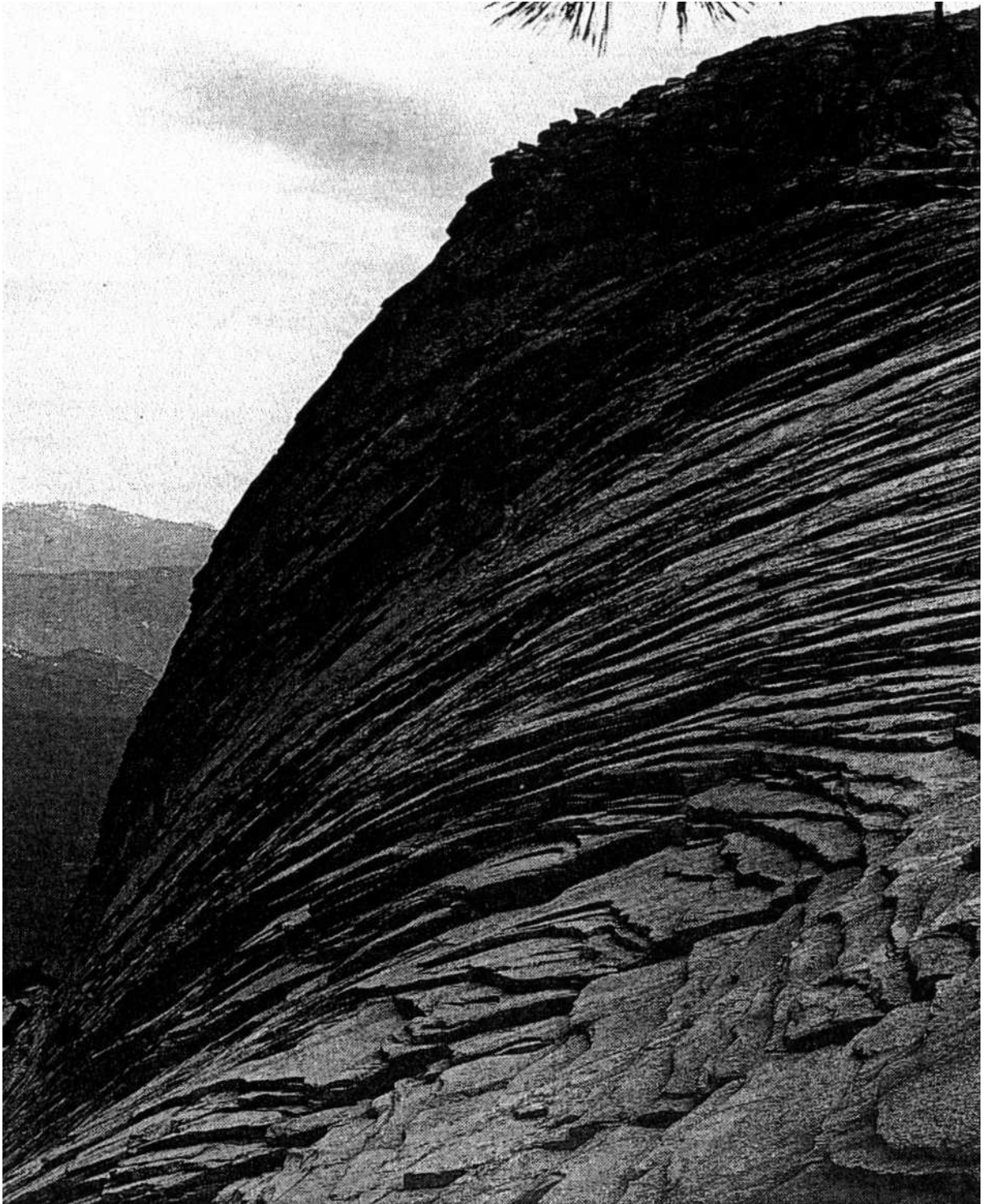
Figure 1.14: Sheet joints at Little Shuteye Pass, Sierra Nevada (Twiss and Moores, 1992, fig. 3.5, p. 40)
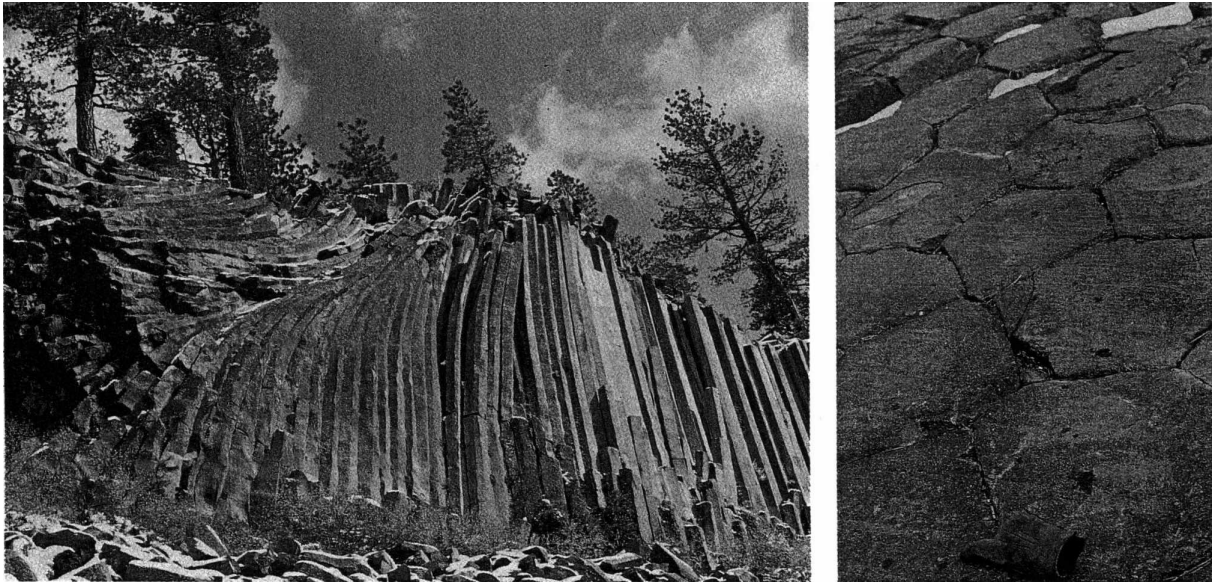
Figure 1.15: Columnar jointing at Devil's Postpile National Monument, California, U.S.A.; left: Columnar jointing in an andesitic flow; right: Cross section of the columnar joints (Twiss and Moores, 1992, fig. 3.6, p. 40)

Magma dikes

Due to buoyancy forces acting on the rim of a magma chamber, cracks may open and be filled with magma. Such magma filled cracks are called dikes and are often visible at the surface in regions with a high grade of volcanism, like a constructive or destructive plate boundary. They have different extensions in the three dimensions of space, being very thin and moderately wide horozontally, and relatively long in the vertical direction. The most important fact about dikes, with respect to the stress field, is that its large horizontal extension develops along the trajectories of the most compressive principal stress σ_1. Fig. 1.17 a) shows a complex pattern of dikes around a central volcanic complex in the Spanish Peaks area, Colorado, U.S.A. This example is taken from Ramsay (1967) after a work of Odé, H. (1957) who suggested that the dike pattern may be explained by the superposition of a radial stress distribution around the volcanic centre on a regional field related to the mountain front situated to the west of the Spanish Peaks. The stress trajectories of this combined stress field (fig. 1.17) are remarkably close to the stress distribution pattern determined from the dikes. This is an excellent example for an inhomogeneous stress field.

Folds

Up to now, only features that are related to cracking of rock have been presented, but rock may also react with ductile deformation in the form of folds to the presence of stress. Particle displacement in such folds also yields information about the underlying stress field during formation, but the discussion of folds with respect to the stress field is beyond the scope of this work. A good starting point are text books on structural geology, e.g. Ramsay (1967), Ramsay and Huber (1987), or Twiss and Moores (1992).

a)

b)

c)
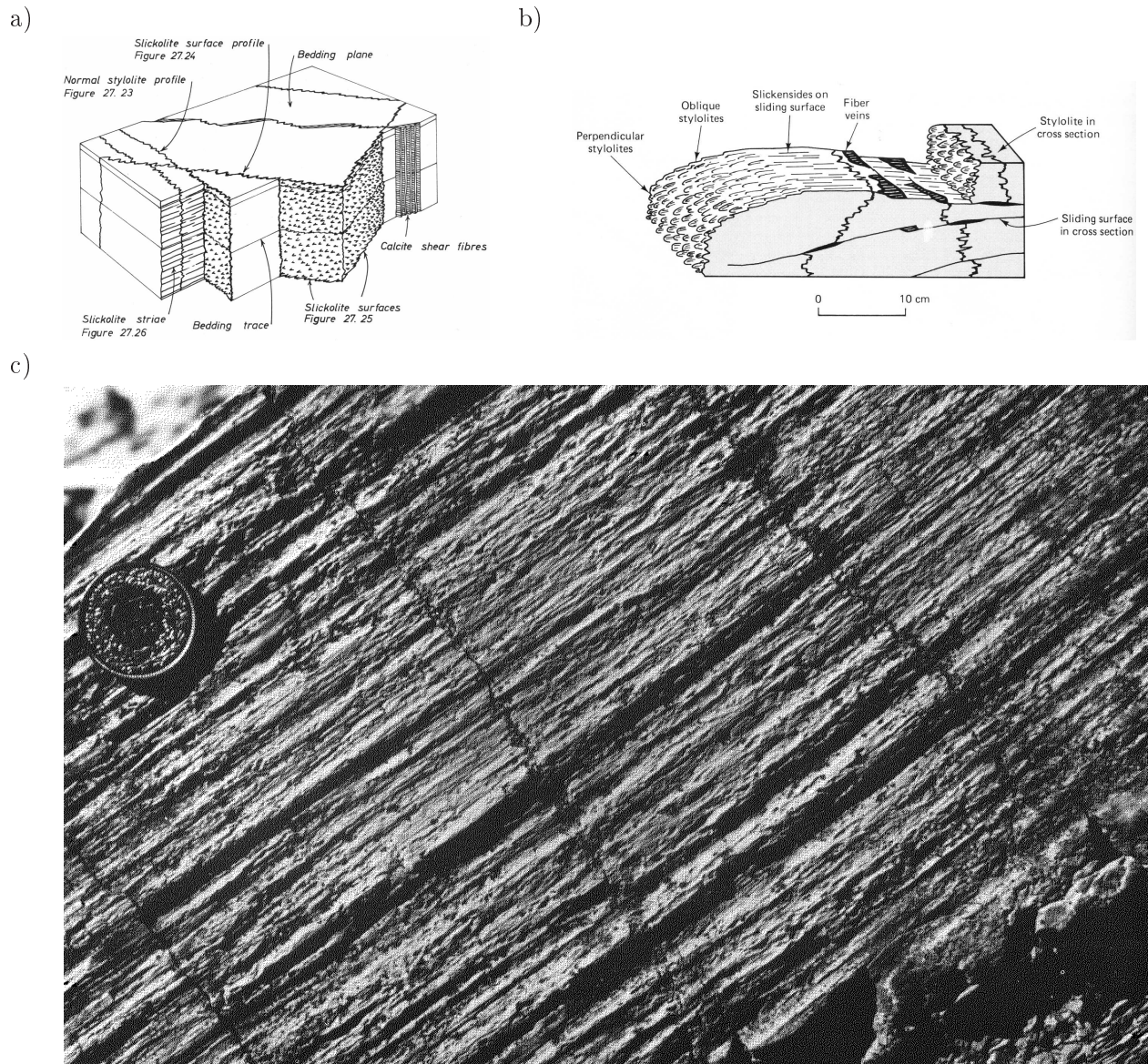
Figure 1.16: Stylolite surface examples: a) Schematic block diagram of the types of fracture surfaces seen in the Holderbank quarry, N Switzerland (Ramsay and Huber, 1987, p. 658); b) Schematic drawing of relationship among perpendicular and oblique stylolites, sliding surfaces, and veins in deformation of limestones by pressure solution (Suppe, 1984, p. 136); c) Surface where the stylolites run parallel to the joint face (slickolite striae); note the traces of joints with normal stylolites oriented perpendicular to the face; Holderbank, N Switzerland (Ramsay and Huber, 1987, p. 657)
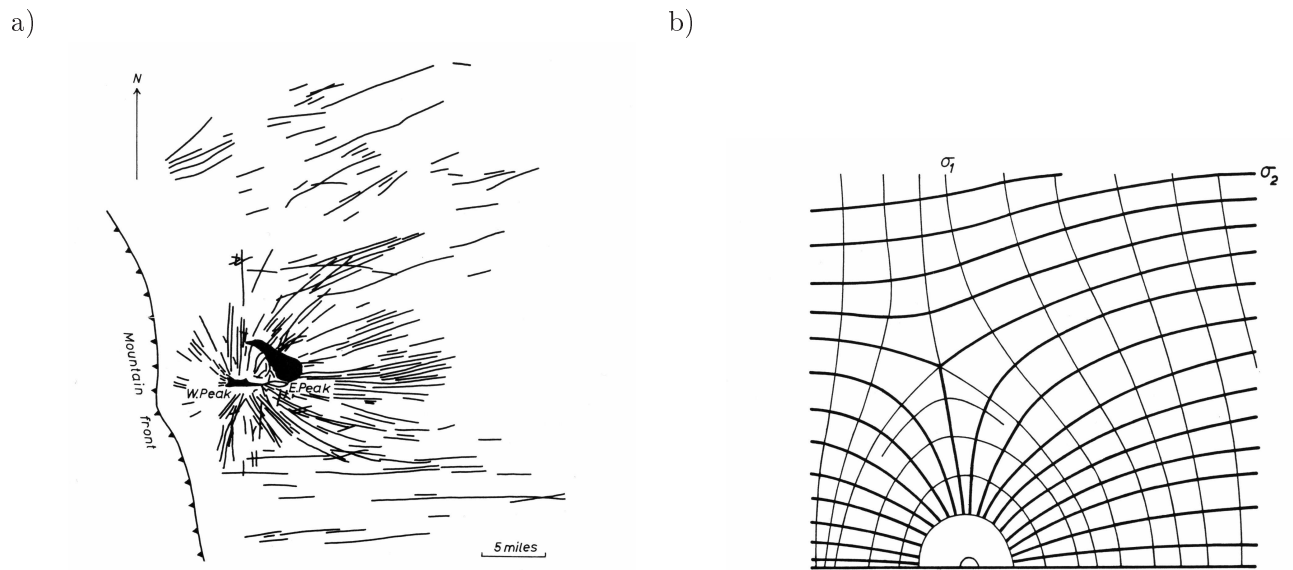
Figure 1.17: Dike pattern near Spanish Peaks, Colorado (Ramsay, 1967, fig. 2-14 and 2-15, pp. 45); a) mapping of dike orientation on the surface near the Rocky Mountains mountain front; b) Theoretical stress trajectories generated by the superposition of a compressive and a radial symmetric stress regime

Other

There are a number of other stress indicators including micro structures of crystals in rock, veins, micro-faults, or extension lineations that are not covered here. For further reference check out text books on structural geology (e.g. Ramsay and Huber, 1987; Twiss and Moores, 1992; Suppe, 1984) and Mattauer (2002).

1.3.2 Seismological stress indicators

The seismicity of the Earth is not distributed arbitrarily but concentrates mostly at plate boundaries (see fig. 1.18). It also occurs as intra-plate activity far away from the plate boundaries like at hot spot volcanoes (e.g. the Hawaiian Islands, the Eifel area in germany, or the Galápagos Islands) or regions with high rates of fluid migration (e.g. Vogtland/NW-Bohemia). For many of these seismically active regions, there exist large datasets of seismograms containing all the information necessary to extract properties of the earthquake that give an idea of the stress field that caused the appropriate rupture.

Earthquakes are the consequence of brittle failure that leads to fast slip on a fault which in turn emits elastic waves. These waves can be recorded with seismometers at the Earth's surface as seismograms. Accurate analysis of these seismograms yields physical parameters like the hypocentre and the magnitude of the event. For an inversion of the stress field, the most important parameter is the focal mechanism which indicates the motion direction of seismic waves as a function of the take-off and azimuth angles. It is an approximation of the radiation pattern of a double-couple force (see fig. 1.19 and fig. 1.1). The focal mechanism can be calculated if several polarities of certain phases of a seismic wave are known at different stations with a preferably wide range of azimuth angles Snoke (2003). The focal mechanism is described by three angles defining two perpendicular planes, of which one is the correct fault plane and the other is named auxiliary plane. The biggest disadvantage in dealing with focal mechanisms is that the correct fault plane is not known, so a priori information from the related geology is needed for the correct selection.

16
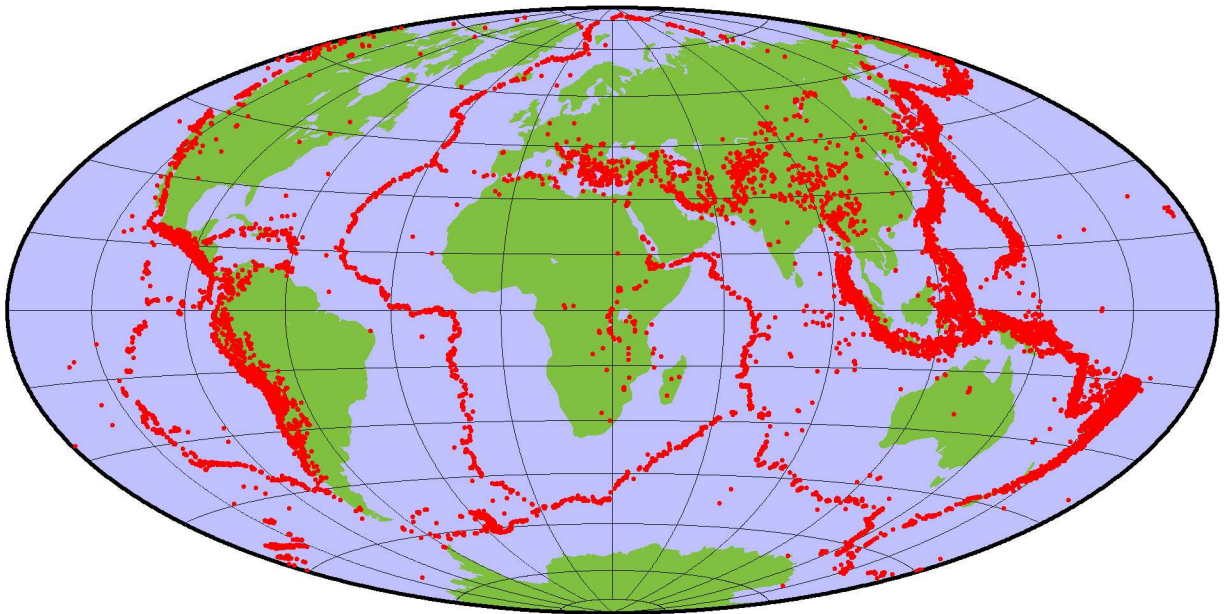
Figure 1.18: Seismicity of the world; epicentres from Harvard CMT catalogue (Harvard-Seismology, 2006); 18995 events from 1976 until today with moment magnitudes greater or equal to $M_W = 5$ are marked as red dots

a)

b)
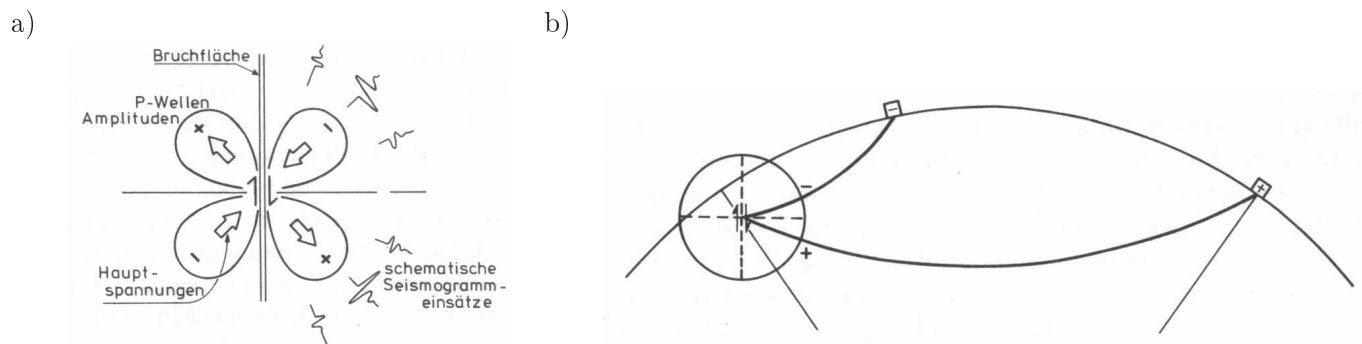
Figure 1.19: a) Principal 2D-projection of the radiation pattern of an earthquake; areas denoted by a $+$ and $-$ mean positive and negative first motion, respectively; b) projection of ray takeoff angles onto the focal sphere: a ray leaving the dihedra denoted by $+$ generate positive first motion, while rays leaving the $-$-dihedra result in negative first motion (Berckhemer, 1990, fig. 5.7 and 5.8, p. 71)

A more complex model for the radiation of elastic waves from the seismic source of an earthquake is the second rank moment tensor which consists of nine moment couples, six of which are independent, as will be discussed in section 3.1.3. There are different approaches to calculate the moment tensor. Full waveform inversion algorithms try to fit real seismograms with displacement seismograms calculated by assuming Greens functions (as a model for the Earth's transfer function) and a certain source time function. Many such methods for routine determination of the moment tensor have been established which have been reviewed comprehensively by Jost and Hermann (1989).

Knowledge of only one focal parameter is not sufficient to derive a unique solution for the underlying stress field. Though it is possible to determine four linearly independent parameters of the spatiotemporally homogeneous stress field, if at least four focal mechanisms from preferably different faults are known.

1.3.3 In-situ stress measurements

Another source for stress indicators is the drilling of a borehole. There are different methods to obtain directions of principal stress directions under appropriate assumptions. In the following paragraphs, the most popular methods are described. Reading chapter 5 of the book of Brady and Brown (2004) is highly appreciated.

Overcoring

In this method the state of stress is determined indirectly by the usage of triaxial strain cells. Fig. 1.20 shows the principle of the method. A slightly different approach is to place and fixe the strain cell is on the ground after drilling the wide hole. Now, another hole is drilled, leaving it on a pedestal. The stress relief now causes strains in the vicinity of the borehole, so that the strain cell is deformed and therefore records the occuring strain. Taking the elastic properties and a solution for the stress distribution around a hole (Leeman and Hayes, 1966), it is then possible to reconstruct the stress that has acted on the untouched rock. The only difference between these two approaches is the type of strain cell that is used.

Flatjack measurements

This method can be applied at sites where there exist cavities of about man size. Three more prerequisites are required: First, a relatively undisturbed surface is needed; second, the opening must have a geometry for which a solution of the stress field alteration is well known; third, the rock must act elastically by means of Hook's Law. The principle of this method is illustrated in fig. 1.21 and also described in Brady and Brown (2004). The basic idea is to measure the normal stresses for some arbitrarily oriented planes and to reconstruct the complete stress tensor using an analytic model of the stress distribution around a cavity.

Hydraulic fracturing

This technique destroys the borehole wall and is therefore only applied when the borehole is not needed for other purposes anymore. Two different methods are used to measure the magnitude of the minimum principal stress σ_3 and its direction, respectively. The setup of a hydraulic fracturing experiment is shown in fig. 1.22. As described in the figure's caption, the magnitude of σ_3 is determined by the
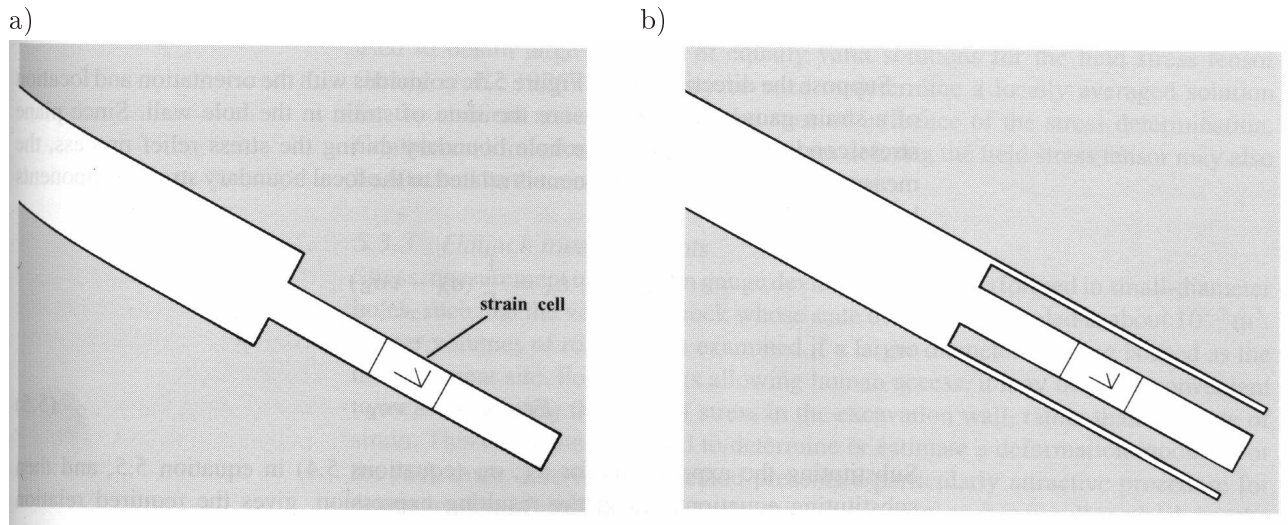
Figure 1.20: Principle of the overcoring technique: a) a small hole is drilled on the ground of a borehole and a strain cell is fixed inside; b) around the small hole, a thin tubular hole is drilled or overcored (Brady and Brown, 2004, fig. 5-4, p. 149)
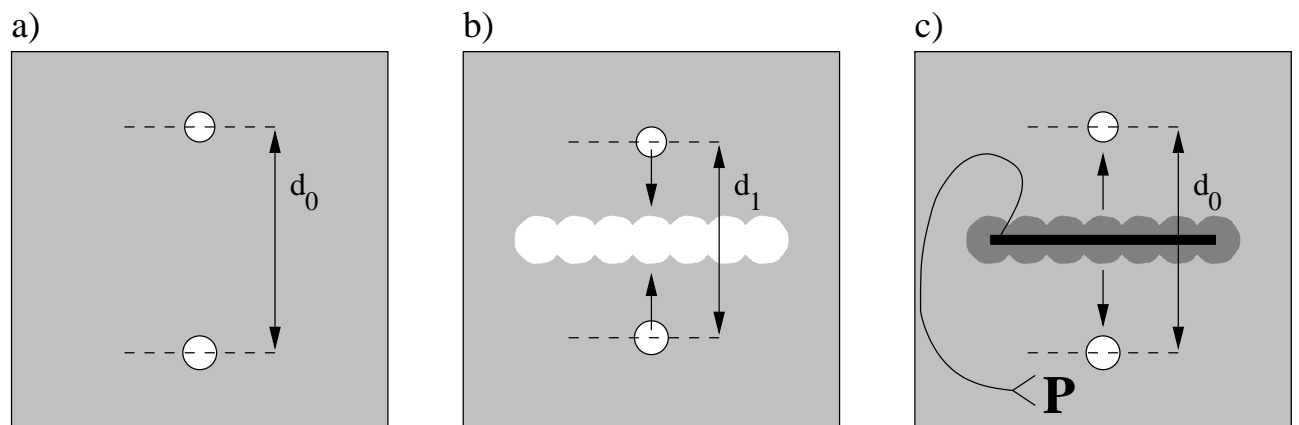
Figure 1.21: Principle of the flatjack measurement to quantify magnitudes of normal stress after (Brady and Brown, 2004, fig. 5-6, p. 154): a) two small holes are drilled and the distance between them, d_0, is measured; b) a thin cavity is drilled between the two first holes, causing closure between the first two holes; c) the flatjack consists of two parallel plates that are welded along the edges and attached to a pump that hydraulically generates the pressure **P** via a non-return connection inside the flatjack (bold line); it is grouted to the slot and pressurised to restore the original distance between the first two holes; the displacement cancellation pressure corresponds closely to the normal stress component directed perpendicular to the slot axis prior to slot cutting
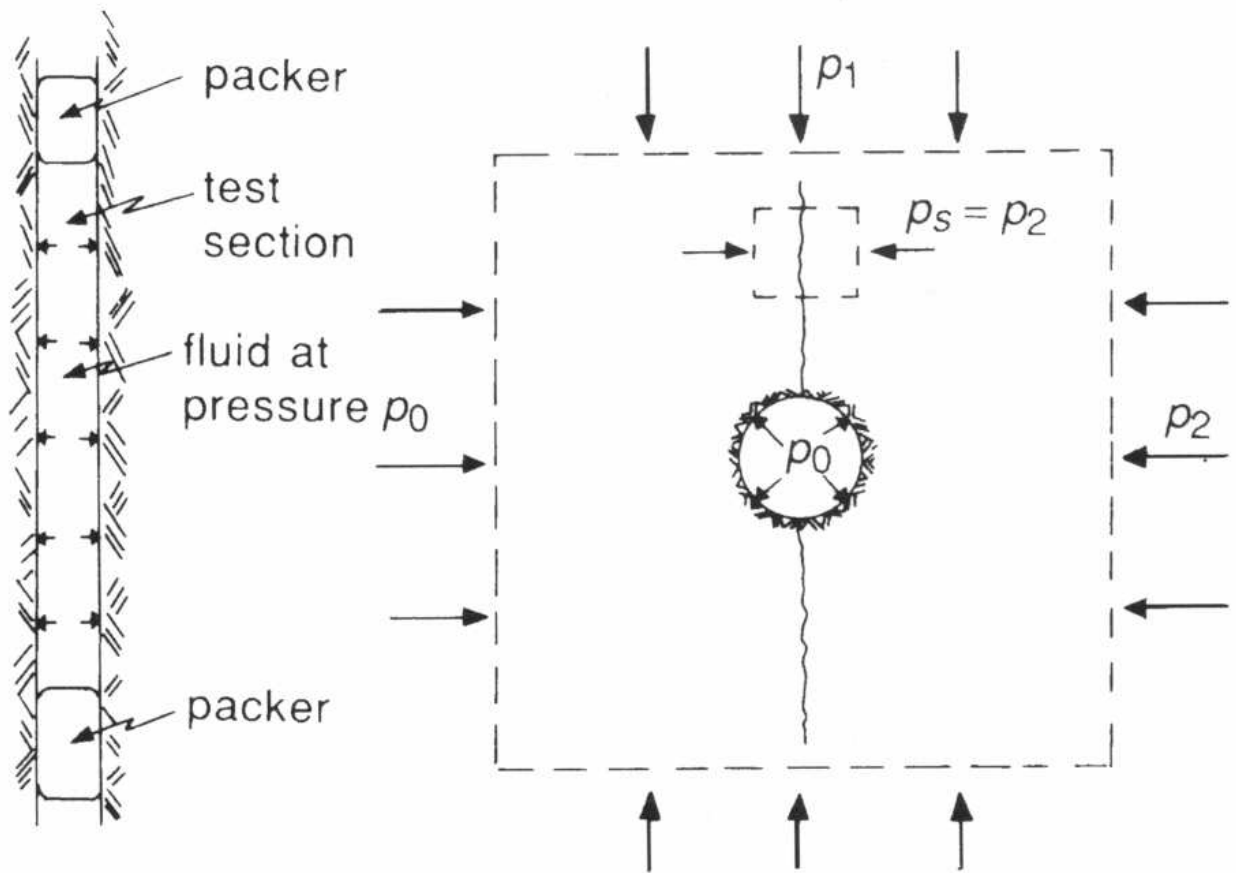
Figure 1.22: Principle of the hydraulic fracturing technique: the borehole is set under pressure by using some fluid which causes cracks to open parallel to the maximum compressive stress p_1 (Brady and Brown, 2004, fig. 5-6, p. 154): left) part of the borehole is sealed with packers, fluid is brought in and pressurised (p_0); right) after p_0 has reached a magnitude of at least $p_2 (\equiv \sigma_3)$, a fracture develops perpendicular to the borehole wall

minimum pressure to cause a crack to open. The orientation of this crack can not easily be determined. An indirect approach is to record the primary and secondary seismicity ("aftershocks") caused by the fracture opening. From the focal mechanisms of these induced earthquakes, the orientation of the main fracture may be estimated.

Drilling induced fractures

Drilling induced fractures are small-scale tensile fractures in the borehole wall that are induced by the drilling process. The physics behind this phenomenon is mainly the same as for the formation of hydraulically induced fractures. They open along the axis of a vertical borehole and the opening direction is mainly governed by the direction of the most compressive principle stress σ_1. The orientation of the fractures is obtained through well logging techniques (see e.g. Brady and Brown, 2004).
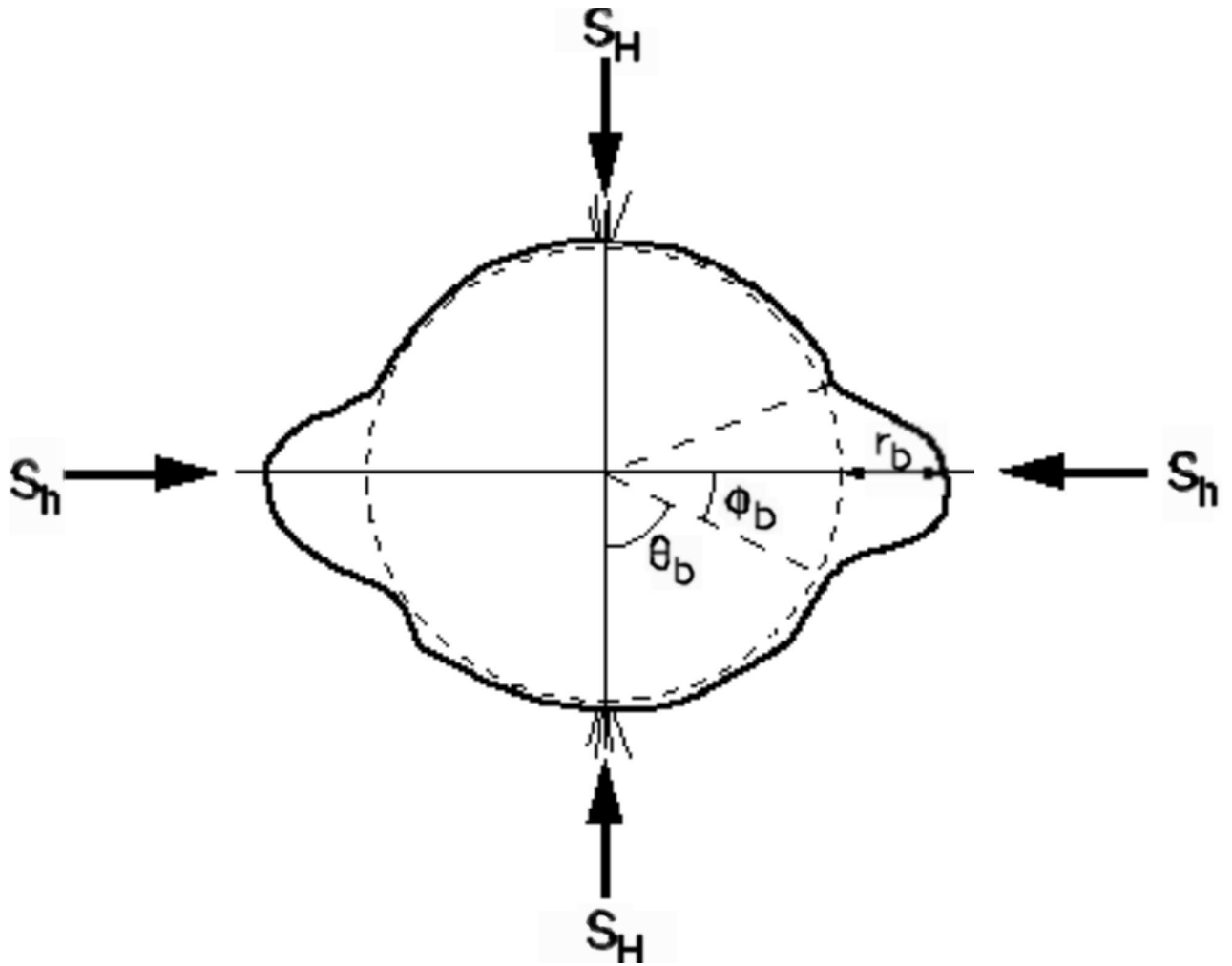
Figure 1.23: Borehole breakout in the wall of a vertical borehole subject to the maximum (S_H) and minimum (S_h) principal horizontal stresses: θ_b is the breakout orientation, ϕ_b the breakout opening half-angle and r_b the breakout depth (NASA, 2003)

Borehole breakouts

After the borehole has been drilled, the hole itself acts like a thin cylindrical cavity under stress. Most likely, the wall of the well fails to resist the stress and shows brittle failure. Measuring the orientation of these borehole breakouts according to fig. 1.23 yields the direction of the maximal (S_H) and minimal (S_h) horizontal stresses. For a comprehensive review of the method see Zoback et al. (1985) and Zoback et al. (2003).

1.4   Stress inversion

Since faulting is a consequence of failure in zones of weakness due to stresses acting inside a body, the observation of indicators for such failure, can be inverted for the causing stress field. Every inversion approach has the goal to determine model parameters which explain a number of observations with a minimum deviation from its predictions. In designing an inverse method, three conceptional decissions have to be made. First, an appropriate description of the misfit between prediction and observation has

21
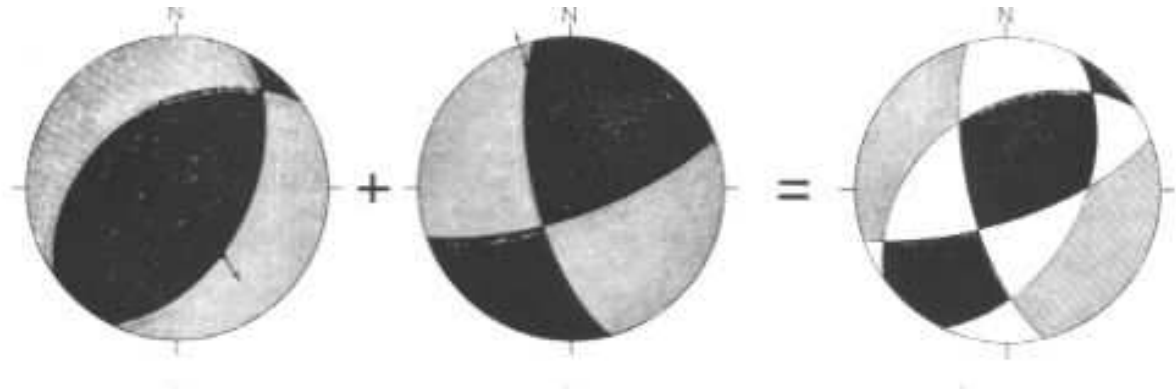
Figure 1.24: Principle of the right dihedra method: Areas of positive and negative first motion constrain the directions of the most extensive and most compressive principal stress directions, respectively (Angelier and Mechler, 1977)

to be formulated. Second, a normative measure of misfit to be minimized has to be defined. Third, the method to find the best-fitting model and its associated range of uncertainty has to be specified. In the following sections, I will present several methods to invert geological fault striations, fault mechanisms, or sense of slip information for the homogeneous regional stress field. All methods have in common that they assume the stress field to be homogeneous in time and space in the volume under study. Most of the methods presented deal with fault slip data, while some also allow focal mechanism data to be used.

1.4.1 Inverting fault slip data

Angelier and Mechler (1977) follow a graphical approach and develop the right dihedra method to use fault slip or focal mechanism data to constrain the directions of the principle axes of stress. They set up basic vector relations between the pressure and tension axes of the focal mechanism ($\vec{P}$ and $\vec{T}$) and the orientations of the principle axes of stress. The idea is that the most compressional principle stress axis σ_1 must lie in the quadrants of the focal mechanism with dillatational first motion, as illustrated in fig. 1.19. Then for a population of events originating from a region with a homogeneous stress field all dillatational quadrants are superposed, as illustrated in fig. 1.24, so that σ_1 is most probably lying in the region with the highest number of dillatational quadrants. This method can be used to check for the uniformity of fault slip data in the way that for a homogeneous stress field, the σ_1 and σ_3 areas should be well defined.

Albarello (2000) proposes a resampling approach to test the uniformity of the stress field from fault data. He uses the same vector relations introduced with the right dihedra method to check for the compatibility of a certain stress tensor with the observed data. Then a procedure is defined to check stress-field uniformity by a statistical analysis of the available fault data. First the volume under study is subdivided into subdomains with an approximately homogeneous stress field. Then the probability that a number of faults is compatible with a given stress field by chance (i.e. that they actually slipped due to a different stress configuration) is evaluated. If this probability becomes significantly small, heterogeneities can safely be excluded. In this case approximate confidence intervals for the principal stress directions can be obtained.

Angelier (1979) suggests a direct inversion method based on an earlier least squares minimization problem. He seeks to minimize the component of tangential stress perpendicular to measured slickenslides. To achieve this, he assumes the components of the stress tensor and minimizes a polynome of these
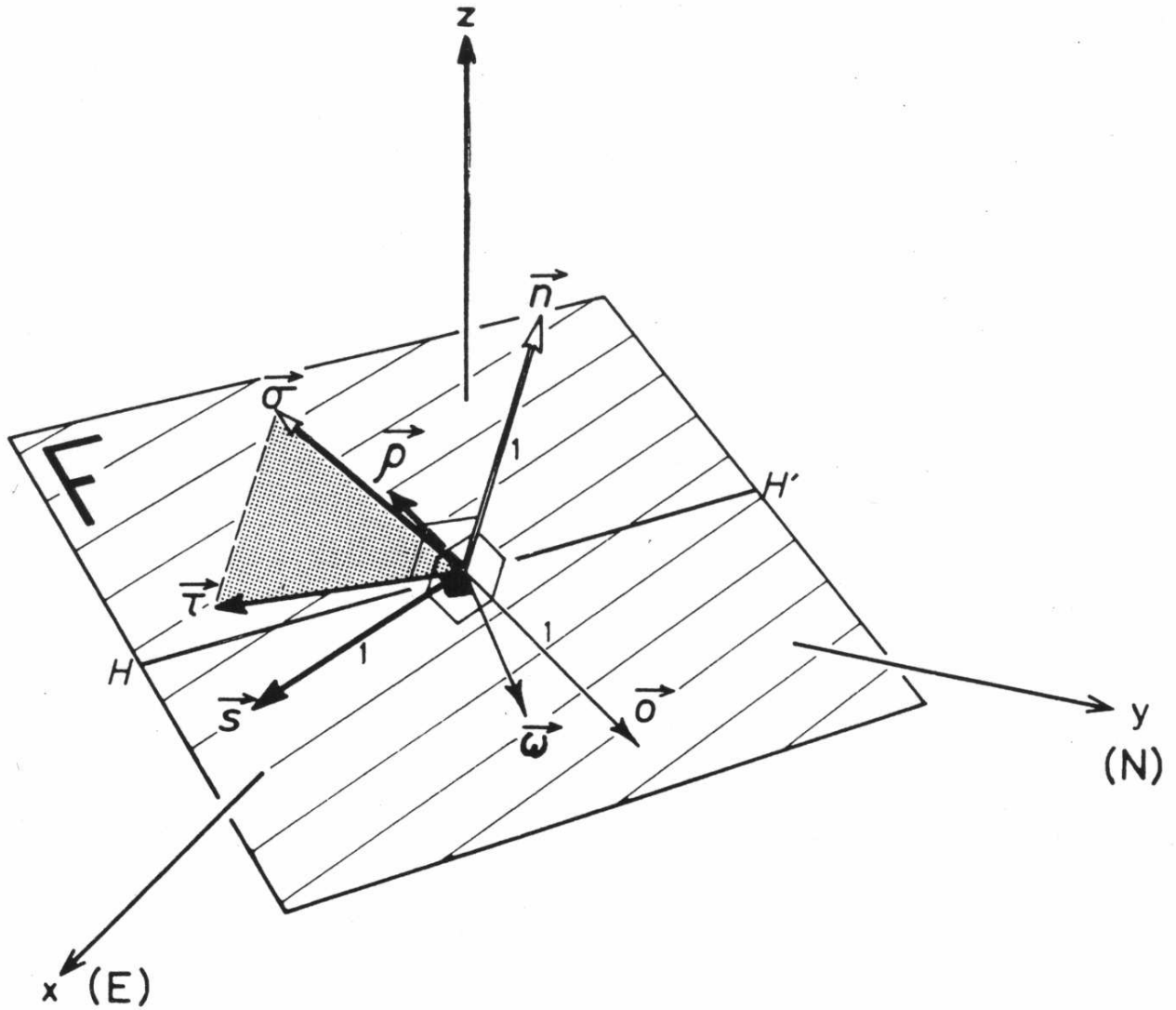
Figure 1.25: Definition of unitary vectors plane normal $\vec{n}$, slip $\vec{s}$, traction $\vec{\sigma}$ tangential stress $\vec{\tau}$, residual $\vec{\rho}$, vector $\vec{o} = \vec{n} \times \vec{s}$, and vector $\vec{\omega} = \vec{n} \times \vec{\sigma}$ in relation to plane F (Angelier, 1979, fig. 3)

components.

Another approach is presented by Michael (1984). Under the assumption that all earthquakes under study have similar magnitudes, some relatively simple equations are derived that give the values for five of the six parameters of the stress tensor. He also suggests to take faults that are related to folds into account for stress inversions and shows that reliable results can be obtained.

In situations where only the sense of slip is known for a given fault (i.e. if it is a normal, reverse, or strike-slip fault) it is not obvious how the underlying stress field looks like in detail. Lisle et al. (2001) propose a method to invert such data for the orientation of the principal axes of stress. They are able to show that its uncertainties are similar to those obtained by the right dihedra method (Angelier and Mechler, 1977).

1.4.2 Inverting focal mechanism data

Inverting fault slip data for the homogeneous stress field is a problem, that has been solved in many different ways, as discussed previously. All approaches take advantage of the knowledge of the slip vector, while in the case of a focal mechanism this information is ambiguous. If the correct fault plane can be determined by a different method, like alignment of hypocecentres on some structure in space for a set of several focal mechanisms, the task reduces to the inversion of fault slip data. In any other case, the inversion algorithm either has to distinguish between fault plane and auxiliary plane or it has not to care about it (Michael, 1987).

Maybe the crudest way to deal with the problem is to ignore it and to use both nodal planes as possible fault planes in the inversion process as proposed by Angelier (1984). He states that this unphysical attempt will work, if the generating stress field is uniaxial (i.e. $\sigma_1 = \sigma_2$ or $\sigma_3 = \sigma_2$).

Gephart and Forsyth (1984) and Gephart (1990) describe a different approach for defining the misfit function by using the minimum rotation angle about an arbitrary axis of the fault plane geometry. They suggest to compute the misfit of both nodal planes of a focal mechanism and to select the one with the smallest misfit. To find the best fitting stress model, they select the most basic inversion technique to search on a grid for the minimum of the misfit function.

In the approach of Michael (1984) the isotropic stress is constrained to be zero and the events are assumed to have similar magnitudes. He then sets up a system of linear equations that is minimised using a standard LSQR technique. One important statement is that also folding-induced faults can be used for a stress inversion, instantly increasing the available data for stress inversions.

Yin (1996) describes an algorithm that deals with the ambiguity in the identification of fault and auxiliary plane. He finds that the stress directions are well defined, but that the stress ratio suffers from this uncertainty. Finally he states that the correct fault plane cannot be distinguished on the basis of a stress inverion of fault plane solutions alone.

An example for an algorithm that doesn't care about the ambigiuty is the right dihedra method presented by Angelier and Mechler (1977) which is described earlier in the previous section.

Angelier (2002) proposes to maximise the slip shear stress component (SSSC) which is the scalar product of the slip $\vec{s}$ and the shear stress $\vec{\tau}$. The SSSC is large if $\vec{s}$ is parallel or sub-parallel to $\vec{\tau}$, while it becomes smaller if the vectors differ. He shows that the value of the SSSC does not depend on the choice of nodal plane, so that the following inversion algorithm can take focal mechanisms into account.

Dahm and Plenefisch (2001) follow a different approach by assuming that slip occurs in pre-existent zones of weakness in the direction of maximum energy radiation. They derive the formulas describing the forward problem from the relation between the energy radiation, stress drop and the moment tensor. They propose to determine the fault plane from the two nodal planes of a focal mechanism by selecting the nodal plane with the minimum error for the inversion process.

1.5 Stress inhomogeneities

The most common assumption that holds for many tectonic settings is that the stress field is regionally homogeneous. However, inhomogeneities in the stress field can occur as variations in the directions of the principal stress axes as well as in their magnitudes. They can be caused by a wide variety of tectonic features like the presence of faults or different interacting tectonic units, dike ascent, or other
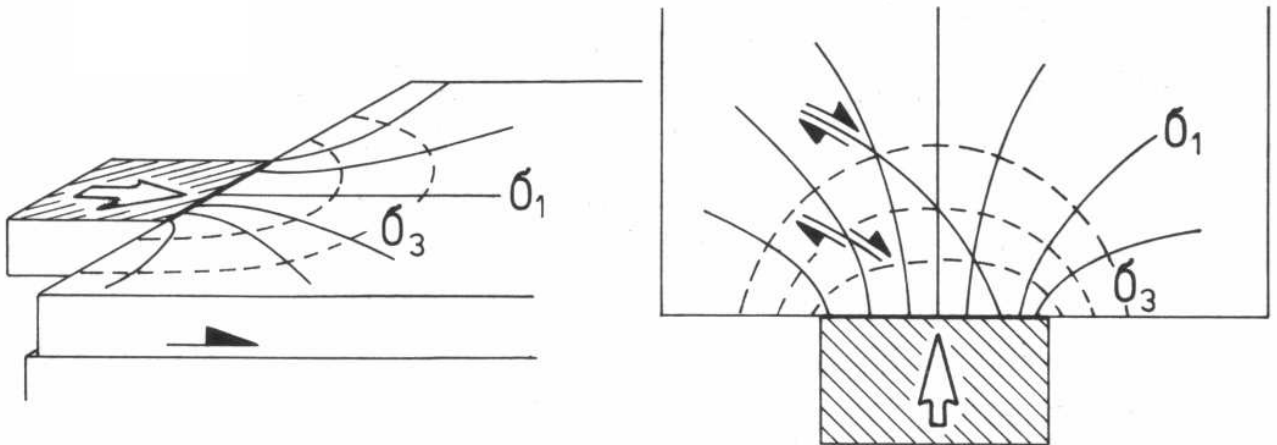
Figure 1.26: Stress trajectories for an elastic plate under directional load (Eisbacher, 1991, fig. 11.15 a), p. 79)

migrating fluids. The nature of these phenomena is discussed in the upcoming sections.

1.5.1 Tectonic features and faults

There are several different tectonic features like faults, graben structures, etc. that in some way change the local stress field. A very common feature is a fault for which it is well known that it disturbs the stress field locally (Atkinson, 1987, article from Pollard). If a fault has just slipped, it is free of load so that no shear stress acts on the fault plane anymore. In this case one of the principal axes of stress is constrained to be perpendicular to the fault plane (e.g. Ramsay and Lisle, 2000). It follows that the regional stress field is disturbed by a local inhomogeneity. When the fault is fully loaded (i.e. it is stressed and hasn't slipped yet), it just resists the shear force caused by the regional stress. That means that there is no perturbation of the regional stress field. There is nearly the same situation at the free surface, where there also exist no shear forces. Therefore an air filled cavity perturbs the stress field in a body in that way that one principal axis of stress is always oriented perpendicular to the edge of the cavity.

Another source for stress inhomogeneities is gravitational load or directional pressure along one edge of a plate. According to Newton's third axiom, every force generates a counter force, so if a force acts on some body, it is cancelled with stress of the same magnitude inside the body. The direction of this internal counter force is described by the stress tensor. A basic scenario is a uniform load along a bounded part of an elastic plate, as illustrated in fig. 1.26.

For other tectonic settings, like for normal faulting regimes, the appropriate stress trajectories look different. Fig. 1.27 shows two different scenarios where normal faulting occurs. Earthquakes happening in these regions are subject to quite variable, heterogeneous stress.

Last, intersecting tectonic systems result in a very heterogeneous stress distribution, because all stress sub-fields generated by each system are superposed. Fig. 1.17 shows such a superposition of regional stress fields caused by the combination of a mountain push and a magma chamber below a volcano.

a)   b)
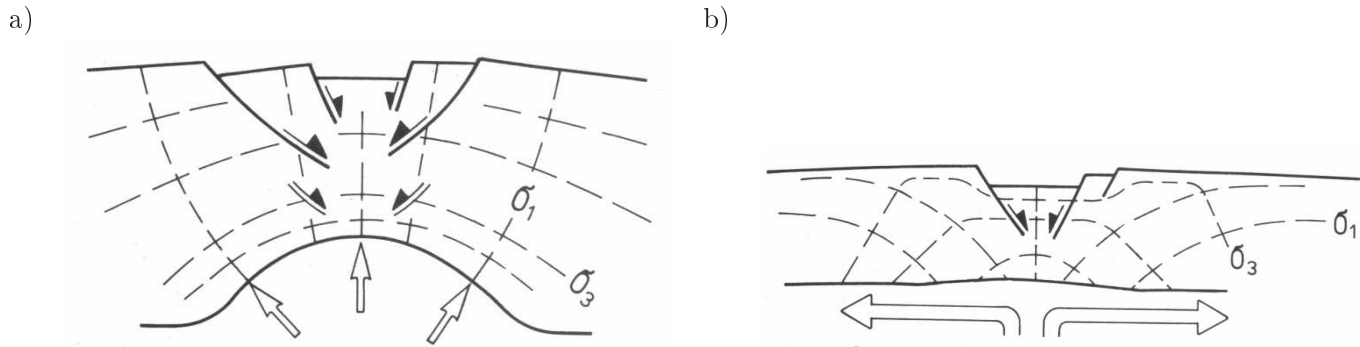
Figure 1.27: Stress trajectories for different normal faulting scenarios: a) dome uplift (e.g. magma dome development); b) symmetric stretching (e.g. mid ocean ridges) (Eisbacher, 1991, fig. 9.9)

1.5.2   Change in physical parameters

Stress inhomogeneities may also be caused by changes in material parameters. Variation in strength of material leads to the presence of zones which consist of rock that is weaker than its surroundings. It therefore can't last the same load and is more likely to deform causing perturbations of the stress field.

Especially in volcanic zones there exist caverns filled with hot magma. These zones of high temperature of about $800^oC - 1200^oC$ also heat the surrounding material which is expanding consequently. This extension results in a radial symmetric stress inhomogeneity, like in fig. 1.17. A good example of dome uplift, as shown in fig. 1.27 a, are salt domes in north Germany.

In many layers in the Earth's crust there are fluids present that result in a pore pressure inside the rock. If such a layer is sealed off from the other layers and the layer's volume is reduced due to some tectonic event then the fluid inside the pores is compressed and therefore causes a pressure to the wall of the layer. In some distance in the surrounding layers the resulting forces are approximately radial symmetric. This also causes an inhomogeneity in the stress field. Another effect of the presence of fluids is the reduced frictional resistance which results in a higher rate of small earthquakes within a highly damaged rock mass, and thus a deformation and weakening of these parts of the rock.

1.6   Study Areas

For the methods described in this work, areas with a high density of stress indicators are needed. There are two nearby spots in the region of SE-Germany and NW-Czechia which meet this prerequisite very well. NW-Czechia and the Vogtland region are well known for the periodical occurence of earthquake swarms and single event seismicity, so a large number of data is available because moment tensor or focal mechanism data has been published for many earthquakes. For this work, waveform data of the 1997 Vogtland/NW-Bohemia earthquake swarm has been made available in GSE 2.0 format (Horálek et al., 2000). Throughout the rest of the work, the term "1997 swarm" will be used. About 60-70 km apart is the location of the Continental Deep Drilling Project "Kontinentale Tief-Bohrung" (KTB). This borehole has been studied intensively since the early 1980's with several different methods yielding orientations of stress axes, focal mechanisms, and in-situ stress measurements (e.g. Dahlheim et al., 1997; Brudy et al., 1997; Zoback and Harjes, 1997).

26

1.6.1 Vogtland/NW-Bohemia

The area Vogtland/NW-Bohemia shown in fig. 1.28 is one of the most seismoactive intra-plate areas in Central Europe. Since the early 1980s the permanent seismic network WEBNET of the Academy of Sciences, Prague of three component seismometers is in operation and records event-triggered seismograms (Horálek et al., 2000). Therefore the swarms that have occured since then are very well documented.

Tectonic features

The main tectonic features exposed at the Earth's surface in NW-Bohemia are the Marianske Lazne Fault (MLF) and the Eger Graben (EG), which lies east of the MLF (see fig. 1.29). In the centre of the tertiary Eger Basin (EB) which is located west of the MLF lies the small town of Nový Kostel which is located nearly directly above the epicentres of the events of the 1997 swarm.

Near the seismoactive zone there are the two non-active quarternary volcanoes. Wagner et al. (2002) estimates the age of Železná Høurka (german: Eisenbühl) and and Komorní Høurka (german: Kammerbühl), which lie approximately 12 km to the ESE of the MLF to be $519 \pm 51 ka$ and $726 \pm 59 ka$, respectively.

Earthquake swarms near Nový Kostel

Neunhöfer and Meier (2004) present an overview of the observed swarm activity in the area Vogtland/ NW-Bohemia. They conclude that the majority of the seismicity is released during earthquake swarms. They identify six swarm zones, from which the Nový Kostel area is most active. An earthquake swarm is defined as a sequence of earthquakes with no particular outstanding main event that dominates in size (Richter, 1958; Mogi, 1963; Scholz, 1990). The occurence of swarms in this region is well known and documented since the mid 16th century (e.g. Skácelová et al., 1998) by several authors. Two historical examples for swarm activity are shown in fig. 1.30. Earthquake swarms are commonly associated with volcanic active regions, as stated by e.g. Sykes (1970), but only pleistocenic volcanism is reported in this area (Wagner et al., 2002). The seismic activity is often related to the main tectonic features Mariánské Lázně Fault and the Eger Graben. However, Bankwitz et al. (2003) relate the seismicity to the newly identified N-S trendind Počatky-Plesná zone whose orientation is defined by a mofette line. Schunk et al. (2003) find the N-S oriented Nový Kostel - Plesná deep shear zone which influences the tectonic development of the Eger Basin (situated at the western extension of the Eger Graben and delimited by the Mariánské Lázně Fault to the E) since middle pleistocene (781 ka).

1.6.2 KTB vicinity

The German Continental Deep Drilling Program (Kontinentale TiefBohrung - KTB) drill holes are situated in NE Bavaria at the western rim of the Bohemian Massif and the SW extension of the Cenozoic Ohre/Cheb rift. They have final depths of 4.0 km for the pilot hole and 9.1 km for the main hole. A permanent network of four stations has been installed prior to drilling of the holes (Dahlheim et al., 1997) and temporary networks have been established during two hydraulic fracturing injection experiments in 1994 consisting of 73 short-period seismometers which is described by Zoback and Harjes (1997) and Jost et al. (1998) and in 2000 using 39 stations (Baisch et al., 2002; Bohnhoff et al., 2004). For both experiments, a sonde inside the pilot hole was also installed.
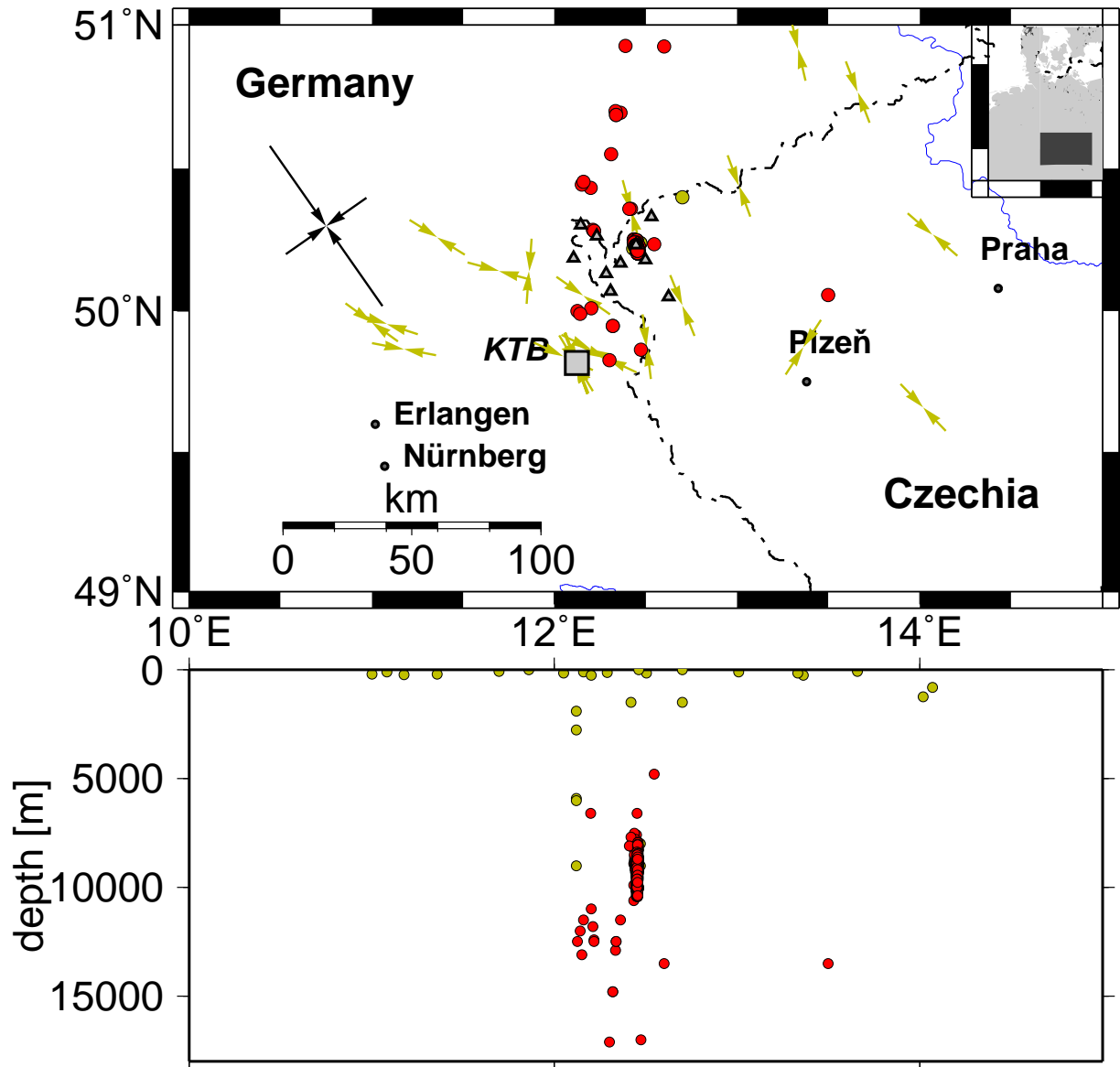
Figure 1.28: Example for inhomogeneities in the regional stress field: region SE-Germany/NW-Czechia; upper part: arrows indicate horizontal stress directions (black: σ_H and σ_h from regional stress field (Müller et al., 1992); yellow: σ_H from the World Stress Map (Reinecker et al., 2004)), circles: earthquake epicentres (yellow: from WSM; red: 1997 swarm, swarm 2000, single events), triangles: stations used in this work; lower part: depth subsection of measurements
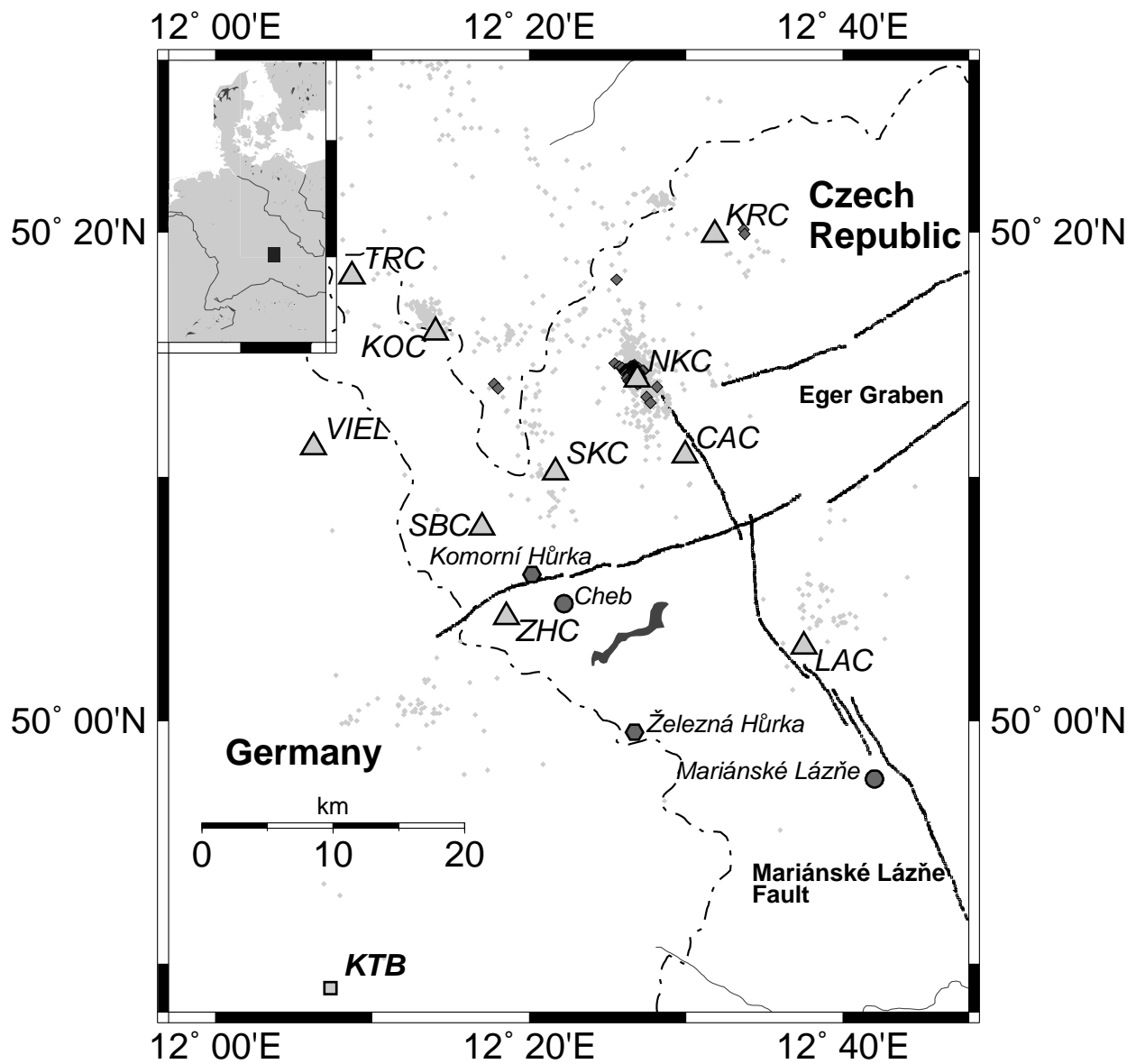
Figure 1.29: Study area Vogtland/NW-Bohemia with local seismological network WEBNET; triangles mark stations; dots indicate seismicity from 1985-1997; diamonds mark seismicity of the 1997 swarm; major geological features are the Mariánské Lázně Fault, the Eger Graben, and the volcanoes Komorní Hůrka and Železná Hůrka
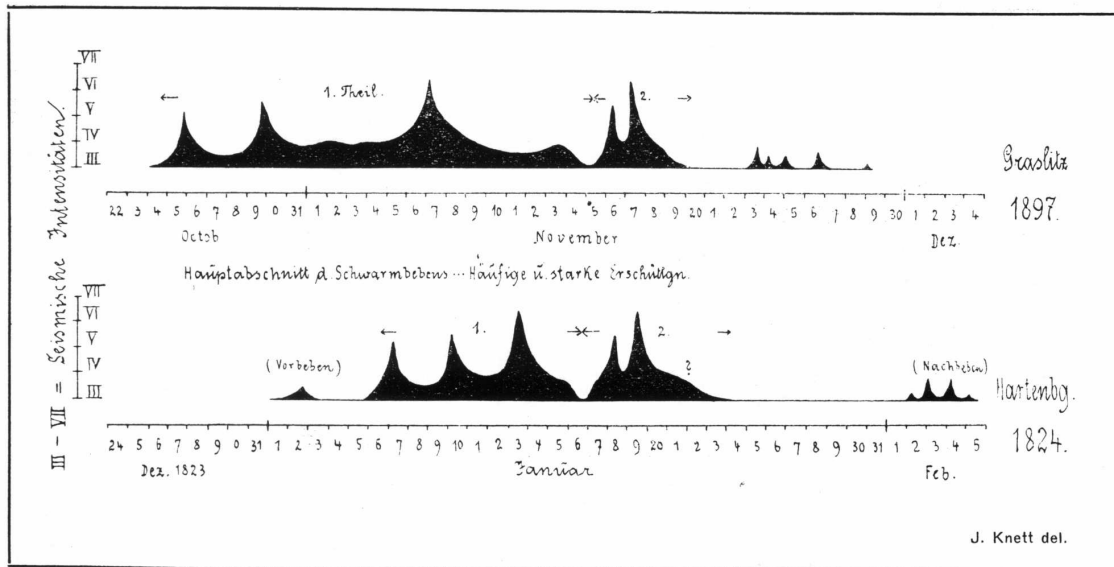
Figure 1.30: Qualitative activity of two historical swarms in the Vogtland/NW-Bohemia area from 1897 and 1824 (taken from Knett, 1899, p. 175)

Chapter 2

Methods

There are three basic tectonic faulting regimes that may occur alone or mixed in nature, normal, reverse, and strike-slip faulting, which are all associated to simple stress regimes. Analysis of the interaction of such tectonic features with the underlying stress field shows that they are disturbing the stress field in the way that principal stress directions are rotated. Such disturbances are called stress inhomogeneities and their inversion, detailed description, and interpretation are the main goal of this work.

Although there are almost always inhomogeneities in the stress field present, in many cases the regional stress can be approximately assumed to be homogeneous since the magnitude of its component outnumbers the local inhomogeneity. This also holds for an infinitesimal part of the stress field, or even a small finite part of it on a local scale. It follows that for high densities of stress measurements, a volume with a probably inhomogeneous stress field can be subdivided so that in its parts a homogeneous stress inversion can be applied to approximate inhomogeneities.

Nevertheless, a large number of stress measurements has to be known and in this work moment tensors or focal mechanisms are used. For the study area Vogtland/NW-Bohemia (see section 1.6) some moment tensors are already known but their spatial distribution is not sufficient for an identification of stress inhomogeneities. Therefore a relative moment tensor inversion, a relative relocation algorithm, and a coherence analysis have been applied to receive a significantly larger dataset of moment tensors together with precise locations and multiplet group information. This information is used to derive inhomogeneities in the stress field.

The first section of this chapter deals with the determination and visualisation of the inhomogeneous stress field, while the second covers the methods used for the estimation of the homogeneous stress tensor for a given fault population. The last part describes the methods that have been developed and adopted to produce a large dataset of relative moment tensors.

2.1   Identifying stress inhomogeneities

For the majority of stress inversion techniques the stress field that causes slip on pre-existing faults is assumed to be homogeneous. This supposal fails in many cases due to the existence of stress field perturbations and disturbances. Reasons for such inhomogeneities in the stress field have already been presented in the introduction and will be further discussed in this section. For an inversion of a dataset from an area with stress inhomogeneities, a homogeneous inversion will result in a somehow
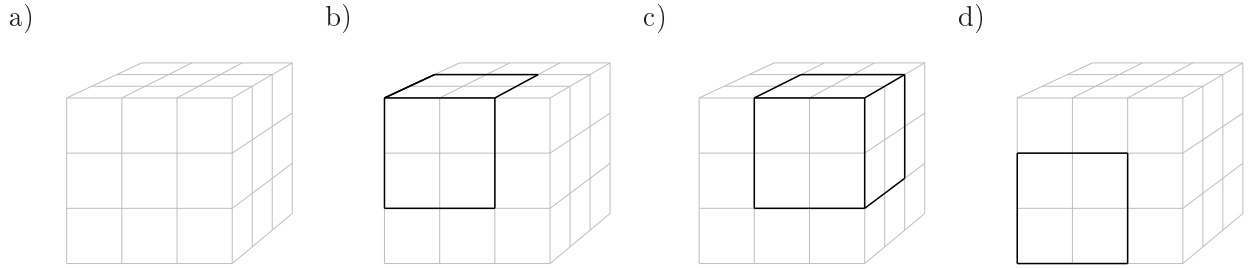
Figure 2.1: The source volume is segmented into small boxes which are assembled to larger volumes; events that lie inside these larger boxes are used for homogeneous stress inversions; example: a) the source volume is sliced into 3x3x3 small boxes; b) the first subvolume consists of 2x2x2 small boxes in the upper left corner; c) the second subvolume lies in the upper right corner; d) subsequent subvolumes are generated in the same way until all subvolumes are covered

averaged stress field. This fact together with the observation of horizontal stress directions compiled in the World Stress Map (Reinecker et al., 2004) in figure 1.28 show that in general, a single stress measurement is only useful for interpretation of local features of the stress field. However, a large number of stress indicators allows not only for estimates of a regional trend of stress directions but also for tracking down local stress inhomogeneities in the form of stress trajectories which are traces of principal stress directions.

2.1.1   Method of source volume segmentation

If the volume where stress measurements are present is divided into small boxes, the stress field can be approximated as being homogeneous inside them if the curvature of stress trajectories is small inside the subvolumes. This is equivalent to a linearisation of the stress field and measurement of stress gradients without knowing stress magnitudes. Consequently, methods to invert for the homogeneous stress field are applicable to the subsets.

In my approach, the method described by Dahm and Plenefisch (2001) (which is described in detail later in section 2.2) is used to compute the homogeneous stress field for the best double-couple calculated for a given set of moment tensors. This is done by slicing the hypocentre volume into n^3 boxes of constant size following fig. 2.1, where n denotes the number of slices in each direction (for simplicity, the volume under study is divided in boxes of constant size). In the stress inversion four parameters describing the deviatoric stress tensor are sought, so an over-determined sytem of equations is desired. For a successful inversion a number of at least 10 measurements per box has shown to be appropriate.

2.1.2   Smooth stress field

One disadvantage of the source volume segmentation is that the estimates of stress obtained for one box is associated to a certain grid point in space, representing a volume. Another disadvantage are gaps in the grid where boxes have not been considered because too few input data are available inside a box. Nevertheless knowledge of the stress tensor at every point in space is desired for the detection and interpretation of inhomogeneities. Two algorithms for determining values at points where there is no data are interpolation and approximation. The first assumes that the function under study runs directly through the measured data points, while approximation tries to fit a curve to the data by some minimisation criterion such as LSQR. Fig. 2.2 shows an example for an interpolation and an approximation. Regarding stress inversions, an approximation algorithnm using spline functions is

a)   b)
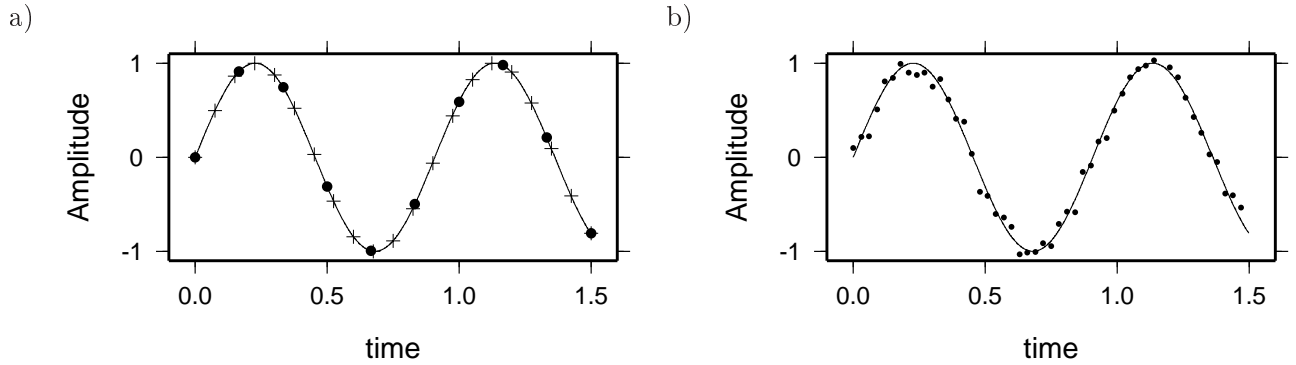
Figure 2.2: Sketch illustrating the definition of interpolation and approximation: a) interpolation to reconstruct a band-pass filtered signal (solid line) to its original form with a higher sampling frequency (indicated by crosses) than that given by the recording system (indicated by circles); b) approximation to fit a low frequency signal (solid line) through noisy samples (circles) recorded with a high sampling rate

prefered to avoid oscillations in regions where no data are present.

There are several different approaches to interpolation and approximation problems. The most easiest way to interpolate a sampled function is to use linear equations that are defined by two neighboring data points. However, for dealing with the stress tensor field, a more complex approach is needed, because with a linear interpolation curvature is not taken into account. The method of choice uses Non-Uniform Rational B-Spline functions (NURBS) which are piecewise polynomial functions that are arbitrarily often continous differentiable depending on the order of smoothness (i.e. the higher the degree, the larger the somoothness and the differentiability). This is usefull for further analysis of the stress field which may consequently use derivatives of the stress field.

Appendix E gives an overview of the basic concepts of NURBS and related definitions. For further reading on this topic the textbooks of e.g Piegl and Tiller (1997) and Rogers (2001), the internet (e.g. Shene, 2003; Weisstein, 2005), and a Ph.D thesis from Kesper (2001) are appreciated.

In this work, the data points are stress tensor measurements on a regular grid, the number of spatial parameters is three, and the number of components of the data vectors is six because the six independent components of the stress tensor are smoothed independently. The degree of the NURBS is restricted to be two to smooth outliers, but still resolve local deviations in the stress field.

The advantage of NURBS over other interpolation techniques are the possibility to extend the dimension of the data very easily because vector values are interpolated. It is also straightforward to extend the number of parameters the function to be interpolated depends on. Another benefit is that NURBS do not need much memory. Finally, weighting of the input data is implemented in the definition of NURBS.

A potential disadvantage of this approach is that the stress trajectories are possibly smoothed too strong. This may cause local features and changes in the orientation of the principal axes of stress to be smudged. However, the correct smoothing can have a positive effect, because outliers are canceled out by averaging.

Introduction to NURBS

A first step to the development of NURBS was the invention of mathematical exact functions to describe free form surfaces in the 1950s by Pierre Étienne Bézier. In the 1960s it has been found that Bézier curves are a special case of NURBS. They are a generalisation of B-splines and are commonly used in CAD systems to represent geometric objects. The most obvious use is to interpolate quantities that depend on one parameter only, like a velocity model that depends on the depth only. For CAD applications one of the most interesting application is the use of NURBS surfaces that can be parameterised by two parameters (Piegl and Tiller, 1997). These constructs allow the creation and manipulation of digital objects that represent the surface of 3D-bodies. Recently (Kesper, 2001) has discussed the use of Volume-NURBS (V-NURBS) for the representation of physical parameters in the three dimensional euclidean space. In the applications presented in his work, three dimensional bodies have been defined by control points in the form of three component vectors. None the less not only bodies may be described with V-NURBS. The parametrisation of the volume may also describe a scalar value in space, like temperature or pressure, or just as well, a more complex quantity like the stress or strain tensor.

The basic idea behind NURBS, as for many other interpolation and approximation techniques, is that the value of a quantity at a certain point is calculated taking known values in the vicinity of that point into account. The latter are introduced as weighted control points and the degree of the NURBS curve controls its smoothness. From the number of control points and the degree follows the number of knots that describe how the parameter space is subdivided to tell how strong the impact of the different control points to the calculation of an interpolated value is (see appendix E).

2.1.3   Visualisation of stress trajectories

Using the source volume segmentation described previously, the stress tensor is known at certain points in space. The stress field is smoothed using NURBS so that for each point in the source volume the corresponding stress tensor together with a quality value is available as the weighting factor which depends on the number of available data points in the vicinity of the point of interest and on the weight the input data has been given by the user (see appendix E).

Rotating the stress tensor into its corresponding principle axis system yields the direction unit vectors for all three principal axes whose piercing points on the unit sphere can be projected into the horizontal plane giving a good idea of the orientation of the axis. However, this gives only direction information at certain points in space while the trajectory itself has to be imagined. Another approach in visualising stress directions is to not only plot the piercing points of the principal axis, but also the projected unit vector itself. The azimuth of the axis can then be read directly and the length of the projected vector gives an idea of its plunge: the shorter the projected vector, the steeper the plunge (see fig. 3.28).

However, both visualisation approaches show only stress directions at certain points in space while the state of stress is most beneficially described by the stress trajectory whose tangent is the stress direction. The visualisation of stress trajectories is similar to the problem of tracing particle motion in flow physics. There is a wide variety of possible visualisation techniques available once the position of a particle can be determined for every time and every point in space. Because in this work the stress field is assumed to be constant in time, the problem reduces to be dependent only on space coordinates. Tracing freely movable particles in a velocity field is equivalent to the estimation of the direction of trajectories of principal stress directions in a stress field. The idea is to define a set of seed positions from which the appropriate trajectories are traced until the quality of the stress measurement (i.e. weight) becomes too weak or the edge of the source volume is reached.

Two steps are needed to model the tracing of trajectories. Since for a given position the principal stress direction is the tangent to the trajectory, a stable algorithm to determine how far to go in that direction has to be established. There are several different approaches dealing with this problem (for an overview see e.g. Dahm, 2001, pp. 76). For simplicity reasons and because high curvature values are not expected in this application, I decided to chose a constant step length. The second step is the visualisation of the trajectories. I decided to define slices with a certain thickness and project all parts of trajectories that lie inside this slice to the horizontal plane as illustrated in fig. 2.3.

2.2 Inversion for homogeneous stress fields

Estimating the stress tensor is a difficult task. As often in physics, approximations are made to simplify the problem. Assuming the stress tensor to be homogeneous in a given volume has shown to be very useful and a number of approaches to solve this problem has been published (see Introduction). Input to these methods are focal mechanisms or fault slip directions.

The following sections give an overview of a selected number of techniques to invert for the regionally homogeneous stress field. The approaches reach from a simple graphical approach to a recently developed energy based method.

2.2.1 Input data

In the introduction of this work, I have presented a wide variety of phenomena that are related to stress acting on rock. Most commonly, geological field observations in the form of slip vectors derived from exposed fault features are used for stress inversion purposes. These data give only an idea of the state of stress at the Earth's surface. However, stresses are present everywhere in the Earth's interior. Therefore the determination of fault mechanisms of earthquakes whose hypocentre lies below the surface has a quite beneficial yield because from these, stress measurements are also possible in greater depths. Moment tensors are a more general representation of the radiation pattern of an earthquake and are also perfect input to stress inversion algorithms because it is always possible to calculate a best double-couple for them.

While in many cases not only the slip direction but also the sense of slip can be determined for an exposed fault feature in the form of geological slip data, the information gained by the seismological analysis resulting in a focal mechanism is ambigous. It can't be told which one of the two nodal planes defined by the focal mechanism represents the fault plane. However, if this information can be obtained by an independant method, it reduces the inversion problem to that dealing with geological slip data.

2.2.2 Right dihedra method

A focal mechanism, like the one shown on the left of fig. 1.24, can be divided into four dihedra, two with extensional deformation (stretching) resulting in positive first motion (black) and two with compressional deformation (shortening) resulting in negative first motion (white). Looking at fig. 1.19, it is obvious that the dihedra that belong to positive first motion correspond to tensional stresses while the opposite dihedra are related to compressional stresses. From these facts, Angelier and Mechler (1977) derived a simple graphical method to estimate the probability for a certain stress model to agree with a given set of fault striae which yield the orientation of the fault plane as well as the direction of slip on the fault. Different slip vectors can be transformed to different focal mechanisms
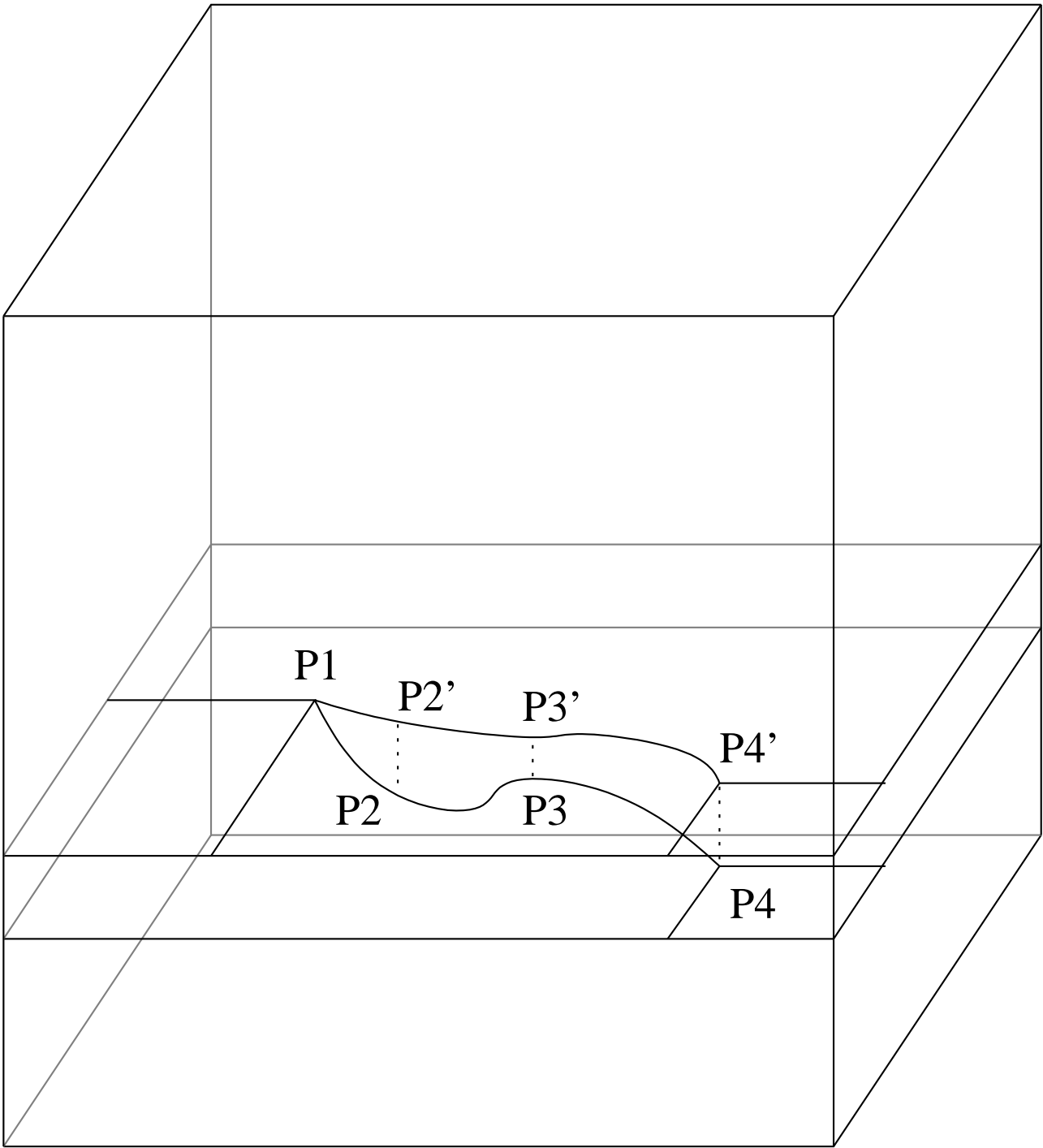
Figure 2.3: Principle of the visualisation of stress trajectories in horizontal layers of a given volume using a synthetic example: the trajectory begins at $P1$ and follows $P2$, $P3$, and $P4$; it is projected to the top of the layer as indicated by the projected points $P1$, $P2'$, $P3'$ und $P4'$; this is done for all trajectory parts inside the layer

which restrict the principal axes of stress to different sets of directions. The idea is to intersect these sets and to estimate the set of best fitting principal axes by checking against the number of intersections: the higher the number of tension dehedra, the higher the probability that σ_3 lies in that direction and vice versa for σ_1. However, this method drops the knowledge of the fault plane for slip vectors and acts on a set of double-couple solutions.

The fit for a given σ_1-axis (most compressive) is the percentage of P-dihedra that contain it (e.g. having 10 focal mechanisms, if 9 of 10 P-dihedra contain σ_1, the fit is 90%, i.e. the misfit is 10%). For the misfit of the corresponding σ_3-axis the appropriate T-dihedra are counted. The program `rdtm` used for this type of inversion is described in appendix A.5.1. The method has been applied in this study to retrieve a fast assessment of the consistency of a data set with a homogeneous stress field.

2.2.3 Inverting slip vectors

The method of Michael (1984) takes slip vectors into account. However, for uniaxial stress fields (i.e. $\sigma_2 = \sigma_1$ or $\sigma_2 = \sigma_3$) he and Angelier (1984) find that both nodal planes from focal mechanisms can be used as input data. For areas where this assumption does not hold, the decision which nodal plane of a focal mechanism to take as the actual fault plane has to be made prior to the application of this method.

2.2.4 Energy based approach

Dahm and Plenefisch (2001) assume that slip occurs in the direction of maximum energy radiation and show that this is equivalent to the assumption that slip occurs in the direction of maximum shear stress. For reference I give a short overview of the method in the following paragraphs.

Forward problem

Eq. 2.1 describes the energy radiation of an earthquake (Aki and Richards, 1980) (summation convention with $i, j = 1, 2, 3$). η is the seismic efficiency, μ is the shear modulus, Δu is the average shear dislocation (slip) on the fault with area A and normal $\vec{v}$, and ($\sigma_{ij} = \sigma_{ij}^1 + \sigma_{ij}^0$) is the sum of the symmetric stress tensor on the fault before and after the event. $M_{ij} = \mu A (v_j \Delta u_i + v_i \Delta u_j)$ is the moment tensor of the earthquake source. σ and the average disclocation over the rupture plane, $\Delta \vec{u}$ are assumed to be constant. Additionally, the shear component of σ is assumed to be similar to the local shear stress before the event.

$$E = \frac{\eta}{2} \int_A \Delta u_i v_j (\sigma_{ij}^1 + \sigma_{ij}^0) dA = \frac{\eta}{4\mu} M_{ij} \sigma_{ij} \tag{2.1}$$

The double couple component of the moment tensor M_{ij} in eq. 2.1 can be used to calculate the slip direction on unfavourably oriented faults. In principle the moment tensor is substituted directly by the representation of its best double-couple by the seismic moment M_0 and the three angles strike Φ, dip δ, and rake λ. Then the equation becomes

$$
\begin{aligned}
\frac{4\mu E}{\eta} &= M_0(\sin\lambda C_1 + \cos\lambda C_2) \\
\text{with} \\
C_1 &= -\sigma_{11}\sin^2\Phi\sin 2\delta - \sigma_{22}\cos^2\Phi\sin 2\delta + \sigma_{33}\sin 2\delta \\
&\quad +\sigma_{12}\sin 2\Phi\sin 2\delta - 2\sigma_{13}\sin\Phi\cos 2\delta + 2\sigma_{23}\cos\Phi\cos 2\delta \\
C_2 &= -\sigma_{11}\sin 2\Phi\sin\delta + \sigma_{22}\sin 2\Phi\sin\delta \\
&\quad +2\sigma_{12}\cos 2\Phi\sin\delta - 2\sigma_{13}\cos\Phi\cos\delta - 2\sigma_{23}\sin\Phi\cos\delta
\end{aligned}
$$

E has an extremum where $\frac{dE}{d\lambda} = 0$, leading to the simple result in eq. 2.2 from which the rake angle for a stress scenario σ, Φ, and δ can be calculated.

$$
\tan\lambda = \frac{C_1}{C_2} \tag{2.2}
$$

Inverse problem with slip vectors

For a given set of slip vectors Φ_k, δ_k, and λ_k, with $k = 1, ..., K$ the generating homogeneous stress tensor in the form of its three principal axes σ_1, σ_2, and σ_3 and the shape ratio $R = \frac{\sigma_1-\sigma_2}{\sigma_1-\sigma_3}$ has to be estimated. Dahm and Plenefisch assume that eq. 2.2 is true for each event k resulting in the system of equations shown in eq. 2.3.

$$
\begin{bmatrix}
-\cos\lambda_k\sin^2\Phi_k\sin 2\delta_k + \sin\lambda_k\sin 2\Phi_k\sin\delta_k \\
-\cos\lambda_k\cos^2\Phi_k\sin 2\delta_k - \sin\lambda_k\sin 2\Phi_k\sin\delta_k \\
+\cos\lambda_k\sin 2\delta_k \\
+\cos\lambda_k\sin 2\Phi_k\sin 2\delta_k - 2\sin\lambda_k\cos 2\Phi_k\sin\delta_k \\
-2\cos\lambda_k\sin\Phi_k\cos 2\delta_k + 2\sin\lambda_k\cos\Phi_k\cos\delta_k \\
+2\cos\lambda_k\cos\Phi_k\cos 2\delta_k + 2\sin\lambda_k\sin\Phi_k\cos\delta_k
\end{bmatrix}^T
\begin{bmatrix}
\sigma 11 \\ \sigma 22 \\ \sigma 33 \\ \sigma 12 \\ \sigma 13 \\ \sigma 23
\end{bmatrix}
= 0, (k = 1, ..., K) \tag{2.3}
$$

It is well known that only four of the six independent components of the stress tensor can be resolved (see e.g. Gephart and Forsyth (1984), Michael (1984)). Therefore two constraints on the stress field are needed which Dahm and Plenefisch introduce as given in eq. 2.4 where b and c are arbitrary nonzero constants and $\vec{a}$ is a 6x1 vector calculated form the eigenvectors $\vec{v}^{ma}$ and $\vec{v}^{mi}$ corresponding to the maximal and minimal eigenvalue of the average moment tensor $\overline{\mathbf{M}} = \frac{1}{K}\sum\limits_{k=0}^{K}\mathbf{M}_k$.

$$
\begin{bmatrix}
1 & 1 & 1 & 0 & 0 & 0 \\
a11 & a22 & a33 & a12 & a13 & a23
\end{bmatrix}
\begin{bmatrix}
\sigma 11 \\ \sigma 22 \\ \sigma 33 \\ \sigma 12 \\ \sigma 13 \\ \sigma 23
\end{bmatrix}
=
\begin{bmatrix}
b \\ c
\end{bmatrix}
\tag{2.4}
$$

Inverse problem with focal mechanisms

To deal with focal mechanisms for which the fault plane and therefore the slip vector is not known, Dahm and Plenefisch use a simple criterion for the decision which plane to select. They first seek the smallest sum of squared residuals for all possible permutations of a limited subset of input mechanisms. The appropriate planes that lead to this minimum are then selected and for each remaining event both planes are tested subsequently and the one with the smallest residual is selected.

2.3 Data set preparation

In this work, the double couple components of moment tensors are used for the inversion of the stress field. For the detection of its inhomogeneities, as many moment tensors as possible should be known. This is the reason why I developed an automated processing of seismogram data of earthquake swarms which possibly generates a large number of realative moment tensors. To achieve this goal, a number of prerequisite information has to be gathered by other methods which are presented here in reverse order from their application in practice. First the method of relative moment tensor inversion is discussed, followed by a decription of a precise location technique, and finished by a discussion on the coherence analysis of waveforms.

2.3.1 Automated moment tensor inversion

For the inversion of the homogeneous deviatoric stress tensor, which consists of four independent parameters, at least four different single focal mechanism solutions are needed. Preferably a larger number of measurements is used in order to solve an overdetermined system of equations, stabilising the result. In the case that inhomogeneities in the stress field are sought, a much larger number of input data is needed, because many deviatoric tensors or parameters describing stress trajectories have to be inverted. So the first problem to be solved is to acquire a sufficiently large dataset. With an automated relative moment tensor inversion, described in this section, such a large number can be provided for an area with high seismicity. The following paragraphs cover the relative moment tensor inversion, the unambiguity between fault plane and auxiliary plane of a focal mechanism, and the definition of the relative magnitude.

Relative moment tensor inversion

For areas where many events occur, the relative moment tensor inversion after Dahm (1996) can be applied, if one or more reference moment tensors have already been computed. This method is based on the fact that for two earthquakes, the raypaths to one station are approximately the same if the events are close together. Dahm shows that the Green functions representing the wave propagation through the Earth can then be eliminated. He also assumes a simple source time function and then needs only the amplitudes of low-pass filtered P-, SH-, and SV-phases of a reference event and some unknown event at different stations as input to determine the MT of the unknown event relative to the reference event. Then a system of linear equations is set up and solved in a least-squares sense. A method which works without a reference mechanism is also presented but not applied in this work.

Phase amplitude picking is automated by an algorithm that is illustrated in fig. 2.4. It depends on the knowledge of phase arrival time differences that can be computed with a cross correlation technique as described later. First for a set $S_{P,S}$ of seismograms of the P- or S-phase, the time of the maximum amplitude of this phase is picked for an arbitrary template event. Adding the arrival time difference to some other event out of S_P or S_S gives the pick time for the appropriate phase of this event. The amplitude is also picked and the procedure is applied to all other events of $S_{P,S}$, successively. The resulting amplitude measurments are used as input for the relative moment tensor inversion if the appropriate correlation coefficient (described later in this section) is larger than a given threshold which is usually about $0.8 - 0.9$.

The picking of the maximum amplitude of the template event can be performed manually or automat-
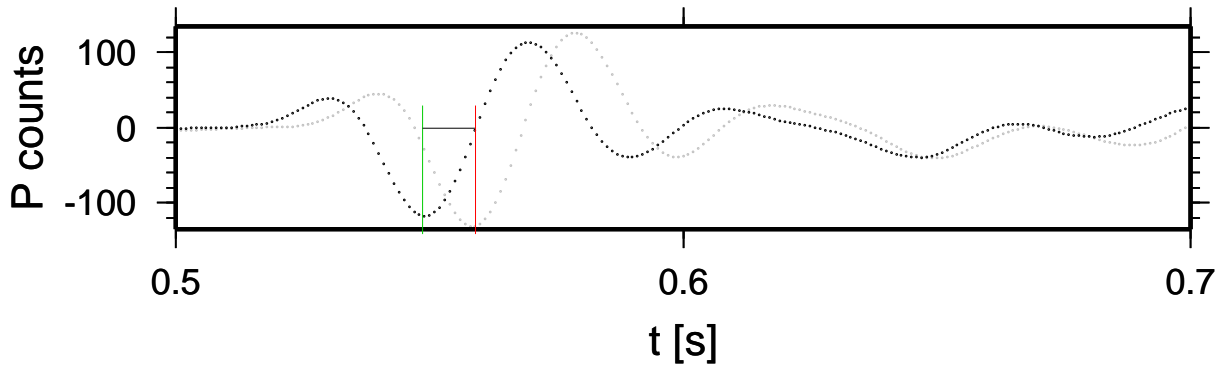
Figure 2.4: Automated phase picking principle: first a significant amplitude is pickedin a template seismogram (vertical green line), second the arrival time difference is added (horizontal black line) and the second amplitude is picked automatically (vertical red line)

ically. The first approach is very time consuming and only semi-automatic. However, one goal of this work is to automate as many processing steps as possible, so I developed a simple automatic phase amplitude picking algorithm that needs a coarse phase pick as input.

To get an idea where to pick the maximum phase amplitude, all similar seismograms in $S_{P,S}$ are shifted against an arbitrary master event out of $S_{P,S}$, normalised by its maximum, and stacked (i.e. normalised and sumated). The resulting stacked seismogram is searched for the maximum with the smallest time shift to the corresponding extrema of the single events. With this master pick, relative phase arrivals can be determined, as illustrated in fig. 2.4.

The P-pick is obtained on the vertical component while for the SH- and SV-wave, the horizontal components are rotated into radial and transverse direction. The SH-pick is then read on the transverse component and the SV-pick is taken from the radial component.

Input preparation is done by collecting information about the phase amplitudes, as described above, and the takeoff angles and the azimuths of the direct rays to the recording stations together with weights for the amplitude measurements. Though the takeoff angles and azimuths can be calculated using a standard ray tracer, the program `hypoDD` implements the relative relocation algorithm of Waldhauser and Ellsworth (2000) is used. It is applied prior to the determination of the relative moment tensors, so the takeoff angles and azimuths can also be adopted from the output of the relocation. For the relative moment tensor inversion weights are needed to account for the accuracy of the picked amplitudes. These will have been obtained during a coherence analysis of waveform data as the squares of the correlation coefficients. Both processing steps are described later in this section.

Fault plane vs. auxiliary plane

As mentioned in earlier sections, the biggest disadvantage of the focal mechanism is the unambiguity between the fault plane and the auxiliary plane. I have applied and developed three slightly different approaches in dealing with this problem by deciding which nodal plane is the fault plane.

The first approach is the

Hypocentre plane fitting which needs locations and multiplet information as input. A multiplet is defined as a set of seismograms with highly similar waveforms. Planes are fit through the hypocentres of every multiplet in a least-squares sense and assumed to be fault zones which should coincide with one of the nodal planes of the focal mechanisms.

In the case that the hypocentres are distributed nearly spherically this approach will fail motivating the second approach of defining groups of multiplets that form structures in space and determine the appropriate fault planes by using all events that belong to these groups. Both methods fit a plane in a least-squares sense, thus weighting outliers very strong. The effect is that the structure of a plane in the hypocentres may be smudged or rotated while it is clearly visible if sought visually. Selecting a norm that doesn't favor outliers that much like the euclidean norm may help to deal with this problem. However, I decided to use a simple visual approach by rotating the hypocentres in a visualisation software (like `gnuplot` or `matlab`) and determine the azimuth, as well as the corresponding plunge of the plane.

Measuring the minimum rotation angle between the previously estimated fault normal and the two given nodal planes of a DC yields an objective criterion for telling the best fitting nodal plane to be the fault plane. If one nodal plane shows a significantly smaller angular difference as the other and if this difference is smaller than a given threshold angle, then it is taken as the correct fault plane.

Clustering of fault plane normals is an effect that is expected for a given population of hypocentres that are distributed on a certain fault plane. Then the slip vectors all point in the same or nearly same direction if the stress field is homogeneous. On the other hand, if there are variations in the stress field, the slip vector directions also vary. In the latter case, all focal mechanisms have a common fault normal, so a clustering of the normal vectors should be observable.

For a given set of focal mechanisms $M = \{M_1, .., M_n\}$, both possible slip unit vectors $\vec{s}_{i1}$ and $\vec{s}_{i2}$ are calculated for every event $i = 1, ..., n$. Then the four angles $\phi_{ijk} = cos^{-1}(< \vec{s}_{1j}, \vec{s}_{ik} >)$ between $\vec{s}_{1j}$ and $\vec{s}_{ik}$ with $j, k \in 1, 2$ are calculated for each subsequent event $i = 2, ..., n$. If the indices j and k of the smallest of these four angles differ, $\vec{s}_{i1}$ and $\vec{s}_{i2}$ are swapped. In the end one of the sets $S_1 = \vec{s}_{11}, ..., \vec{s}_{n1}$ and $S_2 = \vec{s}_{12}, ..., \vec{s}_{n2}$ contains vectors with a small variability in the directions (the fault normals) while the other set therefore contains the most probable slip directions.

Rotated projections of the focal mechanism are used for a visual check for the correctness of the previously obtained information which nodal plane is the fault plane. The previous methods describe how to distinguish between fault plane and auxiliary plane by defining unit vectors and introducing minimum rotation angles between them. The only way to check the quality of the estimation using the direction vectors only, is to look at the direction of the normal axes to see if they really point in similar directions.

Another approach is not to use the lower hemisphere of the focal sphere for visualisation of the moment tensor, as usual, but any arbitrary semi-sphere which is projected into the plane which subdivides it from its counter part, as illustrated in fig. 2.5. I decided to select a semi-sphere whose cutting plane is vertical. This is achieved by rotating a given MT by an arbitrary angle about the vertical axis (to match e.g. the strike) and then about the two horizontal axes (or vice versa), respectively. I call this projection the **back hemisphere projection**.

First, the focal mechanisms are transformed into their appropriate moment tensors because tensors

a)

Φ=228°

φ=42°

Flip at
N−axis

b)

c)

Flip at
E−axis

d)
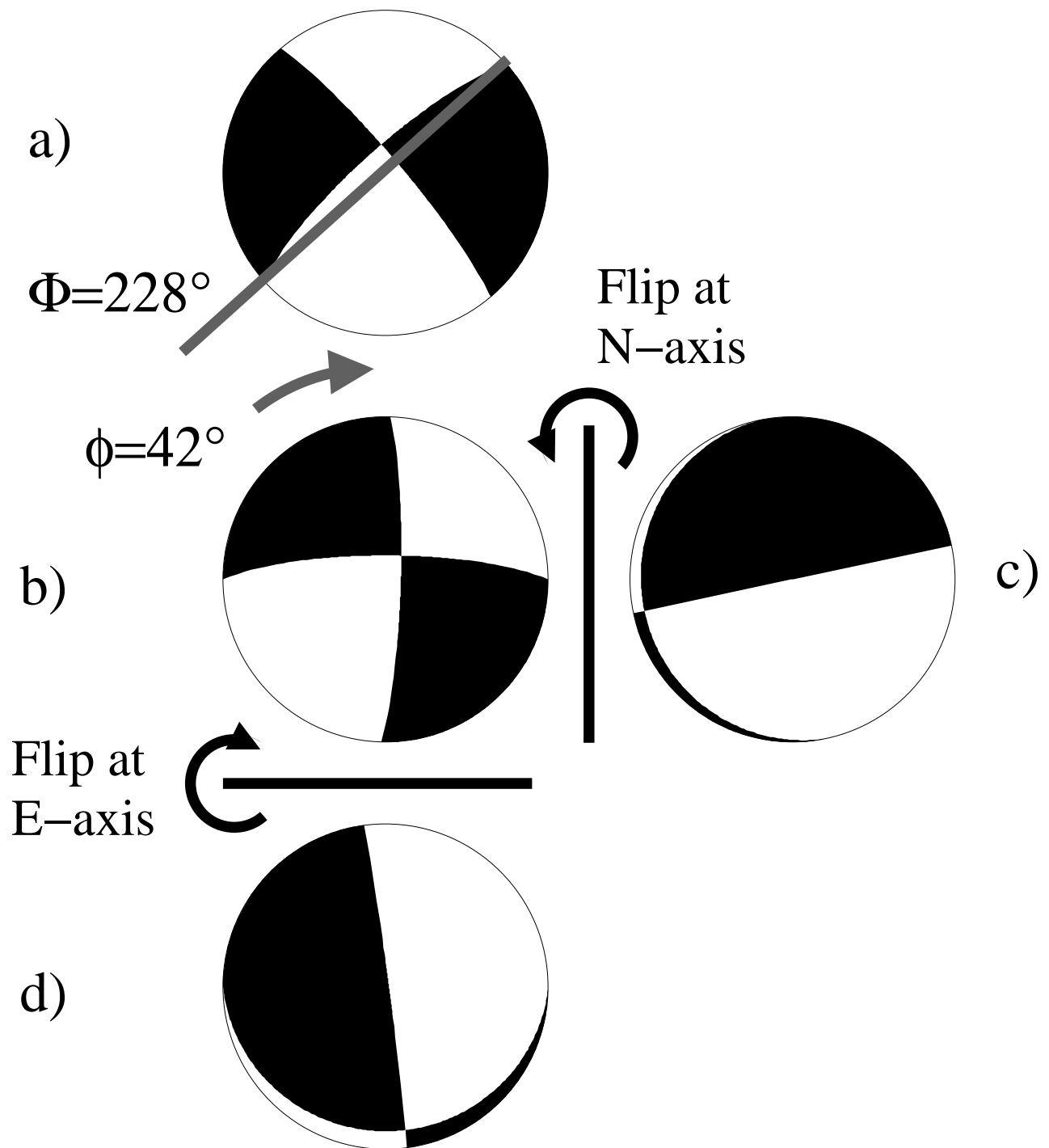
Figure 2.5: Illustration of how to obtain the back projection of a moment tensor: a) a moment tensor with DC-part $\Phi = 228^o$, $\delta = 78^o$, and $\lambda = -8^o$; b) to match a previously determined fault plane with azimuth of 138°, the moment tensor is rotated about $\phi = 180^o - 138^o = 42^o$ clockwise with respect to the Z-axis; c) rotation about -90° about the N-axis which results in the back projection of the western semi-sphere; d) rotation about -90° about the E-axis which results in the back projection of the northern semi-sphere

are rotated by matrix multiplications and can then be decomposed again for visualisation. These are rotated about the vertical axis by the same angle as the plane indicated by the hypocentres and then about the new x'- and y'-axes (rotated N- and E-axes, respectively), resulting in two perpendicular back hemisphere projections. For normal and reverse faulting mechanisms, if the x'-axis is defined as being parallel to the strike of the hypocentre plane, then the rotation about the y'-axis results in a back hemisphere projection that displays one nodal plane as a straight line which subdivides the surrounding circle while the other indicates the slip direction. Unfortunately this does not work for strike-slip mechanisms. The back projection that resulted from the rotation about the x'-axis then allows to read the dip angle of the fault.

The mathematical background is covered in linear algebra. The rotation of a tensor value is achieved by multiplication with rotation matrices. Two rotation matrices can be combined to one matrix R by multiplication of the two single rotation matrices as shown in eq. 2.6 where D_x and D_z represent rotations about the x-axis and the z-axis, respectively. Transformations of tensors are performed as defined in eq. 2.8 where T is the original tensor, P represents some transformation matrix (the equality of P^T and P^{-1} holds for orthogonal row vectors of unit length), and T' is the transformed tensor. Together we have the tensor rotation given in eq. 2.9 where R denotes the combined rotation matrix, M is the original moment tensor, and M' is the rotated moment tensor.

$$D_x(\alpha) = \begin{pmatrix} 1 & 0 & 0 \\ 0 & cos(\alpha) & sin(\alpha) \\ 0 & -sin(\alpha) & cos(\alpha) \end{pmatrix} \tag{2.5}$$

$$D_z(\gamma) = \begin{pmatrix} cos(\gamma) & sin(\gamma) & 0 \\ -sin(\gamma) & cos(\gamma) & 0 \\ 0 & 0 & 1 \end{pmatrix} \tag{2.6}$$

$$R(\alpha) = D_z(\alpha) \cdot D_x(90^o) = \begin{pmatrix} cos(\alpha) & sin(\alpha) & 0 \\ -sin(\alpha) & cos(\alpha) & 0 \\ 0 & 0 & 1 \end{pmatrix} \cdot \begin{pmatrix} 1 & 0 & 0 \\ 0 & 0 & 1 \\ 0 & 1 & 0 \end{pmatrix} = \begin{pmatrix} cos(\alpha) & 0 & sin(\alpha) \\ -sin(\alpha) & 0 & cos(\alpha) \\ 0 & 0 & 0 \end{pmatrix} \tag{2.7}$$

$$T' = P^{-1} \cdot T \cdot P = P^T \cdot T \cdot P \tag{2.8}$$

$$M'(\alpha) = R^T(\alpha) \cdot M \cdot R(\alpha) = \begin{pmatrix} cos(\alpha) & 0 & sin(\alpha) \\ -sin(\alpha) & 0 & cos(\alpha) \\ 0 & 0 & 0 \end{pmatrix} \cdot M \cdot \begin{pmatrix} cos(\alpha) & -sin(\alpha) & 0 \\ 0 & 0 & 0 \\ sin(\alpha) & cos(\alpha) & 0 \end{pmatrix} \tag{2.9}$$

Relative magnitude of moment tensors

The moment magnitude M_w is the most desired value if the strength of an earthquake is sought. It is calculated from the seismic moment M_0 by: $M_w = 2/3 * (log_{10}\frac{M_0}{N.m} - 9.1)$. On the other hand, the seismic moment is related to the fault geometry of the earthquake and the shear modulus μ: $M_0 = \mu \cdot A \cdot \bar{u}$ where A is the area of the fault and $\bar{u}$ is the average slip.

In a relative moment tensor inversion, the strength is calculated relative to a reference mechanism: $M_r = M_{0,i}/M_{0,ref}$. Using this the moment magnitude of the relative event can be determined by

solving for $M_{0,i}$. The moment or moment magnitude are useful for stress inversions if input data are weighted by their magnitude, and may be subject to future studies.

2.3.2 Relative relocation

For the effective calculation of stress field inhomogeneities, it is necessary to know the locations corresponding to the focal mechansims very precisely. Geiger (1910) developed one of the first location techniques by expanding an expression for the arrival time as a sum of origin time and travel time into a Taylor Series. The precission of the location depends highly on the accuracy of the arrival time picks which are in the best case $\Delta t = \pm.01s$ for local earthquakes and up to some seconds for large teleseismic events.

Assuming a crustal P-wave velocity of around $v_P = 7km/s$ this results approximately in errors of $|\Delta \vec{x}| = 700m$ for local events to $|\Delta \vec{x}| = 70000m$ for teleseismic events. The key for the calculation of locations with higher precision is to enhance the pick accuracy. Another approach is the master event location technique (e.g. Douglas, 1967; Spence, 1980; Peppin et al., 1989, etc.). The idea is to use the maximum of the cross correlation function or the linear trend in the cross spectrum like described by Poupinet et al. (1984) to calculate arrival time differences with a precision of few miliseconds resulting in a relative location accuracy of about $|\Delta \vec{x}| = 40m$. The absolute location accuracy is the same as for the master event which is still localised by a standard location technique.

Slunga et al. (1995) has proposed a method for the accurate location of earthquakes taking the absolute location, as well as the relative location between the events into account. They introduce a weighted sum to be minimised consisting of arrival time residuals and arrival time difference residuals. A similar approach has been proposed by Waldhauser and Ellsworth (2000) using the double difference which is computed by the sum of the difference between both theoretical arrival times and the difference between the absolute arrival times for all possible event pairs. The program `hypoDD` implements the latter method and for the sake of its availability as open source software this method has been chosen for this study. It is one of the most accurate relocation techniques that has been widely used during the past years. The input to this method are arrival time differences obtained by cross correlation measurements, weights, coarse previous locations, as well as the station geometry and a velocity model of the underground. The output are precise relocations of the input events together with an origin time, takeoff angle and azimuth of the rays from all relocated events to all stations, and residual values to estimate the location accuracy.

For the relocation of the 1997 swarm, seismograms from the stations of the local seismic network WEBNET (Horálek et al., 2000) which has already been presented in fig. 1.29 have been used. It is well suited to locate events in the Nový Kostel focal region, because of its good azimuthal coverage with maximum azimuthal gaps of about 100 degrees to the north and to the east. Additionally, the focal depth can be observed with good acuracy, because of the station NKC which is located directly above the main active region.

2.3.3 Coherence analysis

In many earthquake sequences (like earthquake swarms or aftershocks) groups of nearly identical seismograms can be observed at different stations if the network configuration does not change during recording. Such similarity is found for earthquakes with similar source-time functions and magnitudes in the same stress field (moment tensors) as stated by Poupinet et al. (1984). Deichmann and Garcia-Fernandez (1992) reviewed many related papers and say that all authors show that the hypocentres

of earthquakes cluster tightly in space and suggest that the reason for the similarity of waveforms is a common focal mechanism.

Similarity of seismograms can be measured objectively by calculating the correlation coefficient from cross correlation function values. Given a certain threshold that depends on the quality and type of the waveform data, two seimograms are said to be similar if the correlation coefficient calculated from them extends the threshold. For a large set of events there may exist similarity between different subsets. Such subsets of similar seismograms are called multiplets and there are several possible approaches to define them. The simplest is to assume the similarity relation between two events to be transitive, i.e. `if a is similar to b and b is similar to c then a is similar to c`. However Maurer and Deichmann (1995) describe a more complex algorithm involving data from all stations of a network which I adopted because of its usability for a seismic network. It is described in appendix A.2.3. For this work I modified the algorithm to be applicable to three component seismograms.

Modified cross correlation function

In eq. 2.10 two one-component seismograms $x_i(t)$ and $x_j(t)$ are used to calculate the correlation function $\Phi_{ij}(t)$. This is quite sufficient for stations that record the vertical component only but means a loss of information in the case of three-component registrations. In my diploma thesis (Reinhardt, 2002), I decided to use only the vertical seismograms for both the P-phase and the S-phase. Since in many cases the P-phase is polarised in the vertical direction while the S-phase oscillates in the horozontal plane, it may also be useful to use the Z-component for the P-phase and a transversal seismogram computed from the horizontal recordings and the backazimuth for the SH-phase. For the latter case the location of the appropriate events must be known to rotate into the correct direction.

$$\Phi_{ij}(t) = \int\limits_{-\infty}^{+\infty} x_i(t) \cdot x_j(t + \tau) d\tau \tag{2.10}$$

The most straightforward approach is to use all three components. The basic problem is that the correlation function is scalar while the seismograms are vector valued functions, so an appropriate mapping (i.e. $f : \mathbb{R}^3 \times \mathbb{R}^3 -> \mathbb{R}$) has to be chosen. In the work of Aster and Rowe (2000) and Rowe et al. (2002), quite sophisticated aproaches are made to define such a mapping. However, there exists an infinite number of sufficient mappings but only three very simple approaches are presented here. The first suggestion presented in eq. 2.11 is to calculate the Euclidean norm (or any other p-norm) of the two three component seismograms $\vec{x}(t)$ and $\vec{y}(t)$ respectively which are substituted into the integrand of the correlation integral. The disadvantage of this approach is the loss of polarity information. The second proposal is to project the three component seismograms onto the z-axis as shown in eq. 2.12. The advantages and disadvantages of this method haven't been analysed, yet, but it is clear that this method introduces also loss of information. Finally, the third approach is to use the canonical scalar product of the two seismograms $\vec{x}(t)$ and $\vec{y}(t)$ as given by eq. 2.13. I have decided to use the last method, because it takes most information into account in comparing two three-component seismograms. A comparison of the coherence analysis with one- and three-component seismograms is shown in appendix B.

$$\Phi_{ij}(t) = \int\limits_{-\infty}^{+\infty} |\vec{x_i}(t)| \cdot |\vec{x_j}(t + \tau)| d\tau \tag{2.11}$$

$$\Phi_{ij}(t) = \int\limits_{-\infty}^{+\infty} < \vec{x_i}(t), \hat{e}_z > \cdot \vec{x_j}(t+\tau), \hat{e}_z > d\tau \qquad (2.12)$$

$$\Phi_{ij}(t) = \int\limits_{-\infty}^{+\infty} < \vec{x_i}(t), \vec{x_j}(t+\tau) > d\tau \qquad (2.13)$$

Chapter 3

Applications

In this chapter I first describe the preprocessing steps for the automatic processing of earthquake swarm datasets consisting of coherence analysis, relocation, and relative moment tensor inversion using the 1997 swarm as example. I present inversion results for the regional homogeneous stress field and, finally, the application of the inhomogeneous stress analysis is presented for both the 1997 swarm and partly for a dataset of hydraulically induced seismicity at the German deep drilling borehole, KTB, 2000. Although data for the 2000 Vogtland/NW-Bohemia earthquake swarm is available, the 1997 swarm has been selected because of its unusual nature compared to other swarms in the region (for an overview of the geometries of recent swarm see Fischer and Horálek, 2000).

3.1 Data preparation

The Discussion in the previous chapter concerning the identification of inhomogeneities in the stress field shows that as many focal mechanisms as possible should be known. In this chapter, two datasets originating from the Czech Vogtland/NW-Bohemia region and the german KTB drilling site are analysed. In the KTB region, there are 125 focal mechanisms from the 2000 hydraulic fracturing experiment available (Bohnhoff et al., 2004), so an inversion will be likely to be successful. For the 1997 swarm, 70 absolute and relative moment tensors are available (Dahm et al., 2000) while the swarm consisted of more than 2000 events. Motivated by this circumstance, an automated relative moment tensor inversion is applied to enlarge the dataset.

During the coherence analysis, which is the first preprocessing step, groups of similar seismograms and precise relative arrival time differences for P- and S-phases are determined. The latter are used as input for a relative relocation of the hypocentres, enhancing the location accuracy. Finally, amplitudes of P- and S-phases are determined automatically and are used as input for a relative moment tensor inversion. In the last part of this section the result of a literature review with regard to focal mechanism and moment tensor data for the area Vogtland/NW-Bohemia as a basis for a regional stress inversion is presented.

3.1.1 Coherence analysis

For the successful application of a coherence analysis of waveforms, several prerequisites have to be fulfilled (see section 2.3.3). The earthquake swarms in the area Vogtland/NW-Bohemia have been recorded with the permanent seismic network WEBNET (Horálek et al., 2000). The waveform data, P-

and S-phase picks, and locations obtained using a master-event location technique have been provided by Fischer and Horálek (2000). A small source volume of about $1km^3$, similarity of source-time functions and common fault planes have already been indicated by Fischer and Horálek who were able to subdivide 750 events of the 1997 swarm into eight groups with similar waveforms and representative source mechanisms (70 absolute and relative moment tensors have been computed by Dahm et al. (2000)). A visual approach has been used for finding waveform similarities. The magnitudes of these events lie in the range of $M_L = -0.9 \ldots 2.7$ and about 85% have a comparable size of $M_L = -0.3 \ldots 0.8$. The results of Fischer and Horálek were one of the motivations for my diploma thesis (Reinhardt, 2002) where I have applied the coherence analysis described by Maurer and Deichmann (1995) to a data set of about 2000 events of the 1997 swarm. The dataset is reduced to 733 events that have been recorded at least at four stations. Threshold values in Reinhardt (2002) have been adopted from the original work of Maurer and Deichmann wth the exception of a slightly modified threshold for the S-phase correlation coefficient ($K = 25\%$, $T_p = 0.0$, $T_s = 0.8$, $T_x = 0.5$, $T_y = 1$). The outcome have been sets of multiplet events (MP) with striking waveform similarity. In the early phase of this thesis I have found that the values of the thresholds have a strong impact on the definition of the MP. So I decided to reprocess the data and to determine threshold values systematically.

The first step of the coherence analysis is the calculation of correlation coefficients for the P- and S-phase of seismograms. The raw data have been filtered with an infinite impulse response butterworth bandpass with 6 poles and corner frequencies of $4Hz$, and $30Hz$. For stability reasons, I dropped the weak station CAC with noisy signals and station VIEL, which recorded only 30 events, from the set of available stations sticking with the eight stations KOC, KRC, LAC, NKC, SBC, SKC, TRC, and ZHC (see fig. 1.29). The same time windows as in Reinhardt (2002) have been used for both P- and S-phases ($\pm0.5s$ around P, and $\pm1.0s$ around S). For the automatic processing, I have developed the program `coma` described in appendix A.2.2 which calculates three matrices containing the cross-correlation-function maxima, the corresponding shift times, and the correlation coefficients for all event pairs, respectively.

Following the discussion in appendix A.2.1, the parameters $K = 0.00$, $T_p = 0.00$, and $T_y = 1$ are fixed. Now appropriate values for only two parameters T_s and T_x are sought. T_s is varied from $T_{s,min} = 0.50$ to $T_{s,max} = 1.00$ and T_x from $T_{x,min} = 0.30$ to $T_{x,max} = 1.00$. These ranges have been chosen because a significant similarity of waveforms is desired and because there are only few values in the modified network correlation matrix below $T_{x,min}$. A grid spacing of $\Delta T_s = \Delta T_x = 0.01$ has been selected and a coherence analysis for each parameter set has been performed. I have written the program `cohana` that implements the algorithm of Maurer and Deichmann which is described in appendix A.2.3. The output parameters for the grid search are the number of MP (NMP) and the number of events in these MP (NEV). I have introduced an MP size threshold of five to keep the complexity low. As a criterion for an acceptable parameter set, it is demanded that as many events as possible should be divided into as many MP as possible. As a norm for the grid search approach I calculate the percentages of the maxima of NMP and NEV, and multiplied both. The result of NMP, NEV, and the percentage are shown in fig. 3.1.

There are only few spots with high values in fig. 3.1 c), and there is only one parameter pair showing an absolute isolated maximum. I choose the parameter values $K = 0\%$, $T_p = 0.00$, $T_s = 0.84$, $T_x = 0.67$, and $T_y = 1$. This set leads to the definition of 19 MP which consist of 489 events in total. For simplicity I drop all MP of size 5 to 7, keeping 457 events in 13 MP which means a loss of 32 events for further processing but a better overview of the results. The appropriate similarity matrix and the multiplet sizes for MP of at least size eight are shown in fig. 3.2. Table 3.1 gives a statistic of MP sizes. The color codes which are associated to the different multiplets are used for all further processing steps.

Comparing the multiplets identified in this work with the groups determined visually by Fischer and
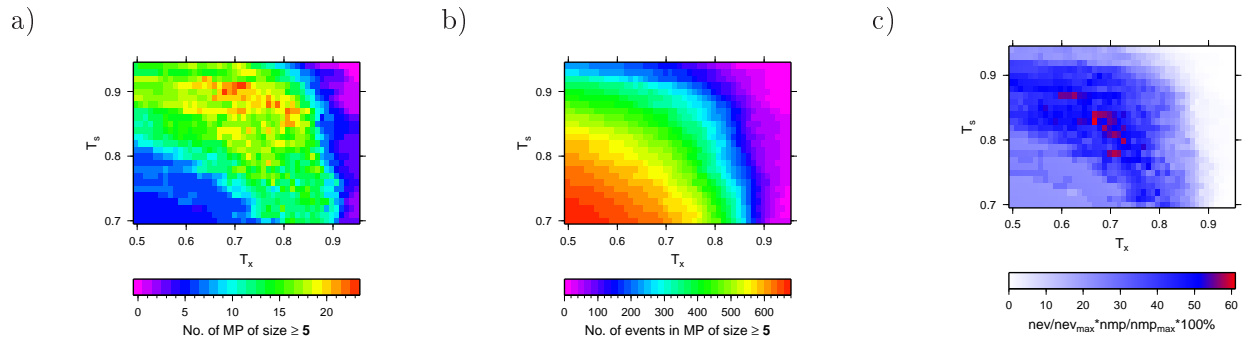
Figure 3.1: Result of the grid search over the coherence analysis parameters T_s and T_x: a) number of MP of at least size 5; b) number of events in MP of at least size 5; c) selection criterion: multiplication of percentages
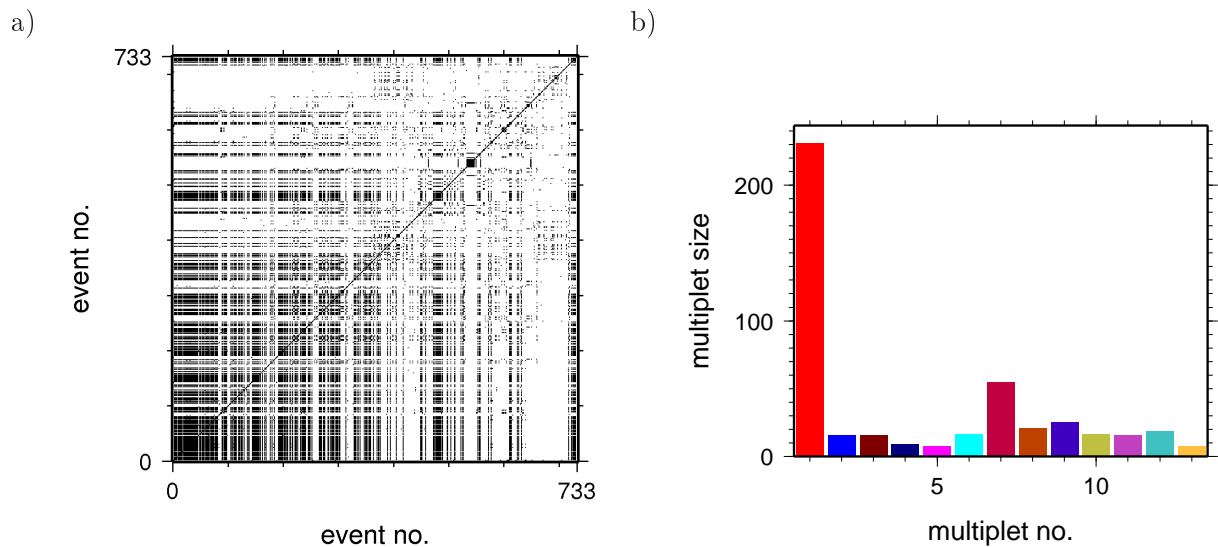
Figure 3.2: Result of the coherence analysis for the 1997 swarm: a) unsorted similarity matrix, where dots indicate similarity between events; the matrix is symmetric; b) sizes of 13 multiplets containing at least 8 events

MP size	1	2	3	4	5	6	8	9	16	17	19	21	25	55	231
no.	174	20	6	3	5	1	2	1	3	2	1	1	1	1	1
total events	174	40	18	12	25	6	16	9	48	34	19	21	25	55	231

Table 3.1: Number of single events, doublets, and MP with 3 up to 231 events from a dataset of 733 events of the 1997 swarm

Group	no. of events in group	Multiplet	no. of events in multiplet	no. of shared events
A	187	2	231	145
		4	9	4
AB	24	2	231	7
B	145	6	17	5
		7	55	44
		9	25	18
		10	17	14
		12	19	16
C	35	2	231	31
D	102	1	16	14
		8	21	19
E	24	2	231	12
		4	9	3
		5	8	2
F	?	-	-	-
G	16	11	16	12
H	19	3	16	16

Table 3.2: Comparison of multiplets determined using the coherence analysis in this work with groups previously defined by Fischer and Horálek (2000)

Horálek (2000) shows that most multiplets can be associated to groups, as summarised in table 3.2. As expected, the largest multiplet 2 is subdivided and associated to different groups. Multiplet 13 can't be associated at all and multiplet 4 is associated partly to groups A and E. All other multiplets are related to exactly one group. The reprocessing of the coherence analysis for the 1997 swarm leads to a more reliable result compared to Reinhardt (2002) because three component seismograms and a more reliable selection of threshold values have been used for the coherence analysis.

3.1.2 Relocation

For the relocation of the events of the 1997 swarm with the program `hypoDD` (Waldhauser and Ellsworth, 2000) initial hypocentres have to be known. I have used the locations obtained from the master event location done by Fischer and Horálek (2000). The arrival time differences and the appropriate weights, calculated as the square of the correlation coefficient are taken from the coherence analysis. The velocity model for the location has been adopted from fig. 3 of Fischer and Horálek (2000). The `hypoDD` input file for the relocation is shown in appendix A.3.

From the precise arrival time difference measurements obtained during the coherence analysis pseudo travel time differences are calculated using the catalogue origin times (`gendtcc` from Reinhardt (2002) is used to create the `dt.cc` file needed by `hypoDD`). By this procedure I have been able to use an initial set of 17281 difference times for the P-phase and 98957 difference times for the S-phase. The significantly lower number for the P-phase can be explained by the fact that there is a smaller number of P-phase waveforms that are similar to each other.

Fig. 3.3 shows one horizontal and two vertical projections of the obtained hypocentres of events that have been associated to multiplets colored in the corresponding multiplet color. Two main features can instantly be identified by the significant difference in the appropriate strike directions. There is one large multiplet that dominates the NNE-SSW striking feature and another cluster which is built

up by at least five single multiplets striking ESE-WNW.

The analysis of the occurence time of multiplet events indicates different types of activity. Some multiplets are active only for a very short timespan while others are active over the complete swarm period (fig. 3.4). There are also mixed types and all have different starting times.

To get a better understanding of the structures that can be seen in the hypocentre plot, I decided to analyse the distribution of multiplets in space by grouping them and trying to identify flat structures that can be interpreted as fault zones. Using this criterion I have been able to identify three multiplet groups. They consist of 3, 6, and 4 multiplets, respectively. Fig. 3.5 shows the hypocentres in two perpendicular vertical sections together with strike and dip angles for the estimated planes of weakness. The corresponding fault planes are assumed to have the same orientation and location.

3.1.3 Relative moment tensor inversion

The previous results are used to calculate a large number of relative moment tensors using a number of well studied earthquakes as reference mechanisms and analysing the radiation patterns of other sources relative to them (Dahm, 1996). I have decided to use 70 absolute moment tensors from Dahm et al. (2000) as reference mechanisms. After cross checking available waveforms a number of 59 reference events have been selected. For the application of this method takeoff and azimuth angles for all events with respect to all stations have been extracted from the `hypodd` output file `hypodd.src` generated during the relocation process. The amplitudes that are needed for the moment tensor inversion have been picked in an automated mannner.

Automatic phase amplitude picking

The first step to determine where to pick amplitudes relative to some template event with a similar waveform is trivial if the pick for the template event is known. Two output parameters of the coherence analysis are used. The relative arrival time allows to precisely pick the correct amplitude for all similar events if a reference time is given. The correlation coefficient enables me to determine the quality of the time measurement. I have developed the program `det-tpl-ev` which seeks sets of similar waveforms and builds clusters so that further operations can act on only these subsets. The algorithm is to find the largest set first, remove the corresponding events from the set to be searched, and iteratively repeat these steps until all events are added to subsets. In the majority of possible cases the last few clusters will contain only one event and only the largest subsets may be used for further processing.

The most challenging problem is to determine the correct reference time. The first approach has been to pick the phase amplitude manually for some template event that is similar to as many other events as possible by means of a high correlation coefficient. This is in contradiction to the goal of an automated processing. Therefore I developed a method that objectively determines a stable reference time. The idea is to shift all similar seismograms relative to an arbitrary reference time and stack the resulting normalised seismograms. Fig. 3.6 shows that the stacking operation will be a great success because of the extremely high similarity of waveforms.

The next step is to pick the absolute maximum as the phase amplitude. Relative to the corresponding time the amplitudes of all similar seismograms are picked subsequently. For a P-phase the vertical seismogram component and for an S-phase both horizontal seismogram components are used. In the latter case both components are stacked and the reference times are picked separately. In some cases, the maxima of each component will be found at slightly different times (fig. 3.6). For both components the closest absolute maximum on the other component is sought. I decided to select the pick with
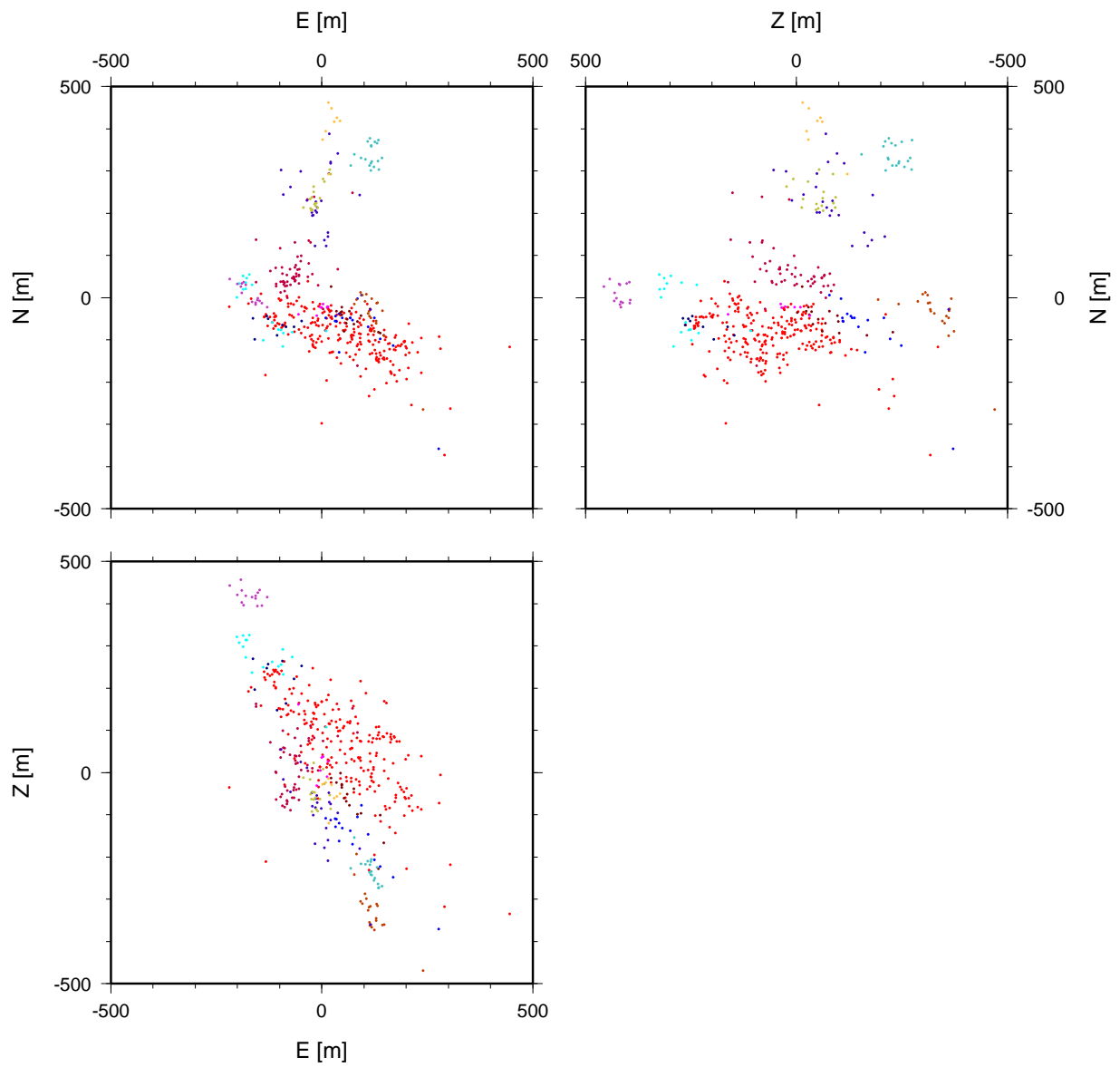
Figure 3.3: Projections of 454 hypocentres for the 1997 swarm events; upper left: epicentre map; upper right: vertical projection into the N-Z-plane; lower left: vertical projection onto the Z-E-plane
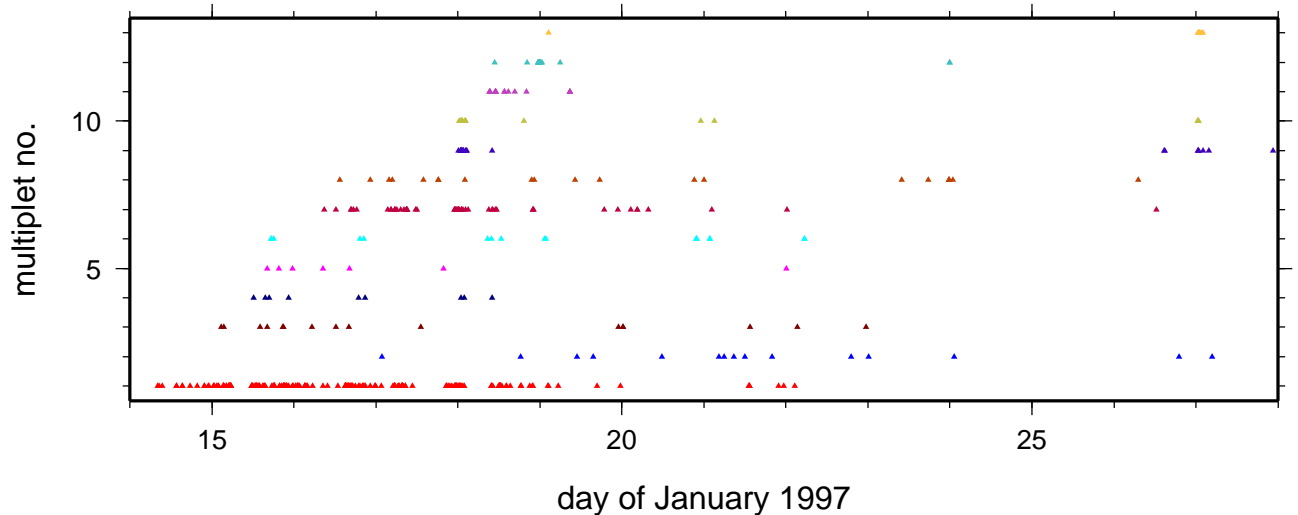
Figure 3.4: Seismicity divided by multiplets for the swam 1997; color coding is the same as in fig. 3.2

the closest maximum on the other component (see the following example). A complete overview of all automatic picks is given in appendix C.

Example: For the stacked E- and N- component seismograms for the S-phase at station KOC the picks have been set to $t_{s,E} = 1.115s$ and $t_{s,N} = 1.136s$, respectively (fig. 3.6). The nearest maximum picks have time differences of $\Delta t_{s,E-N} = 0.001s$ with respect to $t_{s,E}$ and $\Delta t_{s,N-E} = 0.007s$ with respect to $t_{s,N}$. In this case $t_{s,E}$ for the E-component is selected as the phase pick, because the closest maximum on the N-component is only $1ms$ away.

Relative moment tensor inversion

After all information needed for the actual inversion has been collected, the input file (`relref.inp`) for the relative moment tensor inversion program (`relref`) is generated using the `AWK` script `gen.relref.inp.awk` The output of `relref` is written to a table containing all available parameters that have been determined. Two parameters, the rank of the inversion problem (should be 6) and the ratio of the smallest to the largest eigenvalues (should not be too large) are used to establish a quality criterion for the result.

Error estimate

After all ill conditioned events have been eliminated, 352 moment tensors have been inverted. Together with the 59 reference events, 411 moment tensors are ready for further processing. The question arises how large the error for the whole inversion is. The formal error of the relative moment M_r is accepted as a good proxy for the reliability of the corresponding single solution (T. Dahm, pers. comm.) while the distribution of all single M_r errors yields the overall error for the whole inversion. The relative moment $M_{r,i}$ of event i is defined by its moment $M_{0,i}$ divided by the average moment of all reference events $< M_{ref} >= \frac{1}{N} \sum_{k=1}^{N} M_{ref,k}$. The values distribute in the form of a gamma distribution which is described in appendix A.1. Fig. 3.7 shows a histogram of all relative errors with a bin width of 1 for which the parameters δ and λ describing the best fitting gamma distribution are sought. The fit criterion is formulated as the squared sum of the differences between the measured error and the appropriate analytical value of the gamma-distribution. The minimum of the error function is found
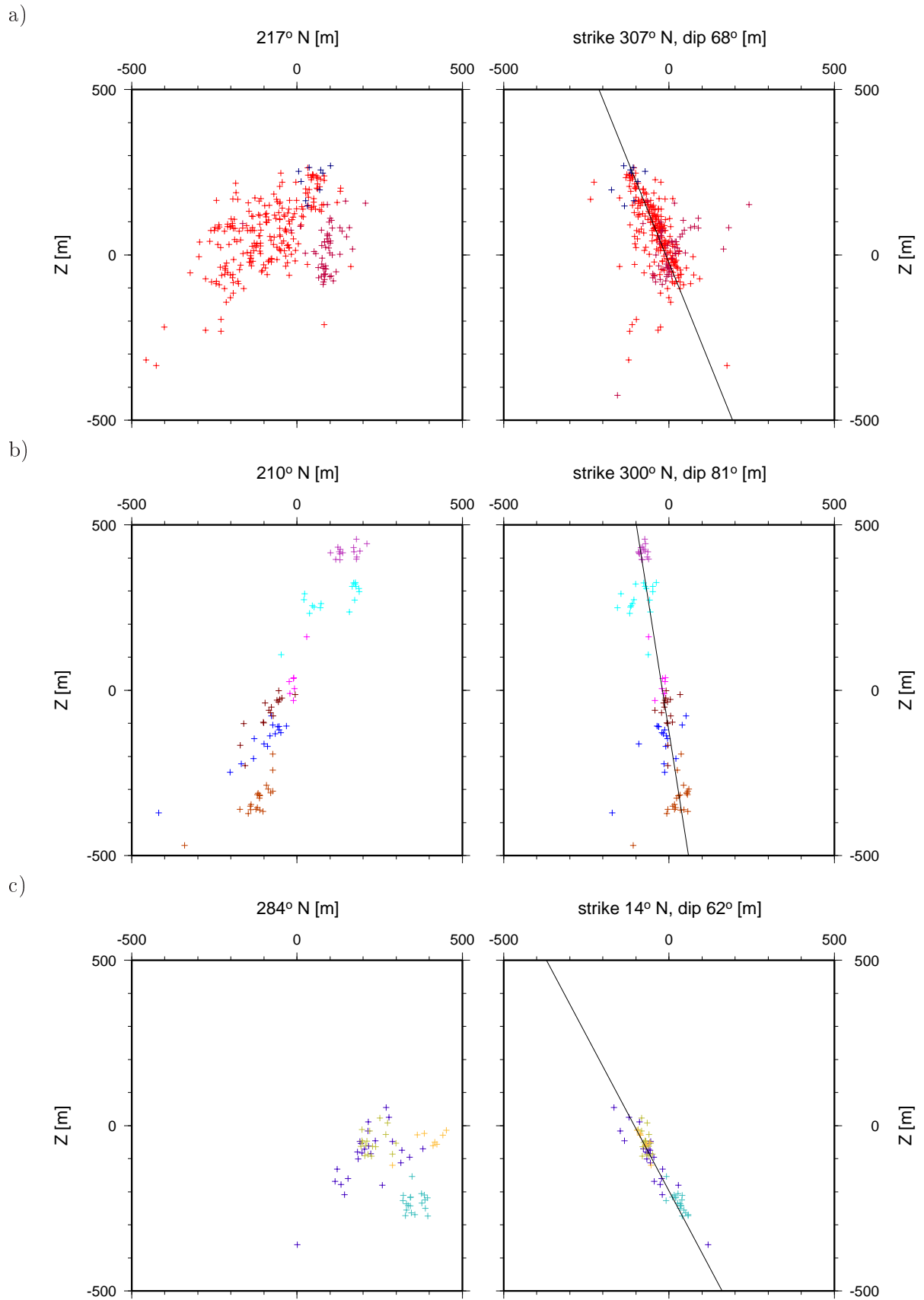
Figure 3.5: Vertical projections rotated about the strike angle to identify the dip angle of the identified fault planes: a) 293 events of multiplets 1, 4, and 7; b) 92 events of multiplets 2, 3, 5, 6, 8, and 11; c) 69 events of multiplets 9, 10, 12, and 13
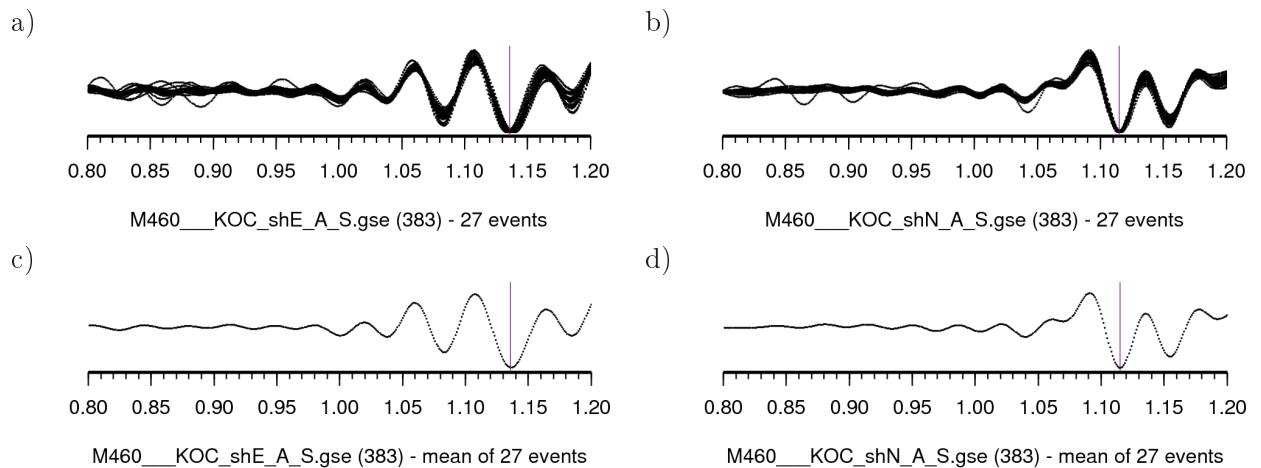
Figure 3.6: Waveform similarity and automatic phase picking for a group of similar seismograms at station KOC: a) normalised and shifted seismograms E-component; b) the same for N-component; c) stacked normalised seismogram E-component; d) the same for N-component

using a grid search algorithm. The fit error and the minimum of the error function are shown in fig. 3.7 b. The minimum is located at $\delta = 3.36$ and $\lambda = 0.227$ from which the mean value of $\mu = 14.8$ and the standard deviation $\sigma = 8.1$ are derived. The error range therefore is $M_r = 6.7 \ldots 22.9$. The resulting gamma distribution fits the observed M_r error data very well, as can be seen from fig. 3.7 c and d.

Double couple solutions

The program `relref` computes the relative moment tensors, i.e. outputs the six independent parameters of the moment tensor as well as the percentages of the isotropic and the double couple component together with the two possible slip vectors (yielding the nodal planes) indicated by the latter. The result of the inversion is visualised by dividing the dataset by multiplets that have been found earlier in this chapter and the projection of the focal sphere defined by the slip vectors. Fig. 3.8 and fig. 3.9 show the double couple solutions of all events associated to the 13 multiplets.

Fault plane determination using the hypocentre distribution

As discussed in section 1.4 the stress inversion is stabilised significantly if fault and auxiliary planes can be separated. Therefore three methods to solve this problem have been presented in section 2.3.1. The methods either assume that cluster of hypocentres from multiplets are indicating zones of weakness and thus fault plane orientations or that composite or common double couple nodal planes of multiplet events indicate fault planes. Table 3.3, table 3.4, and table 3.5 show the appropriate results for the multiplet fitting, the multiplet-group fitting, and the visual fitting, respectively. For the latter I found that 12 of the 13 multiplets can be said to lie on planes while MP 07 extends wide to every direction. However, I decided to keep it in the same group together with multiplets 01 and 04 as for the group-fitting for comparison reasons.

Now that planes are associated to the multiplet-events, it is appropriate to calculate the angles between the two nodal planes of the best DC solution for the corresponding MT with fault plane normals determined by the distribution of hypocentres. Table 3.6 shows the result of the comparison for the
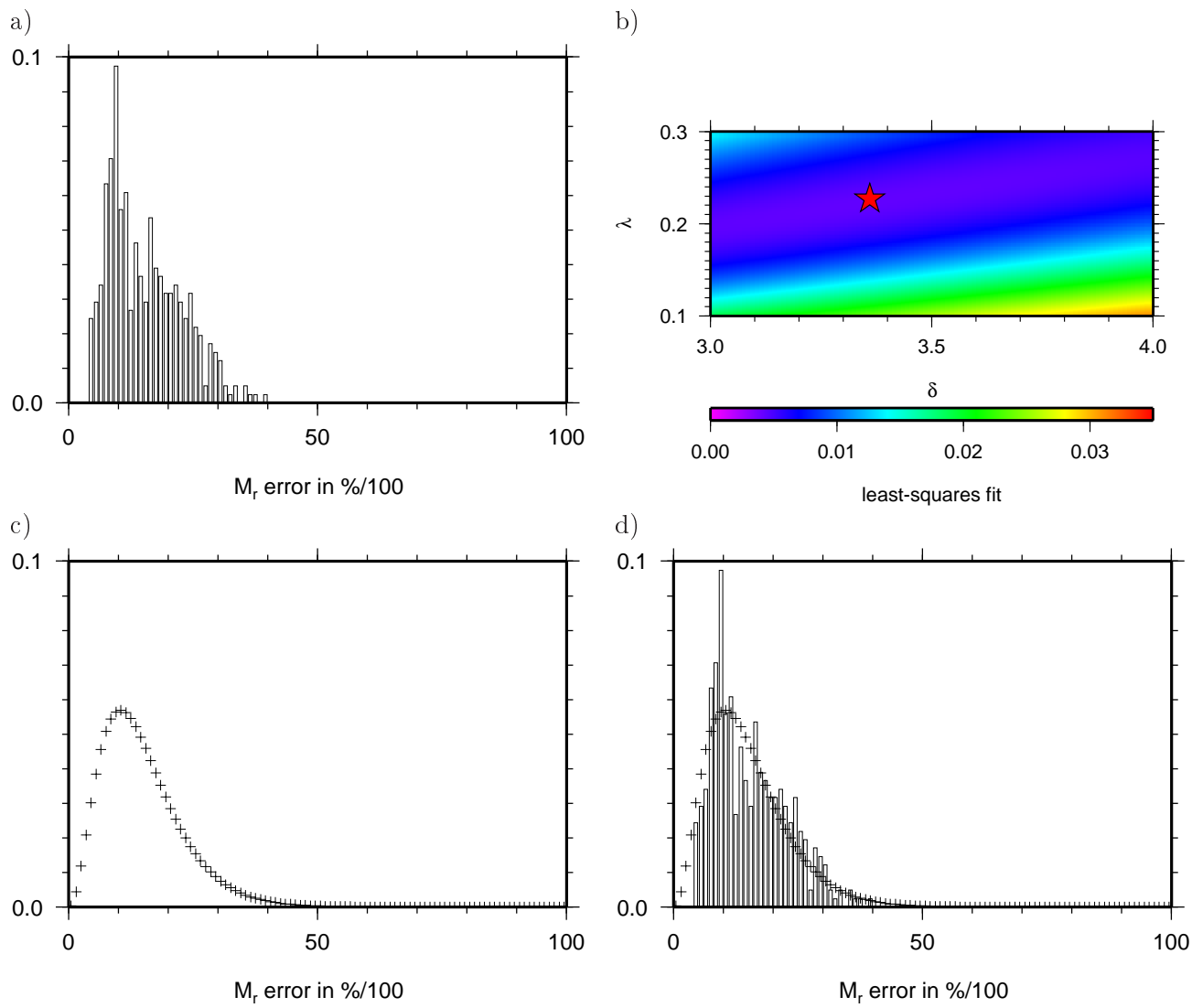
Figure 3.7: Fitting of the error of the relative M_r error: a) M_r error histogram with a bin width of 1; b) error function for gamma-distribution fit; red star indicates minimum; c) gamma-distribution for the minimum ($\delta = 3.36$ and $\lambda = 0.227$); d) comparison of error histogram and gamma-distribution

a1)

a2)
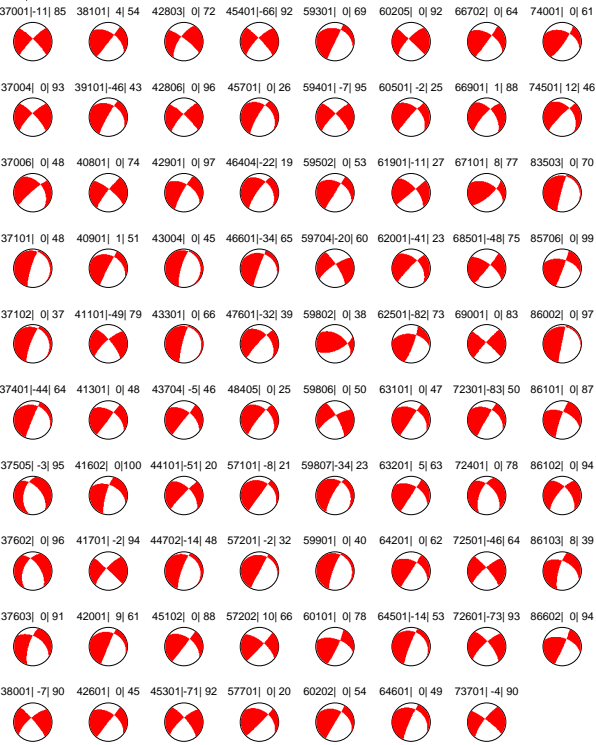
b)
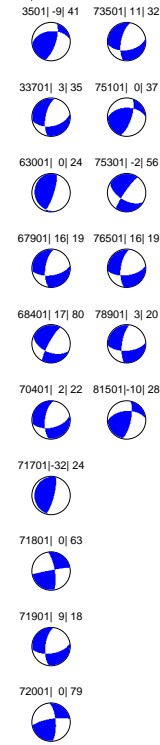
c)

d)

Figure 3.8: 1997 swarm best DC solutions (lower hemisphere projection) calculated from MT components; numbers above focal mechanisms are event ID, isotropic component percentage, and non-DC component percentage of the moment tensor; the color coding is the same as in fig. 3.2 - part 1 of 2

e)

15901| 20| 70

18202| 5| 68

20802| 2| 84

24901| 5| 73

29601| -7| 76

40701| -5| 79

74201| 3| 70

f)

16301| 0| 8   70801| 44| 27

16303| 7| 6   70901| 0| 39

16801| 33| 21 71001| 67| 35

31502| -2| 8   71301| 30| 27

31903| 0| 13   71401| 0| 35

55501| 0| 8   74701| 51| 15

57203| 0| 44   74801| 0| 52

60402| 0| 29

66501| 0| 17

66601| 0| 31

g)

25101| 76| 78 35401| -3| 50 38502| 8| 64   44803| 57| 64 58503| 29| 98 70201| 0| 39

25401| 47| 94 35701| 0| 54   39301| 55| 61 45103| 68| 12 58901| 77| 78 71501| 41| 78

29901| 64| 66 35901| 0| 30   39502| 54| 93 47001| 7| 53   64701| 0| 51   74301| 48| 37

30001| 7| 60   36901| 5| 84   41801| 17| 58 47101| 72| 74 64801| 57| 63 77401| 4| 94

30401| 51| 94 37801| 30| 82 42103| 10| 72 47502| 0| 55   64901| 50| 76 84801| 34| 94

31001| 54| 87 38201| 43| 94 42501| 78| 83 49202| 0| 45   68701| 0| 60

33901| 51| 94 38302| 0| 82   42701| 48| 58 49802| 40| 87 68801| 5| 51

34202| 38| 58 38303| 12| 74 44202| 77| 99 56002| 0| 0   69501| 30| 68

34301| 14| 61 38401| 41| 82 44301| 0| 61   57407| 22| 97 69601| 0| 89

35201| 5| 72   38402| 11| 72 44401| 52| 89 57702| 45| 49 69701| 56| 73

h)

26101| 4| 93   67801| 49| 31 77301| -3| 15

32402|-20| 44 68601| 42| 95

34002| -8| 92 70701| 11| 64

34401| -4| 9   71201| 16| 26

39901| 9| 97   75601| 17| 22

40501| 40| 51 75801| 30| 30

40601|-19| 14 75901| -8| 0

48701| -5| 6   76001| -4| 7

64401| -4| 10 76101| 6| 50

65001| -3| 54 76401| 5| 36

i)

44801| 75| 83 47703|-33| 0   80302| 35| 25

45501| 82| 70 47902| 37| 65 80601| 73| 58

45904| 79| 69 48001| 74| 59 81001| 55| 73

46102| 66| 84 48803| 56| 50 81401| 0| 15

46103|-33| 0   49501| 53| 51 82301|-33| 0

46201| 73| 80 49601| 81| 95

46501| 69| 57 57304| 72| 40

46503| 73| 50 77801| 1| 34

46506| 45| 85 78101| 8| 55

47701| 14| 36 79104| 49| 49

j)

44806| 71| 64 71101| 18| 91

45901| 57| 88 71601| 37| 54

46001| 2| 99   76901| 4| 73

46401| 7| 56   79202| 28| 46

47201| 52| 87 79501| 86| 95

47402| 71| 62 80001| 10| 27

48501| 43| 65 80401| 85| 94

48801| 44| 79

48902| 49| 84

63301| 7| 60

k)

56201| 6| 72   62701|-30| 78

56301| 0| 87   63602|-32| 83

56501| 39| 0   67401| -2| 70

58502| 0| 83   67502| 4| 87

58601| 0| 79   87301|-76| 63

58602| 0| 97

58701|-44| 82

61302| 8| 88

61402| -4| 69

62205|-39| 0

l)

58401| 17| 47 66001| 20| 32

63801| 61| 61 66101| -1| 36

65301| 23| 41 66102| -8| 19

65401|-28| 0   66103| 17| 61

65403| 28| 0   66201| 2| 39

65501| 0| 43   66401| -6| 19

65601|-28| 0   67201| 7| 50

65701| -6| 22 76201|-21| 16

65801| 44| 56 76301| -3| 23

65901| 0| 24

m)

66801|-18| 7

79707|-14| 10

80702| -4| 49

80804| 27| 57

80805| 0| 9

80901| -1| 35

81003| 87| 99

82401|-19| 8

Figure 3.9: 1997 swarm best DC solutions (lower hemisphere projection) calculated from MT components - part 2 of 2

MP	avail. MT	strike	dip	mean distance
01	126	246.8	40.2	51.5
02	14	309.5	35.1	55.0
03	11	268.6	54.1	69.2
04	5	354.4	61.6	92.1
05	7	321.1	79.2	90.3
06	10	254.4	45.6	67.7
07	38	9.0	25.6	82.8
08	20	268.5	54.7	65.1
09	20	293.5	51.3	60.7
10	13	298.6	66.7	62.0
11	8	233.9	40.8	38.8
12	16	284.1	50.5	40.7
13	7	294.2	56.0	39.3

Table 3.3: Multiplet groups and available MT together with strike and dip angles of the appropriate best fitting planes; the mean distance is measured from the plane in metres for all hypocentres

MP numbers	strike	dip	mean distance
01 04 07	301.0	40.3	41.5
02 03 05 06 08 11	287.6	67.4	64.0
09 10 12 13	254.4	58.0	30.3

Table 3.4: Multiplet groups together with strike and dip angles of the appropriate best fitting planes, estimated by grouping of multiplets and LSQR fitting; the mean distance is measured for all hypocentres in m perpendicular to the plane

MP numbers	strike	dip
01 04 07	307	68
02 03 05 06 08 11	300	81
09 10 12 13	14	62

Table 3.5: Multiplet groups together with strike and dip angles of the appropriate visually estimated best fitting planes

MP	MP group	avail. MT	bymp	bypg	byvi
01	1	126	11.2	**53.2**	8.8
02	2	14	14.3	21.5	**42.9**
03	2	11	0.1	9.1	**27.3**
04	1	5	20.1	**80.0**	20.1
05	2	7	14.3	14.3	**85.8**
06	2	10	0.1	20.1	**60.0**
07	1	38	68.5	**79.0**	0.1
08	2	20	35.0	**45.0**	35.0
09	3	20	**15.0**	5.0	5.0
10	3	13	*7.7*	**7.7**	0.1
11	2	8	**50.0**	12.6	12.6
12	3	16	*93.8*	**93.8**	*93.8*
13	3	7	*57.2*	**57.2**	42.9

Table 3.6: Result of the angular multiplet fitting (bymp), multiplet-group fitting (bypg), and visual fitting (byvi) of planes against hypocentres; the numbers in columns 4 to 6 give percentage of angles for which $|angle| <= 30^o$; **boldface** emphasizes the method with the highest rate of plane normal similarity - deselected results are indicated in *italics*

a) b) c) d)
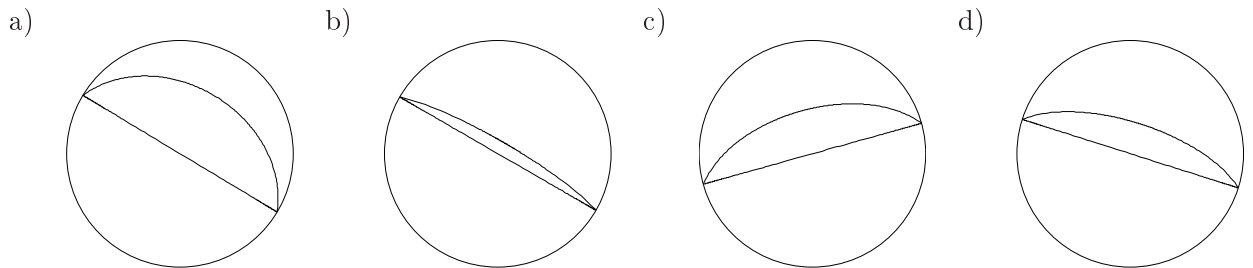
Figure 3.10: Four most populated main fault planes determined from hypocentre distribution: a) strike $\Phi_1 = 301.0^o$, dip $\delta_1 = 40.3^o$, 101 events; b) strike $\Phi_1 = 300.0^o$, dip $\delta_1 = 81.0^o$, 21 events; c) strike $\Phi_1 = 254.4^o$, dip $\delta_1 = 58.0^o$, 20 events; d) strike $\Phi_1 = 287.6^o$, dip $\delta_1 = 67.4^o$, 9 events

three different methods described above. For stability reasons, a maximum angular difference of 30° is introduced. There are two multiplets for which the amount of correctly determined fault planes is the same for the hypocentre planes given by a single multiplet and the one given by the appropriate planegroup. For one multiplet this is the case for all three methods of determining a fault plane from hypocentres. All these ambiguous multiplets belong to multiplet group 3. I decided to choose the method using the multiplet group and drop the result of the method involving single multiplets because this method is the least successful for multiplet groups 1 and 2. Besides, the only ambigous multiplet that prefers the method involving single multiplets is multiplet 9 which has a low success rate of only 15%.

Table 3.7 summarises the results of the previous paragraphs. For 158 of 295 available MT, the fault plane can be detected. I define main fault planes by counting the events that lie on the differently oriented planes. The four most populated ones are chosen and are shown in fig. 3.10. In relation to these planes' normals, the angles to the nodal planes normals are calculated and used to divide them between fault plane and auxiliary plane. The result of this analysis is shown in fig. 3.11. If the smaller of the angles is larger than 30° both angles are marked not to be dividable.
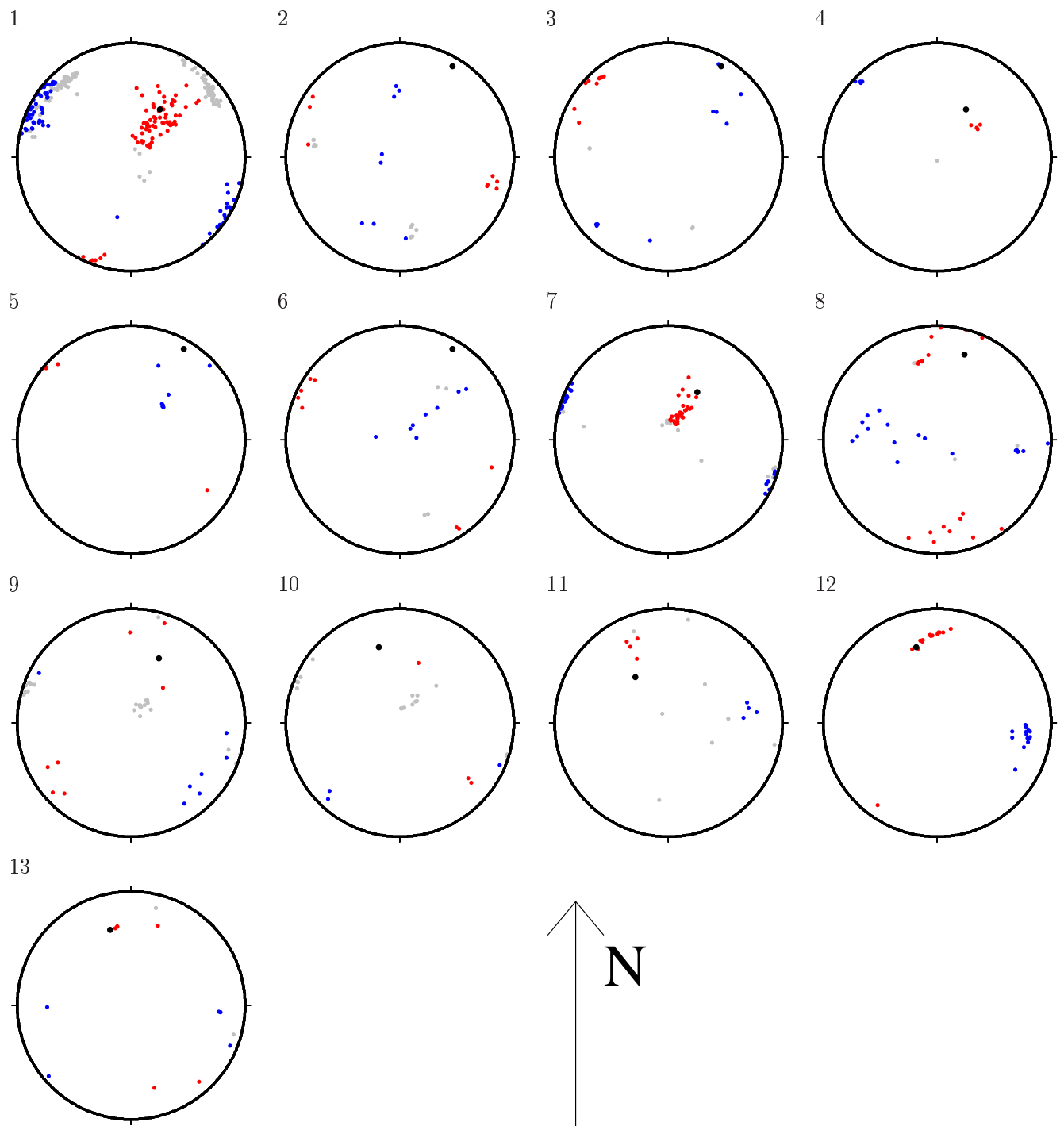
Figure 3.11: Result of the fault plane determination using hypocentres for 13 multiplets counted horizontally from the upper left to the lower right; dots indicate the piercing point of the appropriate unit vector; the black dot indicates the normal direction for the suggested fault plane, red circles are clustered fault normal directions and blue circles mark the auxiliary normal; grey circles denote undetermined axes

MP	no. of avail. mechanisms	no. of det. fault planes	strike	dip
01	126	67	301.0	40.3
02	14	6	300	81
03	11	3	300	81
04	5	4	301.0	40.3
05	7	6	300	81
06	10	6	300	81
07	38	30	301.0	40.3
08	20	9	287.6	67.4
09	20	3	293.5	51.3
10	13	1	254.4	58.0
11	8	4	233.9	40.8
12	16	15	254.4	58.0
13	7	4	254.4	58.0

Table 3.7: Multiplet no., size, and the number of detected fault planes together with strike and dip angles of the best fitting planes selected in table 3.6

Fault plane determination using fault normal clustering

The result of the fault plane normal clustering analysis is shown in fig. 3.12. For most multiplets one particular cluster of axes can be identified. However, for multiplets 8, 11, and 13 the result is ambigous because both axes groups are widely spreading over the unit sphere. It is also remarkable that although a minimum rotation angle criterion has been defined, there are some cases where auxiliary axes are very close to the cluster and, therefore, the expected fault normal axis seems far away.

Comparison of hyponcentre plane fitting and fault normal clustering

Two independent methods for the selection of one nodal plane as the most probable fault plane have been presented in the previous chapter. If both methods yield the same result the estimate of the fault plane is most reliable. For the method of nodal plane selection by hypocentre distributions three different methods to determine the appropriate zone of weakness have been presented. One of these has been selected by counting the number of smallest rotation angles in relation to the given threshold angle of 30°. Table 3.8 shows that the estimation of the fault plane using zones of weakness determined by the hypocentre distribution of single multiplets and of multiplet groups does not lead to desirable results in most cases if compared to the fault normal clustering method. For 12 of the 13 multiplets the visual estimation of the zone of weakness is to be preferred while for multiplet 06, the plane indicated by hypocentres of the multiplet gives the best result. For events for which the same nodal plane is selected as the fault plane, this plane is fixed in the input file to the stress inversion program.

Validation of nodal plane selection using back hemisphere projection

To verify the validity of the orientation of the determined zones of weakness, the back projection method has been applied to all moment tensors that can be associated to multiplets. Fig. 3.13 through Fig. 3.16 show that for many events the estimated fault plane coincides very well with at least one of the nodal planes that belong to the best double couple derived from the appropriate moment tensor. For normal and thrust events this method works very well while for strike-slip events it becomes difficult
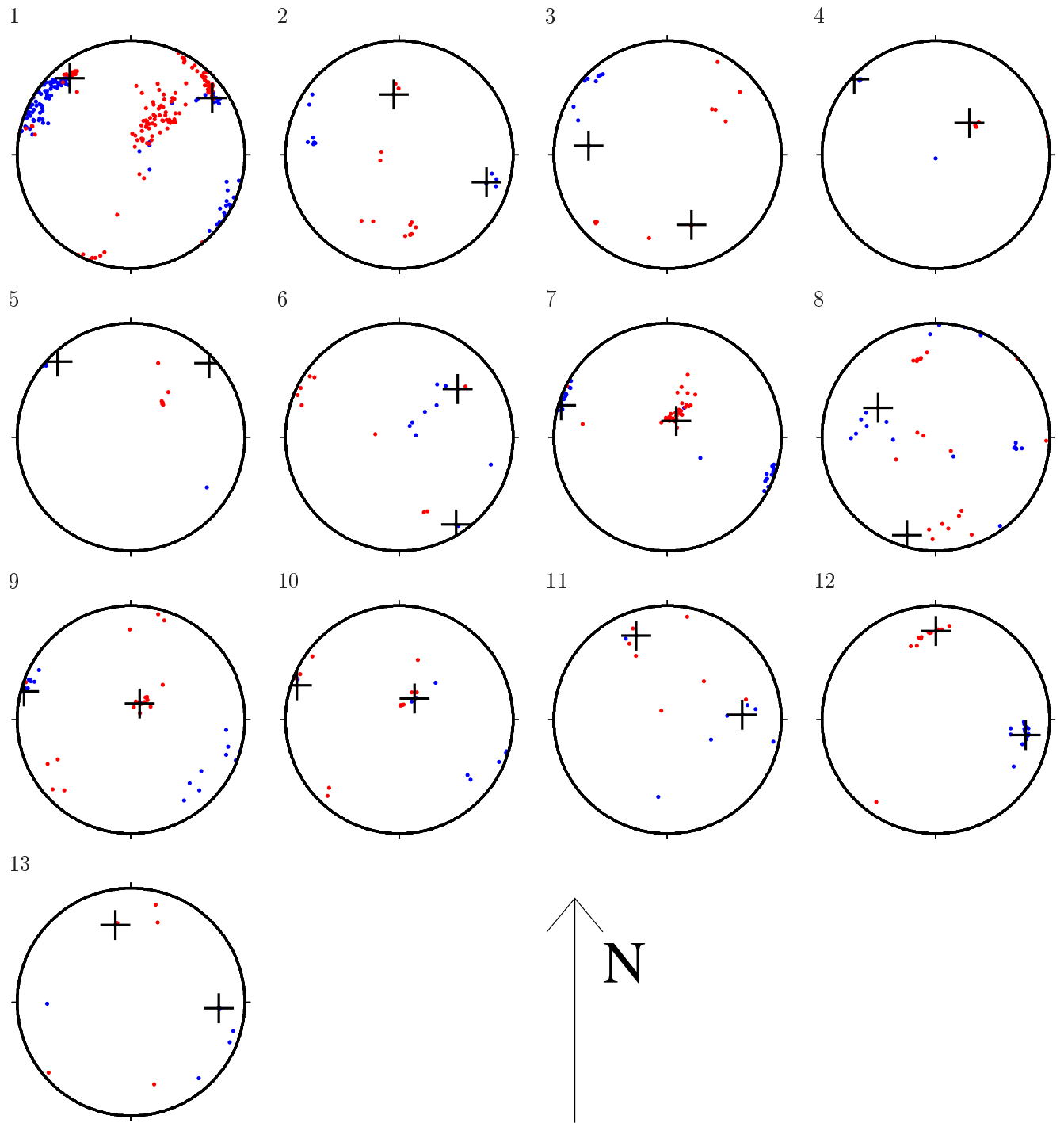
Figure 3.12: Result of the fault normal clustering analysis for 13 multiplets counted horizontally from the upper left to the lower right; black crosses denote the normals of the template event; red and blue dots indicate groups of clustered fault normal directions

MP	no. of avail. mechanisms	perc. bymp	perc. bypg	perc. byvi
01	126	41.3	14.3	84.1
02	14	21.4	0.0	57.1
03	11	72.7	0.0	81.8
04	5	0.0	20.0	100.0
05	7	0.0	0.0	100.0
06	10	80.0	70.0	30.0
07	38	5.3	5.3	97.4
08	20	30.0	30.0	50.0
09	20	5.0	30.0	65.0
10	13	23.1	30.8	76.9
11	8	12.5	12.5	87.5
12	16	0.0	0.0	100.0
13	7	0.0	14.3	85.7

Table 3.8: Comparison of the hypocentre plane fitting method and the nodal plane selection methods; columns 3 to 5 contain percentages of identical identified best fitting nodal planes

to distinguish which one of the two nodal planes is related to the determined fault plane. This is because both back hemisphere projections may be interpreted to coincide with a fault plane (i.e. show a straight line).

3.1.4   Database of Stress-Indicators

There is a number of publications available in which stress measurements for the area Vogtland/NW-Bohemia in the form of focal meachanisms, moment tensors, or direct stress measurements can be found. These have been reviewed and the results have been compiled into a dataset of stress indicators presented in this section.

Stress indicators in the area Vogtland/NW-Bohemia including KTB

One of the best observed spots near the area Vogtland/NW-Bohemia is the KTB drilling site where a deep borehole up to a depth of $9101m$ has been drilled in the early 1980's. Several authors have reported stress measurements directly related to the KTB, including Zoback and Harjes (1997), Brudy et al. (1997), Dahlheim et al. (1997), Jost et al. (1998), and Bohnhoff et al. (2004). Besides several single events, there is a high activity of earthquake swarms in the Czech and German Vogtland region. Fig. 3.17 shows the locations and the appropriate focal mechanisms and of a selection of available data mentioned in table 3.9.

3.2   Inversion for homogeneous stress fields

The methods described in section 2.2 are applied. The right-dihedra method (Angelier and Mechler, 1977) is used to estimate rough confidence limits. The result using the method of Michael (1984) is compared with those from the method of Dahm and Plenefisch (2001) and with results published earlier.

a1)
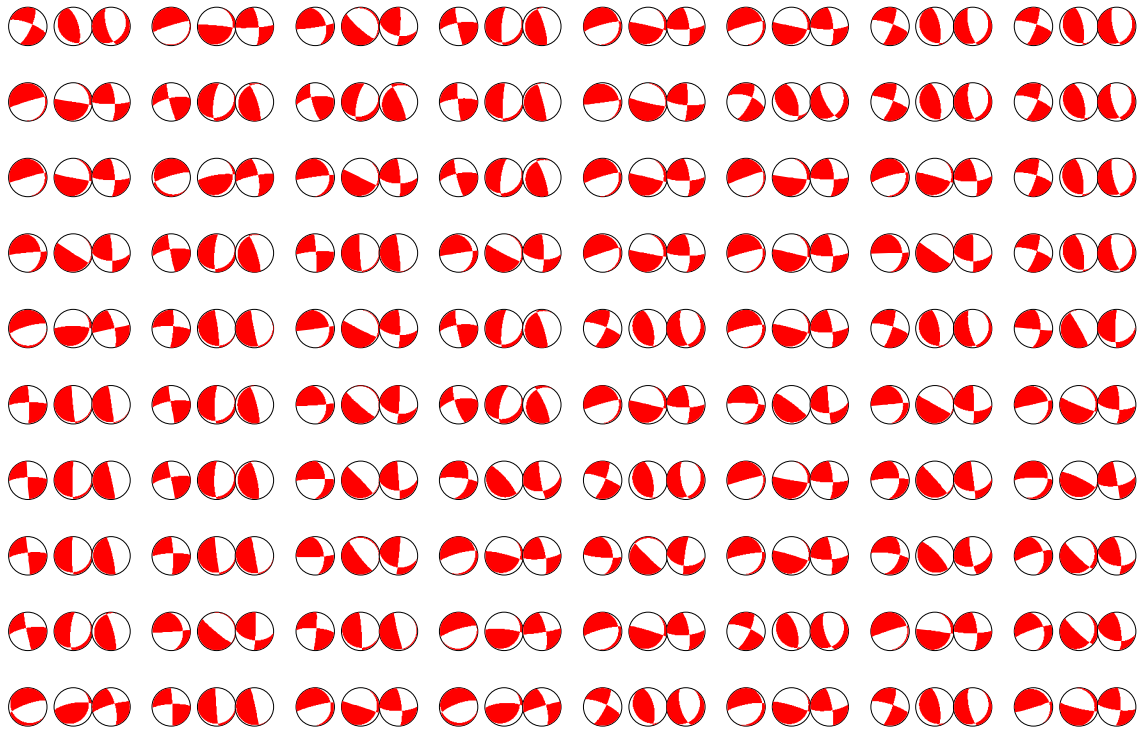
a2)
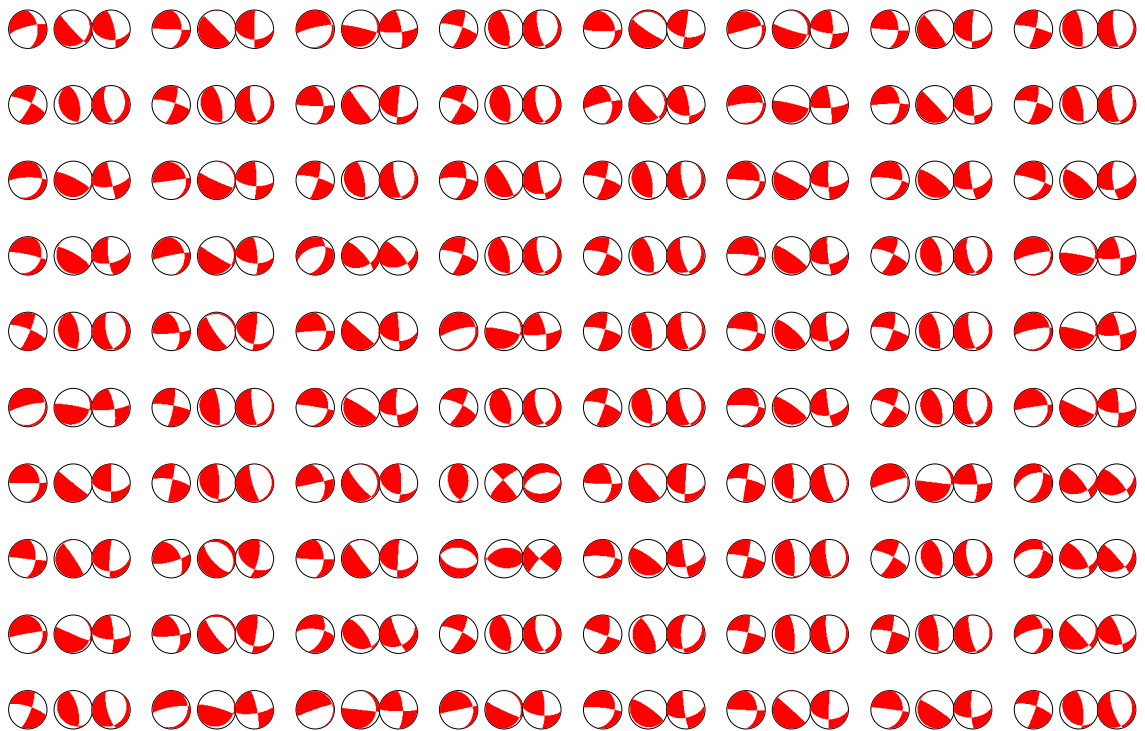
Figure 3.13: Rotated back hemisphere projections for the multiplets identified for the 1997 swarm; columns are organised to consist of three projections: leftmost is the lower hemisphere projection of the best double couple of the original moment tensor rotated about $360^o - \phi$, where ϕ is the azimuth of the zone of weakness associated to the appropriate multiplet, the middle double couple shows the back hemisphere projection in the direction of the strike of the associated zone of weakness and the right shows the view directly onto the plane - part 1 of 4

a3)
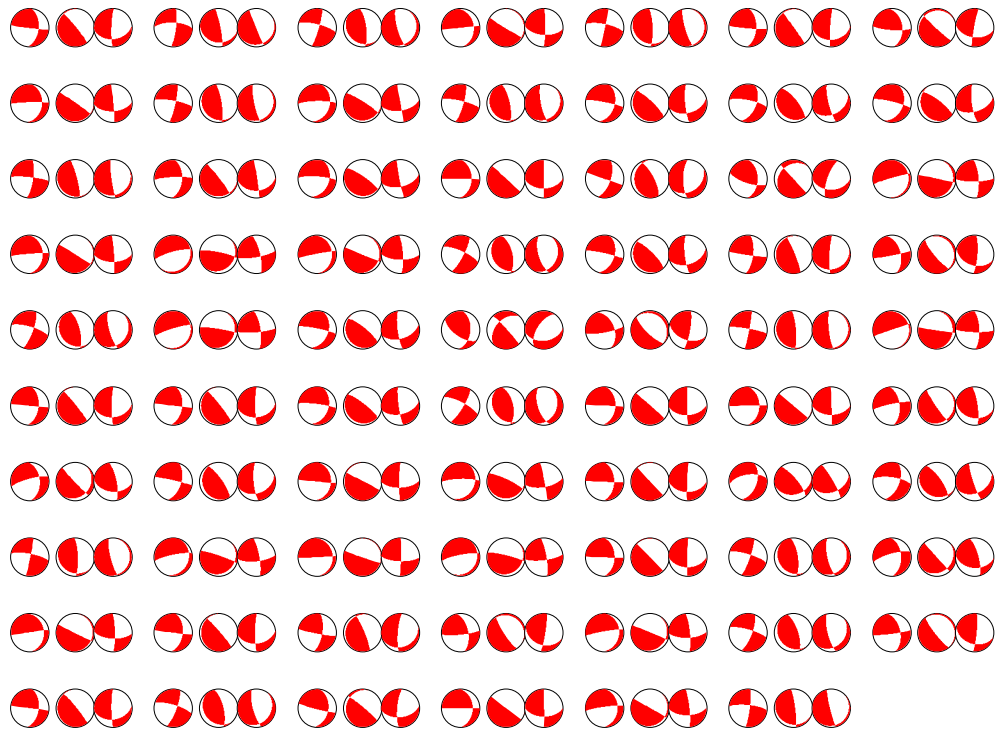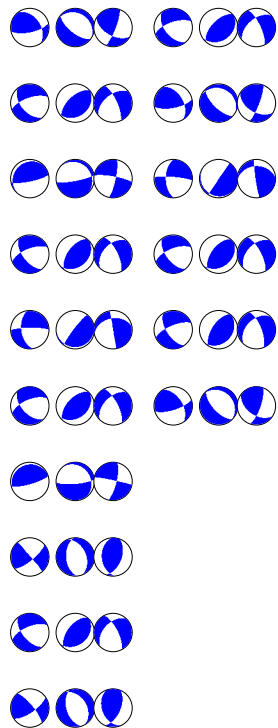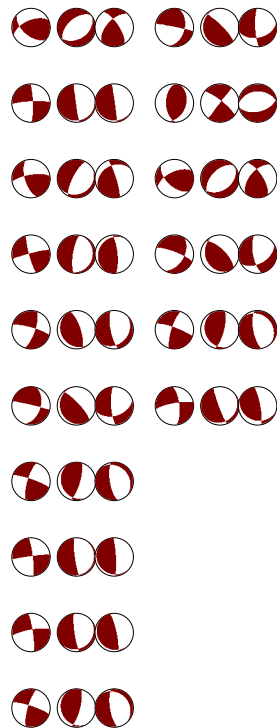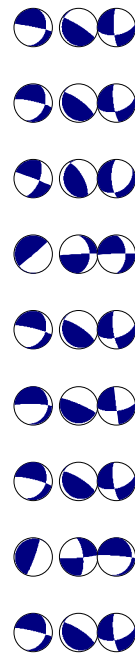
b)   c)   d)   e)
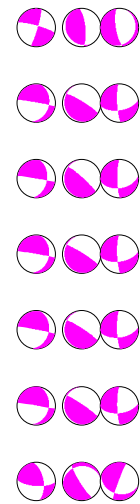
Figure 3.14: Rotated back hemisphere projections for the multiplets identified for the 1997 swarm - part 2 of 4

f) g)

h) i) j)
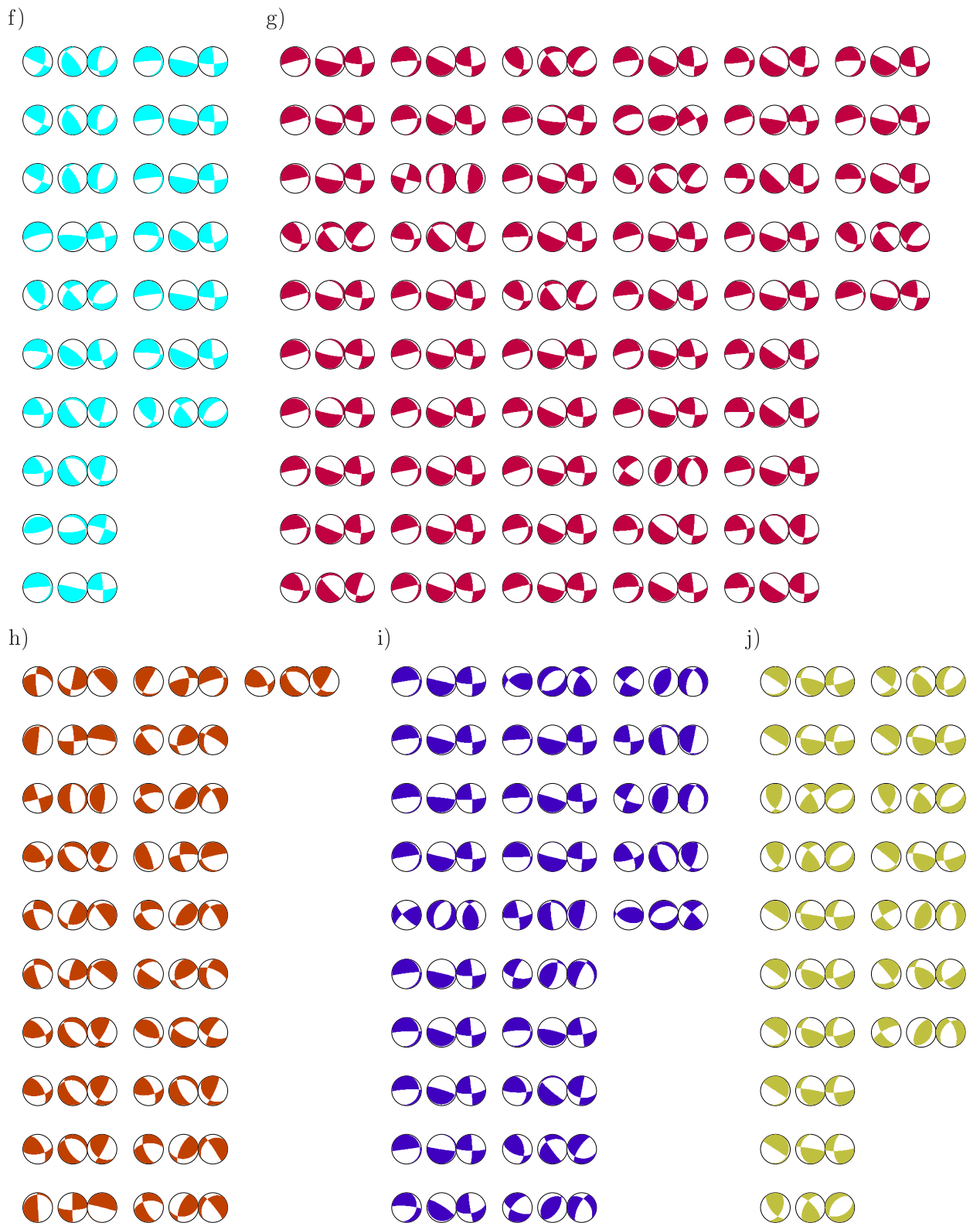
Figure 3.15: Rotated back hemisphere projections for the multiplets identified for the 1997 swarm - part 3 of 4

k)   l)   m)
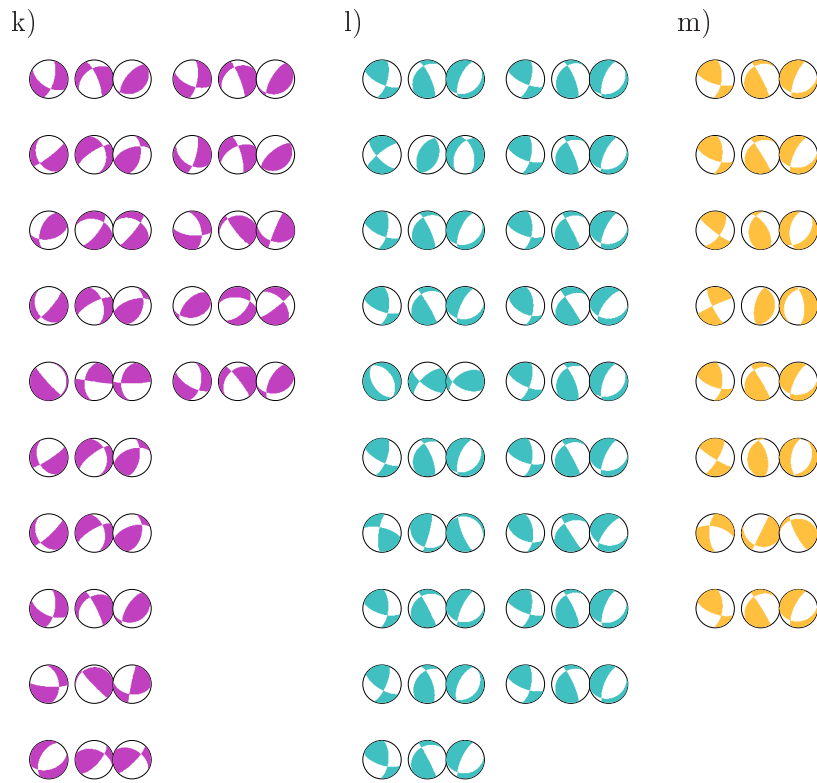
Figure 3.16: Rotated back hemisphere projections for the multiplets identified for the 1997 swarm - part 4 of 4

Dahlheim et al. (1997)	11 focal mechanisms (1991-1994 KTB-NET)
Brudy et al. (1997)	depth profile of the stress tensor (KTB)
Skácelová et al. (1998)	10 focal mechanisms (swarm 1994)
Wirth et al. (2000)	30 focal mechanisms (region Vogtland/NW-Bohemia)
Plenefisch and Klinge (2003)	12 focal mechanisms (swarm 2000)
Ibs-von Seht et al. (2004)	7 focal mechanisms (swarm near Marktredwitz)
	1 Spannungsinversion
Fischer and Horálek (2004)	134 focal mechanisms (swarm 2000)
Dahm et al. (2000)	70 relative und absolute MT (1997 swarm)
Reinecker et al. (2004)	2 stress inversions (near Novy Kostel)
(World-Stress-Map,	20 focal mechanisms (Vogtland swarm 1985/86, etc.)
region Vogtland/	15 hydraulic fracturing measurements
NW-Bohemia, some from KTB)	8 overcoring measurements
	1 slickenside
	7 borehole-breakout measurements

Table 3.9: Publications containing stress measurements and stress indicators located in the area Vogtland/NW-Bohemia and its vicinity
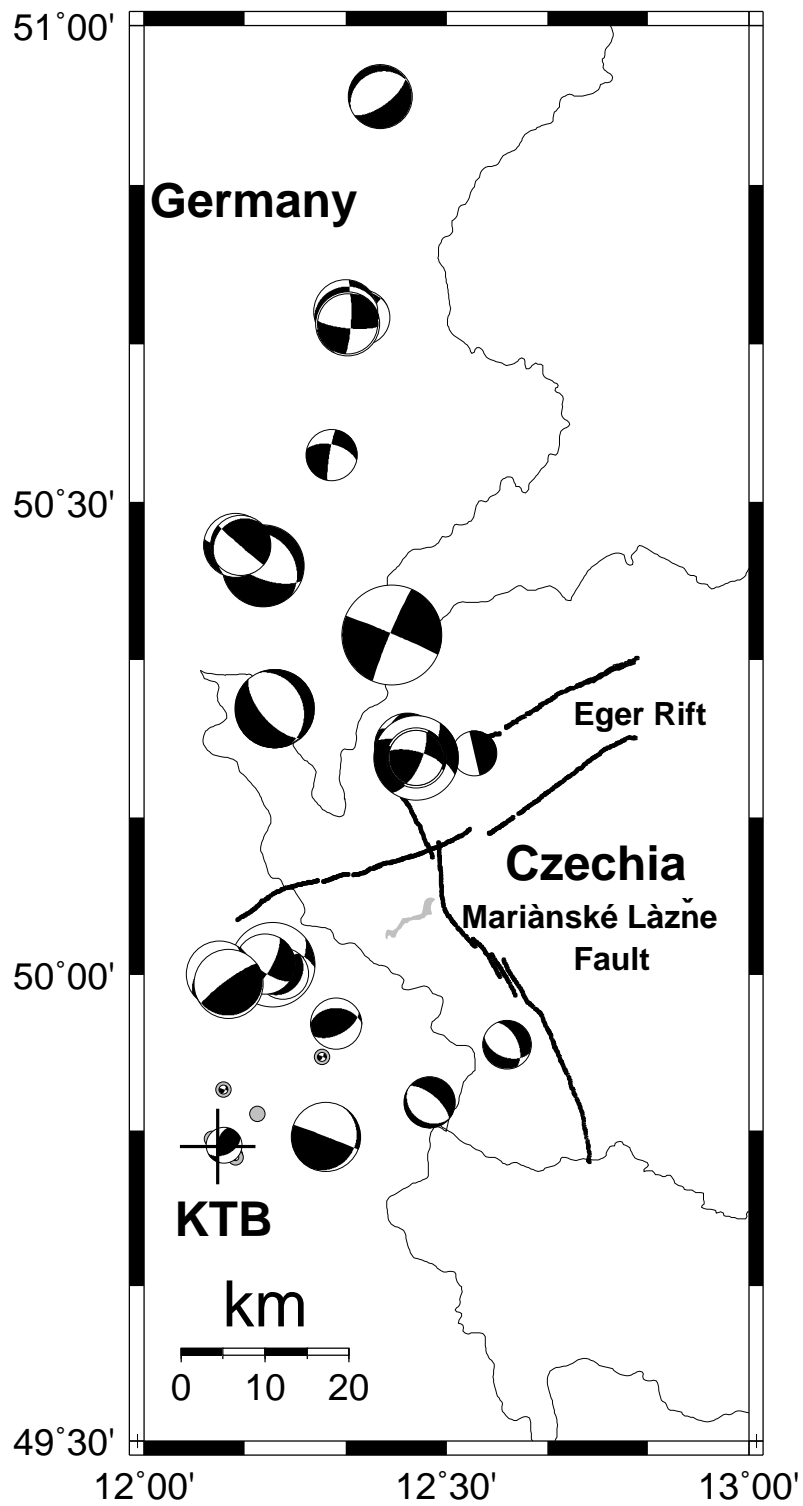
Figure 3.17: Map showing the epicentres of 65 events indicated by grey circles overlain by the appropriate focal mechanisms that have been used for the regional stress inversion; magnitudes range from $M_L = 0.2$ to $M_L = 3.3$

Author	no. of events	remark
Fischer (2003)	5	NW-Bohemia swarm 2000, 5 strongest
Plenefisch and Klinge (2003)	2	single events Vogtland/NW-Bohemia
Dahlheim et al. (1997)	11	single events Vogtland/NW-Bohemia
Wirth et al. (2000)	30	single events and swarm events Vogtland/NW-Bohemia
Ibs-von Seht et al. (2004)	7	single events, German Vogtland
Bohnhoff et al. (2004)	5	KTB injection experiment 2000, 5 strongest
Dahm et al. (2000) this study (see chapter 3.1)	5	NW-Bohemia 1997 swarm 5 strongest of $70 \cup 352$

Table 3.10: Sources of the input data for the inversion of the homogeneous regional stress field

Author	Site	σ_1 (az/pl)	σ_2 (az/pl)	σ_3 (az/pl)	R
This study	Vogtland	$147 \pm 55/$ 9 ± 7	$10 \pm 39/$ 78 ± 6	$238 \pm 16/$ 8 ± 5	0.4 ± 0.3
Vavryčuk (2002)	West Bohemia	156/33	20/48	262/23	0.69
Brudy et al. (1997)	KTB	$160 \pm 10/0$	Vertical	$250 \pm 10/0$	0.72
Müller et al. (1992)	Western Europe	$144 \pm 26/0$	Vertical	$234 \pm 26/0$	——

Table 3.11: Comparison of the results from this study with previous work from several different workers

The first subset of data consists of focal mechanisms and moment tensors from events that occured over the whole area indicated in fig. 1.28 which have been collected in section 3.1.4. The second subset of data consists of the moment tensors estimated in section 3.1.3 by taking the nodal plane information into account. Finally, the third subset of data originates from the KTB drilling site and is taken from Bohnhoff et al. (2004).

3.2.1 Regional stress field

65 focal mechanisms and moment tensors have been collected for an estimate of the orientation of the regional stress field. Table 3.10 gives an overview of the source of the data, the number of used events, and a description where the epicentral area is situated.

Fig. 3.17 shows the epicentres of the focal mechanism measurements used for the regional stress field inversion. Since there are 422, 132, and 125 measurements available for the 1997 swarm, the swarm 2000, and the KTB, respectively, only the five largest events in magnitude of each subset have been selected as representatives for the inversion. This prevents strong influence of these subsets of data consisting of many small events.

In many cases where the regional homogeneous stress field should be analysed the orientation of the pressure and tension axes (P and T) yield a good estimate. The orientations of the axes for the selected dataset are shown in fig. 3.18. According to the orientation of the P- and T-axes the pattern that is observed indicates that the σ_1-axis must lie on a vertical plane in NW-SE direction and the σ_3-axis on a vertical plane in NE-SW direction, respectively. From a logical point of view the minimum and maximum principal axes of stress that match this criterion lie in the horizontal plane, since the axes must be perpendicular to each other. This finding is verified by the result of the right dihedra method (Angelier and Mechler, 1977) and the energy criterion based inversion (Dahm and Plenefisch, 2001) shown in fig. 3.18. The result found with the dataset used here is in good agreement with the findings for this region of several authors (see caption of fig. 3.18 and table 3.11).
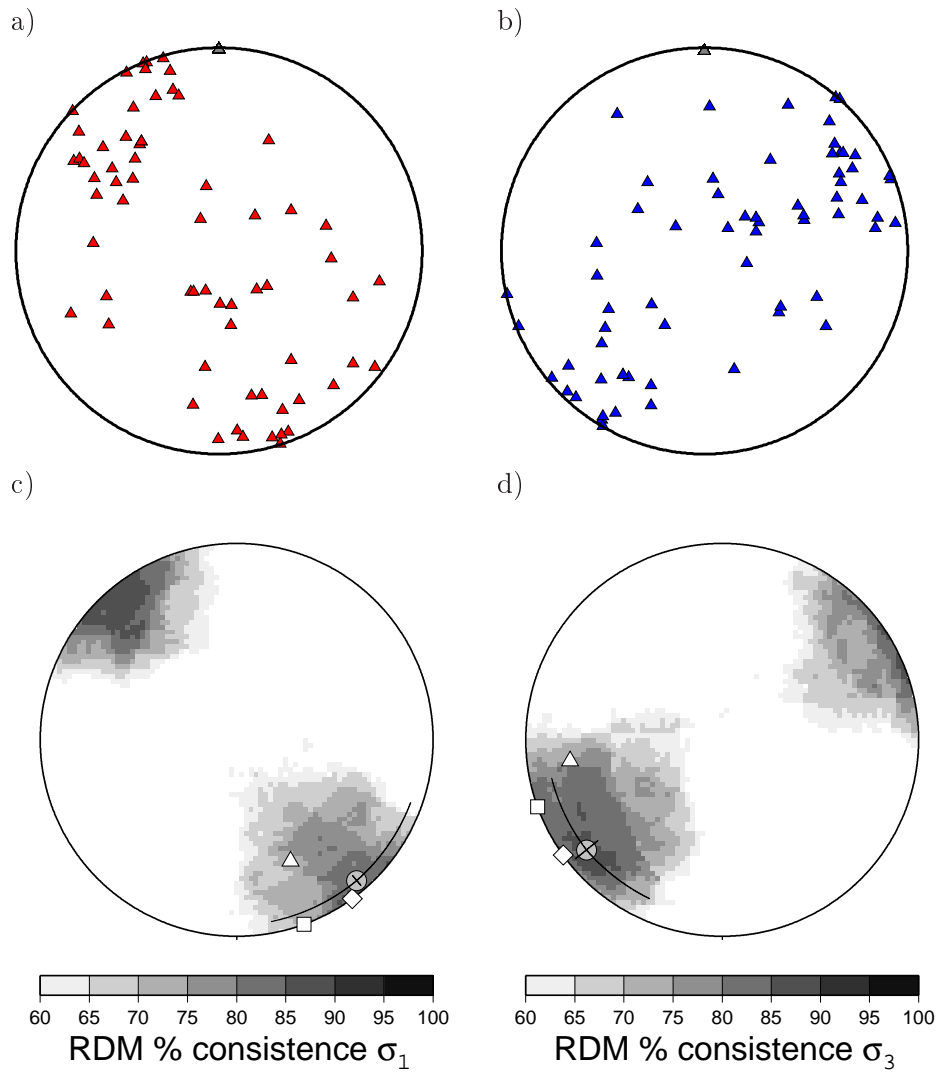
Figure 3.18: P- and T-axes for the dataset of 65 selected focal mechanisms which are taken from several sources (see table 3.10 for details) and homogeneous regional stress inversion with the right dihedra method (Angelier and Mechler, 1977) denoted by gray confidence areas and coloured symbols for the stress inversion after Dahm and Plenefisch (2001) in comparison to results for NW-Bohemia from (Vavryčuk, 2002, triangles), (Brudy et al., 1997, squares), and (Reinecker et al., 2004, diamonds): a) P-axes; b) T-axes; c) σ_1 axis ; d) σ_3 axis
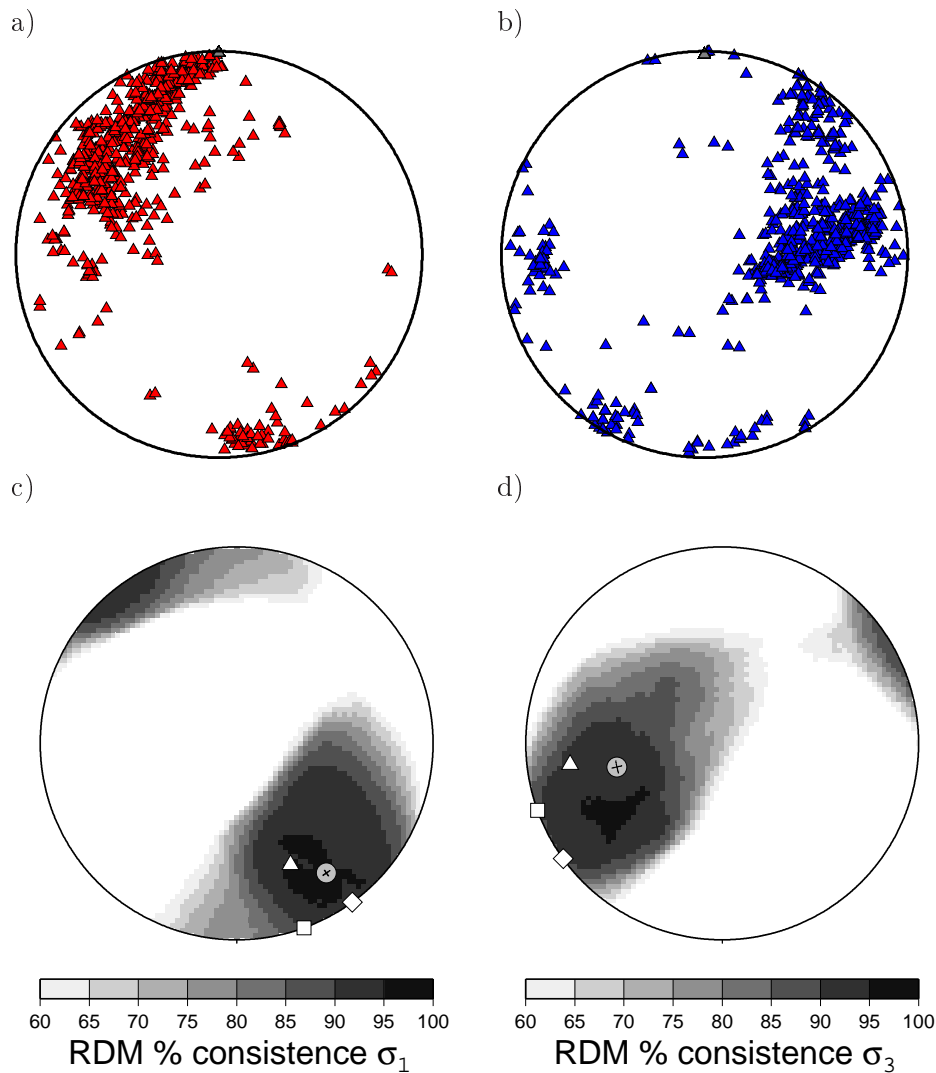
Figure 3.19: Same as in fig. 3.18 except for the dataset which consists of 133 moment tensors of the swarm 2000 taken from Fischer (2003) and 408 selected moment tensors taken from this work

3.2.2 The Vogtland/NW-Bohemia 1997 swarm

The 1997 swarm in the Czech Nový Kostel area is reported not to be caused by an entirely homogeneous stress field by Slancová and Horálek (2000). To verify this finding the moment tensors calculated in this work and those from Fischer (2003) are combined and inverted for the homogeneous stress field. Fig. 3.19 shows the result which indicates that the axes are aligned on thin areas on the focal sphere. Additionaly there are also large areas on the focal spheres visible for which the possible σ_1 and σ_3 directions indicate a wide variety of stress fields that can explain the focal mechanisms of this dataset.

3.2.3 KTB

The same analysis as for the regional dataset and the one for the Czech swarm region has been applied to the dataset of 125 focal mechanisms from the 2000 hydraulic fracturing experiment at the KTB drilling site taken (see Bohnhoff et al., 2004). The first arrival polarities of 237 events were used to calculate 98 single-event focal mechanism solutions. In addition 27 fault mechanisms had been determined as compound solutions for groups of earthquakes which are thought to represent repeated
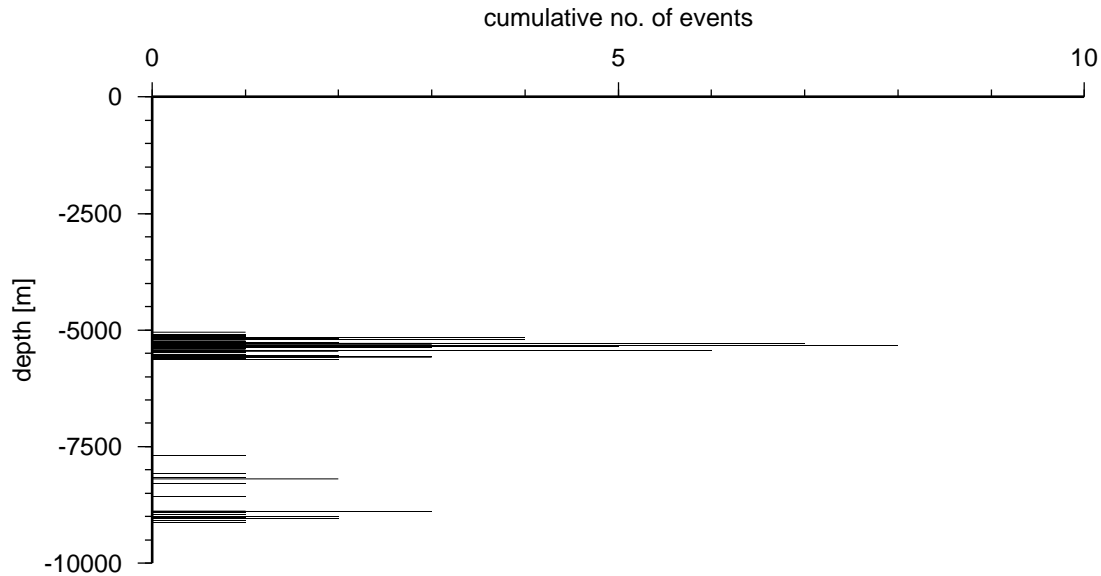
Figure 3.20: Depth distribution of 125 events of the 2000 hydrofracturing experiment at the KTB

slip on particular fracture planes. Looking at the depth distribution in fig. 3.20, the lack of seismicity in the depth range from about $6000m$ to $7500m$ is noticable. The seismicity above this gap can be explained by a leak in the borehole casing in about $5.4km$ depth and that below is related to the open-hole section at the bottom of the borehole as described by Baisch et al. (2002). When looking at the distribution of the P- and T-axes in fig. 3.21 again the observed orientation pattern of the P- and T-axes indicates that the σ_1-axis must lie on a vertical plane in NW-SE direction and the σ_3-axis on a vertical plane in NE-SW direction, respectively. Therefore both minimum and maximum principal axes must lie in the horizontal plane, since the axes are perpendicular to each other. The validity of this finding is approved by the comparison with publications of different other authors in table 3.11.

3.3 Stress inhomogeneities

This section covers the main goal of the work which is to determine inhomogeneities in the stress field. First, some synthetic tests are established to get an idea of the resolution and stability of the method of source volume segmentation. Then the method is applied to the dataset of moment tensors for the Vogtland 1997 swarm and to the focal mechanisms determined during the 2000 hydraulic fracturing experiment at the KTB (Bohnhoff et al., 2004).

3.3.1 Synthetic tests

For testing the method of source volume segmenation, several synthetic test settings are introduced. Slip vectors are calculated for randomly distributed events using eq. 2.2 assuming constant and space dependant deviatoric stress fields with different fault geometry settings. The two properties to test are the stability which depends on the minimum number of events per box for trying an inversion and the resolution which depends on the spatial distribution of events in an inhomogeneous stress field.

a)

b)

c)

d)

RDM % consistence σ_1

RDM % consistence σ_3
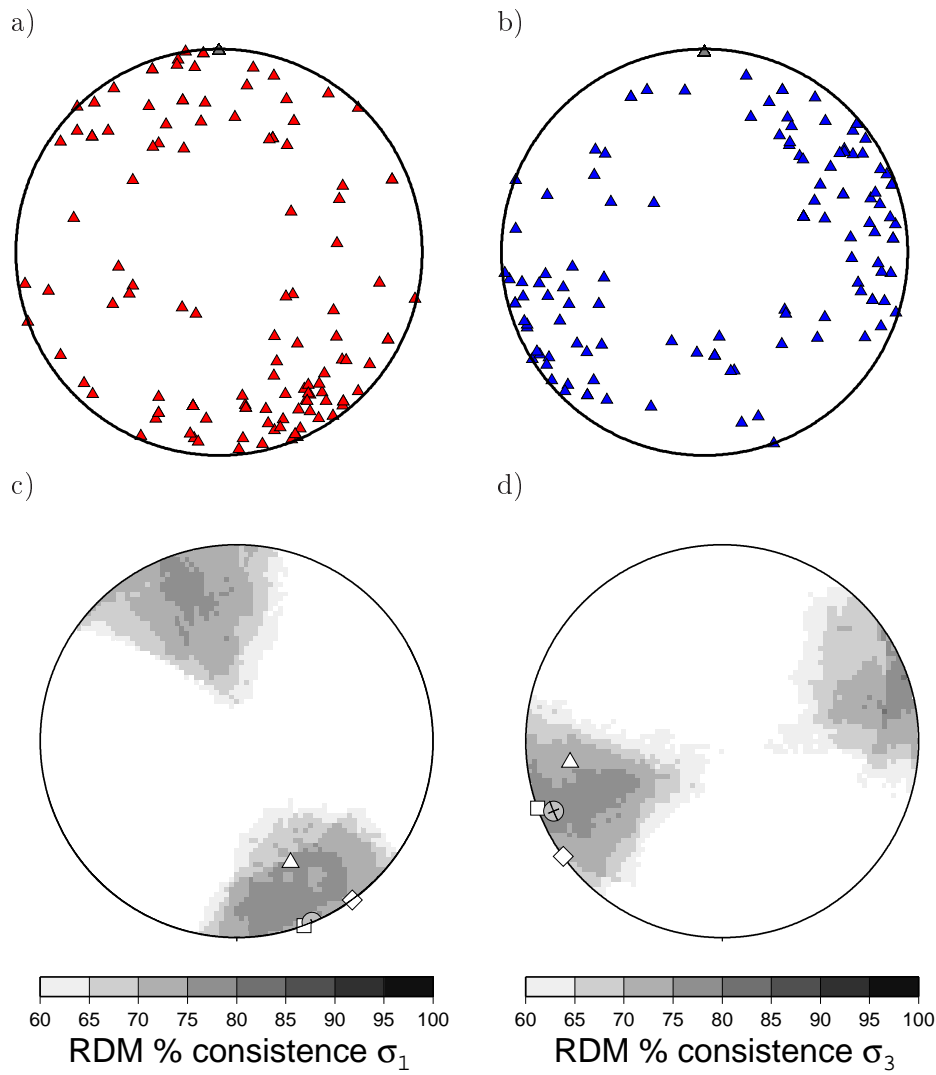
Figure 3.21: Same as in fig. 3.18 except for the dataset of 125 focal mechanisms from the 2000 hydraulic fracturing experiment at the KTB drilling site (Bohnhoff et al. (2004))

The stability is determined by starting with a minimum number of 6 measurements per box for trying an inversion to guarantee a one and a half times overdetermined inversion problem (four independent parameters are sought). This number is increased until the input stress field is inverted with an acceptable small number of outliers.

For the resolution test, the inverted stress field is compared with the input stress field for different scenarios. Four simple test cases covering different stress field and fault geometry distribution conditions are presented in appendices D.1.1 through D.1.4. The fifth test scenario is described in more detail in the following paragraphs.

Fig. 3.22 and fig. 3.22show a summary of the stability test for three selected minimum numbers of events per box for trying an inversion. The test scenario is described in the caption of the figure. For the highest considered setting of 15, all of the inverted stress directions show acceptable differences from the original stress field whose mean σ_1 direction is oriented N-S. Using smaller numbers does not change the result too much until, with a minimum number of 10, some more inversions are taken into account. Some of the inverted stresses at the edges of the slice show a slightly larger difference to the original stress field, but are still acceptable, because the original stress field is quite variable by $\pm 15^o$. By decreasing the value down to 6 measurements per box, with each step more boxes are tried for an inversion. However, many of these are not acceptable, so the usage of at least 10 events per box for trying an inversion is justified.

For the resolution test, the rotation of a synthetic stress field with depth is analysed in fig. 3.24 and fig. 3.25 where the same synthetic dataset as in fig. 3.22 and fig. 3.23 has been used. It is obvious that for all depth slices a reasonable stress field orientation is recovered. Variations regarding the principal stress axis orientations inside the slices can be explained by variations in the event density regarding the rotation of the principal axes of stress (σ_1 rotates from -60° N to 60° N with increasing depth). For a box which, by chance, includes many events at its top but only few at its bottom, the resolved stress directions will indicate a σ_1 direction with an azimuth angle pointing more to the east.

3.3.2 Application to Vogtland/NW-Bohemia 1997 swarm

Source volume segmentation

In this approach, only those moment tensors of the 1997 swarm have been taken into account for which also a location is available. These prerequisite allows 408 moment tensors to be analysed. The synthetic tests in the previous section imply a minimum number of 10 events per box leading to a segmentation into 7x7x7 overlapping boxes. The result of the source volume segmentation is shown in fig. 3.26. When comparing σ_1 directions from different depth slices, it becomes obvious that inhomogeneities in the stress field exist.

Smoothed stress tensor field

For the determination of stress trajectories, the components of the stress tensors are transformed into 6-component vectors featuring the six independent components of the stress tensor. These are used as control points for a 3D-NURBS spline algorithm. For a validity test, the NURBS spline functions are evaluated on a regular grid, transformed into stress tensors and compared to the input data by the orientation of the principal axes of stress. Stress inhomogeneities are evaluated in slices of constant depth. The comparison of the NURBS smoothed stress directions with the input data for the central depth slice of the earthquake swarm is shown in fig. 3.27. It becomes clear that the stress tensor is

Figure 3.22: Test for the stability of the source volume segmentation by decreasing the number of measurements per box from 15 over 10 to 6 for trying an inversion; the synthetic dataset for the inversion is calculated using a stress field rotating with depth with σ_2 (yellow square) vertical and σ_1 (red triangle) varying from -60° N to 60° N (σ_3 - blue triangle - is perpendicular to both by definition); for comparison reasons only the centre horizontal slice is shown where σ_1 lies between -15° N and 15° N; 600 slip vectors are computed using eq. 2.2 (see section 2.2) for 200 events on each of the three main fault plane orientations identified in section 3.1.3 whose hypocentres are gauss distributed around the centre of the source volume; part 1 of 2

Figure 3.23: Test for the stability of the source volume segmentation by decreasing the number of measurements per box from 15 over 10 to 6 for trying an inversion; part 2 of 2

obtained correctly by the NURBS algorithm because the direction of the smoothed axes are similar to those of the input data in its vicinity. The result for the seven innermost depth slices is shown in fig. 3.28.

Stress trajectories

The source volume's size is about $1000x1000x1000m^3$. It has been subdivided into 21 layers of equal thickness and the trajectories are visualised using the technique described in 2.1.3. Since the patterns for the σ_1 and σ_3 trajectories, respectively, are quite different, they are examined separately.

The σ_1 trajectories in the shallowest depth slice 1 are slightly S-shaped with a NNW-SSE orientation in the North and the South and a NNE-SSW orientation inbetween. This pattern does not continue with greater depth, but a half-S-pattern is visible in depth slices 2 through 5 in fig. 3.29 and fig. 3.30 which point to the NNW in the North and to SSW in the South. At the northern edge of the slices 6, 7, 8, and 9 in fig. 3.30 and fig. 3.31 the trajectory orientation tends to diverge from the NNW to the NNE. This pattern further develops to a Y-shaped pattern which is visible in depth slices 10 through 19 (fig. 3.32 through fig. 3.35) whose legs point to the NW, S, and NE, respectively. Additionally, the NW leg ends in a convergence zone in slices 10, 11, 12, and 13 while it is bended with greater depth to an S-shaped pattern which points to the E near the focal point of the Y-shaped pattern and to the NE at its end in slices 14, 15, and 16. In slice 17 the leg points to the W. The NE leg is rotated with greater depth from NE in slice 10 over N in slice 12 (fig. 3.32) over NNW in slice 13 and 14 back to N in slice 15 (fig. 3.33) keeping this orientation in slices 16 through 19 (fig. 3.34 and fig. 3.35). The S leg keeps its orientation over the complete depth range. In depth slices 14 through 16 (fig. 3.33 and fig. 3.34) a second Y-shaped pattern with legs in the NNW, NE, and S direction that do not change
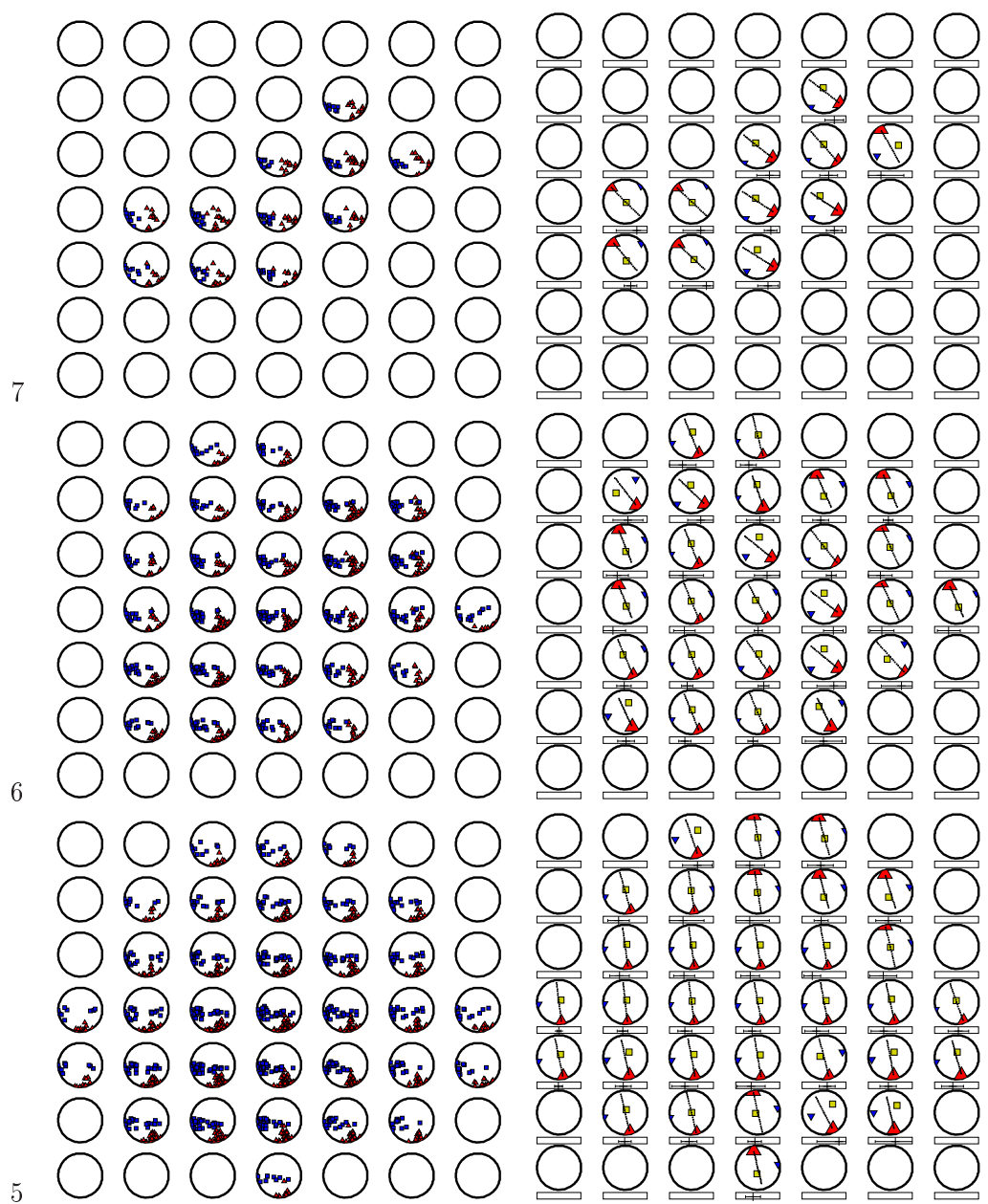
Figure 3.24: Synthetic test for a resultion estimatie of the source volume segmentation; for the test the same synthetic setup with the σ_1 direction rotating from -60° N (slice 7) to 60° N as in fig. **??** is used; seven slices in each direction have been introduced; numbers denote z-slice: smallest number means deepest slice; left column: P-axes (red triangles) and T-axes (blue triangles) of all measurements inside a box; right column: orientations of principal stress axes σ_1 (red triangle and projected unit vectors as black line), σ_2 (yellow square), and σ_3 (blue triangle); part 1 of 2

Figure 3.25: Synthetic test for a resultion estimatie of the source volume segmentation; part 2 of 2

depth of box center

8512.5 m

8625.0 m

8737.5 m

size of source volume:

− 700 m x 950 m x 900 m

number of boxes:

− 7 x 7 x 7

size of boxes:

− 187.5 m x 225 m x 225 m

min. number of obs. per box:

− 10

8850.0 m

8962.5 m

9075.0 m

9187.5 m

950 m

700 m
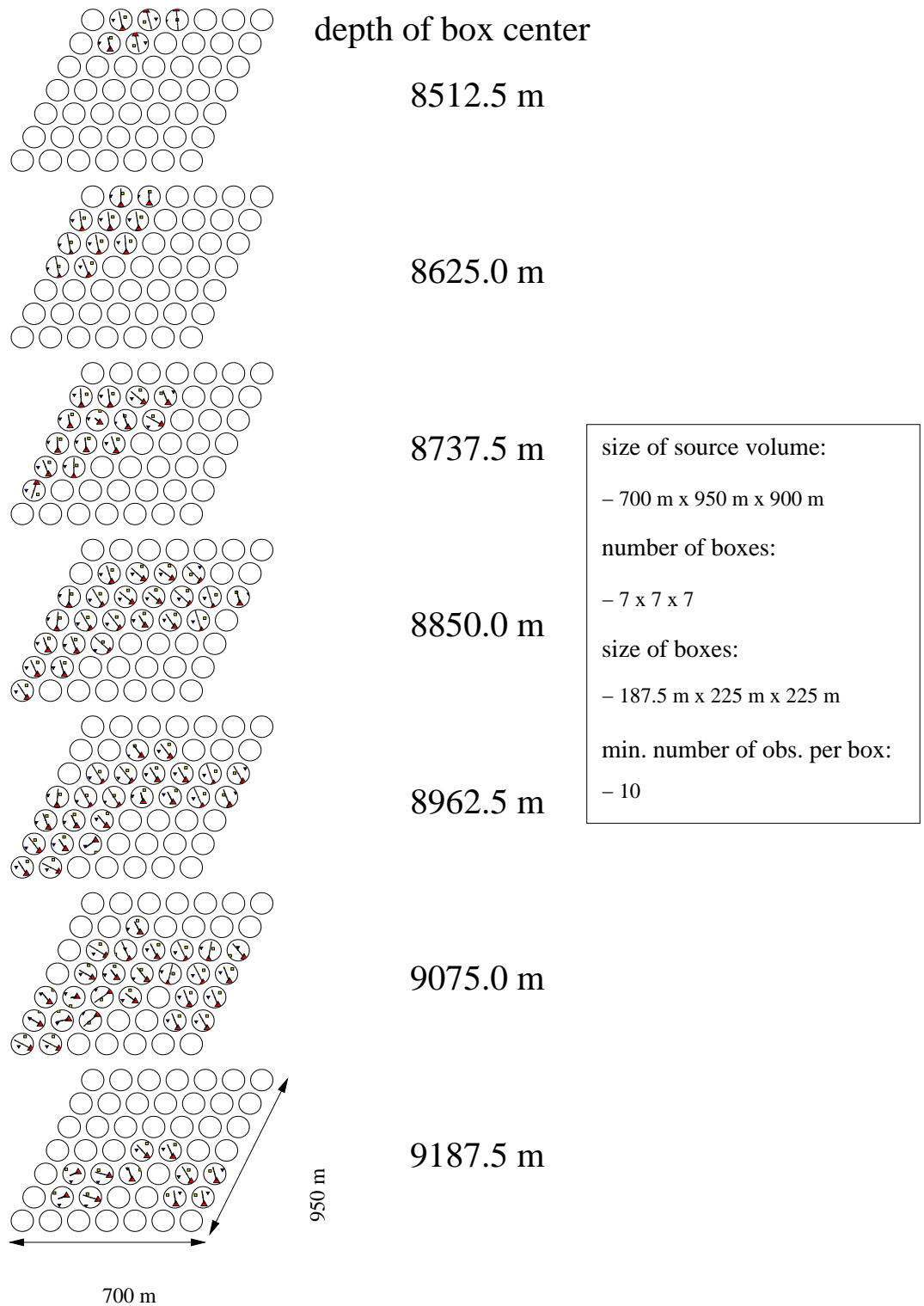
Figure 3.26: Source volume segmentation 1997 swarm: the seismogenic zone has been separated into cuboids of same size, then a homogeneous stress inversion with all data inside the appropriate cuboid is performed; equal area lower hemisphere projections of the intersecting points with the unit sphere for σ_1 (red triangles), σ_2 (yellow squares), and σ_3 (blue triangles), together with the axis of the most compressive principal stress σ_1
are shown
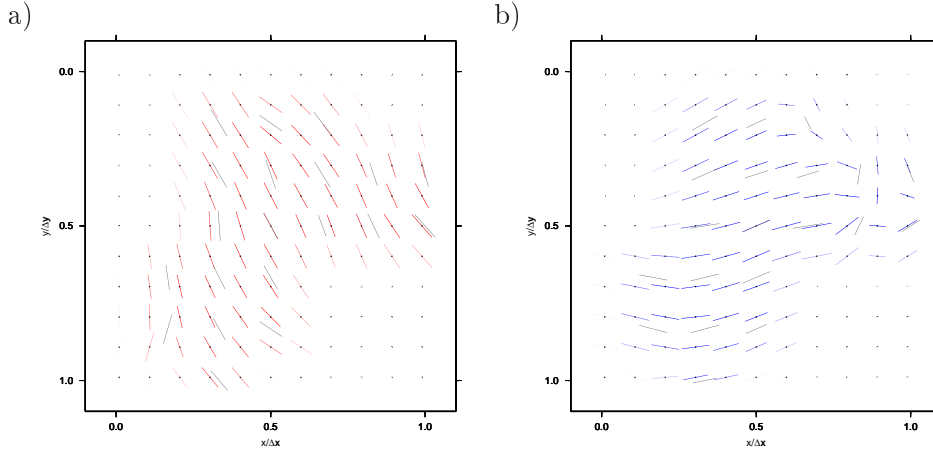
Figure 3.27: NURBS smoothed principal stress directions obtained from the results of the source volume segmentation in fig. 3.26 for the centre depth slice in comparison to the input stress field denoted by grey lines (length is proportional to the cosine of the appropriate plunge): a) σ_1 (red); b) σ_3 (blue)

their orientation is visible. Its NNW leg is connected to the S leg of the previously described Y-shaped pattern. South of the swarm centroid the trajectories coming from the NW through the NNE converge in depth slices 9 through 16 (fig. 3.31 through fig. 3.34). The deepest slices 20 and 21 show a nearly homogeneous, slightly curved stress trajectory pattern which turns from a E-W orientation in the West to a NE-SW orientation in the East.

The σ_3 trajectories in the shallowest slices 1 and 2 (fig. 3.29) indicate almost homogeneity with a stress direction WNW-ESE. A convergence zone develops SE of the swarm centroid in depth slices 3 and 4 (fig. 3.29 and fig. 3.30). This pattern changes to slightly curved trajectories which are visible in depth slices 5 through 16 (fig. 3.30 through fig. 3.34). In slices 5, 6, 7, and 8 the legs of the curves point to E in the West and to SE in the East while in greater depths in slices 9, 10, 11, and 12 the East leg is bended from SE to E. In slices 13, 14, 15, and 16 the leg is bended even more and points to ENE. A second bended feature to the NE from the swarm centre becomes visible in depth slice 11 and 12 (fig. 3.32) which changes to a divergent pattern visible in slices 13 through 19 (fig. 3.33 through fig. 3.35) whose eastern trajectories diverge in direction from NE to E. In slices 14, 15, and 16 (fig. 3.33 and fig. 3.34) a pattern of convergent trajectories is present at the SW edge of the study area. It looks like a Y-shaped structure with legs pointing in directions N, SE, and SW of which the N leg ends on the concave side of a bended trajectory trace. Slices 20 and 21 (fig. 3.35) show an almost homogeneous trajectory pattern oriented W-E where only the E part tends to the NE direction.

3.3.3 Application to KTB data

Because of the gap in the depth distribution for the KTB dataset illustrated in fig. 3.20, I decided to split the dataset at a depth of $6000m$ into an upper part consisting of 102 focal mechanisms and a lower part consisting of 23 focal mechanisms. The analysis using the source volume segmentation for the upper part is given in fig. 3.36 and for the lower part in fig. 3.37. In both depth parts, the stress field does not change much inside a depth slice. In the upper part, changes between the directions of the higest and the intermediate compressive stress (σ_1 and σ_2, respectively) is observed in the centre and the lowest slice. It is remarkable, that for the upper part σ_1 points preferably in the NNW direction

depth of layer

8604.5 m

8686.4 m

8768.2 m

8850.0 m

8931.8 m

9013.6 m

9095.5 m

950 m

950 m

700 m   700 m
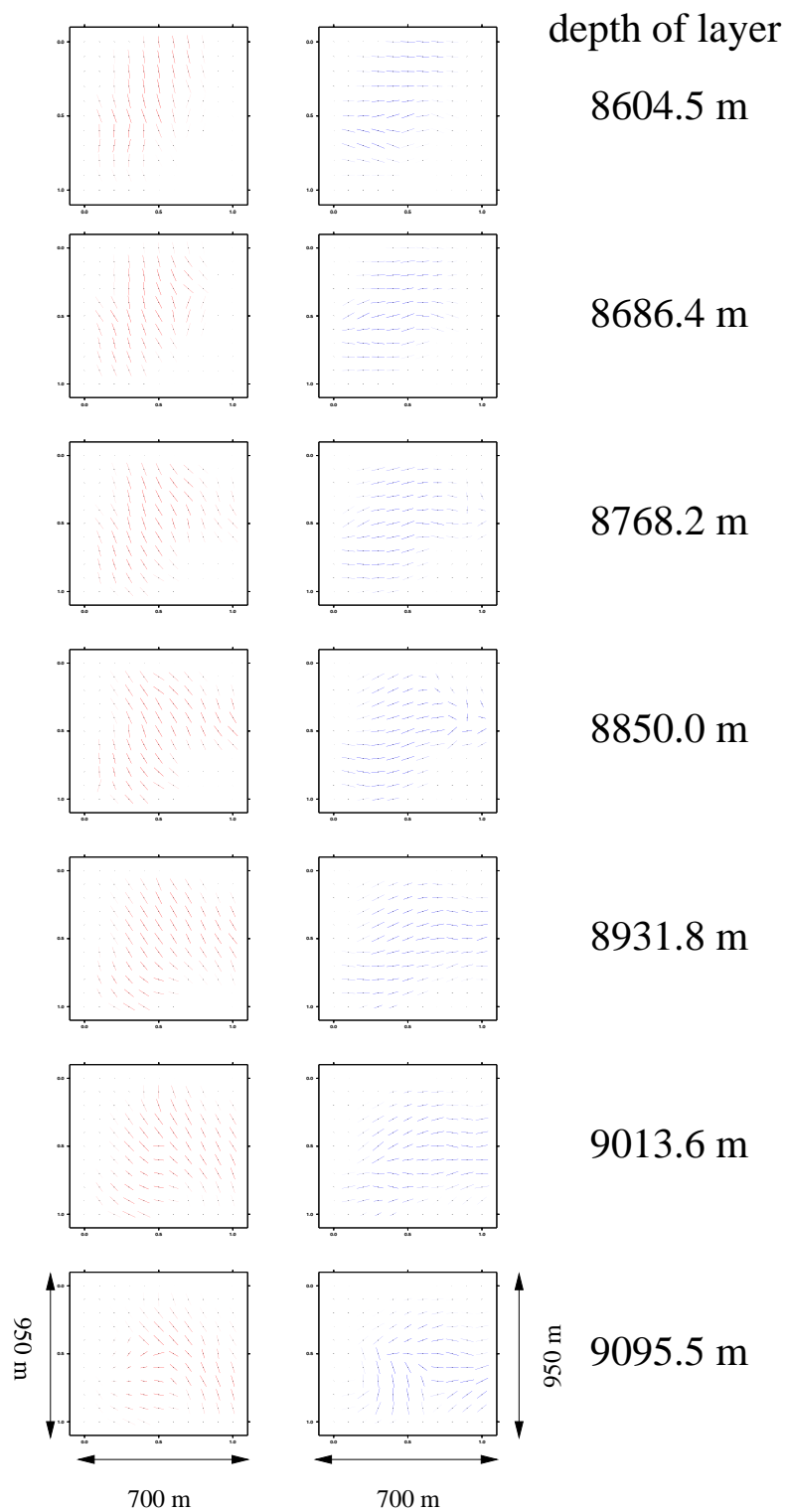
Figure 3.28: Smoothed stress directions horizontal slices through the tensor volume of the seismogenic zone of the 1997 swarm, generated with NURBS of degree 1; the seven innermost slices of eleven have been selected; stress data is the same as in fig. 3.26; opacity indicates the quality of the smoothed data point (the more opaque the fewer measurement have contributed to the estimate): a) σ_1 (red); b) σ_3 (blue)
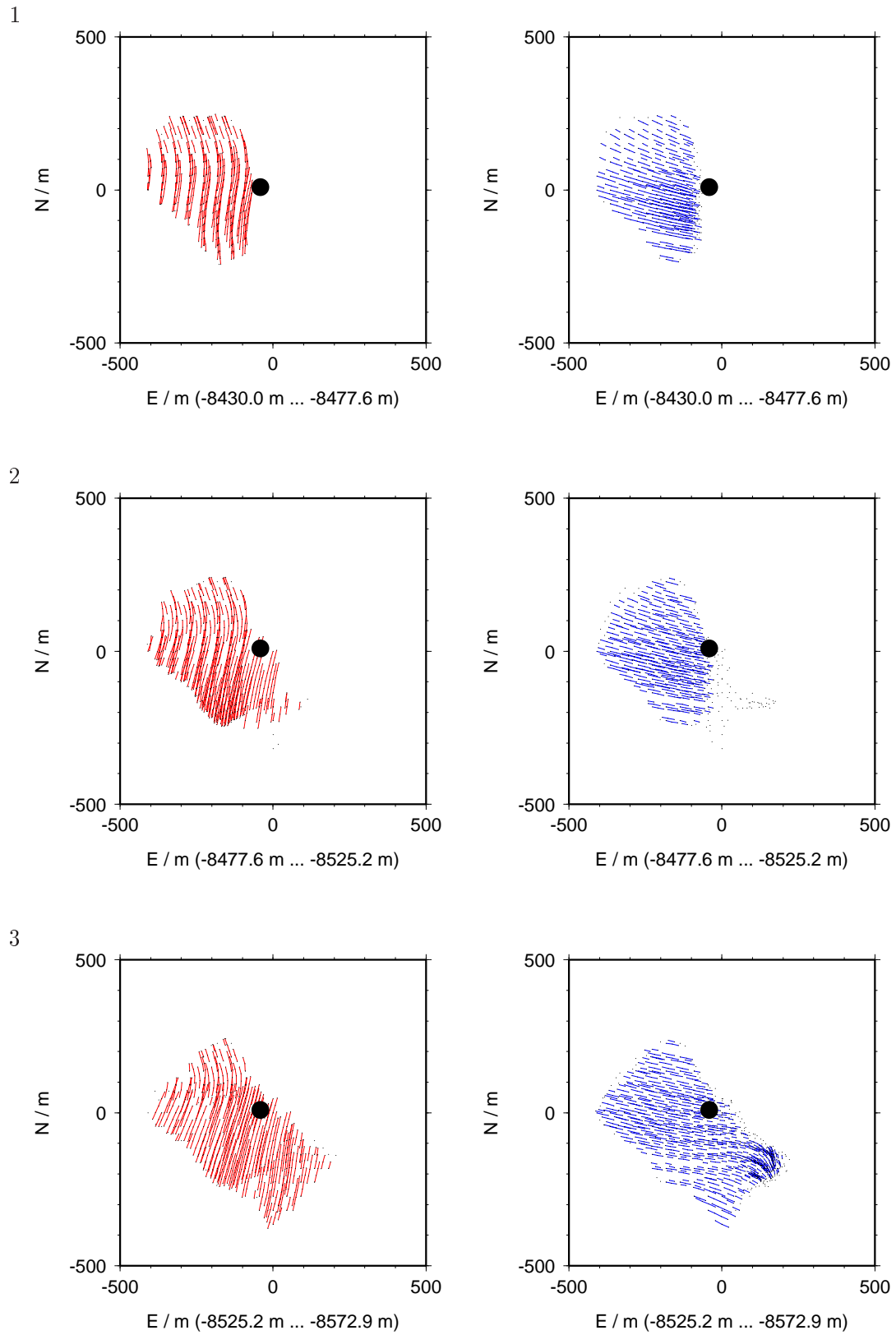
Figure 3.29: NURBS trajectories; left column: number of depth slice for reference; centre column: σ_1; right column: σ_3; depth layers 1-3; black circle indicates hypocentre centroid
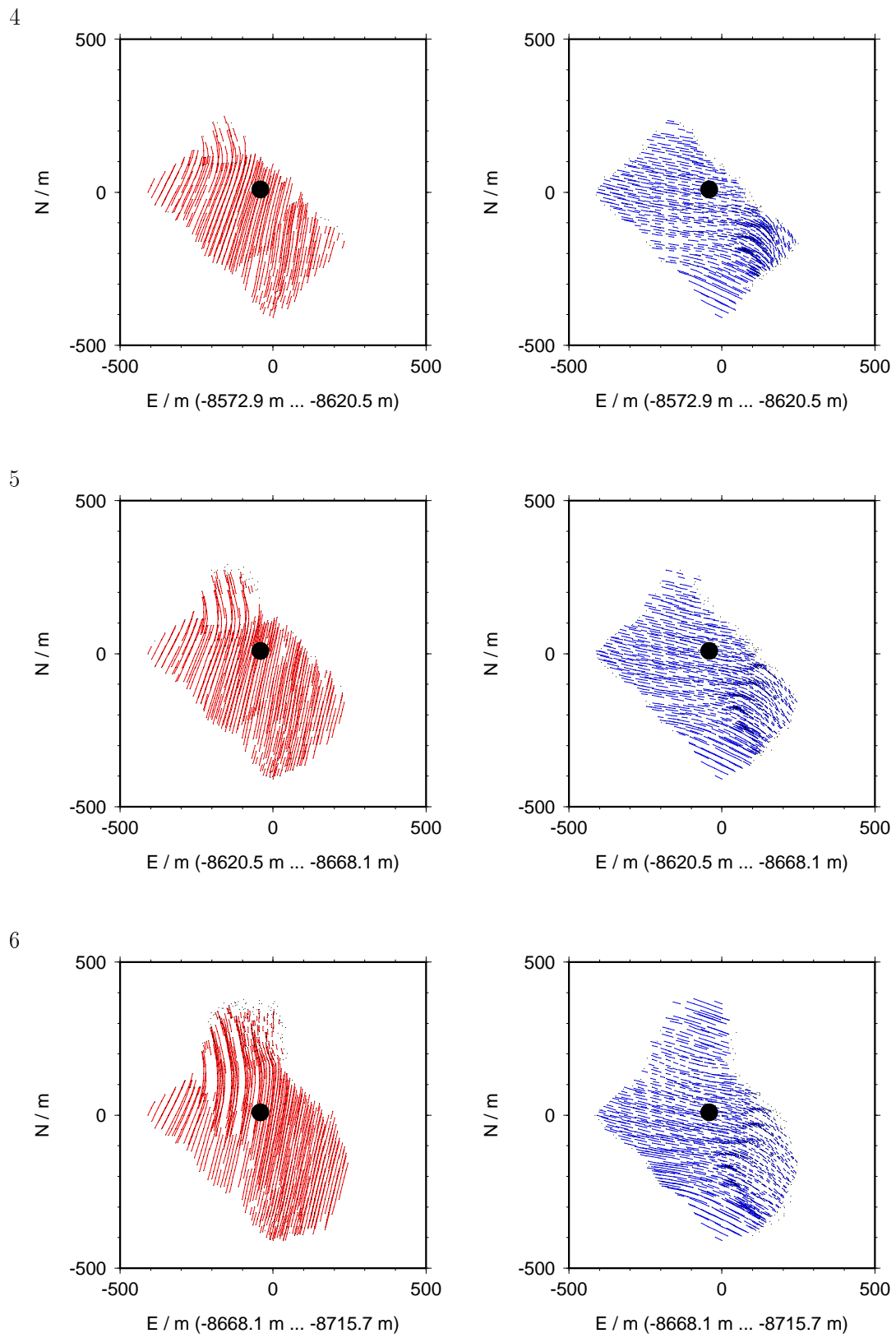
Figure 3.30: NURBS trajectories; depth slices 4-6

7

N / m

E / m (-8715.7 m ... -8763.3 m)

E / m (-8715.7 m ... -8763.3 m)

8

N / m

E / m (-8763.3 m ... -8811.0 m)

E / m (-8763.3 m ... -8811.0 m)

9

N / m

E / m (-8811.0 m ... -8858.6 m)

E / m (-8811.0 m ... -8858.6 m)
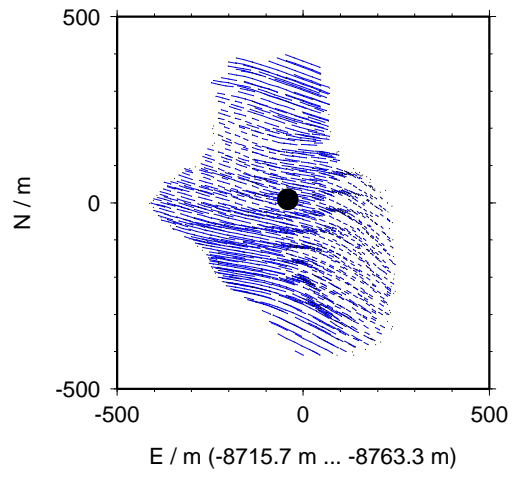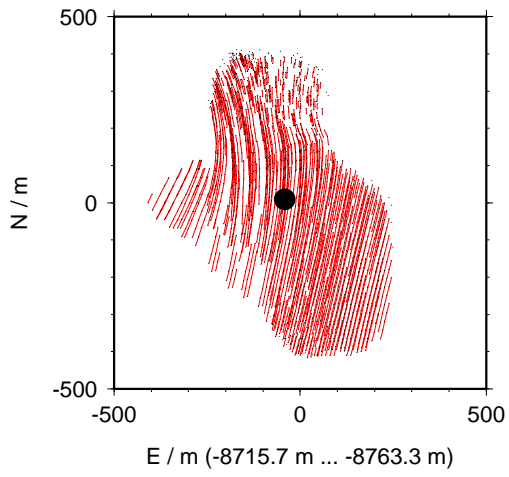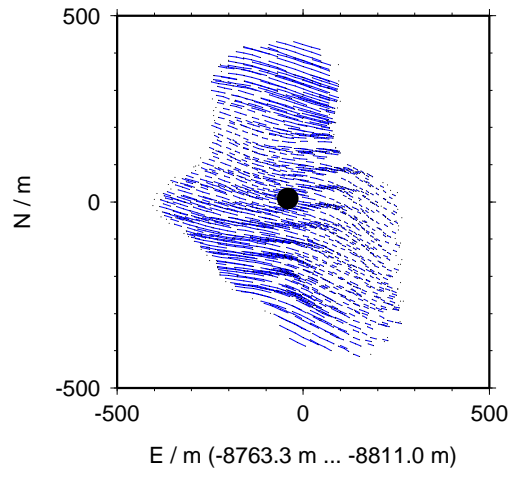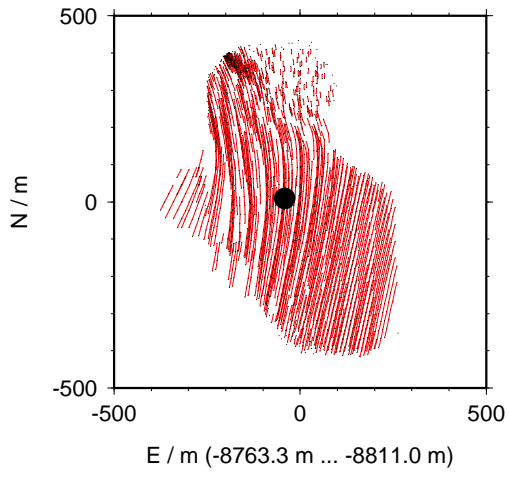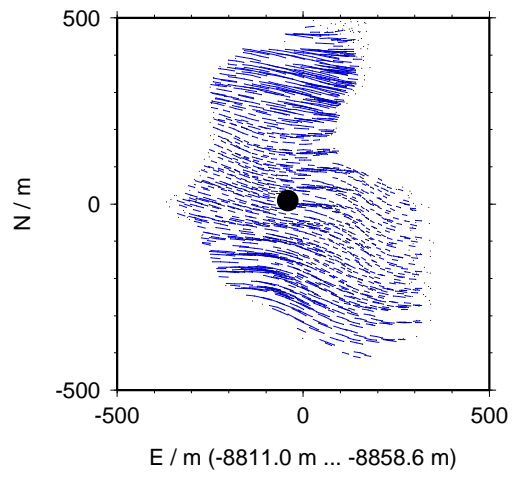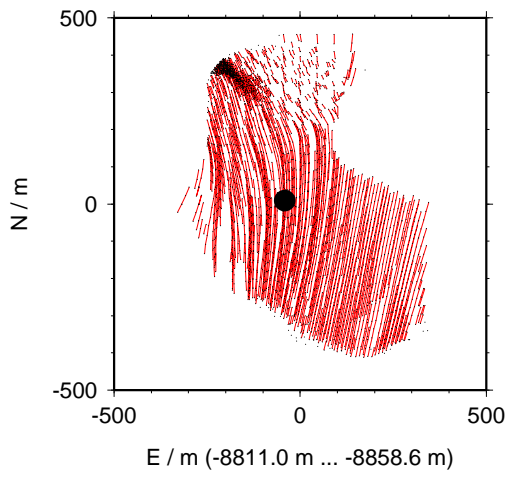
Figure 3.31: NURBS trajectories; depth slices 7-9
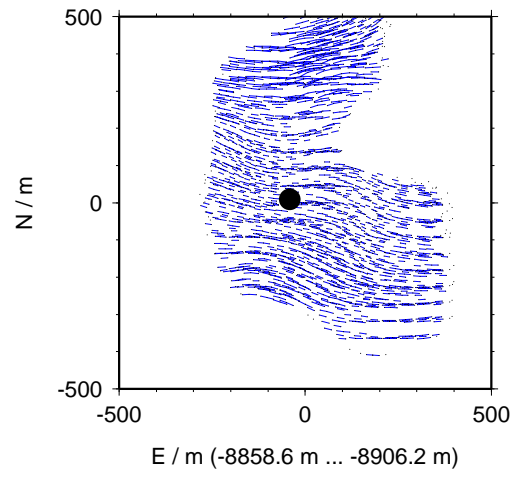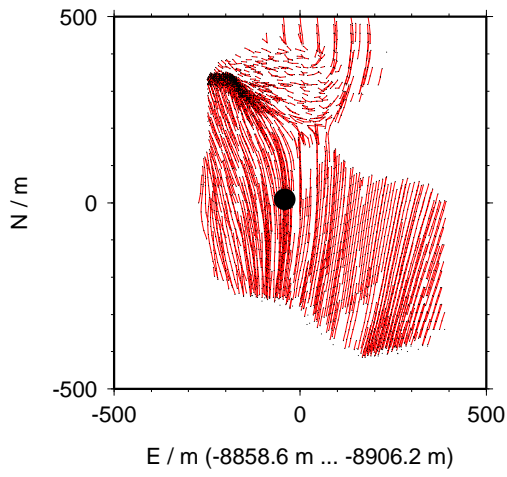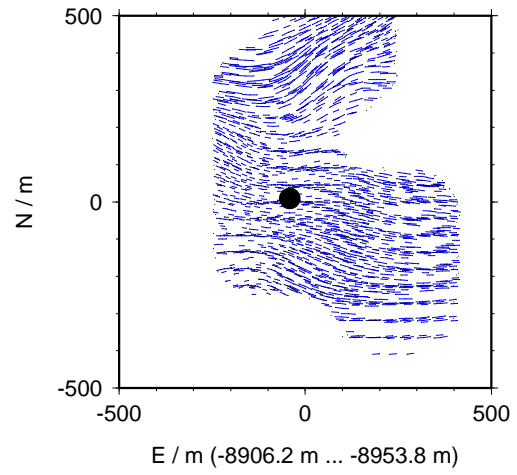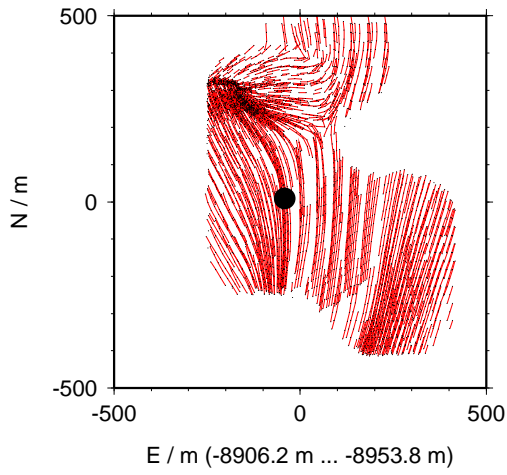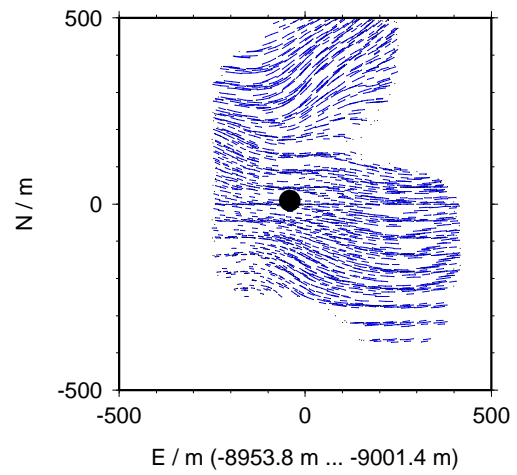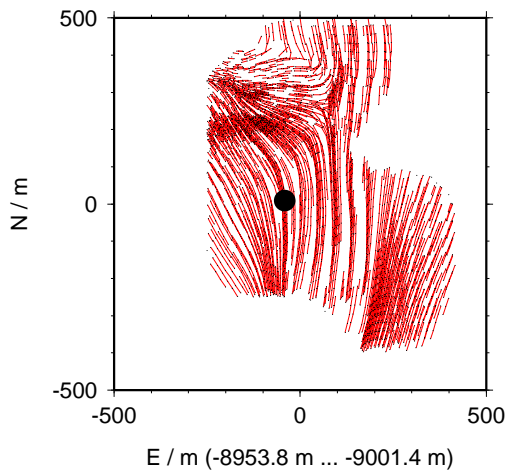
Figure 3.32: NURBS trajectories; depth slices 10-12

13
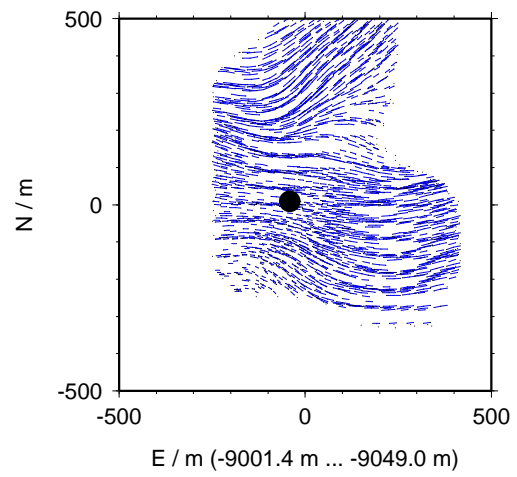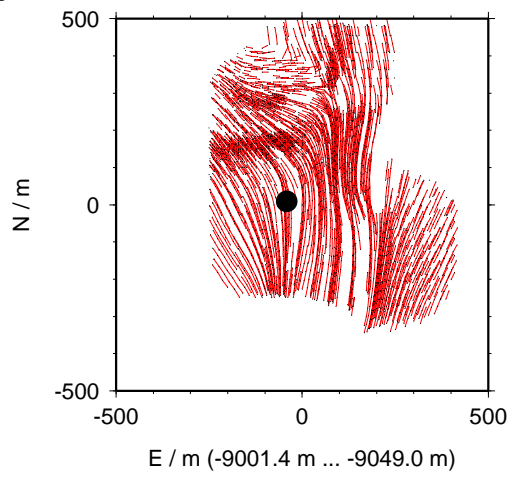
14
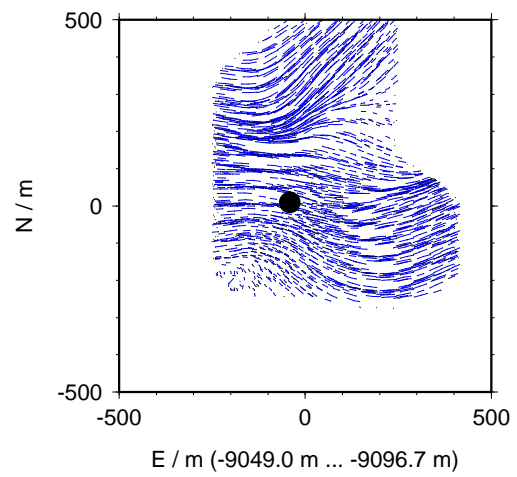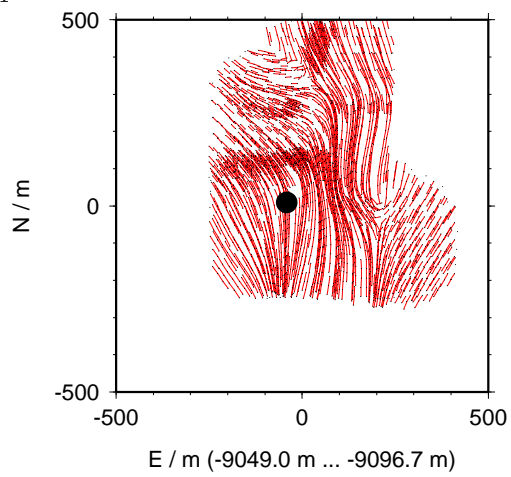
15
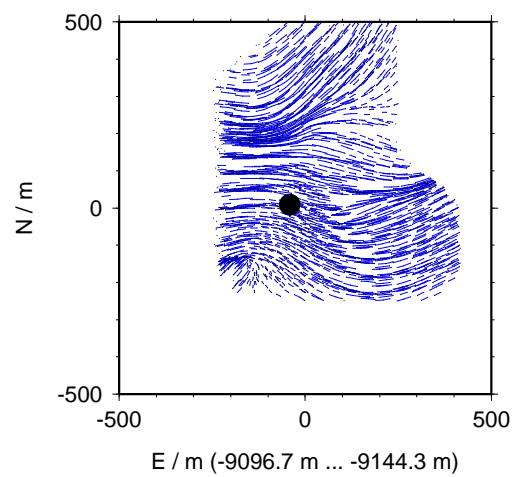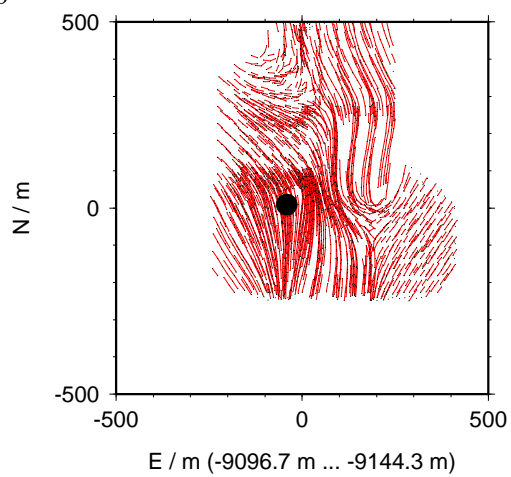
Figure 3.33: NURBS trajectories; depth slices 13-15

16
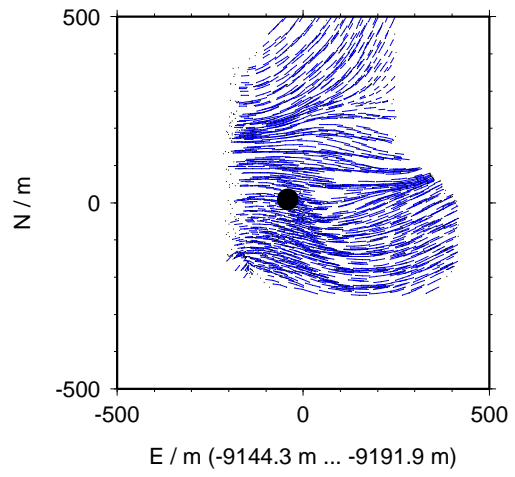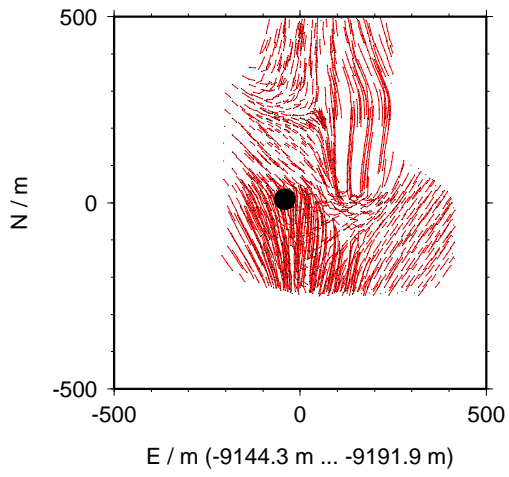
17
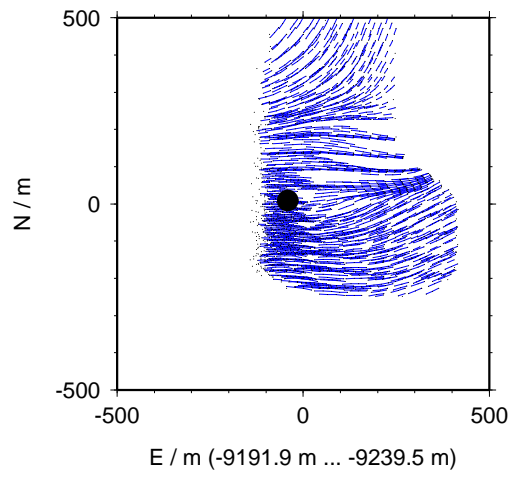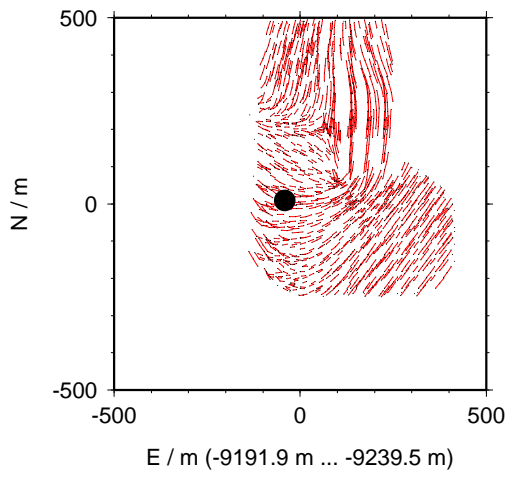
18
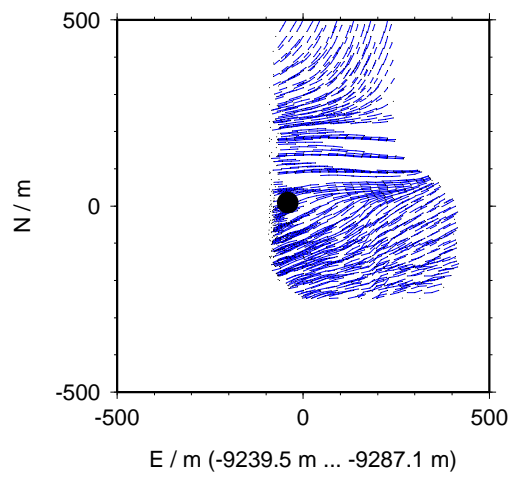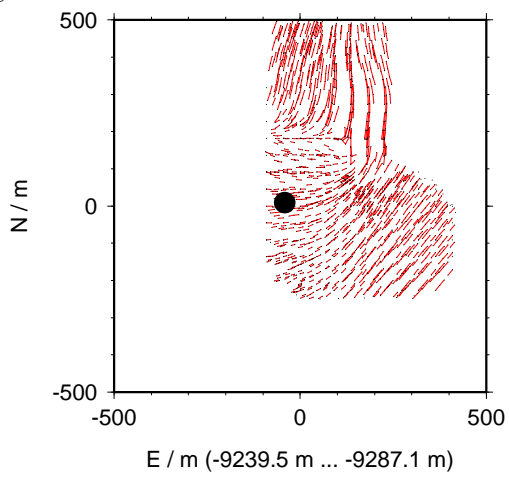
Figure 3.34: NURBS trajectories; depth slices 16-18

19
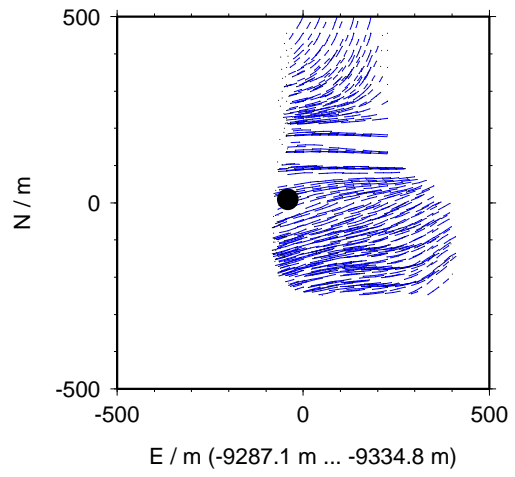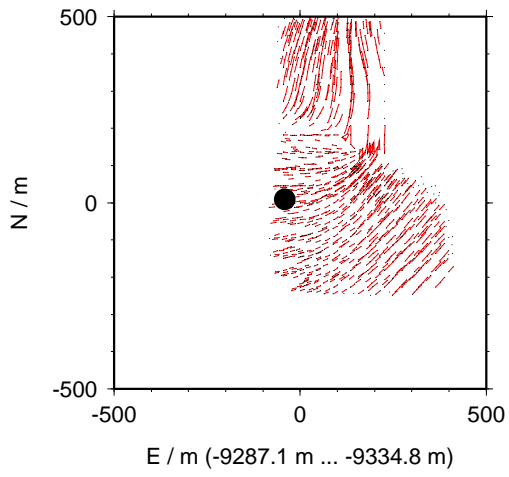
20
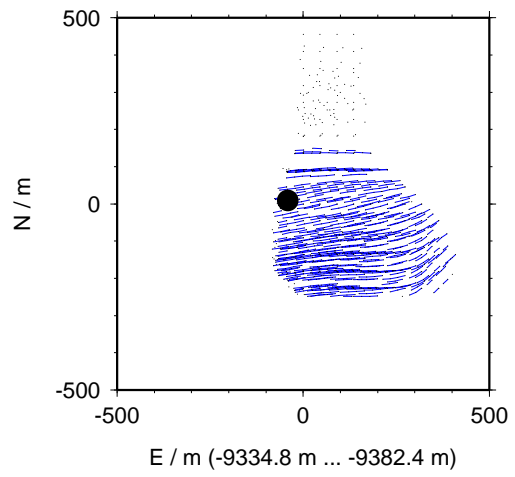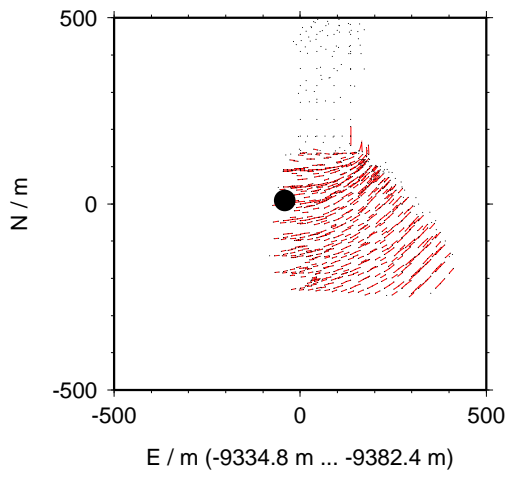
21
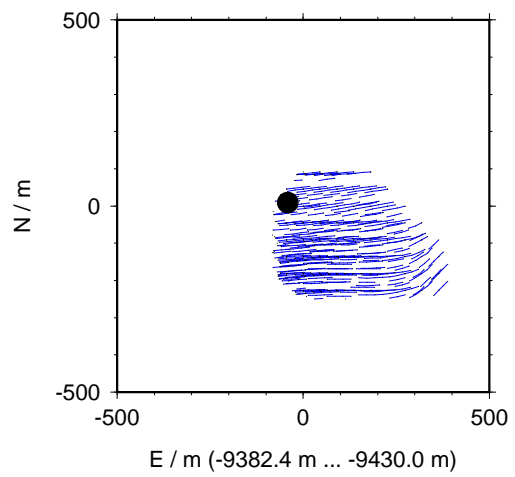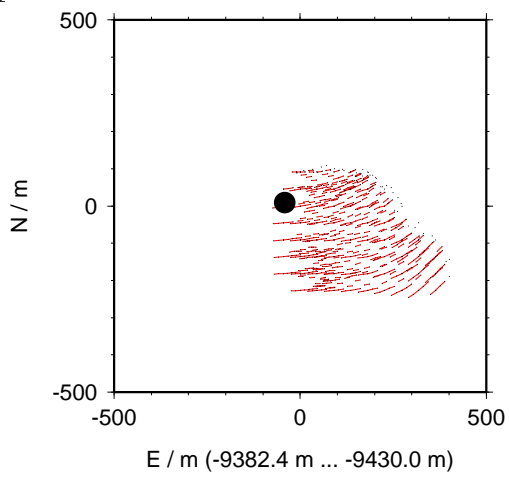
Figure 3.35: NURBS trajectories; depth slices 19-21

while in the lower part, the direction of σ_1 varies slightly around the North direction. Because only small variations in the stress field are observed for the KTB dataset, the processing by means of a stress trajectory analysis has not been tried.
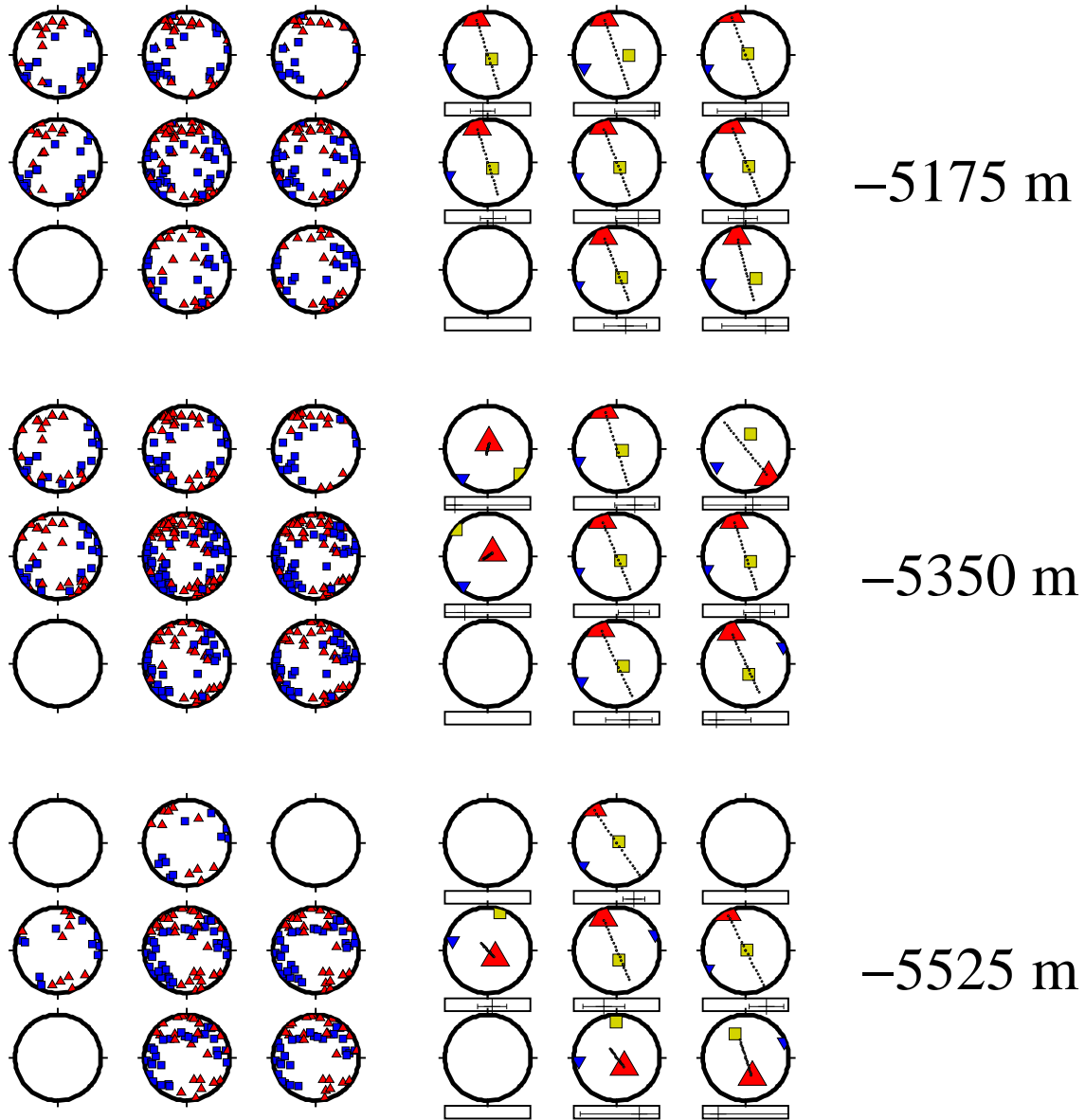
Figure 3.36: Source volume segmentation for the upper part of the KTB dataset (above $-6000m$, $x = -400\ldots300m$ E and $y = -500\ldots300m$ N of KTB) consisting of 102 focal mechanisms; left column: P- (red triangles) and T-axes (blue squares); centre column: projected piercing points of the unit vectors of the inverted principal axes of stress: red triangles - σ_1, yellow squares - σ_2, blue triangles - σ_3

−8800 m

−9200 m
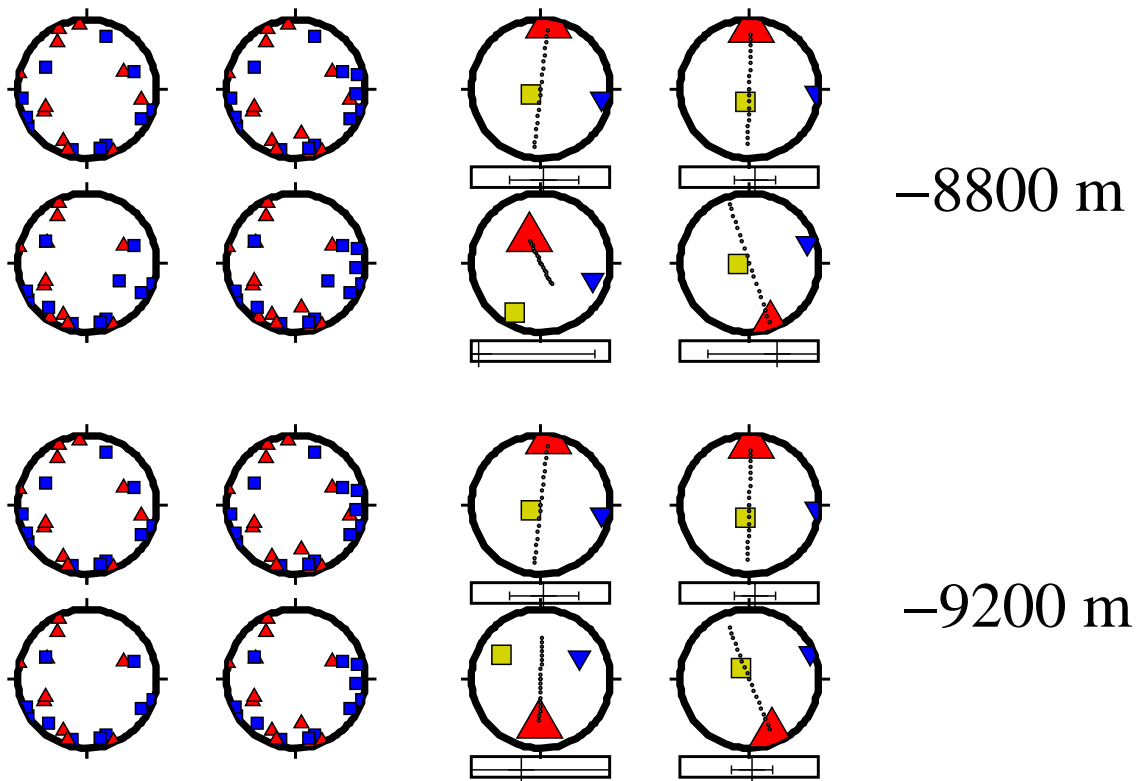
Figure 3.37: Source volume segmentation for the lower part of the KTB dataset (below $-6000m$, $x = -100 \ldots 700m$ E and $y = -600 \ldots 700m$ N of KTB) consisting of 23 focal mechanisms; left column: P- (red triangles) and T-axes (blue squares); centre column: projected piercing points of the unit vectors of the inverted principal axes of stress: red triangles - σ_1, yellow squares - σ_2, blue triangles - σ_3

Chapter 4

Discussion

In this work, many different methods have been applied and improved or even newly developed from scratch. A framework of computer applications that implement these methods has been setup and applied to a dataset of seismograms obtained for the 1997 earthquake swarm in the area Vogtland/NW-Bohemia and partly to a dataset of induced earthquakes from the KTB drilling site. Benefits, problems, and the reliability of the results will be discussed in the following sections.

4.1 Coherence analysis

The most obvious difference regarding the result of the coherence analysis for the two different pre-processing approaches using an acausal bandpass filter on 1 component seismograms (see Reinhardt (2002)) and using a butterworth bandpass on 3 component seismograms (this work) is that 68% more events can be associated with multiplets using the 3 component method (458 against 274), but only 13 multiplets can be identified instead of 14 using the 1 component method. The parameter set used for the determination of multiplets looking at T_s and T_x changed significantly. For the 3 component inversion much higher threshold values are chosen as a consquence of higher correlation coefficients resulting in a more restrictive distinction between similar events and those that are not similar. There is one large multiplet identified in the 3 component analysis consisting of over 50% of the events indicating weak linkage between the events. A higher link ratio can be demanded using the T_y threshold but the impact of this threshold on the result is not analysed in this work. The good agreement of the multiplets identified here with the visually determined groups of Fischer and Horálek (2000) (section 3.1.1) shows that the systematic determination of parameters for the coherence analysis yields reliable results.

There is one aspect to keep in mind when dealing with the automatic processing of correlation functions. The highest influence on the position of the maximum of the cross correlation function is given by the largest extremum in the seismograms. The form of the coda of the P- and S-phases depends on the source-time function which may have several extrema that may be larger in amplitude than the first motion and the amplitude ratio may be altered due to scattering effects. Another reason can be that multiply reflected waves introduce larger amplitude extrema in the coda for appropriate reflection coefficients. Consequently, wrong time differences can be estimated because not the arrival time difference for the first onset is calculated, but for some later arrival of group of arrivals which may have different offsets to the first onset for two similar events. This leads to erroneous locations for which the error may be in the order of few to some tens of miliseconds resulting in a location uncertainty of some tens to few hundreds of metres.

A number of algorithms that are potentially usable for the calculation of a correlation function using 3-component seismograms is available. Some simple examples have been presented in 2.3.3 from which one has been selected for the processing. Aster and Rowe (2000) and Rowe et al. (2002) introduce a more complex algorithm, which may be implemented in future work.

The distribution of correlation coefficients shown in appendix B is quite complicated. At some stations, like LAC, the cutoff thresholds for the P- and S-phase, respectively, can clearly be identified. For other stations, like NKC, a plateau for positive correlation indicated by a dataset containing similar seismograms is not present at all. Moreover, the intuitively selected thresholds are not the same for all stations. These effects should be analysed in more detail in some future study. It may also be a good idea to select different filter operations for the different stations to enhance the result of the coherence analysis.

Maurer and Deichmann (1995) introduced a very complex algorithm for identifying sets of similar waveforms for some network of seismic stations. It depends on five parameters from which four are implemented as threshold values. Two of these, namely T_s and T_x have been discussed in this work, but the impact on the result of the coherence analysis is not well understood for the two other threshold parameters T_p and T_y. The parameter for the systematic elimination of potential statistical outliers, K has been roughly analysed in my diploma thesis (Reinhardt, 2002), but there is still some need for a more detailed analysis.

In this work the parameter K has been set to 0 since there are only few stations available. For networks consisting of only few stations, it may be convenient to require at least two correlation coefficients to be present for the calculation of entries of asymmetrically trimmed mean matrix (see Maurer and Deichmann, 1995). This may reduce the impact of stations that generally show high values of correlation because of e.g. strong site effects or high coherent noise.

4.2 Relocation

Relocations of earthquakes for the 1997 swarm have been compared for four different processings of Fischer and Horálek (2000), Reinhardt (2002), and this study using 1 and 3 component seismograms, respectively. Fig. 4.1 shows the distributions of event distances between four different location datasets. The largest deviations are found between the master-event-location dataset and the locations obtained in my diploma thesis. The smallest distances are observed for the both datasets calculated in this work. When comparing the master event locations with those obtained in this work, the distribution involving the 1 component result is slightly thinner. This result is explained by the fact that the master event locations have also been obtained using 1 component seismograms. However, I stick with the 3 component locations produced in this work, because the relative arrival times are estimated very precisely using 3 component seismograms as can be seen from the picks in the shifted seismograms shown in appendix C. The formal RMS error which is determined during inversion is quite low for the cross-correlation data. For about 6% of the locations the RMS value is $0.001s$ and for the rest it is $0s$. For the catalogue data, the mean and standard deviation are $(0.0093 \pm 0.0024)s$.

There are several structures visible in the hypocentre distribution which have already been discussed in section 3.1.3 during the selection of the fault plane from the two possible nodal planes of a focal mechanism. Three groups of multiplets have been defined which represent plane structures in space (see table 3.5) which are illustrated in fig. 4.2. Two of the estimated plane orientations differ only marginally in azimuth and dip, but can clearly be divided.

When the orientation of the apropriate zone of weakness for a multiplet group has been estimated
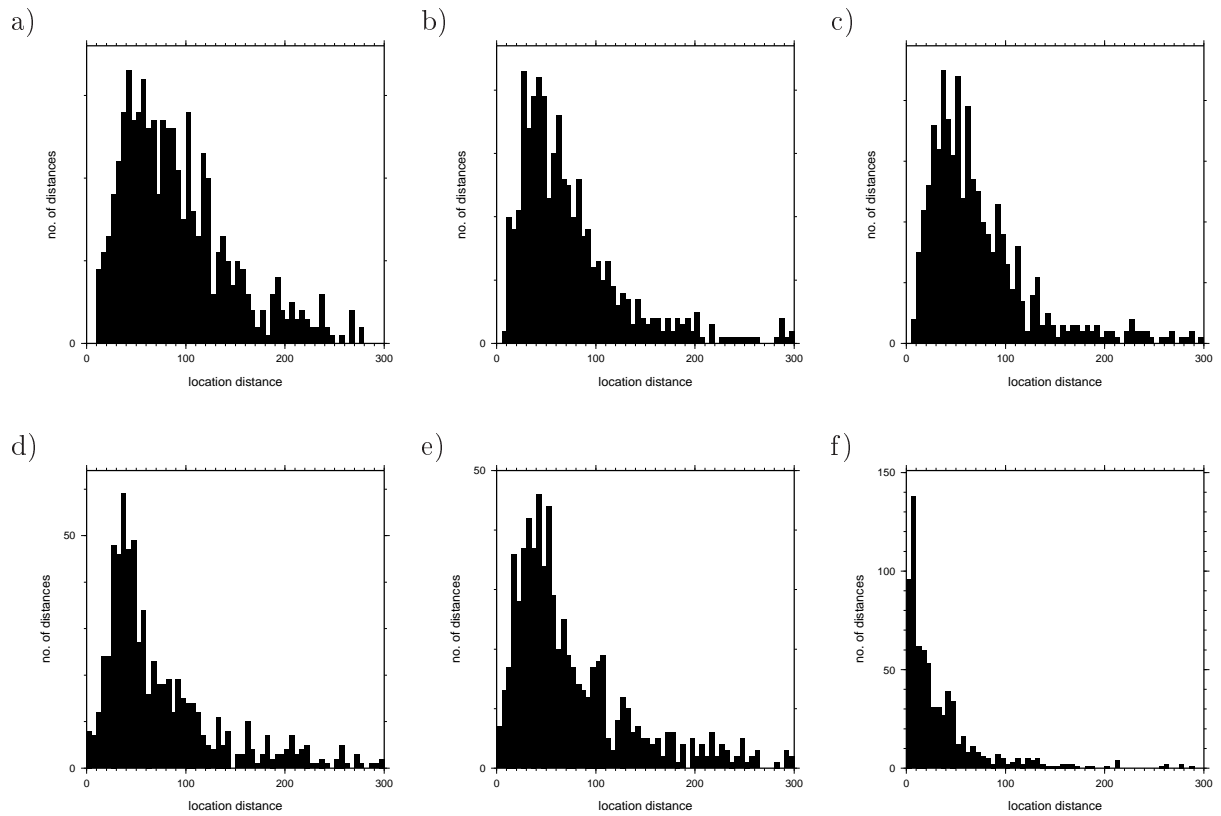
Figure 4.1: Distances in m between the hypocentres obtained using different location techniques and data preprocessing for pick determination; the four datasets of locations that are compared against each other are those from Fischer and Horálek (2000) (1), from Reinhardt (2002) (2), and from this work obtained by using `hypoDD` and arrival time differences calculated with butterworth filtered 1 component (3) and 3 component seismograms (4): a) (1) against (2); b) (1) against (3); c) (1) against (4); d) (2) against (3); e) (2) against (4); f) (3) against (4)
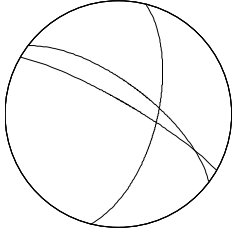
Figure 4.2: Orientations of three visually estimated fault planes as intersection lines with the unit sphere in lower hemisphere projection
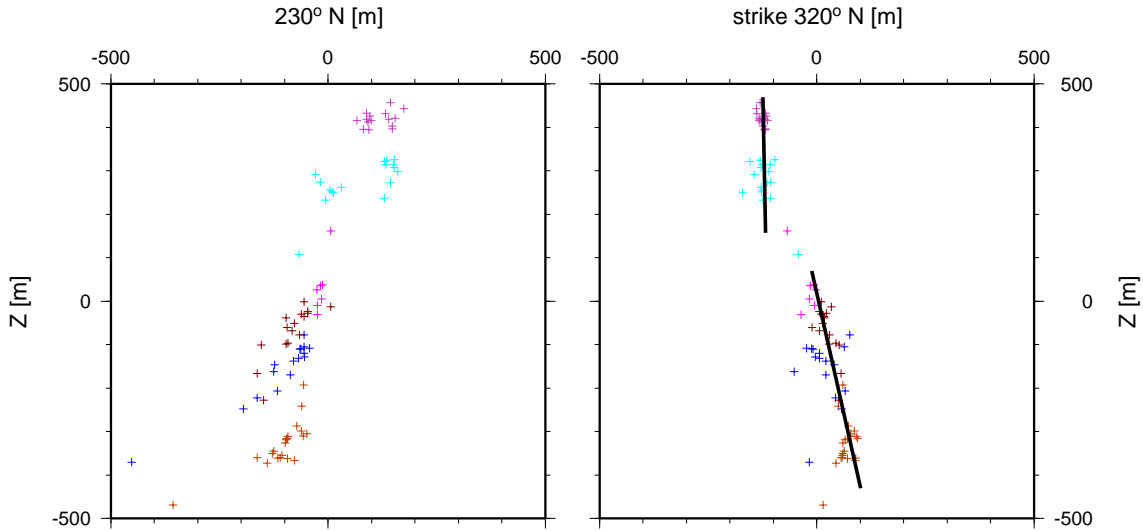
Figure 4.3: Vertical projections of multiplets 02, 03, 05, 06, 08, and 11 rotated about the strike angle $\Phi = 320^o$; a step like structure becomes visible which is emphasised by thick black lines

visually, I tried to optimise the view so that a plane becomes visible in the direction perpendicular to the strike as in the right part of fig. 3.5 b. For this particular multiplet group, the rotation into a different direction allows to interpret two different dip angles for two parts of the hypocentres. Fig. 4.3 shows a slightly rotated view of this multiplet group where the different dip angles have been explicitly marked. I interpret this configuration as two subfaults which belong to a fault zone that developed under the influence of a palaeo stress field. The difference in the dip angles can be explained as the result of the development as part of a shear zone: One of the planes describes the main fault and the other a Riedel shear fault indicating a normal fault setting. This pattern is also in good agreement with geological models of normal faulting which predict steeply dipping fault planes.

During the determination of the correct fault plane using fault normal clustering sometimes the normal of the predicted auxiliary plane is closer to the cluster centre than to the predicted fault plane that has been observed in the hypocentre distribution. The reason for this is most likely a faulty selection of the template event to whose axis all other axes are compared to. In this implementation I randomly chose one of the events as template and compared the others to this one. However, it is more appropriate to solve the problem iteratively by first choosing one arbitrary template event. Starting from this result, the mean axes together with their variances should be computed. For the subsequent steps, the axis with the smallest standard deviation should be selected as the axis to compare all nodal plane pairs with. The procedure is to be repeated until either only small changes in the nodal plane selection are observed or the result diverges in which case the problem is rendered not to be solvable.

Multiplet	no. of associated events	classification
a	229	83 strike-slip, 70 thrust, 76 oblique
b	16	*9 obl. normal*, 5 obl. thrust, 2 thrust, 1 strike-slip
c	15	**12 strike-slip**, 3 mixed oblique thrust
d	9	**7 oblique normal**, 2 thrust
e	7	**6 oblique normal**, 1 strike-slip
f	17	8 thrust, 9 obl. normal
g	55	**46 thrust**, 7 oblique thrust, 2 strike-slip
h	21	various (no dominant nor major group)
i	25	*14 thrust*, 4 mixed oblique, 6 various strike-slip
j	17	**11 thrust**, 4 obl. thrust, 2 strike-slip
k	15	**10 oblique normal**, 5 mixed
l	19	**19 oblique thrust**
m	8	*5 oblique thrust*, 3 mixed

Table 4.1: Summary of the mechanism classification of multiplets: **boldface** indicates dominating mechansim types and *italics* mark major groups in multiplets with various types of mechanisms

4.3   Moment tensors

For comparison reasons, the moment tensor inversion has also been applied to the arrival time differences obtained in my diploma thesis (Reinhardt, 2002) for which the result is shown in fig. 4.4 and fig. 4.5. 14 multiplets that have been identified and the moment tensors that are not asssociated to any multiplet are shown. The similarity of the moment tensors in the multiplets is stronger than for the moment tensors obtained during the processing of 3 component seismograms in fig. 3.8 and fig. 3.9. On the other hand, only 274 events have been associated to multiplets, so relatively more outliers are to be expected if a higher number of events is associated to multiplets. This fact is most obvious looking at multiplet a1 and a2 in fig. 3.8 and the second multiplet coloured in light green in fig. 4.4. In both multiplets, different types of mechanisms are present, even though for multiplet a, there is a higher variety of quite different mechanisms.

Most obviously there are three different types of mechanisms in multiplet a: a flat thrust faulting with slip directions WNW-ESE (or steep dip-slip which is quite improbable), a strike-slip type with strike Φ WNW-ESE or NNE-SSW, respectively, and an oblique normal faulting which shares one nodal plane with the flat thrust faulting regime. Some multiplets are dominated by one specific type of mechanism, others are composed of one major type and some minor classes of mechanisms, and the multiplet h shows a wide variety of event types. The classification is summarised in table 4.1.

For further processing regarding the stress field inversion, a very important information is which nodal plane of the best double couples represents the fault plane. Two different approaches have been applied and the appropriate results are shown in fig. 3.11 and fig. 3.12. It is obvious that the approach of comparing the nodal plane normal vectors with the normal vector of a zone of weakness identified using the hypocentre distribution is more stable than analysing the clustering of nodal plane normals. This is because in the latter, also unreliable orientations are considered to be correct, while in the first, these are safely excluded. Therefore, the first is the method of choice and its result has been used.
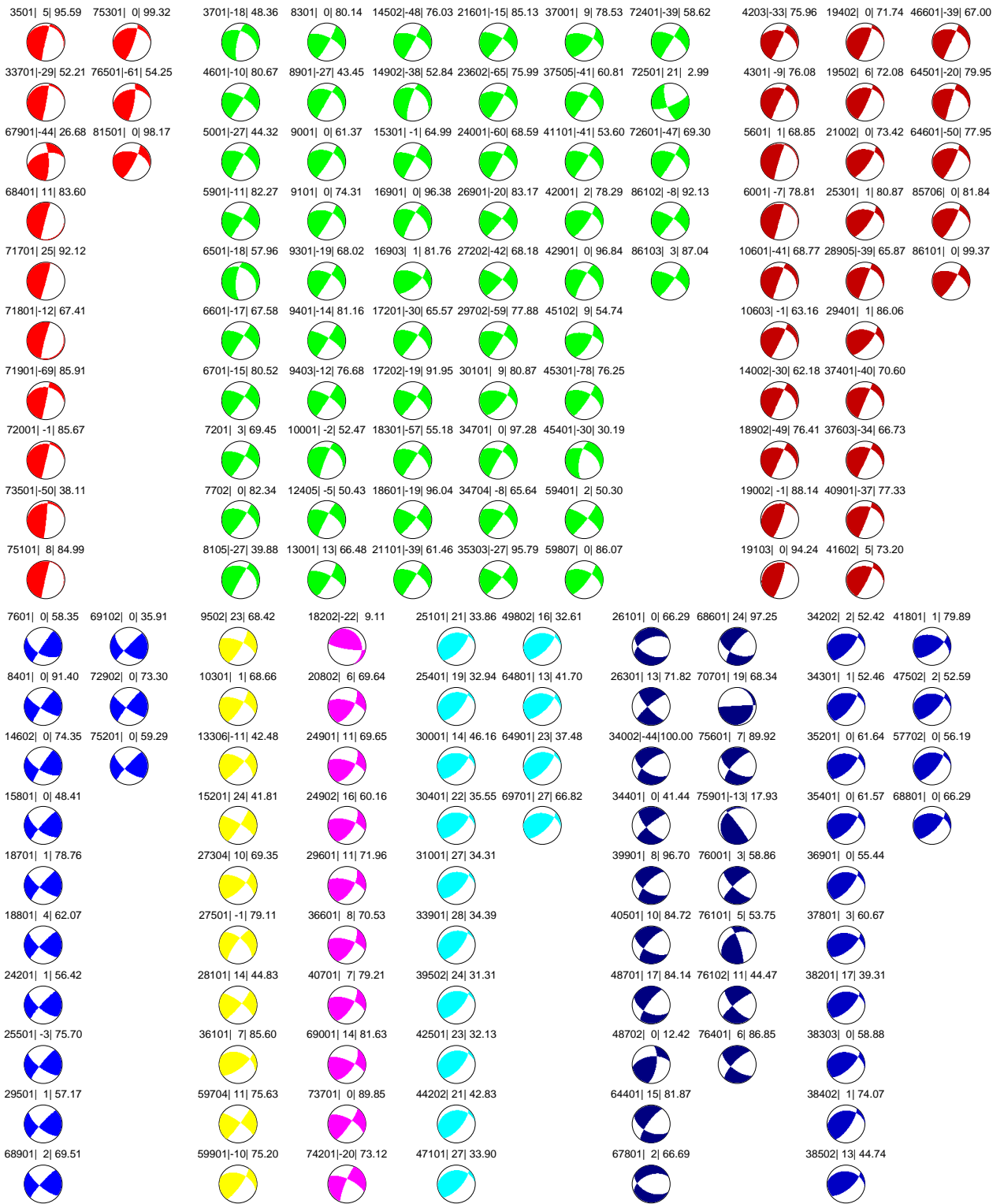
Figure 4.4: 1997 swarm best DC solutions (lower hemisphere projection) calculated from moment tensors using arrival time differences obtained by analysis of 1 component seismograms filtered with an acausal $4 - 30 Hz$ bandpass; numbers above focal mechanisms are event ID, isotropic component, and non-DC component of the moment tensor - part 1 of 2

Figure 4.5: 1997 swarm best DC solutions - part 2 of 2

4.4 Automated relative moment tensor inversion

The first approach in determining phase amplitudes was to pick the amplitude and the appropriate time manually. Seismograms from a group of events that are connected by high correlation coefficients were shifted and plotted together. Then a common extremum was chosen and the appropriate time was picked. Knowing the absolute time of a reference event, the times for the other events were determined by applying the relative arrival time difference subsequently.

In this work the manual amplitude picking is exchanged by an automatic algorithm. An extremum that is shared by all seismograms is identified and for all of them the appropriate local extremum is selected. For all events the deviation in time from to the local extremum to the shared extremum is calculated. Since there are several shared extrema the one with the smallest standard deviation regarding the time differences to the local extrema in the seismograms is selected.

This algorithm may lead to erroneous results if the polarity of the waves is not correctly estimated. This effect may explain why on one hand many events are associated to multiplet 1 by analysis of waveform similarity but the moment tensors are diverse. Therefore, a better algorithm for the automatic determination of amplitudes for the moment tensor inversion has to be established in future work.

For the algorithms that select a fault plane from the two possible nodal planes, different results are obtained. The algorithm that uses the similarity of nodal plane normal vectors to a normal vector associated with a zone of weakness determined by hypocentre distribution provides a stable result, looking at the normal clusters in fig. 3.10. On the other hand, the result of the nodal plane normal clustering algorithm selects some nodal planes wrongly, as can be seen in fig. 3.12. This effect is especially visible for multiplet 1 where there are actually three normal clusters visible. In such a situation this algorithm fails. This effect may be reduced by introducing an algorithm that selects the template normals by some cluster criterion, i.e. first clusters are sought, the template axes are defined as mean axes of these clusters and the nodal plane normals are compared to these successively.

4.5 Stress inversion

Dahm and Plenefisch (2001) suggest in their approach in inverting for the homogeneous stress field to first seek the minimum inversion error for a number of focal mechanisms systematically. Then the algorithm distinguishes between fault plane and auxiliary plane of a focal mechanism by selecting the nodal plane which results in the smallest formal error as the fault plane. This may be erroneous if both nodal planes are unfavourably oriented and their error is similar in magnitude. To minimise this problem, I suggest to modify both steps of the algorithm. In the first step, only events that show significant differences in the error for the two nodal planes should be considered. This may be achieved by a bootstrap approach where a number of events is selected randomly and the configuration with the smallest error is selected. Then all events which allow for the selection of the fault plane from the smallest error are selected as basis. The second step is modified so that in a first pass only events with two significantly different error values are selected and the remaining events are treated as proposed by Dahm and Plenefisch.

4.6 Stress field inhomogeneities

In this section, first the visualisation technique for stress trajectories will be discussed. Later certain inhomogeneities in the stress field that have been identified in this study will be related to stress patterns and an interpretation in the context of the tectonic setting in the region will be given.

4.6.1 Smoothing stress trajectories

In this work NURBS have been successfully implemented to calculate smoothed stress trajectories from stress measurements associated to positions on a regular grid in space. The result of the stress inversion is given in the form of three angles describing the orientation of the principal axes of stress and the stress shape ratio which is transformed into a representation as a deviatoric stress tensor. These tensors have been used as control points in the NURBS definition formula which results in a smoothing effect. For one and two dimensional NURBS problems, there exist two basically different algorithms to deal with data. The first interpolates between the measured values by adjusting the control points so that the NURBS values coincide with the measured values. The second approximates a NURBS with fewer control points to fit the data in a least squares sense. Both algorithms are well established for one and two dimensional problems but need to be adopted for stress trajectories in three dimensional space. This is beyond the scope of this work but should be considered in future work.

4.6.2 Visualisation technique

A simple approach for the visualisation of stress inhomogeneities has been implemented. The basic concepts are the tracing of trajectories by using the orientation of principal stress axes and a fixed vector length to step along the trajectory. Although this approach leads to the identification of stress inhomogeneities, it may fail in areas where the trajectories are strongly curved.

The algorithm consists of three steps. First, a grid of equally distributed points is defined in the volume of interest. Then, these points are used as starting positions from which to calculate trajectories in the positve and negative direction of the principal stress unit vectors. Finally the volume is subdivided into a number of layers of constant thickness and all parts of trajectories are projected onto the top of the layer. If the number of seed positions and the vector length for stepping along the trajectory are selected appropriately, inhomogeneities in the stress field can be identified. However, there are more advanced visualisation techniques for trajectories for which e.g. Becker (2004) gives a complete overview. He develops a new 3 component method to trace the movement of freely movable particles in a velocity field by illuminating the traces with different colours. This method can also be aplied to stress trajectory data and should be considered in future work.

4.6.3 1997 Vogtland/NW-Bohemia swarm: stress inhomogeneities

The first part of fig. 4.6 shows how a regional stress field is disturbed by a loaded mode-II crack (see section 1.3 for its definition) whose stress field is calculated under the assumption that it extends inifinitely in the direction perpendicular to the viewing plane. The stress trajectories are bended and seem to "flow" around the edges of the crack. The stress field related to more complex crack models which allow the crack walls to be curved, which allow σ_2 to vary, or which fix the crack length in all three directions of space will look more complex. Also, if more cracks are present, their stress fields
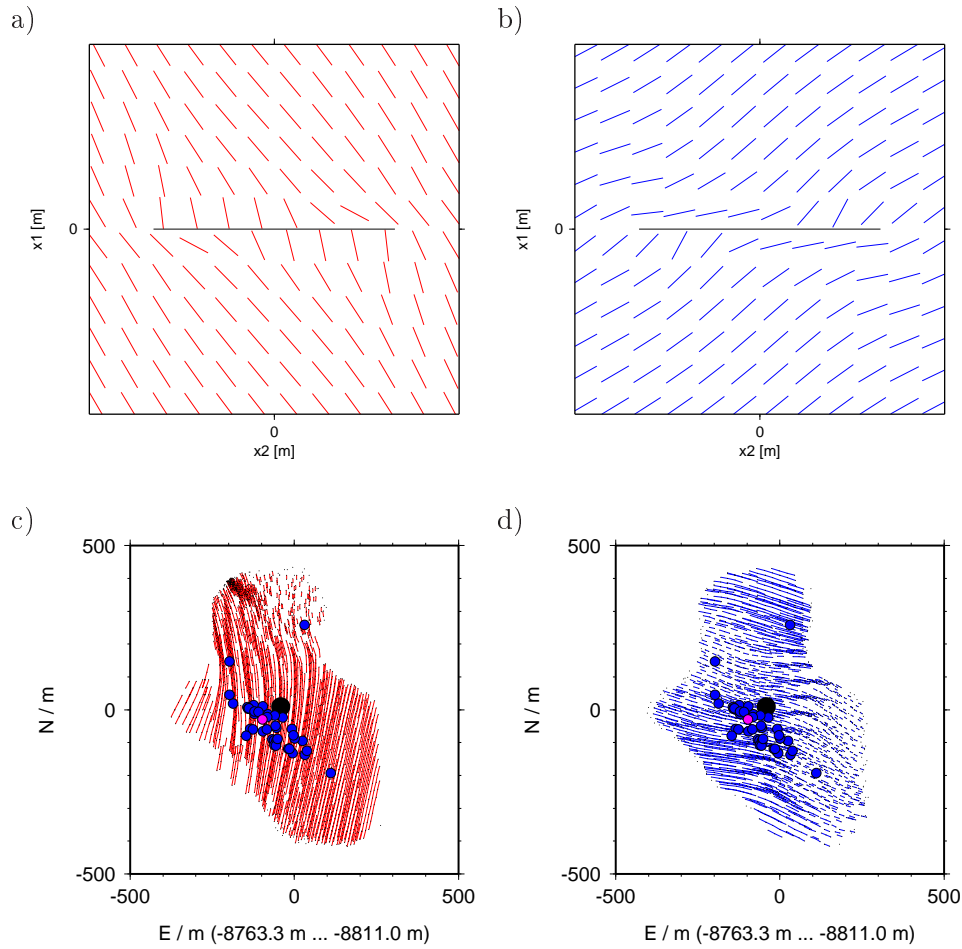
Figure 4.6: a) and b): Synthetic stress trajectories for a $300m$ long, mode II crack (gray thick line), extending infinitely in z-direction (Pollard and Segall, 1987); c) and d): Comparison with patterns found for the 1997 earthquake swarm; σ_1 is coloured red and σ_3 is coloured blue

will be superposed, increasing the complexity of the stress field.

The stress trajectories that have been determined for the 1997 swarm are very complex in that they are curved almost everywhere (e.g. lower part of fig. 4.6). The S-shaped structure which is visible in layers 1-9 (fig. 3.29 through fig. 3.31) indicates the presence of a uniform perturbing feature over a wide depth range that shows a faint similarity with the stress pattern visible at the edges of a mode-II crack.

An interpretation of the location and orientation of possible cracks using the pattern of a single loaded shear crack is difficult, because such a simple pattern can't be found anywhere in the volume under study. However, to do so, it would be necessary to systematically analyse stress patterns that result from the superposition of single crack stress perturbations using different crack models.

To understand the structures in deeper layers, I recall the concept of neutral points which indicates that the two principal axes of stress in 2-dimensions are equal in magnitude as defined in e.g. (Ramsay and Lisle, 2000, pp 709). Examples for the shape of stress trajectories in the vicinity of neutral points in 2D are given in fig. 4.7. In three dimensions, the occurence of neutral points can be interpreted by minimum and maximum horizontal stresses, σ_h and σ_H, respectively, of equal magnitude.
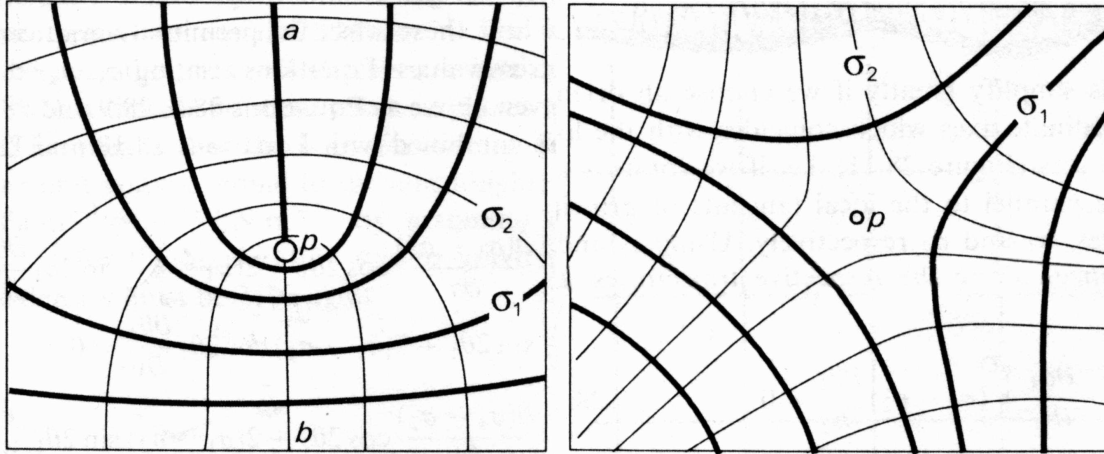
Figure 4.7: Examples for neutral points, taken from (Ramsay and Lisle, 2000, fig. 28.14, p 709); left: trajectories converging near the neutral point; right: trajectories diverging near the neutral point

In layers below the C- or S-shaped structure, which is visible in layers 1-9, a neutral point can be found in the σ_1 trajectories in layers 10-19, ca. $200 - 250m$ N of the centroid moving slightly to the E in greater depth. The patterns in layers 20-21 neither speak against its presence nor do they deny it. A second neutral point develops in layer 13, ca. $200m$ E of the centroid and is present down to layer 18. In layers 9-16, $300m$ s and $100m$ W of the centroid and in layers 7-13, $300 - 400m$ N and $100 - 200m$ W of the centroid there are areas visible where the trajectories are converging. These are located at the edge of the measurement volume, so it is difficult to decide if they represent real features or only artifacts due to uncertainties introduced with the smoothing algorithm. Example layers visualising the previously described features are presented in fig. 4.8 and fig. 4.9. In the σ_3 trajectories, features of the stress field are not so obvious as for σ_1. There are some converging features at the edges, similar to those described for the σ_1 trajectories, but they are only faintly visible.

The neutral points, described above can be interpreted as the result of the superposition of the stress field perturbation of differently oriented faults or zones of weakness. The trajectory pattern for the mode II crack in fig. 4.6 shows diverging trajectories in the middle of the crack and converging trajectories at its edges. Assuming that the perturbation of the stress field of zones of weakness show a similar pattern, such can be interpreted to be located directly at or near the neutral points. Because of the complexity of the trajectory patterns it is difficult to tell the orientation of the fault zones. For the neutral point that is visible in layers 10-19 an orientation of about NW-SE is most likely, while for the neutral point in layers 13-18 a related fault zone may be either oriented NNW-SSE or NE-SW.

Another possible source for stress inhomogeneities is a fluid filled cavern that is impermable at its rim. Such a structure induces a radial symmetric stress field and a superposition of several such fields may also result in the development of neutral points. There are no radial symmetric features visible, so the presence of spherical fluid chambers can be excluded as reason of the inhomogeneities with high probability.

In the previous chapter, zones of weakness have been derived from the distribution of hypocentres which belong to different groups of multiplets. Fig. 4.10 shows the trajectories in three different depth layers together with the hypocentres that lay in the same layer. In depth layers a and b, the trajectory pattern for σ_1 is quite simple and only hypocentres belonging to multiplet group 1 and 2 (which are associated to similar zones of weakness) are visible. In greater depth, layer c shows a complex trajectory pattern for σ_1 together with hypocentres from all three multiplet groups under study. The appropriate patterns for the σ_3 trajectories look much more simple, but they also become
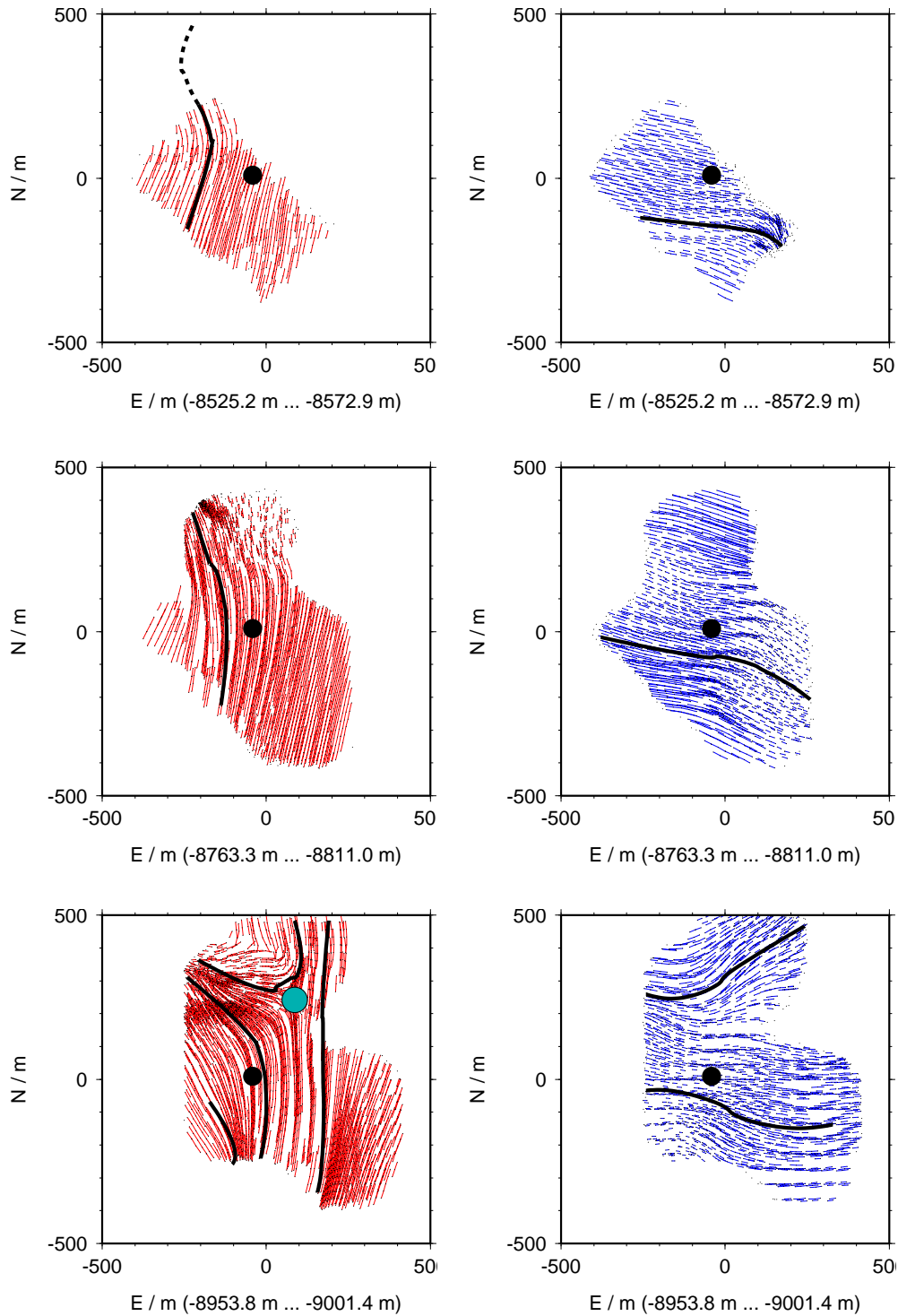
Figure 4.8: Result of the visualisation of stress trajectories: layers 3, 8, and 12; left column: σ_1 (red); right column: σ_3 (blue); black circle indicates centroid of hypocentres; thick black lines emphasise trajectory patterns; cyan circle indicates a neutral point
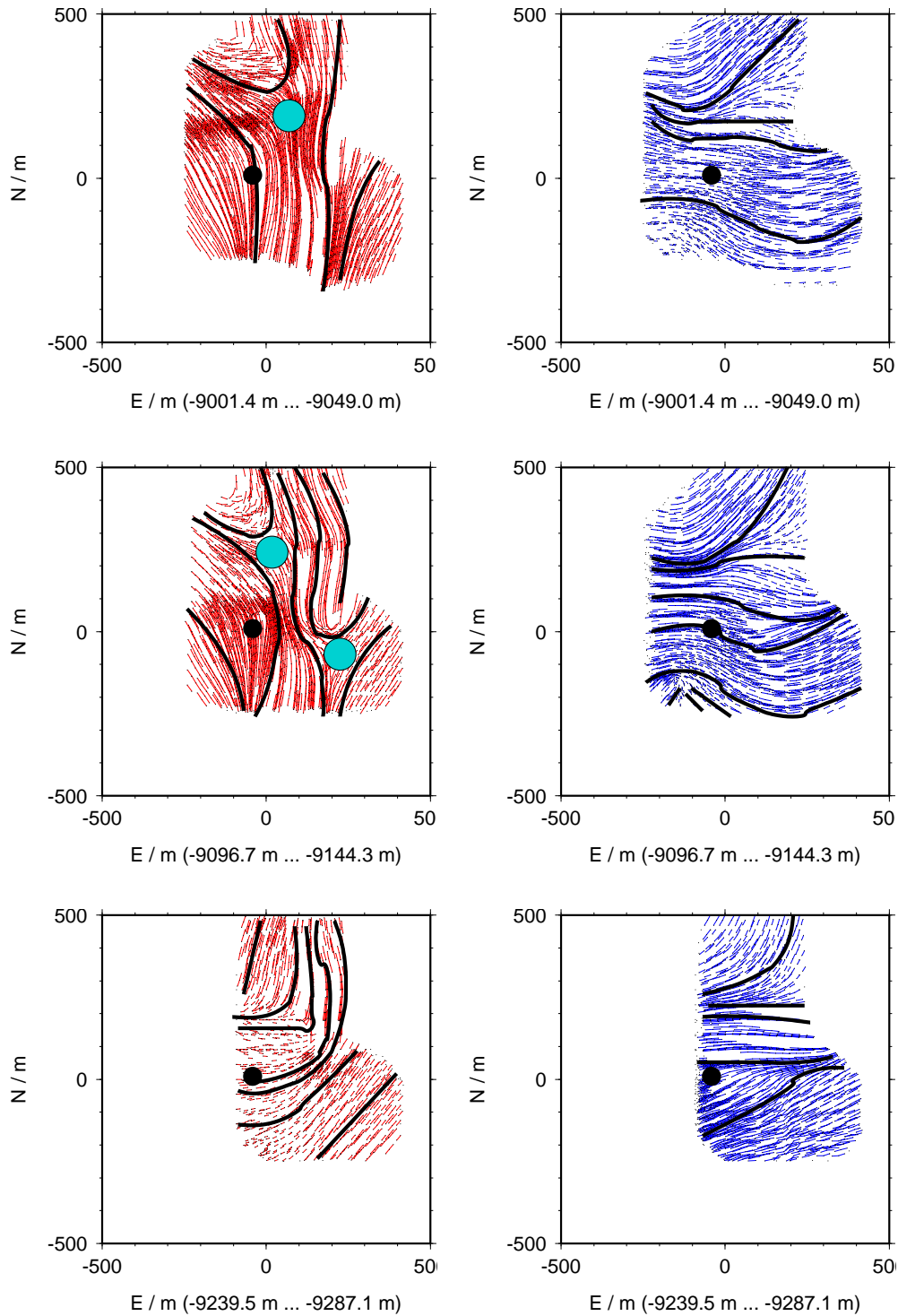
Figure 4.9: Result of the visualisation of stress trajectories: layers 13, 15, and 18; left column: σ_1 (red); right column: σ_3 (blue); black circle indicates centroid of hypocentres; thick black lines emphasise trajectory patterns; cyan circles indicate neutral points

more complex with greater depth.

These findings can be interpreted with a model of interacting zones of weakness from which one is present in the whole volume of interest while the other is only present in the deeper part. In the shallow part, there is no interaction and the inhomogeneities are therefore simple, but in the deeper part, the perturbing stress fields of at least two zones of weakness are superposed, thus leading to complex trajectory patterns including neutral points and zones of diverging and converging stress trajectories.

4.6.4 Estimating stress magnitudes from stress trajectories

For two dimensional stress pattern analysis the curvature of stress trajectories can be used for the determination of stress gradients. Assuming a state of equilibrium for a surface element, the Lamé-Maxwell equations given in eq. 4.1 can be derived from the body- and surface-forces acting on the element. There, σ_1 and σ_2 are the principal stress directions, s_1 and s_2 are distances along the respective trajectories, and θ_1 is the angle measured counterclockwise between the x-axis and the σ_1-direction. This is a complete set of partial differential equations that can be solved by posing a boundary value problem and find its solution using conventional solver algorithms. These equations can be extended for three dimensions and applied to the trajectories obtained by the methods presented in this work. The application may be subject to future work.

$$
\begin{aligned}
\frac{\partial \sigma_1}{\partial s_1} + (\sigma_1 - \sigma_2)\frac{\partial \theta_1}{\partial s_2} = 0 \\
\frac{\partial \sigma_2}{\partial s_2} + (\sigma_1 - \sigma_2)\frac{\partial \theta_1}{\partial s_1} = 0
\end{aligned}
\tag{4.1}
$$

4.6.5 KTB dataset analysis

The dataset of 125 induced earthquakes from the KTB drilling site has been analysed in section 3.3.3. The application of the source volume segmentation has proved that there are are only marginal lateral inhomogeneities in the stress field, although a rotation with depth is observed. Because there are obviously no strong inhomogeneities, stress trajectories are not analysed.

4.7 Mechanisms for earthquake swarm triggering

With respect to tectonic features, the area Vogtland/NW-Bohemia is characterised by the intersection of the Eger Rift with the Mariánské Lázně fault system, CO_2-rich mineral springs, and the periodic occurence of earthquake swarms (see e.g. Weise et al., 2001). For the latter, there exist two prinicipally different models to explain the phenomenon. One model takes tectonic mechanisms into account and the other deals with fluids like ascending magma filled cracks (dikes). Examples of both kinds are presented in the following sections and tested as possible causes for the swarm activity in the Vogtland/NW-Bohemia earthquake swarm region.

4.7.1 Faulting

Many authors like Poupinet et al. (1984) and Deichmann and Garcia-Fernandez (1992) have reported waveform similarity in tectonically active regions. The general model to explain this phenomenon is
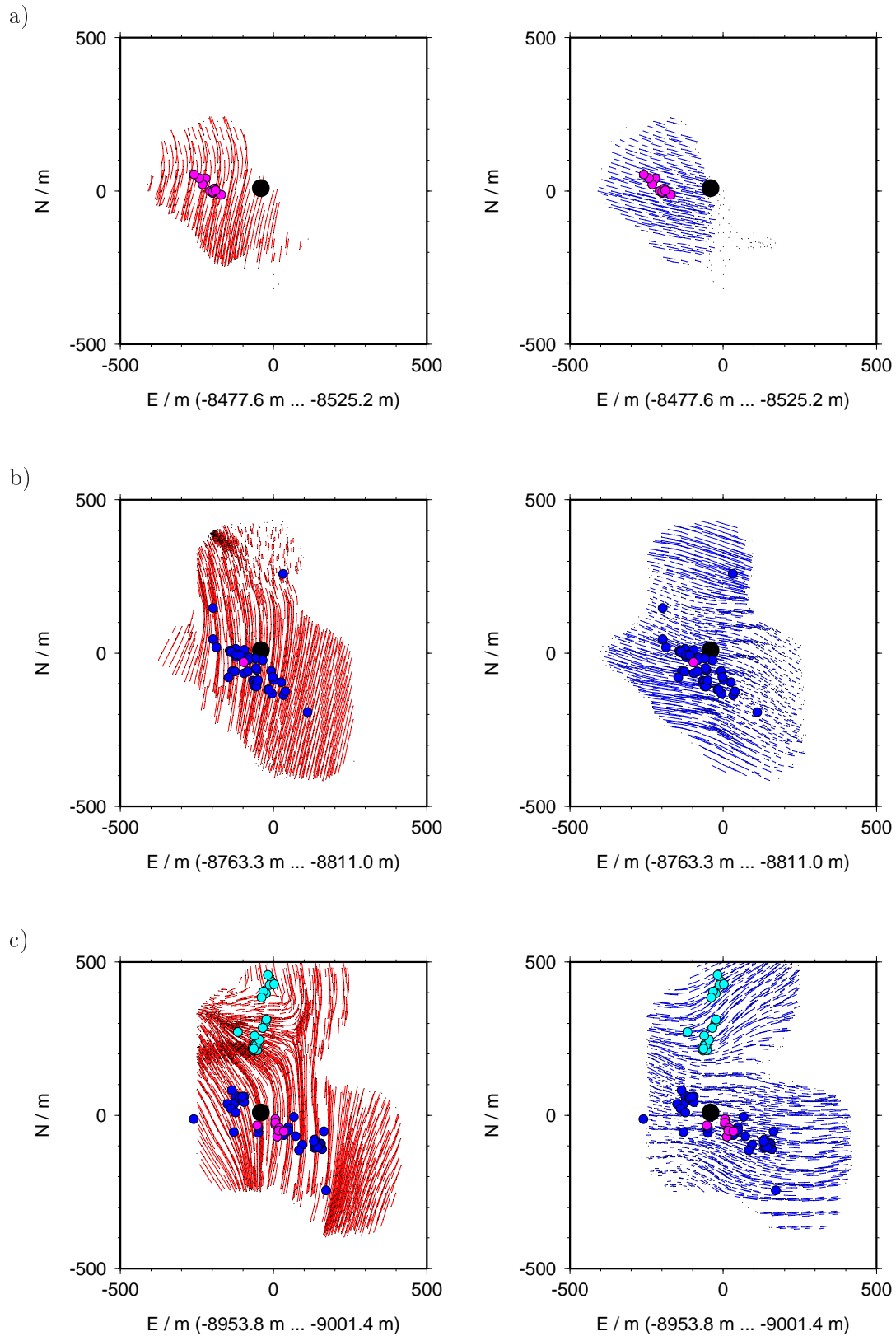
Figure 4.10: Comparison of the stress trajectory patterns for the 1997 swarm with the hypocentres of different groups of multiplets (blue: multiplet group 1, magenta: multiplet group 2, turquoise: multiplet group 3)
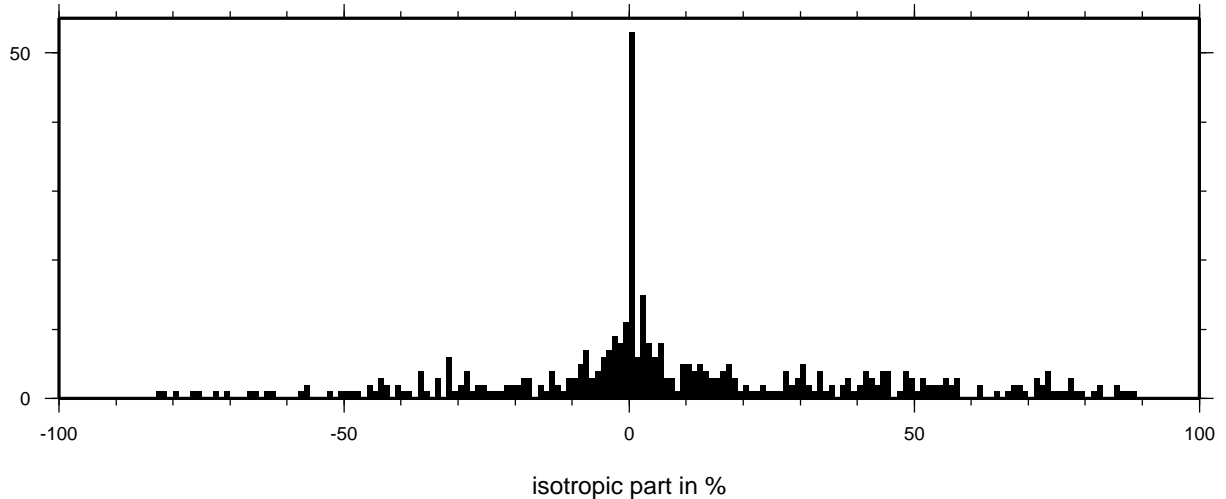
Figure 4.11: Histogram of the isotropic component

rupture on a common fault plane which has been caused by a homogeneous constant stress field. In agreement with this model Hainzl (2004) reported successive rupturing for the 2000 swarm. Due to stress drop during the rupture process, the stress field will be altered resulting in a typical pattern of stress trajectories. Fig. 4.6 shows that such a pattern can be found using the moment tensors obtained by the 1-component inversion result. This finding is valid only for a small part of the source volume but there is no evidence for a large common fault plane on which slip occurs.

4.7.2 ISO part of the moment tensor

From the moment tensor, its isotropic part (ISO) can be extracted as $ISO = \frac{\sigma_{11}+\sigma_{22}+\sigma_{33}}{3} \cdot \frac{100\%}{M_0}$. The isotropic moment tensor component depends linearly on the volume change in the source and thus can be physically explained by openening and closing of cracks or an isotropic radiation pattern like that of an explosion. Since there are several spas and mofettes in the region (Bankwitz et al., 2003), possibly expanding or migrating fluids may be discussed in relation to the ISO component.

Fig. 4.11 shows a histogram of the isotropic components of all available moment tensors. Most moment tensors don't have a significant $ISO \neq 0$. The seismicity, the ISO, and the mean relative moment are plotted against time in fig. 4.12. The isotropic moment, which is defined as $M_{r,ISO} = M_r * ISO$, is depends linearly on the volume change during an earthquake. Fig. 4.13 shows the rate of the isotropic moment and its sum against time.

There are phases in which the seismicity is dominated by events with a significant ISO while most of the time ISO is nearly vanishing. The first phase of "ISO activity" from day 14 to day 16 of january 1997 is dominated by negative ISO. It is followed by a phase from day 16 to day 19 with positive ISO of small magnitude in the beginning and a large rise at the end. Then the positive ISO is small again from day 19 to day 22 and it follows a phase with no significant isotropic energy release from day 22 to day 27 until a step like rise of positive ISO is observed. The remainder of the swarm from day 27 to day 29 lacks isotropic dominated events.

The ISO might be related to migration of fluids. In this context, the negative gradient in the development of ISO in the beginning might be interpreted as being caused by fluids that migrated out of the seismogenic zone, resulting in closure of cracks. The positive ISO might be related to a re-entering of fluids causing an overall volume increase of cracks. From ISO, a volumetric change associated to

108

a)

b)

c)
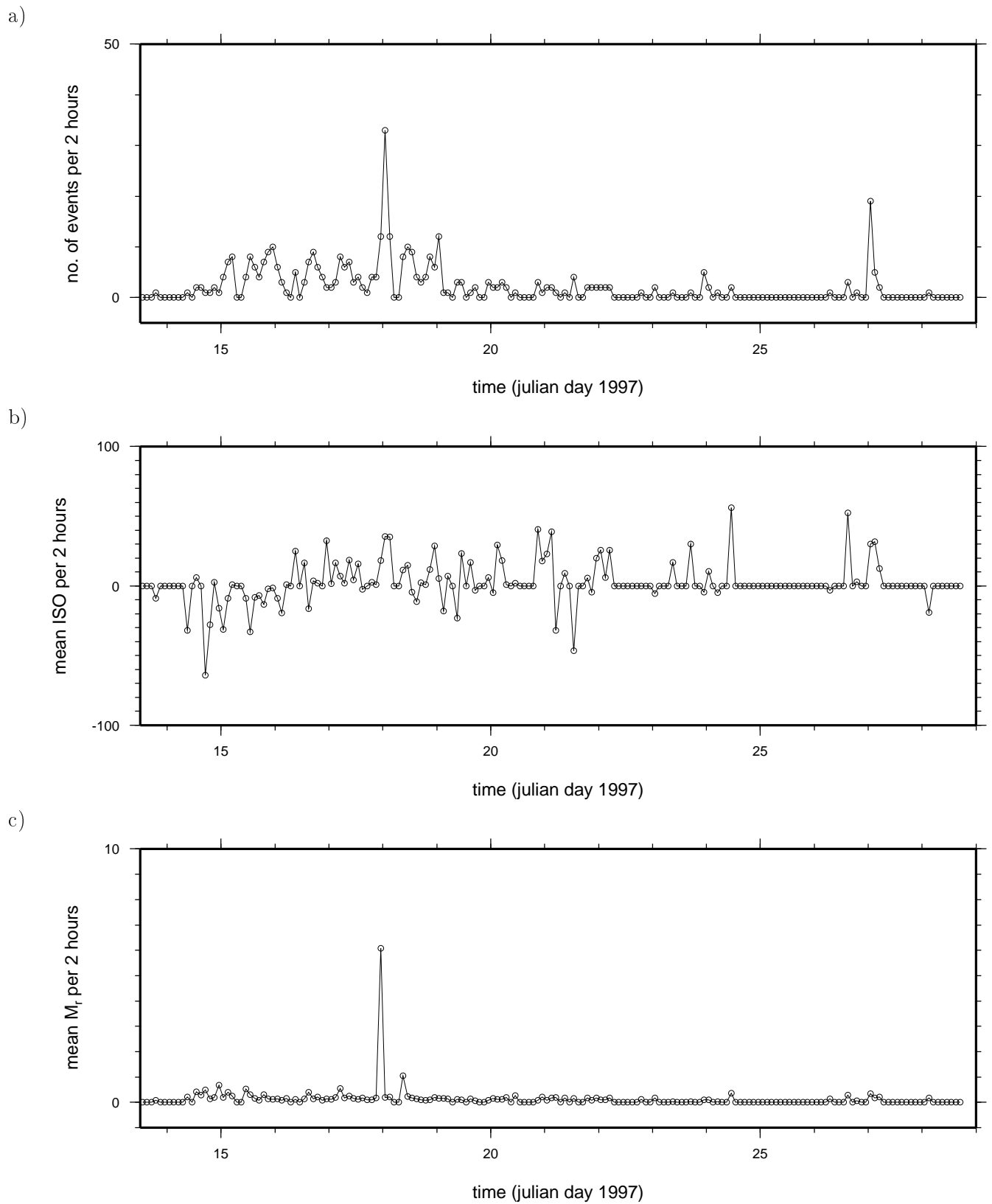
Figure 4.12: Analysis of the isotropic component of the relative moment tensors for the 1997 swarm: a) seismicity rate; b) mean isotropic component rate; c) mean M_r (relative moment) rate

d)
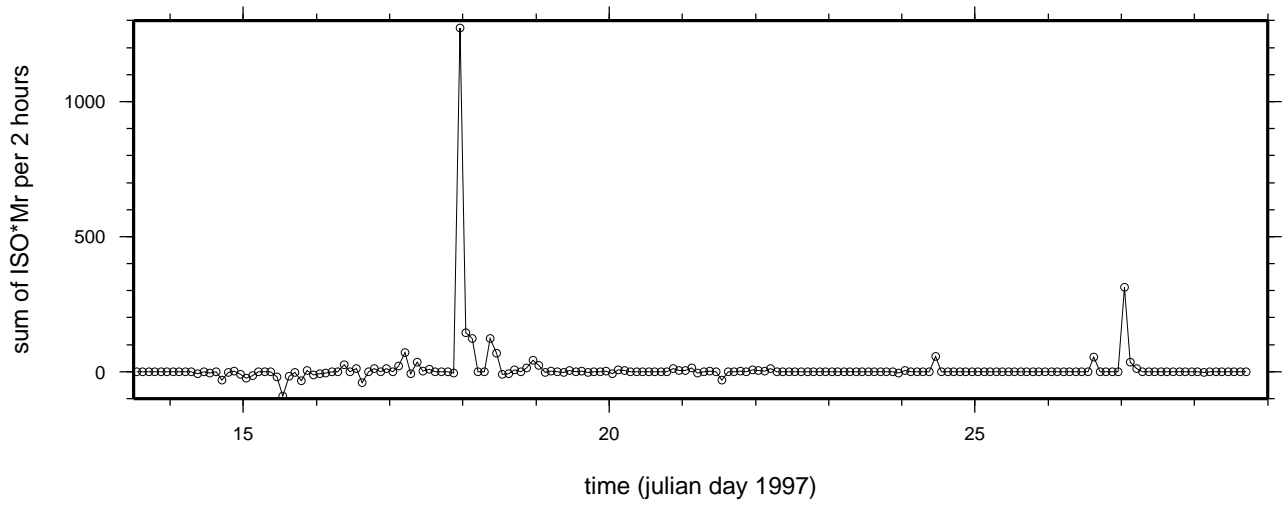
e)
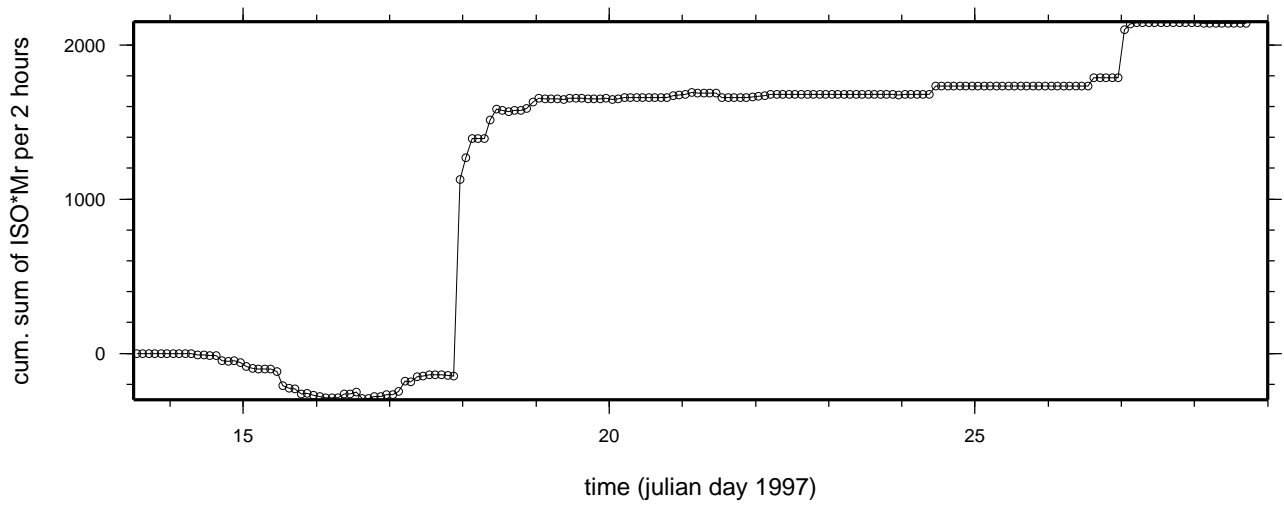
Figure 4.13: Analysis of the isotropic component of the relative moment tensors for the 1997 swarm: d) isotropic relative moment $(ISO * M_r)$ rate; e) cumulative relative isotropic moment

the source mechanism can be obtained if either a spherical symmetric source or a tensional crack is assumed, as presented by Müller (2001) and shown in eq. 4.2 where λ and μ are the elastic parameters and $M = 1/3(M_{11} + M_{22} + M_{33})$ is $1/3$ of the trace of the moment tensor. Using these formulas, ISO of the relative moments obtained during the relativ moment tensor inversion, and the scalar moments of the reference events, the volumetric change may be determined in a subsequent study.

$$\Delta V_{spheric} = \frac{M}{\lambda + 2\mu/3}$$
$$\Delta V_{crack} = \frac{M}{\lambda + 2\mu} \tag{4.2}$$

A critical comment on this interpretation is that the ISO component derived from the moment tensors is assumed to be generated coseismic, i.e. during the rupture process with the rupture velocity which is about 70% of the appropriate S-wave velocity (or less in rare special situations like slow earthquakes which rupture at about 50% or less of the S-wave velocity). Fluid flow, on the other hand, is assumed to be small if it has to open a narrow crack that was closed before the earthquake. For instance, the ascend velocity of a magma dyke is in the order of about $1m/s$ which is identical to the velocity of crack opening.

A solution may be the model of Dahm and Brandsdottir (2004) where the isotropic source is assumed to be triggered, but decoupled from the shear crack source while both sources are radiating simultaneously. The volume source consists of a fluid filled dike which has a possible length of few to several km and a thickness of cm to several m. This model may be applied for the peaks of negative and positive isotropic moment in fig. 4.13 between days 14 and 16, and around day 18 and 27, respectively .

Gas triggered earthquakes

Weise et al. (2001) have proved that the contents of gases collected at the Eisenquelle mineral spring has been altered after an earthquake swarm on December 4th and 5th, 1994. They have analysed the ratio of carbon and helium indicator isotopes which normally characterises a gas origin near the Earth's Mantle. They find that the ratio changes and conclude that the fraction of gases originating from the crust increases. They further conclude that the seismic activity has been triggered by migrating fluids which increase the pore pressure and therefore reduce the frictional strength of the material. This makes the material more likely to fail. The triggered earthquakes set free crustal fluids and Weise et al. state that this contamination has caused the alteration of the gas isotope ratio.

I interpret significant changes in ISO for the relative moment tensors of the 1997 swarm as volume changes due to the migration of fluids. Therefore I suggest that the reduction of the frictional resistance due to the presence of fluids is the mechanism for triggering the earthquakes of the 1997 swarm.

4.8   Conclusions

In this work, a coherence analysis involving 3-component seismograms has successfully been applied to a dataset of 733 events recorded by the seismic network WEBNET situated in West Bohemia, Czechia, for the 1997 earthquake swarm near Nový Kostel. Initial locations have been provided by the network operators and together with the results of the coherence analysis in the form of precise arrival time differences these are provided as input to the double-difference relocation algorithm implemented in the program `hypoDD`. From the hypocentres, laminar structures have been derived, giving a good idea of the structures in the depth range of about 8500-9500 m. The orientation of these zones of weakness can help to distinguish between fault plane and auxiliary plane for focal mechanism data.

Previously determined reference moment tensors, the azimuths and take-off angles between the events and the stations together with amplitude information derived from the arrival time differences and the appropriate correlation coefficients as weights are fed into the relative moment tensor inversion program `relref`. The inversion has been problematic in the way that for some multiplet groups the moment tensor were not similar to each other. However, the analysis of fault and auxiliary plane shows that also for these multiplet groups the nodal plane orientation is consistent with the previously determined zones of weakness indicating that the result is at least partly correct and acceptable regarding the automatic processing. The right-dihedra method is fed with the best double couple solutions of the moment tenors and proves to indicate the presence of stress inhomogeneities well. Finally, the inversion for local stress field inhomogeneities has been successfully applied. From the source volume segmentation alone it is possible to roughly estimate the orientation of stress inhomogeneities by means of the direction of the principal axes of stress. Tracing stress trajectories reveals different patterns in them helping to interpret complex tectonic features.

All in all, a framework consisting of four basic seismological analysis techniques, namely coherence analysis, relocation, relative moment tensor inversion, and stress inversion featuring the systematic determination of stress field inhomogeneities has been developed. Many tools have been implemented in the AWK programming language, in the form of BASH shell scripts, and as C++ programs. The single processing steps are connected through result files. The output of one program serves as input to the other, converted to some usable format if aplicable. This framework may be used for the analysis of any dataset of seismograms recorded by a seismic network for which the events have been located, i.e. phase picks for the P- and S-phase are available and for which the data is available in GSE 2.0 format (Provisional GSE 2.1, 1997). The framework may be extended at either end, e.g. an automatic phase picking algorithm may be attached prior to the coherence analysis or an automatic stress trajectory pattern analysis tool may be applied after the trajectories are determined. The tools used for the single processing steps may be exchanged by those which implement other techniques or new branches may be introduced, e.g. a hypocentre pattern determination tool may be applied right after the relocation, or the scalar moment of the moment tensors may be used by some magnitude analysis tool. This framework is intended to be applied to many more datasets and will hopefully be used and enhanced intensively.

Strong stress inhomogeneities within the small source volume of about $1km^3$ of the 1997 Vogtland/NW-Bohemia earthquake swarm have been identified. Although the responsible structure cannot be resolved easily due to the complexity of the problem, it becomes clear that plane-like, small features disturbed the regional stress field during the time of the swarm activity. The stress trajectories found in the volume under study did not coincide with the regional stress field expected from the Alps push. They point in totally different directions which means that either the result is not stable at the edges or that there are more structures in the vicinity that cause further perturbations of the regional stress field. Since zones of weakness with different orientation are identified, it is likely that the earthquake swarm occured in a region where fault systems are crossing which is in good agreement with the tectonic setting (very old, highly faulted crust; Eger Graben and Mariánské Lázně fault system exposed at the surface). The findings are consistet with a fluid (gasses or magma) injection in a highly faulted region and the earthquakes are possibly triggered by gas movement. However, a purely tectonic model cannot safely be excluded as possible cause of the swarm.

While strong stress heterogeneities have been found for the 1997 swarm, only small stress inhomogeneities have been identified for the KTB region during the time of the 2000 hydraulic fracturing experiment.

This work is the first attempt to resolve small scale local stress inhomogeneities in great detail in the source region of an earthquake swarm. Only spatial patterns have been studied, but the method would

in principle be able to resolve temporal changes of stress, additionally.

The stress patterns that have been found are complex and it was not yet possible to relate them to simple source models. However, this does not mean that the stress inhomogeneities are not reliable. The stress inhomogeneities from a crossing and inclined, finite area dislocation is expected to look quite complex in three dimensions, especially when overlayn by an additional regional stress field and superposed with stress perturbations caused by other features of comparable complexity.

Future work should aim to develop models and theories to better understand complex stress inhomogeneities as the ones found in this work.

Acknowledgments

References

Aki, K. and Richards, P. G., 1980. Quantitative Seismology, Theory and Methods. W. H. Freeman and Company, San Francisco.

Albarello, D., 2000. A resampling approach to test stress-field uniformity from fault data. Geophys. J. Int., 140(3):535–542.

Anderson, E. M., 1951. The Dynamics of Faulting, 2nd ed. Oliver and Boyd, Edinburgh.

Angelier, J., 1979. Determination of the mean principal directions of stresses for a given fault population. Tectonics, 56:T17–T26.

Angelier, J., 1984. Tectonic analysis of fault slip data sets. J. Geophys. Res., 89(B7):5835–5848.

Angelier, J., 2002. Inversion of earthquake focal mechanisms to obtain the seismotectonic stress IV - a new method free of choice among nodal planes. Geophys. J. Int., 150:588–609.

Angelier, J. and Mechler, P., 1977. Sur une méthode graphique de recherche des contraintes principales également utilisable en tectonique et en séismologie: la méthode des deèdres droits. Bull. Soc. géol. France, 6:1309–1318.

Aster, R. and Rowe, C., 2000. Automatic phase pick refinement and similar event association in large seismic datasets. C. Thurber and N. Rabinowitz, eds, Advances in Seismic Event Location, published by Kluwer, Amsterdam, pp. 231–263.

Atkinson, B. K., 1987. Fracture mechanics of rock (ed.). Academic Press, London.

Baisch, S., Bohnhoff, M., Ceranna, L., Tu, Y., and Harjes, H. P., 2002. Probing the crust to 9 km depth: Fluid injection experiments and induced seismicity at the ktb superdeep drilling hole, germany. Bull. Seism. Soc. Am., 92:2369 2380.

Bankwitz, P., Schneider, G., Kämpf, and Bankwitz, E., 2003. Structural characteristics of epicentral areas in central europe: study case cheb basin (czech republic). J. of Geodynamics, 35:5–32.

Becker, J., 2004. Strömungsvisualisierung mit Partikelsystemen in 3D. Master's thesis, Univerität Potsdam.

Berckhemer, H., 1990. Grundlagen der Geophysik. Wissenschaftliche Buchgesellschaft.

Bohnhoff, M., Baisch, S., and Harjes, H. P., 2004. Fault mechanisms of induced seismicity at the Superdeep German Continental Deep Drilling Program (KTB) borehole and their relation to fault structure and stress field. J. Geophys. Res., 109(B1, C4):B02309, doi:10.1029/2003JB002528.

Brady, B. H. G. and Brown, E. T., 2004. Rock Mechanics for undergound mining, 3rd edition. Kluwer Academic Publishers.

Brudy, M., Zoback, M. D., Fuchs, K., Rummel, F., and Baumgärtner, J., 1997. Estimation of the complete stress tensor to 8 km depth in the KTB scientific drill holes: Implications for crustal strength. J. Geophys. Res., 102(B8):18453–18475.

Dahlheim, H.-A., Gebrande, H., Schmedes, E., and H., S., 1997. Seismicity and stress field in the vicinity of the KTB location. J. Geophys. Res., 102(B8):18493–18506.

Dahm, T., 1996. Relative moment tensor inversion based on ray-theory: Theory and synthetic tests. Geophys. J. Int., 124:245–257.

Dahm, T., 2001. Nichtlineare Inversionsprobleme (Teil II des Skriptes Inversionsprobleme). Universtät Hamburg.

Dahm, T. and Brandsdottir, B., 2004. Moment tensors of microearthquakes from the Eyjafjallajökull volcano in South Iceland. Geophys. J. Int., 130:183–192.

Dahm, T., Horálek, J., and Šílený, 2000. Comparison of absolute and relative moment tensor solutions for the january 1997 West Bohemia earthquake swarm. Studia geoph. et geod., 44:233–250.

Dahm, T. and Plenefisch, T., 2001. A new energy-based approach in stress inversion. Unpublished.

Deichmann, N. and Garcia-Fernandez, M., 1992. Rupture geometry from high-precision relative hypocenter locations of microearthquake clusters. Geophys. J. Int., 110:501–517.

Douglas, A., 1967. Joint epicentre determination. Nature, 215:47–48.

Eisbacher, G. H., 1991. Einführung in die Tektonik. Ferdinand Enke Verlag Stuttgart.

Fischer, T., 2003. The august-december 2000 earthquake swarm in NW-Bohemia: The first results based on automatic processing of seismograms. J. of Geodynamics, 35:59–81.

Fischer, T. and Horálek, J., 2000. Refined locations of the swarm earthquakes in the Nový Kostel focal zone and spatial distribution of the january 1997 swarm in Western Bohemia Czech Republic. Studia geoph. et geod., 44:210–226.

Fischer, T. and Horálek, J., 2004. Triggering mechanisms of swarm earthquakes: observations in the NW-Bohemia/Vogtland area (Central Europe). J. Geophys. Res., submitted.

Geiger, L., 1910. Herdbestimmung bei Erdbeben aus den Ankunftszeiten. K. Ges. Wiss. Gött., 4:331–349.

Gephart, J. and Forsyth, D., 1984. An improved method for determining the regional stress tensor using earthquake focal mechanism data: Application to the San Fernando earthquake sequence. J. Geophys. Res., 89:9305–9320.

Gephart, J. W., 1990. Stress and the directions of slip on fault planes. Tectonics, 9(4):845–858.

Google-earth, 2006. Satellite photo of NW-Bohemia. http://earth.google.de/.

Guzzetta, G., 1984. Kinematics of stylolite formation and physics of the pressure-solution process. Tectonophysics, 101:383–394.

Hainzl, S., 2004. Seismicity patterns of earthquake swarms due to fluid intrusion and stress triggering. Geophys. J. Int., 159:1090–1096.

Harvard-Seismology, 2006. Centroid Moment Tensor (CMT) database. http://www.seismology.harvard.edu/CMTsearch.html.

Horálek, J., Fischer, T., Boušková, A., and Jedlička, P., 2000. The Western Bohemia/Vogtland region in the light of the WEBNET network. Studia geoph. et geod., 44:107–125.

Ibs-von Seht, M., Plenefisch, T., and Schmedes, E., 2004. Focal Parameter Investigations of Swarm Earthquakes in the German Vogtland. Abstract; ESC Gen. Ass. 2004, Potsdam, pp. 92–93.

Jost, M., Buesselberg, T., Jost, O., and Harjes, H.-P., 1998. Source parameters of injection-induced microearthquakes at 9 km depth at the KTB Deep Drilling Site. Bull. Seism. Soc. Am., 88:815–832.

Jost, M. L. and Hermann, R. B., 1989. A students guide to and review of moment tensors. Seism. Res. Lett., 60:37–57.

Kennett, B. L. N., 2001. The seismic wavefield, Vol. 1: Introduction and theoretical development. Cambridge Univ. Press.

Kesper, B., 2001. Konzeption eines Geo-Datenmodells unter Verwendung von Freiformkörpern auf der Basis von Volume Non Uniform Rational B-Splines. PhD thesis, Universität Hamburg, Fachbereich Informatik, Vogt-Kölln-Straše 30, 22527 Hamburg, Germany.

Knett, J., 1899. Das erzgebirgische Schwarmbeben zu Hartenberg vom 1. Jänner bis 5. Feber 1824. Sitzungsber. des Deutschen Naturw.-Med. Vereins für Böhmen "Lotos" in Prag, 19:167–191.

Lawson, C. L. and Hanson, R. J., 1974. Solving Least Squares Problems. Prentice-Hall Inc., Englewood Cliffs, N. J.

Leeman, E. R. and Hayes, D. J., 1966. A technique for determining the complete state of stress in rock using a single borehole. Proc. 1st Congr., Int. Soc. Rock Mech., Lisbon,, 2:17–24.

Lisle, R., Orife, T., and Arlegui, L., 2001. A stress inversion method requiring only fault slip sense. J. Geophys. Res., 106(B2):2281–2289.

Lund, Björn, 2003. Photo of borehole breakouts. `http://www.geofys.uu.se/bl/Avh/node22.html`. UPPSALA UNIVERSITY.

Mattauer, M., 2002. Was die Steine uns erzählen. Spektrum der Wissenschaft Compact, 2:5–146.

Maurer, H. and Deichmann, N., 1995. Microearthquake cluster detection based on waveform similarities, with an application to the western Swiss Alps. Geophys. J. Int., 123:588–600.

Michael, A. J., 1984. Determination of stress from slip data: faults and folds. J. Geophys. Res., 89:11517–11526.

Michael, A. J., 1987. Use of focal mechanism to determine stress: a control study. J. Geophys. Res., 92:357–369.

Miller, M. B., 2006. Photo of Riedel Shears. `http://darkwing.uoregon.edu/~millerm/`.

Mogi, K., 1963. Some Discussions on Aftershocks, Foreshocks and Earthquake Swarms - the Fracture of a Semi-infinite Body Caused by an Inner Stress Origin and Its Relation to the Earthquake Phenomena (Third Paper). Bull. Earthq. Res. Inst., 41:615–658.

Müller, B., Zoback, M., Fuchs, K., Mastin, L., Gregersen, S., Pavoni, N., Stephansson, O., and Ljunggren, C., 1992. Regional patterns of tectonic stress in Europe. J. Geophys. Res., 97:11783–11803.

Müller, G., 2001. Volume Change of Seismic Sources from Moment Tensors. Bull. Seism. Soc. Am., 91(4):880–884.

NASA, 2003. Photo of New Zealand, South Island. `http://earthobservatory.nasa.gov/NaturalHazards/Archive/Jul2003/NewZealand.TMOA2003192_lrg.jpg`.

Neunhöfer, H. and Meier, T., 2004. Seismicity in the Vogtland/Western Bohemia earhquake region between 1962 and 1998. Studia geoph. et geod., 48:539–562.

Odé, H., 1957. Mechanical Analysis of the Dike Pattern of the Spanish Peaks Area, Colorado. Geol. Soc. Am. Bull., 68:567–578.

Papoulis, A., 1984. Probability, Random Variables, and Stochastic Processes, 2nd ed. New York: McGraw-Hill.

Peppin, W., Honjas, W., Somerville, R. M., and Vetter, R. U., 1989. Precise master-event locations of aftershocks of the 4th October 1978 Wheeler crest earthquake sequence near Long Valley, California. Bull. Seism. Soc. Am., 79(1):67–76.

Piegl, L. and Tiller, W., 1997. The NURBS Book. Springer, Berlin [u.a.].

Plenefisch, T. and Klinge, K., 2003. Temporal variations of focal mechanisms in the Novy Kostel focal zone (Vogtland/NW-Bohemia) - Comparison of the swarms of 1994, 1997 and 2000. J. of Geodynamics, 35(1-2):145–156.

Pollard, D. D. and Segall, P., 1987. Fracture Mechanics of Rock (Atkinson, B. K ed.), Kapitel Theoretical displacements and stresses near fractures in rock: with applications to faults, joints, veins, dikes, and solution surfaces. , pp. 277–349. Academic Press, London.

Poupinet, G., Ellsowrth, W. L., and Frechet, J., 1984. Monitoring velocity variations in the crust using earthquake doublets: An application to the calaveras fault, california. J. Geophys. Res., 89(B7):5719–5731.

Price, N. J., 1966. Fault and joint development in brittle and semibrittle rock. New York: Pergamnon Press.

Provisional GSE 2.1, 1997. Provisional GSE 2.1, Message Formats & Protocols.

Ramsay, J. G., 1967. Folding and fracturing of rocks. McGraw-Hill Book Company.

Ramsay, J. G. and Huber, M. I., 1987. The Techniques of Modern Structural Geology Vol. 2: Folds and Fractures. Academic Press.

Ramsay, J. G. and Lisle, R. J., 2000. The Techniques of Modern Structural Geology Vol. 3: Application of continuum mechanics in structural geology. Academic Press.

Reinecker, J., Heidbach, O., Tingay, M., Connolly, P., and Müller, B., 2004. The 2004 release of the World Stress Map. available online at www.world-stress-map.org.

Reinhardt, J., 2002. Automatisierte Kohärenz-Analyse und Relokalisierung für den Erdbebenschwarm 1997 in der Region Vogtland/NW-Böhmen. Diplomarbeit, Universität Hamburg, Institut für Geophysik, Bundesstraße 55, 20146 Hamburg, Germany.

Richter, C. F., 1958. Elementary Seismology. W. E. Freeman, London.

Riedel, W., 1929. Zur Mechanik geologischer Brucherscheinungen. Centralbl. f. Mineral., Geol. u. Pal., 1929B:354–368.

Rogers, D. F., 2001. An introduction to NURBS. Morgan Kaufmann Publishers, San Francisco, Calif. [u.a.].

Rowe, C., Aster, R., B., B., and C.J., Y., 2002. An automatic, adaptive algorithm for refining phase picks in large seismic data sets. Bull. Seism. Soc. Am., 92:1660–1674.

Scholz, C. H., 1990. The Mechanics of Earthquakes and Faulting. The Press Syndicate of the University of Cambridge.

Schunk, R., Peterek, A., and Reuther, C. D., 2003. Untersuchungen zur quartären und rezenten Tektonik im Umfeld der Marienbader Störung und des Egerer Bekens (Tschechien) - erste Ergebnisse. Mitt. Geol.-Paläont. Inst. Univ. Hamburg, 87:19–46.

Shene, C.-K., 2003. CS3621 Introduction to Computing with Geometry Notes. Published as online course in WWW. URL: http://www.cs.mtu.edu/ shene/COURSES/cs3621/NOTES/.

Sherbon Hills, E., 1972. Elements of Structural Geology, 2nd ed. Chapman and Hall Ltd.

Skácelová, Z., V., N., and Havíř, J., 1998. Seismicity in the area of western bohemia. Exploration Geophysics, Remote Sensing and Environment, 2:7–15.

Slancová, A. and Horálek, J., 2000. Analysis of state of stress during the 1997 earthquake swarm in western bohemia. Studia geoph. et geod., 44:272–289.

Slunga, R., Rögnvaldsson, T., and Bödvarsson, R., 1995. Absolute and relative location of similar events with application to microearthquakes in southern Iceland. Geophys. J. Int., 123:409–419.

Snoke, J. A., 2003. FOCMEC: FOcal MEChanism determinations. W. H. K. Lee, H. Kanamori, P. C. Jennings, and C. Kisslinger, Eds.: International Handbook of Earthquake and Engineering Seismology, published by Academic Press, San Diego, chapter 85.12, pp. –.

Spence, W., 1980. Relative epicenter determination using P-wave arrival-time differences. Bull. Seism. Soc. Am., 70:171–183.

Suppe, J., 1984. Principles of Structural Geology. Prentice Hall College Div.

Sykes, 1970. Earthquake Swarms and Sea-Floor Spreading. J. Geophys. Res., 175(32):364–373.

Twiss, R. J. and Moores, E. M., 1992. Structural Geology. W.H.Freeman and Company, New York.

USGS, 1999. Photo of the San Andreas Fault. `http://pubs.usgs.gov/gip/dynamic/San_Andreas.html`.

Vavryčuk, V., 2002. Non-double-couple earthquakes of 1997 january in west bohemia, czech republic: evidence of tensile faulting. Geophys. J. Int., 149:364–373.

Wagner, G. A., Goegen, K., Jonckhere, R., Wagner, I., and Woda, C., 2002. Dating of the Quaternary volcanoes Komorni Hurka (Kammerbühl) and Zelezna Hurka (Eisenbühl), Czech Republic, by TL-, ESR-, alpha-recoil and fission track chronometry. Z. geol. Wiss., 30:191–200.

Waldhauser, F. and Ellsworth, W., 2000. A double-difference earthquake location algorithm: Method and application to the northern hayward fault, california. Bull. Seism. Soc. Am., 90:1353–1368.

Weise, S. M., Bräuer, K., Kämpf, H., Strauch, G., and Koch, U., 2001. Transport of mantle volatiles through the crust traced by seismically released fluids: a natural experiment in the earthquake swarm area Vogtland/NW Bohemia, Central Europe. Tectonophysics, 336:137–150.

Weisstein, E. W., 2005. Mathworld - a wolfram web resource. Published online in the WWW. URL: http://mathworld.wolfram.com/.

Wirth, W., Plenefisch, T., Klinge, K., and Stammler, K., 2000. Focal Mechanisms and Stress Field in the Region Vogtland/Western Bohemia. Studia geoph. et geod., 44:126–141.

Yin, Z.-M., 1996. An improved method for the detemination of the tecotnic stress field from focal mechanism data. Geophys. J. Int., 125:841–849.

Zoback, M. D., Barton, C. A., Brudy, M., Castillo, D. A., Finkbeiner, T., Grollimund, B. R., Moos, D. B., Peska, P., Ward, C. D., and Wiprut, D. J., 2003. Injection-induced earthquakes and crustal stress at 9 km depth at the KTB deep drilling site, Germany. Int. J. Rock Mech. Min. Sci., 40(7-8):1049–76.

Zoback, M. D. and Harjes, H.-P., 1997. Injection-induced earthquakes and crustal stress at 9 km depth at the KTB deep drilling site, Germany. J. Geophys. Res., 102:18477–18491.

Zoback, M. D., Moos, D., Mastin, L., and Anderson, R. N., 1985. Well bore breakouts and in situ stress. J. Geophys. Res., 90:5523–5530.

Appendix A

Programs and algorithms

This appendix serves as a reference to the usage of the developed programs and scripts. Available command line options are explained and simple examples are given. For many processing step there exists a script called *jobs.sh* that gives an overview how and in which order the programs involved should be used.

A.1 Gamma distribution

When analysing the distances between events for a given correlation coefficient threshold and for the analysis of the error of the relative moment during the relative moment tensor inversion (see section 3.1.3) the distributions of the parameter under study have the form of a gamma distribution (e.g. Papoulis, 1984, pp. 103-104) whose probability density function is defined in eq. A.1. x is the observable while δ and λ are parameters describing the shape of the gamma-distribution. The meaning of δ and λ in the original definition of the gamma-distribution (which arises naturally in processes for which the waiting times between Poisson distributed events are relevant) are to control the "thickness", skewness (degree of asymmetry), and kurtosis (degree of peakedness) of the distribution and the reciprocal of the time between changes, respectively. In the applications here these parameters don't have an obvious meaning, except that they can be used to calculate the mean and the variance of the distribution, as defined in eq. A.2 and eq. A.3. The standard deviation is simply the square root of the variance.

$$P(x) = \frac{x^{\delta-1}\lambda^{\delta}}{e^{\Gamma(\delta)}}e^{-\lambda x} \tag{A.1}$$

$$\mu = \delta/\lambda \tag{A.2}$$

$$\sigma^2 = \frac{\delta}{\lambda^2} \tag{A.3}$$

number of recording stations	10	9	8	7	6	5	4	3	2	1
number of events		4	21	39	84	168	220	259	192	187	449

Table A.1: Number of events with both P- and S-picks recorded at a given number of stations

A.2 Coherence analysis

A.2.1 Algorithm

The algorithm described here is designed to compute a coherence relation for a given set of seismograms of events recorded at an arbitrary number of stations. It mostly follows the article of Maurer and Deichmann (1995) but also introduces a fundamental change in the computation of the cross correlation function by using all three components of the seismogram instead of only one. The cross-correlation functions are calculated between all possible pairs of events at each station. The algorithm to actually create the correlation relation is described in detail in the original work of Maurer and Deichmann and it is explained to some extent in my diploma thesis (Reinhardt, 2002).

In accordance to the approach in this work, the general steps that lead to the desired correlation are:

1. calculate correlation coefficients for every event pair at every station

2. set K, T_p, T_y to reasonable values

3. vary T_s and T_x in reasonable intervals

4. calculate coherence relation for every pair of T_s and T_x

5. select appropriate parameter pair by some objective criterion (e.g. as many multiplets with as many events as possible)

Parameter for coherence analysis

The coherence analysis algorithm with its five threshold parameters defines a highly non-linear process, because of the usage of a step function to get rid of unwanted matrix entries. The impact of the threshold values is discussed only briefly in the work of Maurer and Deichmann. In this section, I will discuss reasonable parameter settings for K, T_p, and T_y.

The parameter K is used to drop statistical outliers. Because there are only ten stations and because many events are recorded at only few stations, as can be seen from table A.1 , I set $K = 0\%$ to avoid massive loss of information ($K = 25\%$, as proposed by Maurer and Deichmann (1995) would result in losing 2 of 8 measurements for recordings at eight stations and 1 of 4, 5, 6, and 7 for recordings at four, five, six, and seven stations, respectively).

Looking at the histograms of correlation coefficient values in appendix B, in most cases the necessary tail is visible more clearly for the S-phase. But increasing the parameter T_p will also increase the influence of the P-wave seismograms. Therefore I follow the suggestion of Maurer and Deichmann to just demand positive P-phase correlation coefficients (i.e. $T_p = 0.0$).

To find an appropriate value for T_y, I first estimate reasonable correlation coefficients for nearby events

In my diploma thesis (Reinhardt, 2002, see fig. A.1) I found that the corner frequency for most events of the 1997 swarm at far stations is $f_c = 30Hz$ and the major frequency $f_{major} = 15Hz$. In the source

depth of about 9000m I assume velocities for compressional and transversal waves of $v_P = 6500\frac{m}{s}$ and $v_S = 3892\frac{m}{s}$ respectively (with $\frac{v_P}{v_S} = 1.67$). One of the prerequisites for two earthquakes to produce similar waveforms is that the maximal distance of the hypocentres d is at most a quarter of the major wavelength λ_{major}. Here I set $\lambda_{major} = \frac{v_S}{f_c} = 130m$, so $d = \frac{\lambda_{major}}{4} = 33m$. In comparison to the size of the seismogenic zone of about $(700m)^3$ this is a quite small distance.

Assuming a common fault plane for a small set of aligned earthquakes like in fig. A.5, the calculation of correlation coefficients may result in values like in the matrix shown in eq. A.4. $cc_{1,2}$ and $cc_{2,3}$ will have higher values than $cc_{1,3}$, because of the larger distance between events x_1 and x_3 in the latter case. The threshold T_y introduced earlier controls the link of multiplets. Setting it to a value $T_y = 1$ results in this case to the identification of one "large" multiplet $M = 1, 2, 3$. A higher value $T_y > 1$ does not identify any multiplet. Event x_2 is similar to both events x_1 and x_3, but the small value $cc_1, 3$ breaks the link between all three of them. I prefer weak links which result in larger multiplets, so I pick the value $T_y = 1$.

For the estimation of most reasonable parameters for the gamma distribution the single steps which are described below are combined in a `BASH` script. After the probability of inter-event-distance bins is prepared, a grid search over the two parameters of the gamma distribution is performed. Then a plot of the appropriate error function is produced and its minimum is sought. To exclude inconveniences, the selected gamma distribution and the input data are plotted together into one figure

$$\underline{\underline{cc}} = \left(\begin{array}{ccc} 1.00 & 0.95 & 0.70 \\ 0.95 & 1.00 & 0.95 \\ 0.70 & 0.95 & 1.00 \end{array} \right) \tag{A.4}$$

A.2.2   Calculating correlation coefficients: coma

The program *coma* takes a list of seismogram filenames as input and calculates correlation coefficients for all permutations of seismogram pairs. Output are matrix files that contain the correlation coefficient, the maximum of the correlation function, and the corresponding time. The usage and all parameters that can be provided to the program is described in the following paragraph.

```
Usage: coma [-h] -e events-filename [conf-file] [options]
[-h] - print help on basic usage and options
-e events-filename - contains filenames of GSE 2.1 seismograms
[conf-file] - name of configuration file (def. coma.cnf)
Options:
[-v] - verbose (repeat for higher verbosity level)
[-f fL1/fL2/fH1/fH2] - acausal bandpass filter
[-p percent] - cosine taper percentage
[-F forcedLen] time series will be stretched to $2^{}$forcedLen internally
[-c ccor-file] name of correlation coefficient file (def. cc.mtx)
[-m cmax-file] name of correlation function maximum file (def. cm.mtx)
[-t tmax-file] name of correlation maximum time file (def. tm.mtx)
[-X x] output internal time series for event x (files x.[0-6].c.<desc>.tx)
[-Y y] output second event; also outputs correlation function
(files y.[0-6].c.<desc>.tx and x.y.c.corr.tx)
```
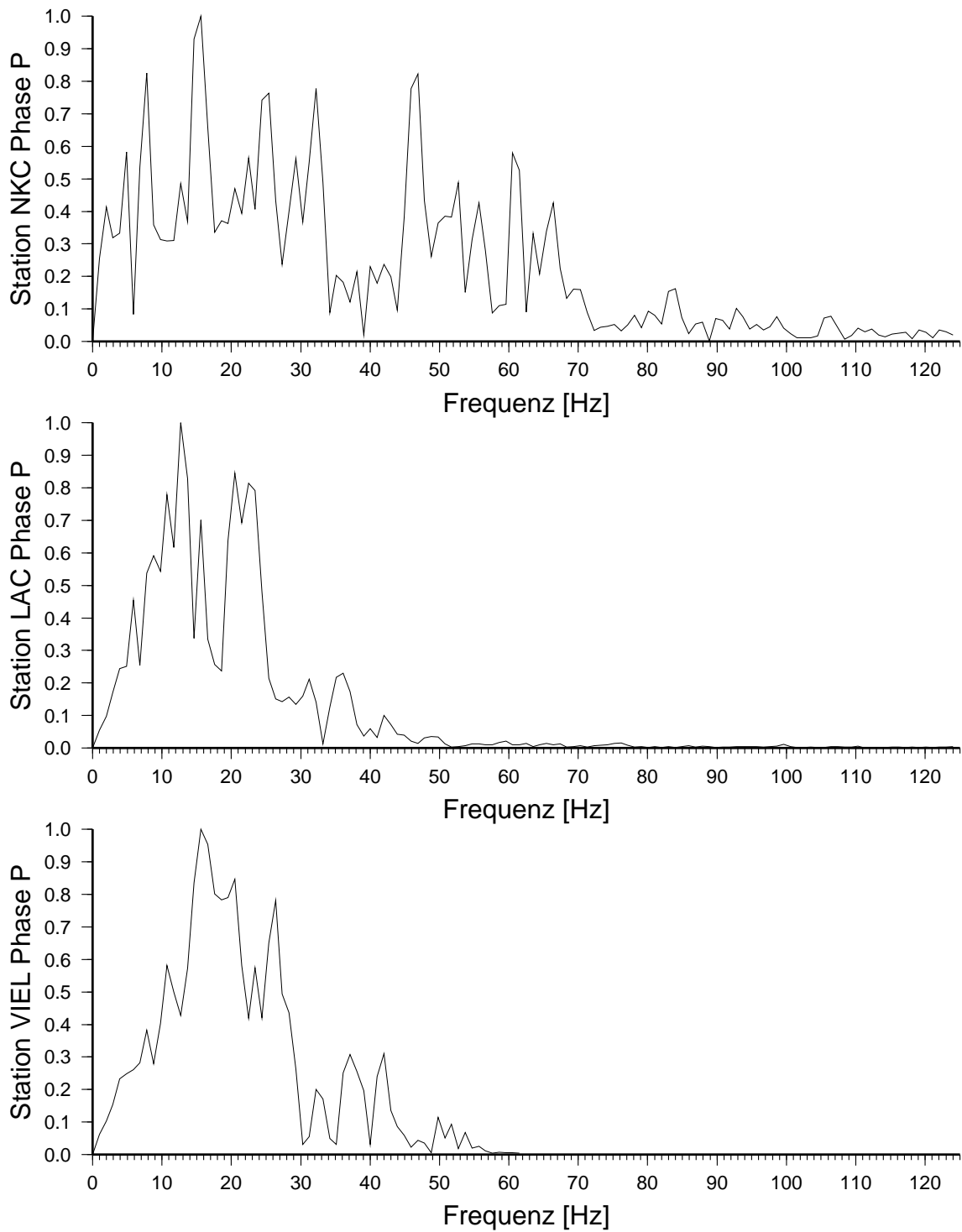
Figure A.1: Stacked spectra for stations NKC, LAC, and VIEL for 1997 swarm
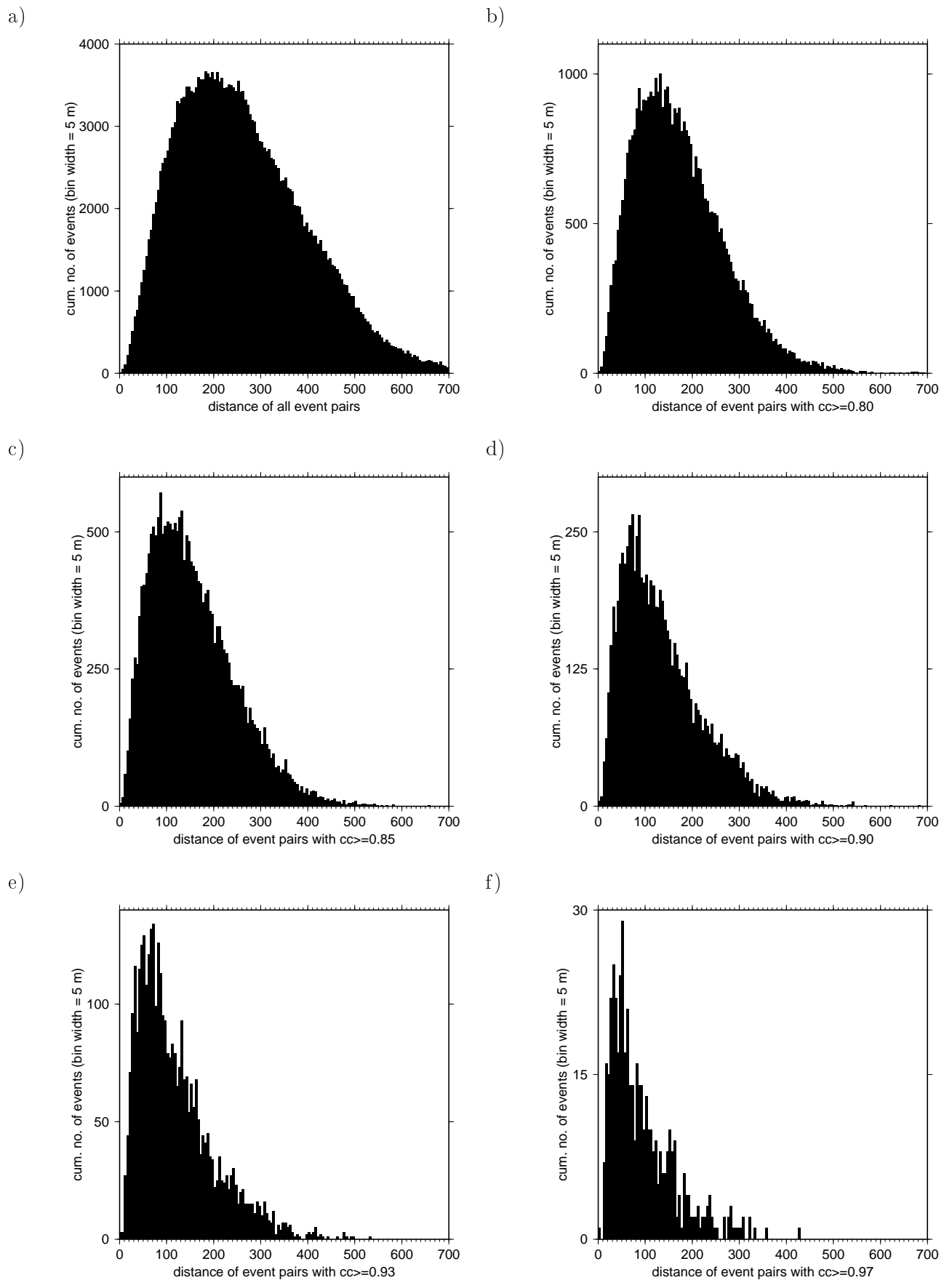
Figure A.2: Event pair distances for different correlation coefficients: a) for all possible event pairs; b-f) event pairs with $cc \geq$ value denoted in figure label
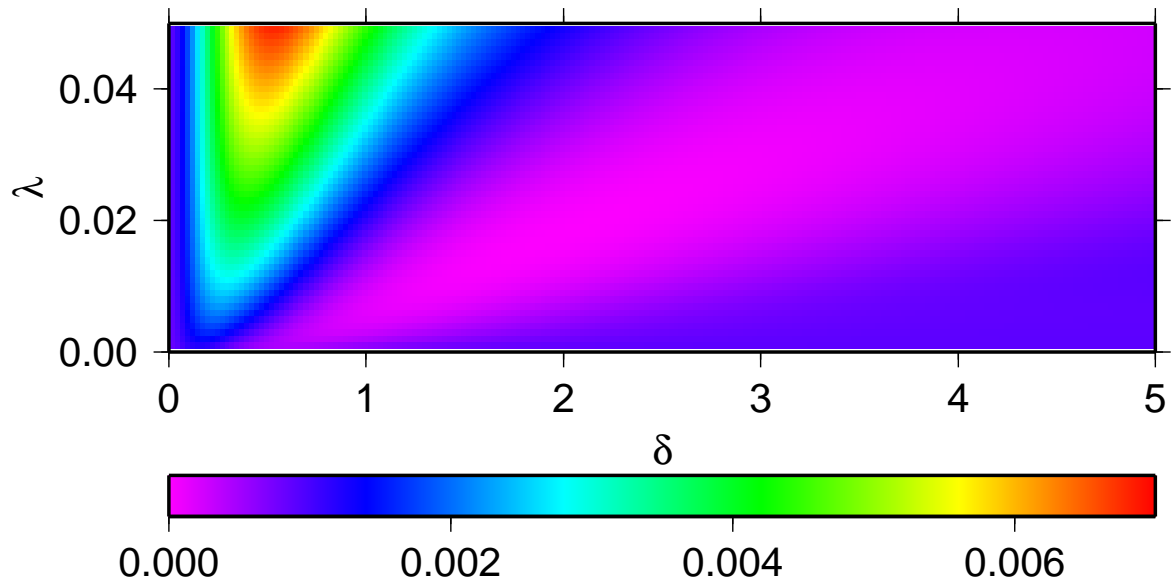
Figure A.3: Error function for gamma distribution fit against event distances; colors indicate least-squares fit

The common output format is a matrix $A = a_{ij}$ in ascii format consisting of one line **x y** defining the dimension of the matrix and **y** lines with **x** columns giving the according values a_{ij} with $1 <= i <= x$ and $1 <= i <= y$. There exists a matrix for every value of time shift (τ_{ij}), cross correlation function maximum ($cc_{ij,max}$), and correlation coefficient (cc_{ij}).

A.2.3 Computing the similarity relation: cohana

The program *cohana* is used to perform a coherence analysis following the algorithm described by Maurer and Deichmann (1995). Input are matrix files as generated by the program *cohana* (see previous paragraph). Output are several matrices containing results of intermediate steps and the final matrix representing the similarity relation.

```
usage: cohana [-h] [-v] [-a] [-c conf-file]
-h: print this help
-v: be verbose
-a: switch algorithm for AEL-calculation to own
-c: specify configuration filename (default: cohana.cnf)
```

Input file format

The format of the input file for *cohana* is as follows:

```
K Ts Tp Tx Ty
Nst Nev event-list-filename
st1-event-list st1-Nev st1-cc-P st1-cc-S
.
.
```
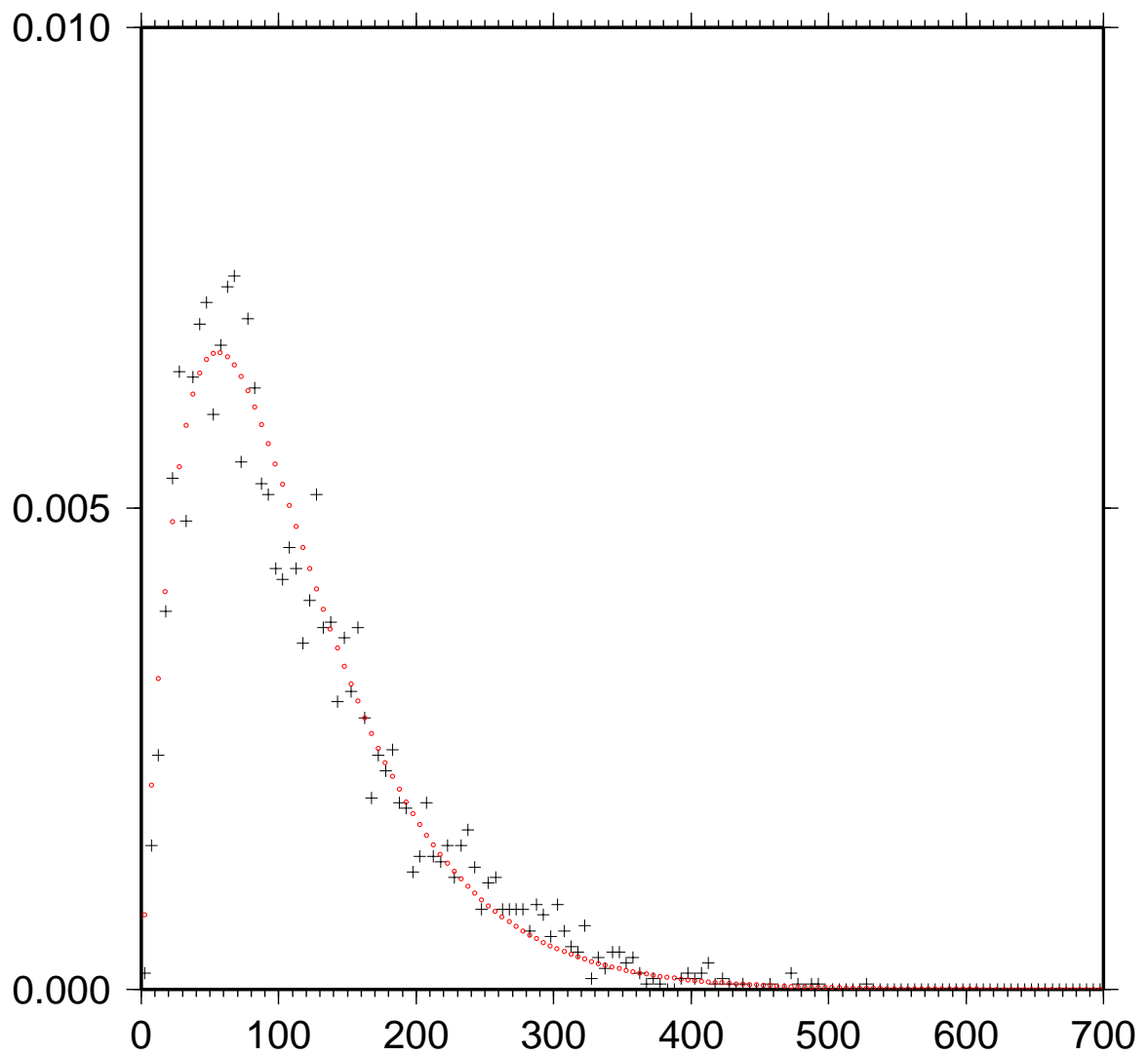
Figure A.4: Best fitting gamma distribution with $\delta = 2$ and $\lambda = 0.018$ (red circles) in comparison to distances of event pairs with correlation coeffients $cc \geq 0.93$ (black crosses); x-axis: inter-event-distance; y-axis: propability
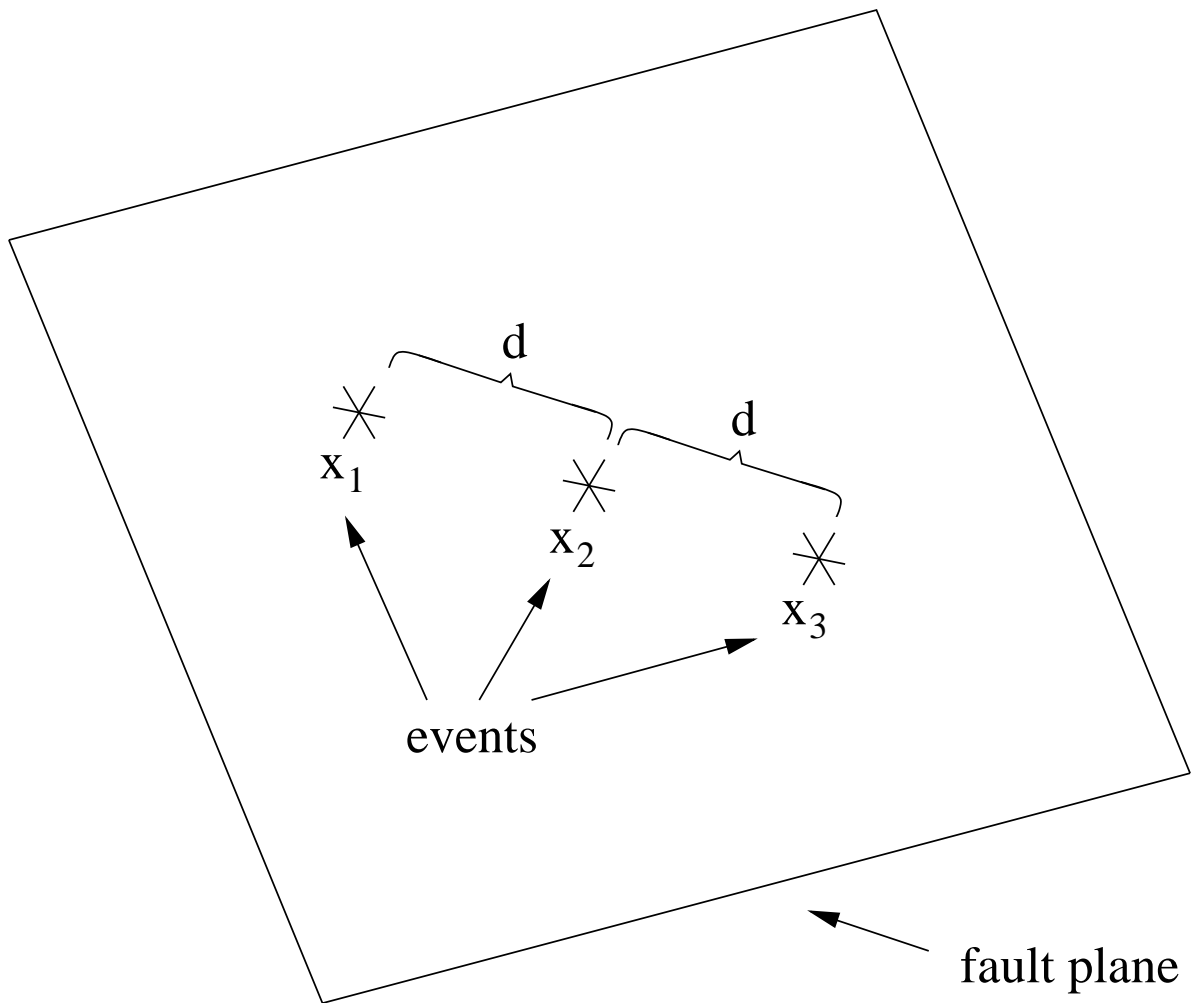
Figure A.5: Sketch of three aligned events on a common fault plane; the distance between events x_1 and x_2 / x_2 and x_3 is denoted by d

```
.
stNst-event-list stNst-Nev stNst-cc-P stNst-cc-S
atmP-filename
atmS-filename
ncm-filename
mncm-filename
concm-filename
ael-filename
sem-filename
sael-filename
saem-filename
```

- K, Ts, Tp, Tx, Ty are the threshold parameters

- Nst and Nev are the number of stations and the number of events, respecitvely

- event-list-filename contains a table with coarse origin time for all events (ID n DD.MM.YYYY hh:mm:ss.sss)

- stN-event-list contains a table with coarse P- and S-phase picks (ID n DD.MM.YYYY hh:mm:ss.sss hh:mm:ss.sss)

- st1-Nev, st1-cc-P, and st1-cc-S are the number of events at this station (also number of entries in stN-event-list),

A.3   Relocation

A.3.1   Generating `dt.cc`

The input file `dt.cc` can be created using the coherence analysis output matrices which contain the correlation coefficients and the relative shift times. The latter is converted to arrival time differences while the first serves as a source for appropriate weights. I developed the program `gendtcc` which performs this conversion and whose usage is described in the following paragraph and in table A.3.1 (`no.` and *ID* are the same for both the overall event list and the station event list).

```
output-filename
event-list-filename Nevents
phase
Mstations
station1 threshold1 event-list-filename1 nevents1 cc-filename1 dt-filename1
.
.
.
stationM thresholdM event-list-filenameM neventsM cc-filenameM dt-filenameM
```

The input file used in this work for the P-phase is as follows:

```
dt.ENZ.P.cc
```

output-filename	name of output file (hypoDD input file dt.cc)
event-list-filename	name of file containing a table: `ID no.  date origin-time`
Nevents	total number of events
phase	one of P or S
Mstations	number of stations
station1	station identifier
threshold1	minimum correlation coefficient threshold
event-list-filename1	name of file containing a table: `ID no.  date P-phase-pick S-phase-pick`
nevents1	number of events at this station
cc-filename1	name of matrix file containing correlation coefficients
dt-filename1	name of matrix file containing relative shift times

Table A.2: Description of `gendtcc` inputfile parameters

```
events/ev.all.mod.lst 712
P
8
NKC .8 events/ev.NKC.mod.lst    729 ../coma/cc.NKC.P.ENZ.mtx ../coma/tm.NKC.P.ENZ.mtx
KRC .7 events/ev.KRC.mod.lst    708 ../coma/cc.KRC.P.ENZ.mtx ../coma/tm.KRC.P.ENZ.mtx
KOC .8 events/ev.KOC.mod.lst    639 ../coma/cc.KOC.P.ENZ.mtx ../coma/tm.KOC.P.ENZ.mtx
LAC .85 events/ev.LAC.mod.lst   549 ../coma/cc.LAC.P.ENZ.mtx ../coma/tm.LAC.P.ENZ.mtx
SKC .65 events/ev.SKC.mod.lst   645 ../coma/cc.SKC.P.ENZ.mtx ../coma/tm.SKC.P.ENZ.mtx
TRC .75 events/ev.TRC.mod.lst   273 ../coma/cc.TRC.P.ENZ.mtx ../coma/tm.TRC.P.ENZ.mtx
SBC .8 events/ev.SBC.mod.lst    179 ../coma/cc.SBC.P.ENZ.mtx ../coma/tm.SBC.P.ENZ.mtx
ZHC .6 events/ev.ZHC.mod.lst    115 ../coma/cc.ZHC.P.ENZ.mtx ../coma/tm.ZHC.P.ENZ.mtx
```

A.3.2   Main hypoDD input file

Here I present the input file for the relocation using hypoDD. Some fields need explanation since they differ from the suggestion of the authors of hypoDD . See table table A.3 for details. The iteration setup is explained below the hypoDD.input listing together with some comments on the resulting iteration output from hypoDD.

```
*--- input file selection
* cross correlation diff times:
dt.cc
*catalog P diff times:
../dt.mod.ct
*
* event file:
../event.mod.dat
*
* station file:
../station.dat
*
*--- output file selection
* original locations:
```

```
hypoDD.loc
* relocations:
hypoDD.reloc
* station information:
hypoDD.sta
* residual information:
hypoDD.res
* source paramater information:
hypoDD.src
*
*--- data type selection:
* IDAT:  0 = synthetics; 1= cross corr; 2= catalog; 3= cross & cat
* IPHA: 1= P; 2= S; 3= P&S
* DIST:max dist [km] between cluster centroid and station
* IDAT   IPHA   DIST
    3      3     400
*
*--- event clustering:
* OBSCC:    min # of obs/pair for crosstime data (0= no clustering)
* OBSCT:    min # of obs/pair for network data (0= no clustering)
* OBSCC  OBSCT
     4       4
*
*--- solution control:
* ISTART:   1 = from single source; 2 = from network sources
* ISOLV: 1 = SVD, 2=lsqr
* NSET:       number of sets of iteration with specifications following
*  ISTART  ISOLV  NSET
     2        2       5
*
*--- data weighting and re-weighting:
* NITER:  last iteration to used the following weights
* WTCCP, WTCCS: weight cross P, S
* WTCTP, WTCTS: weight catalog P, S
* WRCC, WRCT: residual threshold in sec for cross, catalog data
* WDCC, WDCT:   max dist [km] between cross, catalog linked pairs
* DAMP:     damping (for lsqr only)
*        ---  CROSS DATA ------ ----CATALOG DATA ----
* NITER WTCCP WTCCS WRCC WDCC WTCTP WTCTS WRCT WDCT DAMP
* Parameter vom 09.08.2006
   2     0.01  0.01  -9   -9    1.0   0.5    -9   -9  120
   2     0.01  0.01  -9   -9    1.0   0.5     6    4  120
   3     0.8   1.0   -9   -9    0.01  0.005   6    4  150
   5     0.8   1.0    6    2    0.01  0.005   6    4  160
   5     0.8   1.0    6   .3    0.01  0.005   6    4  140
*--- 1D model:
* NLAY: number of model layers
* RATIO: vp/vs ratio
* TOP: depths of top of layer (km)
* VEL:  layer velocities (km/s)
```

```
* NLAY   RATIO
   10      1.67
* TOP
0.0   0.2   0.53  1.0   2.0   4.0   6.0  10.0   20.0   32.0
* VEL
4.305 5.05  5.325 5.585 5.86  6.07  6.345 6.745 7.07    8
*
*--- event selection:
* CID:  cluster to be relocated (0 = all)
* ID: cuspids of event to be relocated (8 per line)
* CID
   1
* ID
```

A.3.3   Running hypoDD

The iteration configuration first adjusts the locations using arrival time differences only from the catalogue data. Then the criteria become more restricted resulting in some outliers to be eliminated. Then the cross correlation arrival time differences are also taken into account. Becoming more restricted in the criteria, more and more outliers are deleted. In the end 11 percent of the catalogue arrival time differences and 36 percent of the cross correlation measurements have been eliminated.

```
starting hypoDD (v1.1 - 10/2004)...          Fri Sep  8 15:56:55 2006
INPUT FILES:
cross dtime data: dt.cc
catalog dtime data: ../dt.mod.ct
events: ../event.mod.dat
stations: ../station.dat
OUTPUT FILES:
initial locations: hypoDD.loc
relocated events: hypoDD.reloc
event pair residuals: hypoDD.res
station residuals: hypoDD.sta
source parameters: hypoDD.src
 Relocate cluster number  1
 Relocate all events
Reading data ...   Fri Sep  8 15:56:55 2006
# events =   733
# stations < maxdist =      10
# cross corr P dtimes =   17338 (no OTC for      0 event pairs)
# cross corr S dtimes =   99351 (no OTC for      0 event pairs)
# catalog P dtimes =   68140
# catalog S dtimes =   66523
# dtimes total =   251352
# events after dtime match =        731
# stations =      10
clustering ...
Clustered events:   730
Isolated events:      1
```

parameter	value	comment
OBSCC	4	also weakly linked pairs are desired because only few stations are available
OBSCT	4	dito
ISTART	2	there already are good locations so use these to start from
ISOLV	2	since the numver of events is quite large, SVD is not usable
NSET	5	five iteration settings needed to smoothly converge to the minimum location error

Table A.3: Explanation of hypoDD parameters

```
# clusters:    3
Cluster  1:   726 events
Cluster  2:     2 events
Cluster  3:     2 events


RELOCATION OF CLUSTER: 1     Fri Sep  8 15:57:02 2006
----------------------
Reading data ...   Fri Sep  8 15:57:02 2006
# events =   726
# stations < maxdist =      10
# cross corr P dtimes =   17281 (no OTC for      0 event pairs)
# cross corr S dtimes =   98957 (no OTC for      0 event pairs)
# catalog P dtimes =   68131
# catalog S dtimes =   66514
# dtimes total =   250883
# events after dtime match =        726
# stations =      10
Initial trial sources =   726
```

IT	EV	CT	CC	RMSCT		RMSCC		RMSST	DX	DY	DZ	DT	OS	AQ	CND
	%	%	%	ms	%	ms	%	ms	m	m	m	ms	m		
1	1	100	100	100	19	-82.3	47	-59.3	56	79	86	122	40	15	0	69
2	2	100	100	100	16	-14.9	36	-22.0	45	28	20	53	8	21	0	67
3	3	100	99	100	9	-41.4	34	-7.7	42	17	14	22	3	23	0	69
4	4	100	97	100	8	-15.7	32	-3.6	41	11	9	13	2	25	0	65
5	5	100	95	100	51	539.2	6	-80.7	64	58	51	41	7	46	0	74
6	6	100	90	100	13	-74.6	5	-12.7	25	12	16	11	2	42	0	71
7	7	100	89	100	11	-12.8	5	-4.2	25	6	7	6	1	41	0	67
8	8	100	89	94	11	-2.7	1	-82.9	18	4	4	2	0	42	0	76
9	9	100	89	90	11	-0.9	1	-35.6	18	2	2	1	0	41	0	73
10	10	100	89	89	11	-0.1	0	-16.6	18	1	1	1	0	41	0	72
11	11	100	89	88	11	0.0	0	-8.3	18	1	1	1	0	41	0	71
12	12	100	89	87	11	0.0	0	-5.0	18	1	1	0	0	41	0	70
13	13	99	89	65	11	-1.3	0	12.0	18	3	3	2	0	42	0	80
14	14	99	89	65	11	-0.6	0	-2.7	18	2	2	1	0	41	0	76
15	15	99	89	65	11	-0.6	0	-2.7	18	2	1	1	0	42	0	77
16	16	99	89	65	11	-0.4	0	-2.1	18	2	1	1	0	41	0	75
17	17	99	89	64	10	-0.3	0	-1.5	18	1	1	1	0	41	0	74

```
writing out results ...
```

parameter	default	description
title	no title	descriptive title that will show up in the output file
evid	evid.sw1997.mod.txt	name of file containing an event table: `ID no.`
evst	evst.sw1997.mod.txt	name of file containing a station table (see below)
result	result.sw1997.mod.txt	result from `autoamp`
masmom	masmom.sw1997.mod.txt	reference (master) moment tensor file
out	relref.inp	name of output file

Table A.4: Description of `gen.relref.inp.awk` input parameters

A.4 Moment tensor inversion

In this section the usage of the `AWK` script `gen.relref.inp.awk` is explained. Its behaviour is controlled via variables that can be given via the command line `-v <variable=value>` mechanism of `AWK` and are explained in table A.4.

The format of the input files is as follows:

```
# input files:
# - evid.sw1997.mod.txt (from ev.all.mod.lst)
#   1) event id
# - evst.sw1997.mod.txt (modified from hypoDD.src)
#   1) station name
#   2) station no.
#   3) event id
#   4) distance ???
#   5) azimuth from event to station
#   6) takeoff angle for fastest ray
# - result.sw1997.mod.txt (from autoamp)
#   1) station name
#   2) component (P, R, T, E, N)
#   3) template event id
#   4) event id
#   5) CC
# - masmom.sw1997.mod.txt
#   1) event id
#   2) 0 (internal format of columns 3-8 for relref)
#   3-8) m11,...,m33
#   9)Mr
```

A.5 Inversion for homogeneous stress fields

A.5.1 Right dihedra method

The method has been implemented by Ramsay and Lisle (2000) in a BASIC program. For my thesis, I translated the code to C due to the lack of a BASIC interpreter.

columns	field description
1-3	event location
4-6	focal mechanism (strike, dip, rake)
7-8	azimuth and plunge of P-axis
9-10	azimuth and plunge of T-axis
11	fault plane selector

A.5.2 Energy based approach

The program `stressinv4` implements the homogeneous stress inversion approach of Dahm and Plene-fisch (2001). Its input file is organised as a table consisting of seven columns: the first three are not used yet (reserved for the event's location), columns 4-6 contain strike, dip, and rake of the event's focal mechanism, and, finally, column seven is used to select the fault plane from the two nodal planes indicated by the focal mechanism: 0 - unknown (will be tested for), 1 - plane given by focal mechanism (same strike and dip), 2 - other nodal plane.

A.6 Inhomogeneous stress inversion

The inversion for the locally inhomogeneous stress field utilises the method of source volume segmentation described in 2.1. For the necessary homogeneous stress inversion, the previously mentioned energy based approach of Dahm and Plenefisch (2001) has been used.

Practically, a set of `BASH` scripts has been set up to automate the inversion process. All necessary information is gathered into one single input file which is then subdivided according to the location information provided within. The organisation of this input file is described in table A.6. The angles for the definition of the focal mechanism and P- and T-axis are defined according to Aki and Richards (1980). The fault plane selector is defined as in the previous section A.5.2. An input file of a specific data set should reside in a separate directory to prevent confusion with other datasets, since output files are named in a common manner.

To simplify the processing, the script `svs.sh` has been designed to collect all necessary information at a common place and to run the scripts that actually perform the processing (like the stress inversion itself or plotting of the results) from a central instance.

The first script that is invoked is called `dosi4.sh` and its usage is given in the following paragraph. Its purpose is to subdivide the dataset according to the selected number of slices in each direction of euclidean space and the postition of the single events. The script may be run in different flavours by selecting different sets of

```
dosi4.sh - invert for homogeneous stress field in boxes of configurable size
depending on output of hypoDD and relref
usage: dosi4.sh [options]
options are:
-e name - input: name of events file (locations, fault, PT-axes)
-d name - output: name of directory to put misc. files into (def. .)
-i name - output: stub of dirname for stressinv4 input (def. si4inp)
-o name - output: stub of dirname for stressinv4 output (def. si4out)
-x boxes - number of boxes in x-direction (def. 7)
-y boxes - number of boxes in y-direction (def. 7)
```

```
-z boxes - number of boxes in z-direction (def. 7)
-D xmin,xmax,ymin,ymax,zmin,zmax - force hypocentre volume
-t thp - threshold for number of events per box (def. 10)
-a - decide to use the awka compilation instead of plain awk
-s - data is synthetic (influences plotting preparation)
-v - switch to verbose mode
-m mode - select one of the following modes (def. c):
        c - constant volume (all boxes have the same volume)
        g - growing volume (boxes may have different vol.)
        n - nearest neighbors (boxes usually have different vol.)
-h - print this help
```

The results obtained by `dosi4.sh` can be visualised by using the script `plot.stress.sh` which is described in the following paragraph. Its output is a set of encapsulated PostScript graphics that reside in the datasets root directory. They are stored in a subdirectory called `plot.T.XX.YY.ZZ`, where `T` denotes the mode of operation and is most commonly named `c`. `XX`, `YY`, and `ZZ` denote the number of slices in the appropriate direction.

```
plot.stress.sh - plot stress orientations for z-slices
usage: plot.stress.sh [options]
options are:
-i name - input: stub of dirname for stressinv4 input (def. si4inp)
-o name - input: stub of dirname for stressinv4 output (def. si4out)
-d name - in/output: dir where misc. files are/for plots (def. .)
-x boxes - number of boxes in x-direction (def. 7)
-y boxes - number of boxes in y-direction (def. 7)
-z boxes - number of boxes in z-direction (def. 7)
-t thp - threshold for number of events per box (def. 10)
-s - data is synthetic (stress axes instead of PT-axes are plotted)
-b - plot a boundary with tick-marks around the slices
-p - plot with perspective
-v - switch to verbose mode
-m mode - select one of the following modes:
        c - constant volume (all boxes have the same volume)
        g - growing volume (boxes may have different vol.)
        n - nearest neighbors (boxes usually have different vol.)
-h - print this help
```

Finally, the results can be summarised in a LaTeX document using the script `mk.stress-plot-tex.sh`. By its invocation, a PostScript file named by the dataset and the mode of operation is generated: `D.T.ps`, wher `D` is the dataset name and `T` denotes the mode.

```
mk.stress-plot-tex.sh - generate and compile LaTeX overview of SVS results
usage: sh mk.stress-plot-tex.sh [options]
-t texout - name of LaTex output file
-d name - input: dir where plots are (def. .)
-m mode - select one of the following modes:
        c - constant volume (all boxes have the same volume)
```

```
        g - growing volume (boxes may have different vol.)
        n - nearest neighbors (boxes usually have different vol.)
-f - output figures only, but no complete document
-h - print this help
```

Appendix B

Correlation coefficient histograms

The following figures show histograms of the correlation coefficients obtained for events of the 1997 Vogtland/NW-Bohemia swarm recorded at at least four stations of the local seismic network WEBNET (Horálek et al., 2000, see introduction, also). For each station five different combinations of the three component recordings have been used for either P- and S-phase: a) E-, b) N-, c) Z-, d) E- and N-, e) all E-, N-, and Z-components. The resulting histogram is presented in a classical fashion where the histogram bins are arranged from -1 to $+1$ and, secondly, as an overlay plot of the histogram part showing negative correlation coefficients abobe the part showing the positive ones. Doing so, a decision where to put the appropriate thresholds for the coherence analysis is supported.

Many histograms do not show the expected tail to positive correlation coefficients. This effect is obvious no matter what kind of filter and which cutoff frequencies are chosen. The calculation has been tried using either an acausal bandpass and a infinite impulse response butterworth bandpass and frequency bands from $2, 4, 6 Hz$ to $14, 20, 25, 30 Hz$. As in no setup a tail was visible for all stations I chose the butterworth bandpass with cutoff frequencies of $4 Hz$ and $30 Hz$, because this filter yields the best result regarding tail visibility.
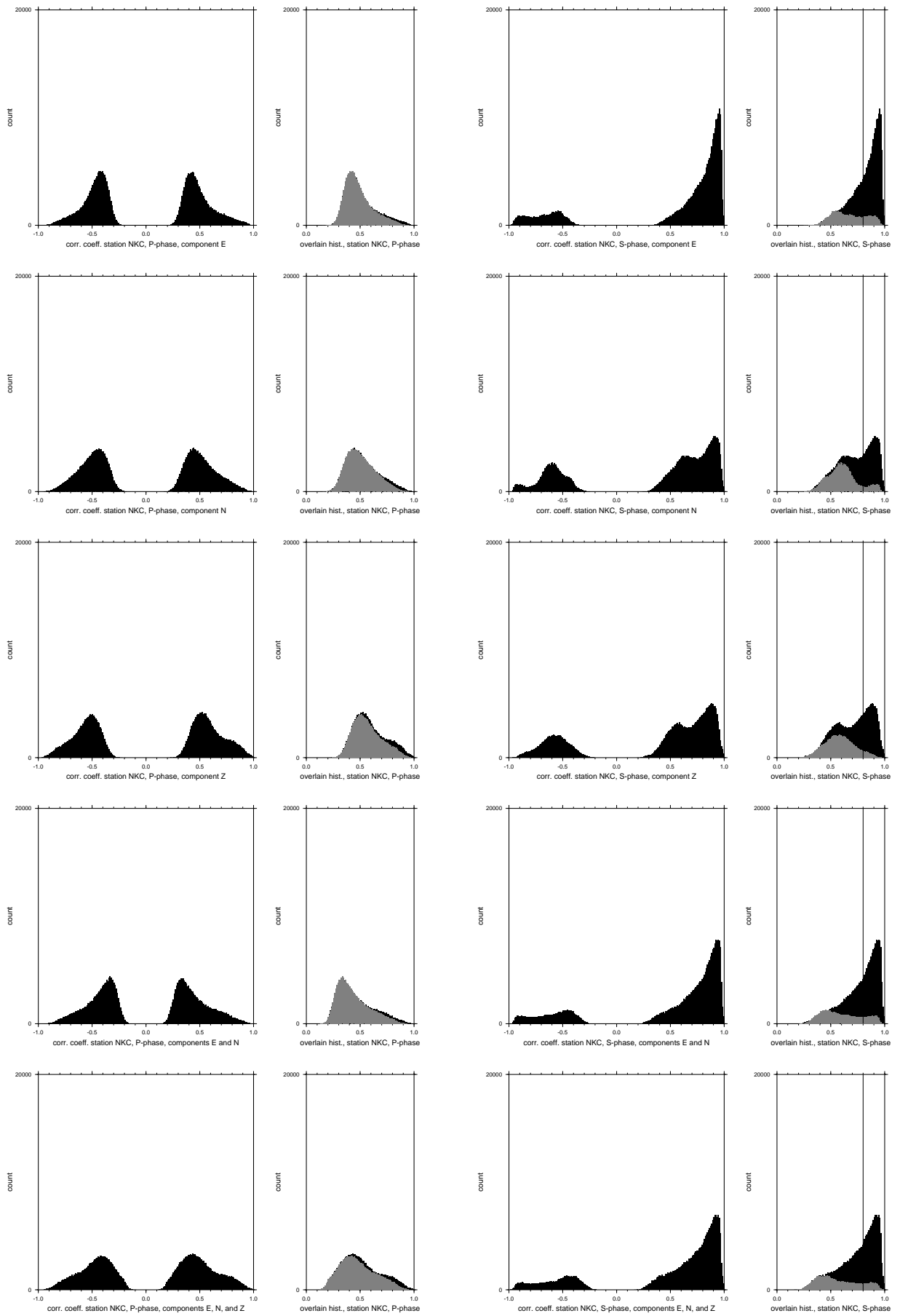
Figure B.1: Histograms of correlation coefficients for station NKC
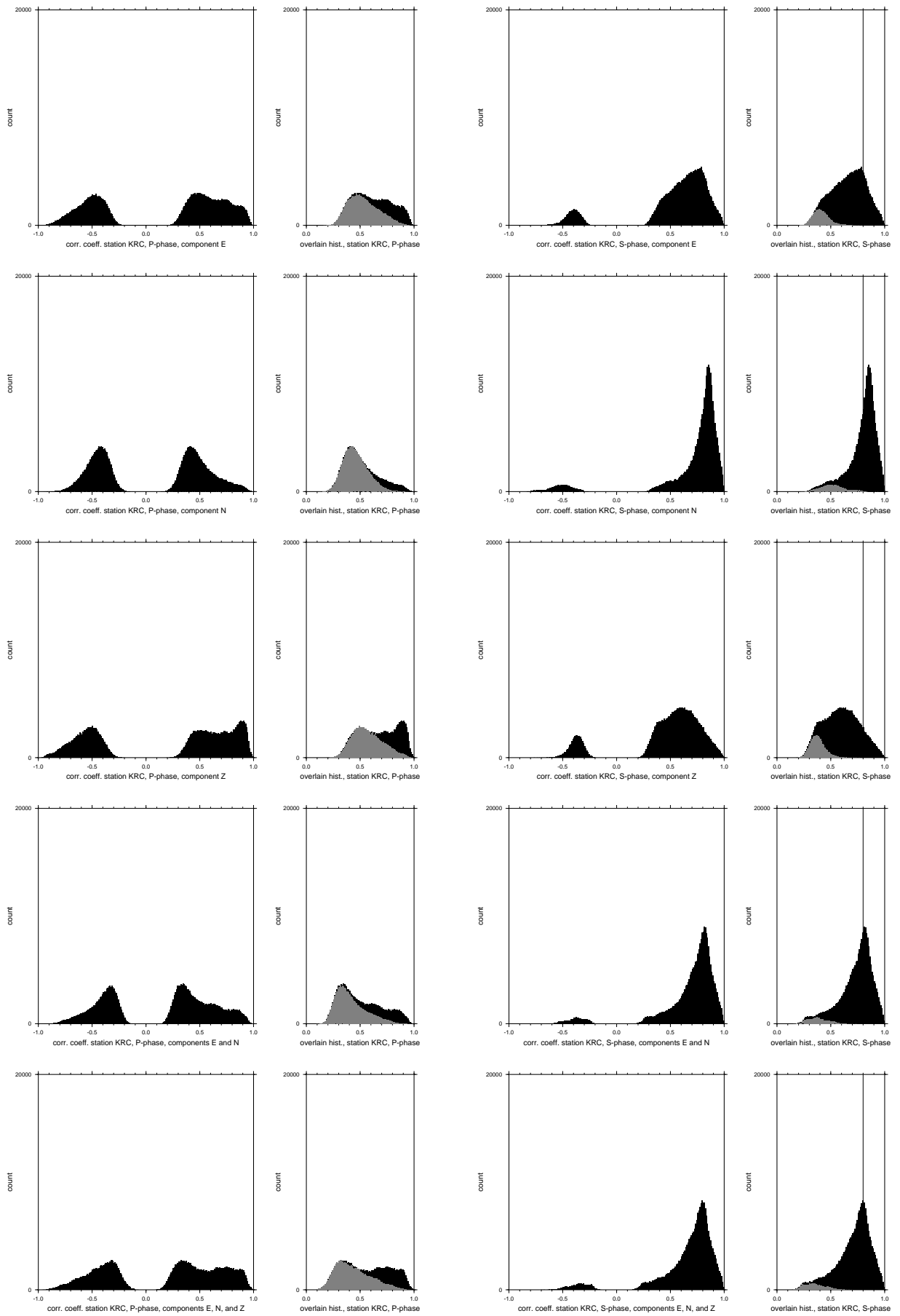
Figure B.2: Histograms of correlation coefficients for station KRC
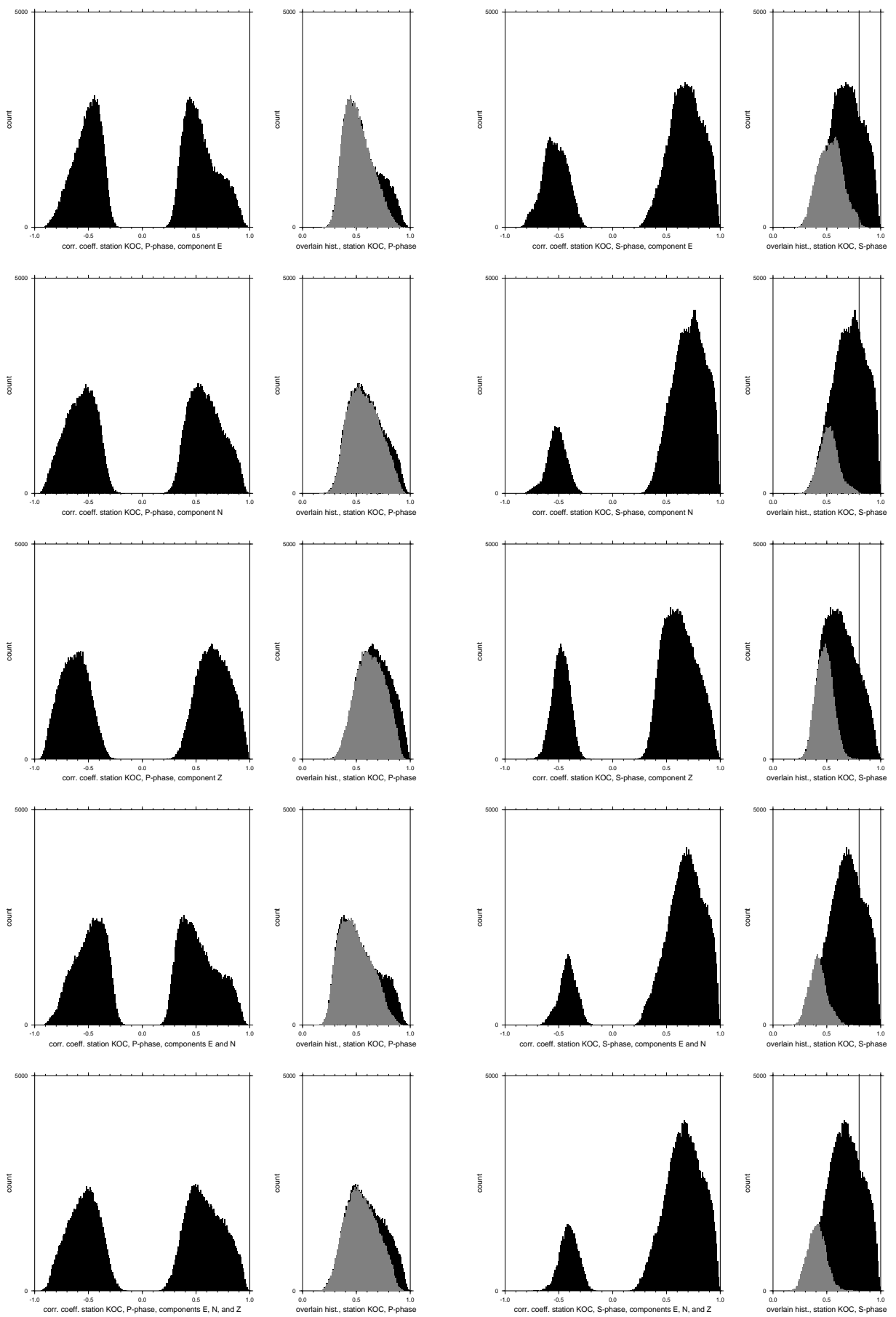
Figure B.3: Histograms of correlation coefficients for station KOC
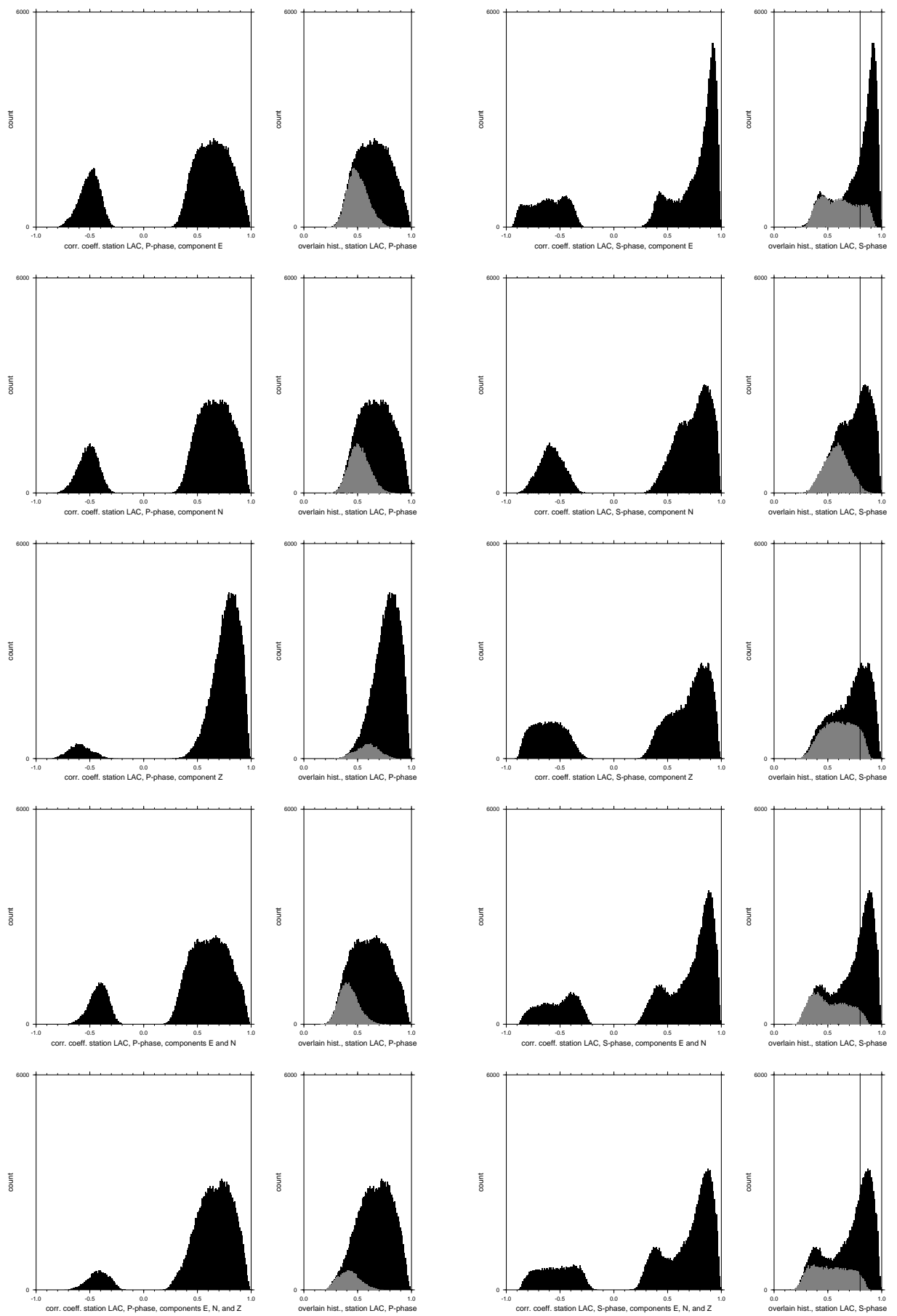
Figure B.4: Histograms of correlation coefficients for station LAC
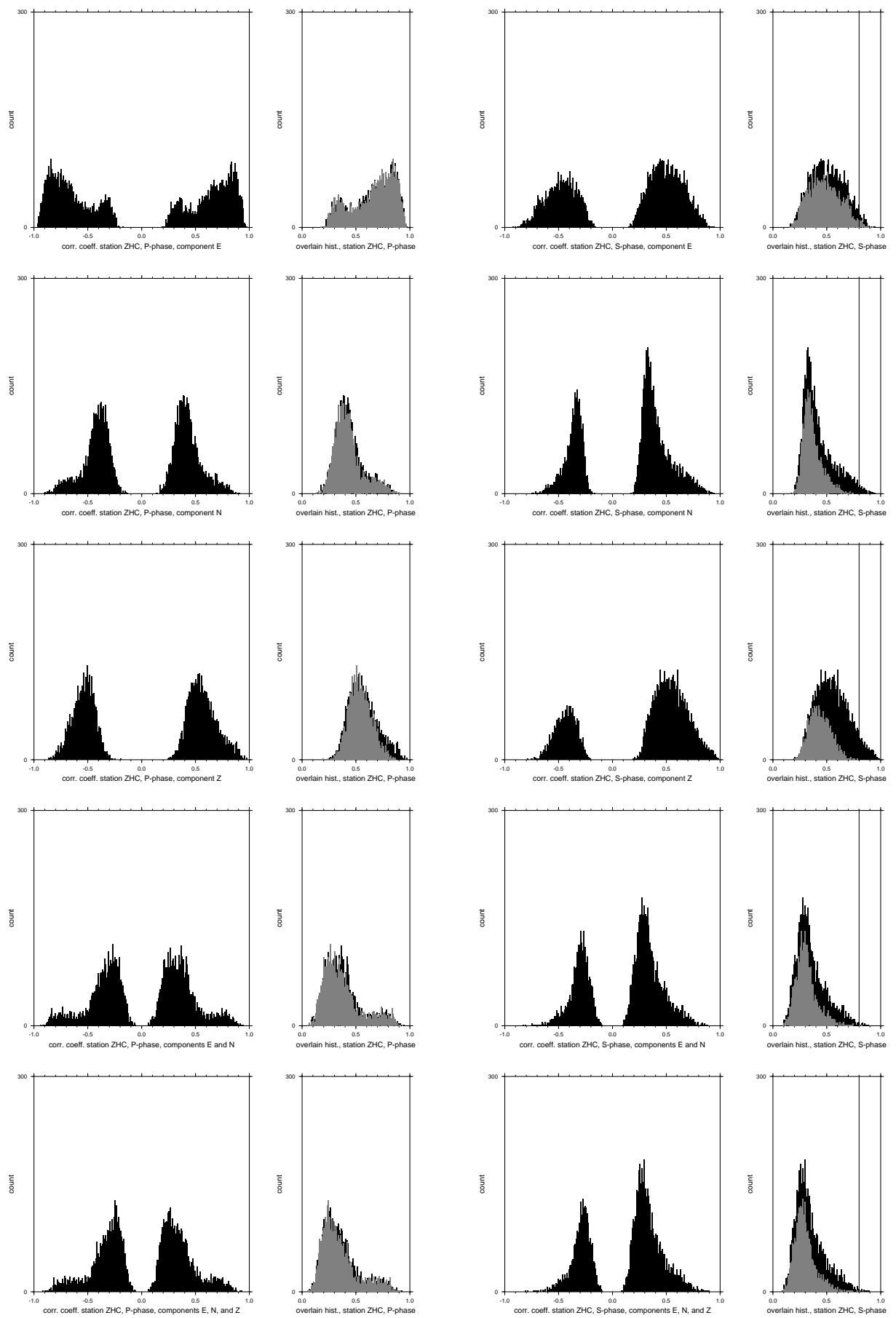
Figure B.5: Histograms of correlation coefficients for station ZHC
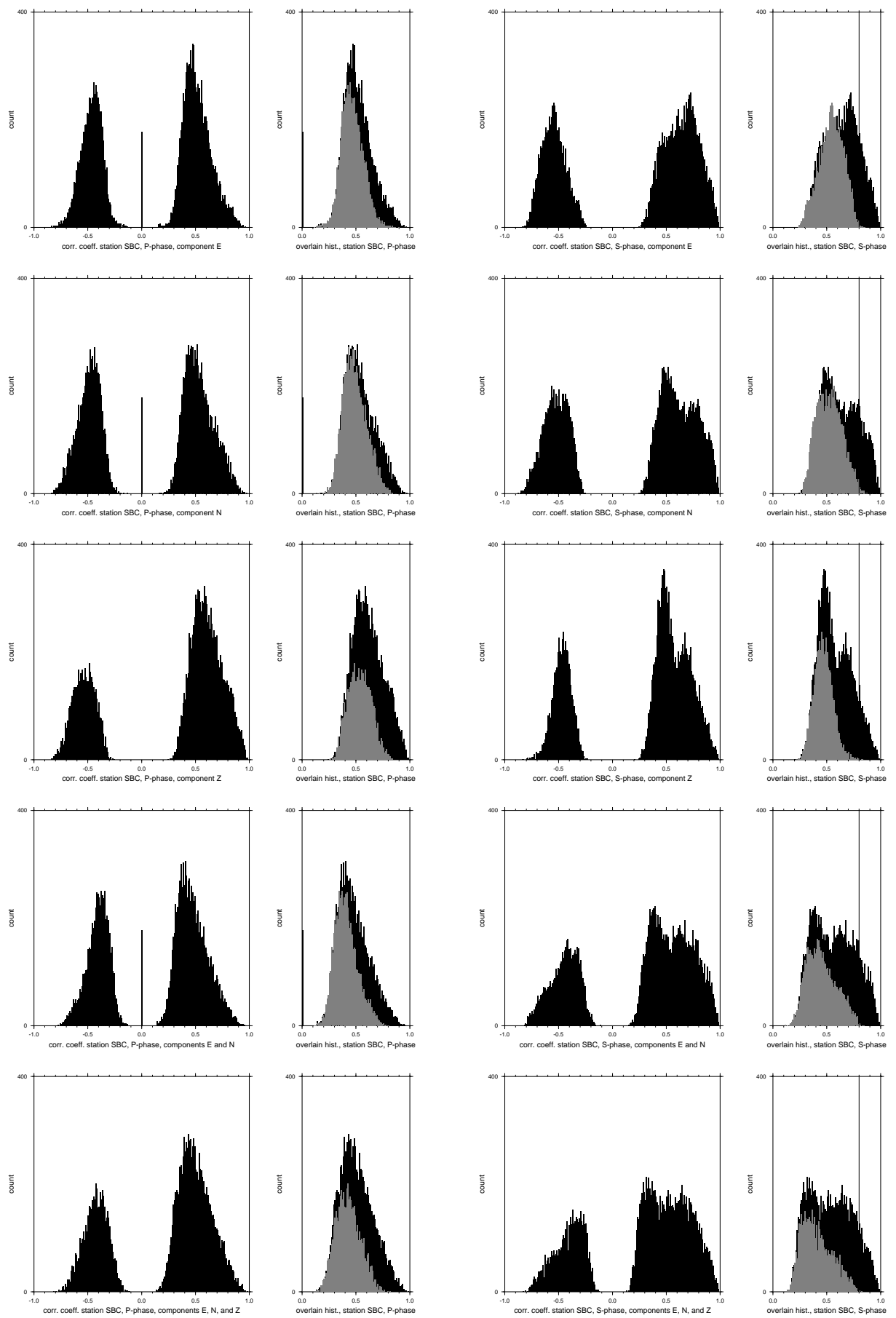
Figure B.6: Histograms of correlation coefficients for station SBC
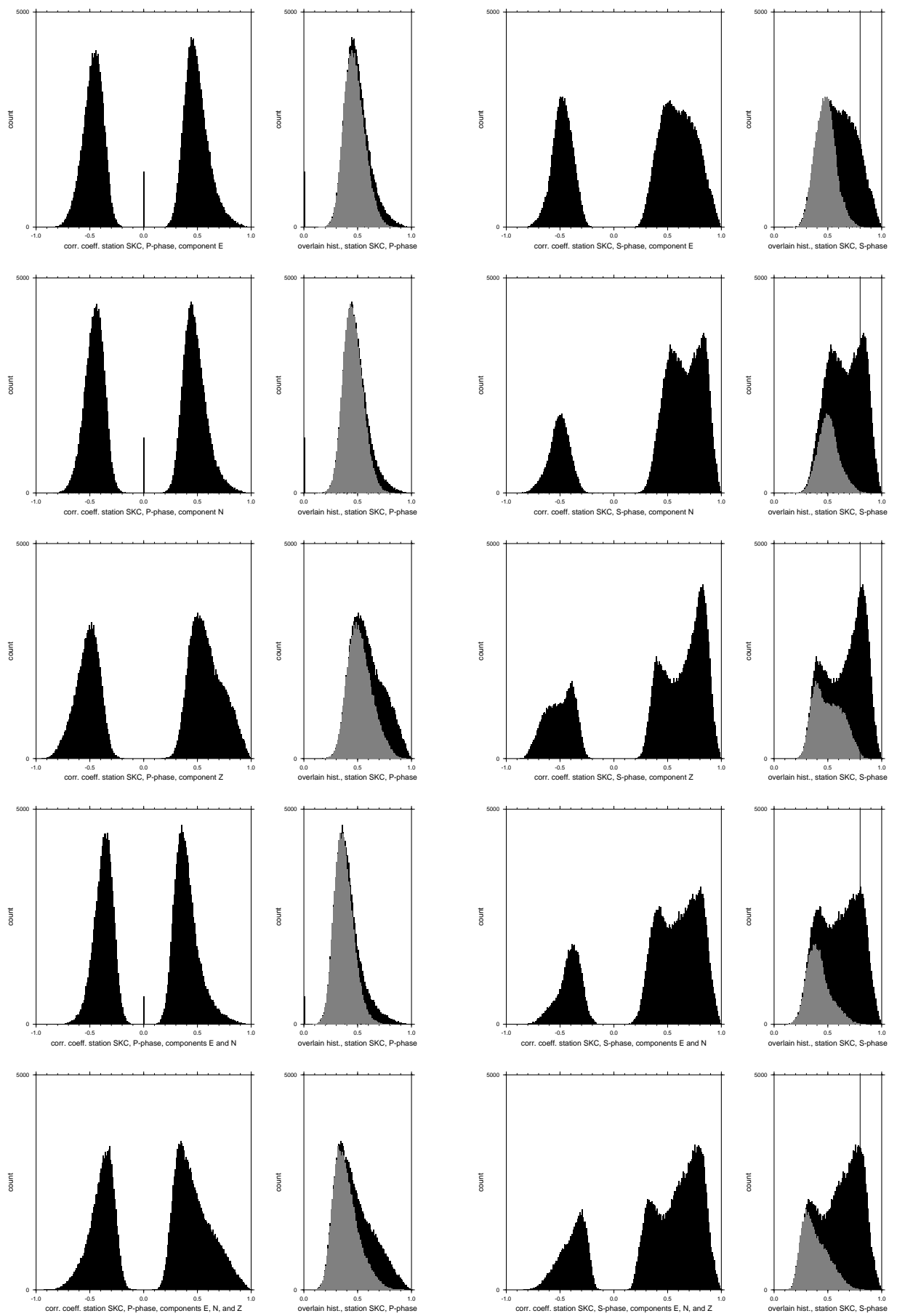
Figure B.7: Histograms of correlation coefficients for station SKC
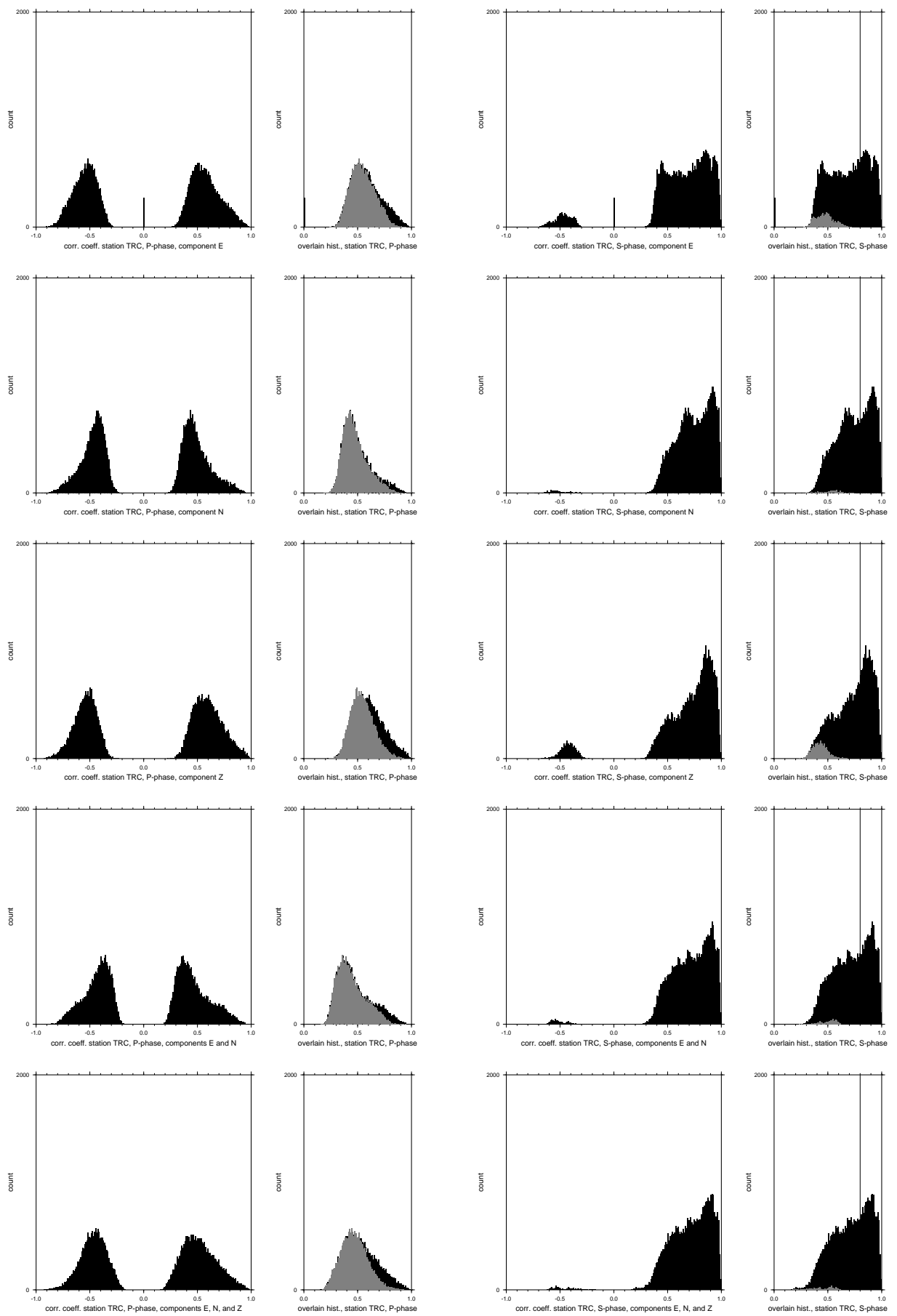
Figure B.8: Histograms of correlation coefficients for station TRC
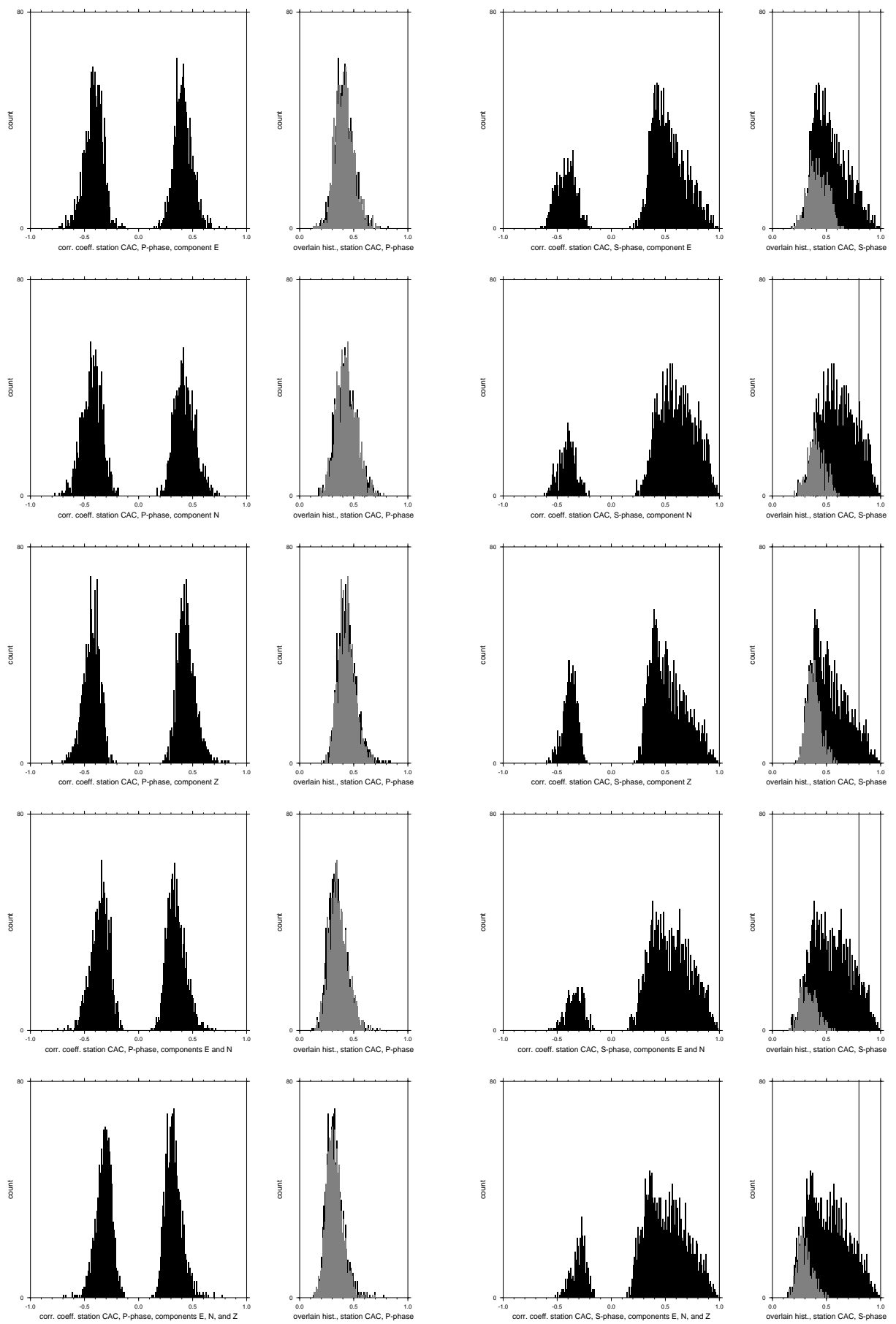
Figure B.9: Histograms of correlation coefficients for station CAC
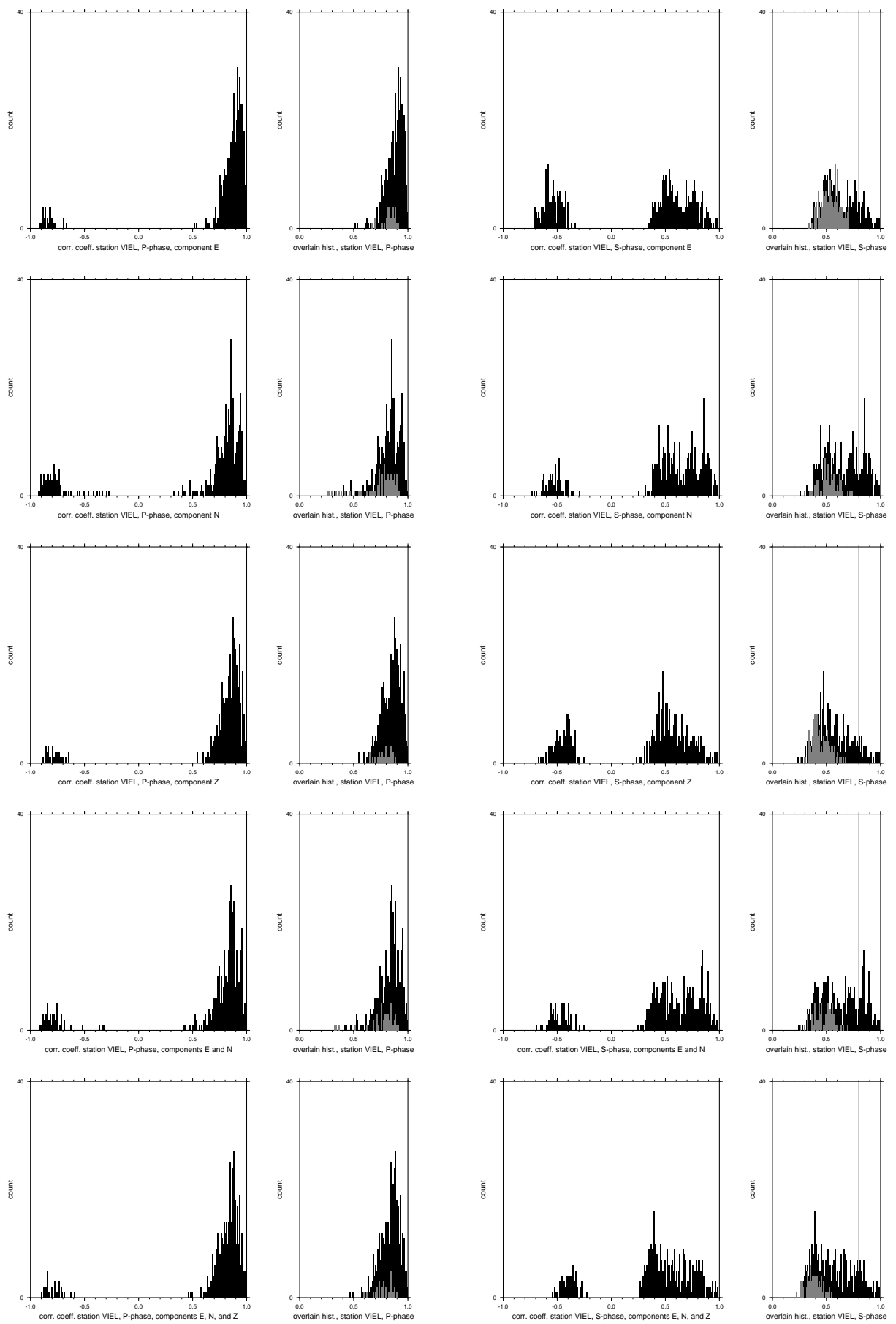
Figure B.10: Histograms of correlation coefficients for station VIEL

Appendix C

Automatically generated amplitude picks

This appendix shows the automatically generated picks that have been estimated using the method described in 2.3.1. First the P-phase picks are shown and the second part covers the S-phase picks. The seismograms have been filtered with an infinite impulse response 4-30 Hz butterworth filter. For the P-phase, first a row containing an overlay plot of all seismograms that belong to one multiplet followed by a row containing a mean seismogram. The selected time window is $\pm .5s$ around the manual P-pick of the template event. For the S-phase, first the overlay plots of the E- and N-component of the 3 component seismogram are shown, followed by the appropriate mean seismograms. The time window has been selected $-.2/+.8s$ around the S-pick of the appropriate template event. Vertical dashes indicate the pick position.

M189___KOC_shZ_A_P.gse (111) - 31 events

M717___KOC_shZ_A_P.gse (606) - 167 events

M189___KOC_shZ_A_P.gse (111) - mean of 31 events

M717___KOC_shZ_A_P.gse (606) - mean of 167 events

M212___KRC_shZ_B_P.gse (139) - 300 events

M177___KRC_shZ_A_P.gse (99) - 35 events

M212___KRC_shZ_B_P.gse (139) - mean of 300 events

M177___KRC_shZ_A_P.gse (99) - mean of 35 events

M132___LAC_shZ_A_P.gse (60) - 165 events

M716___NKC_shZ_A_P.gse (605) - 23 events

M132___LAC_shZ_A_P.gse (60) - mean of 165 events

M716___NKC_shZ_A_P.gse (605) - mean of 23 events

M848___NKC_shZ_A_P.gse (719) - 162 events

M84___SKC_shZ_A_P.gse (31) - 175 events

M848___NKC_shZ_A_P.gse (719) - mean of 162 events

M84___SKC_shZ_A_P.gse (31) - mean of 175 events

Figure C.1: Automatic picks for P-phase (1 of 2)

M89___SKC_shZ_A_P.gse (32) - 21 events

M619___TRC_shZ_A_P.gse (497) - 29 events

M89___SKC_shZ_A_P.gse (32) - mean of 21 events

M619___TRC_shZ_A_P.gse (497) - mean of 29 events

M717___TRC_shZ_A_P.gse (606) - 43 events

M630___ZHC_shZ_A_P.gse (509) - 38 events

M717___TRC_shZ_A_P.gse (606) - mean of 43 events

M630___ZHC_shZ_A_P.gse (509) - mean of 38 events

M46___ZHC_shZ_A_P.gse (9) - 54 events

M46___ZHC_shZ_A_P.gse (9) - mean of 54 events

Figure C.2: Automatic picks for P-phase (2 of 2)

Figure C.3: Automatic picks for S-phase (1 of 7)

M848___KOC_shE_A_S.gse (719) - 28 events

M861___KOC_shE_C_S.gse (728) - 133 events

M848___KOC_shN_A_S.gse (719) - 28 events

M861___KOC_shN_C_S.gse (728) - 133 events

M848___KOC_shE_A_S.gse (719) - mean of 28 events

M861___KOC_shE_C_S.gse (728) - mean of 133 events

M848___KOC_shN_A_S.gse (719) - mean of 28 events

M861___KOC_shN_C_S.gse (728) - mean of 133 events

M429___KRC_shE_A_S.gse (351) - 415 events

M684___KRC_shE_A_S.gse (571) - 20 events

M429___KRC_shN_A_S.gse (351) - 415 events

M684___KRC_shN_A_S.gse (571) - 20 events

M429___KRC_shE_A_S.gse (351) - mean of 415 events

M684___KRC_shE_A_S.gse (571) - mean of 20 events

M429___KRC_shN_A_S.gse (351) - mean of 415 events

M684___KRC_shN_A_S.gse (571) - mean of 20 events

Figure C.4: Automatic picks for S-phase (2 of 7)
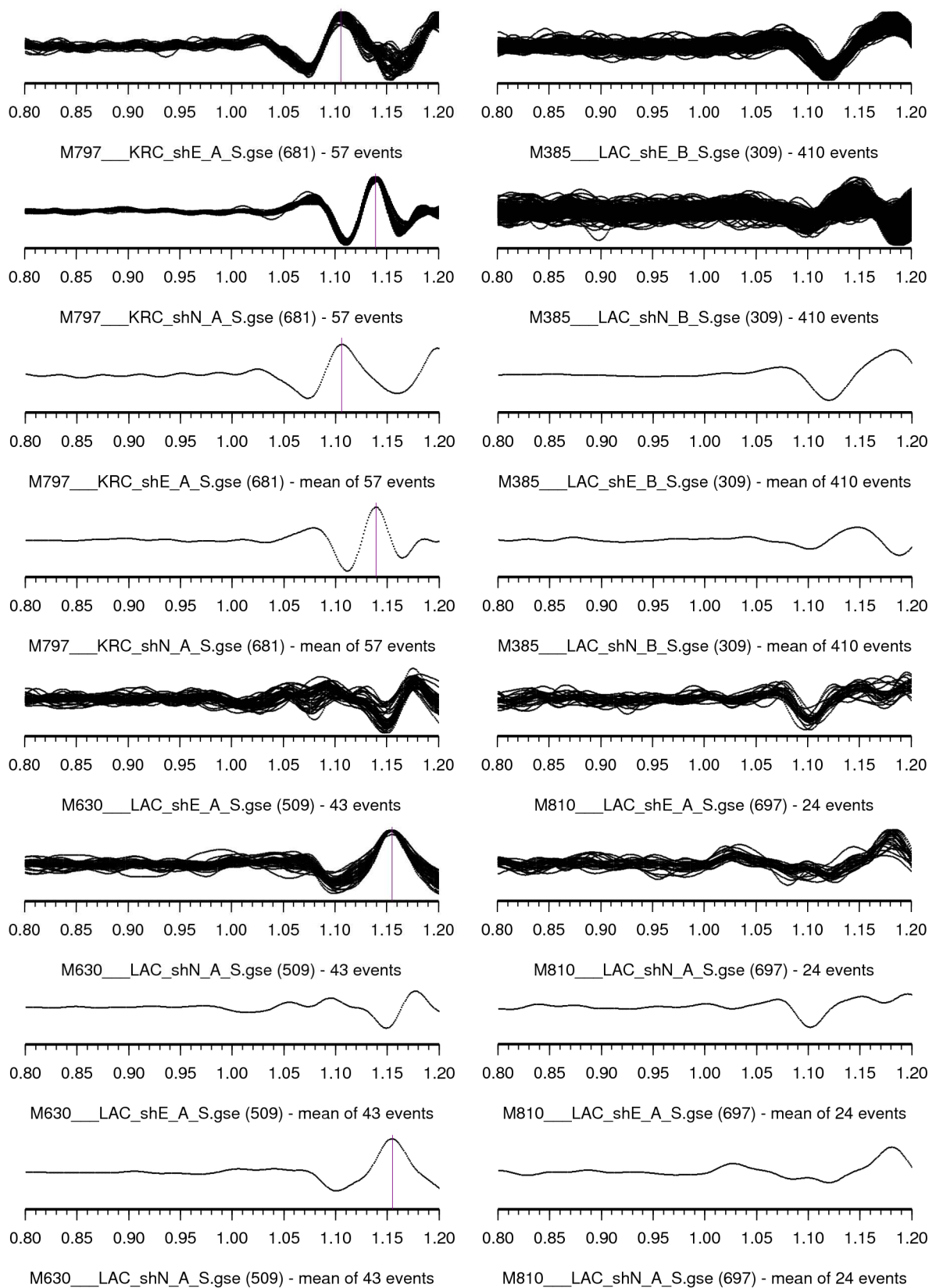
Figure C.5: Automatic picks for S-phase (3 of 7)

M186___NKC_shE_A_S.gse (108) - 65 events

M253___NKC_shE_A_S.gse (180) - 466 events

M186___NKC_shN_A_S.gse (108) - 65 events

M253___NKC_shN_A_S.gse (180) - 466 events

M186___NKC_shE_A_S.gse (108) - mean of 65 events

M253___NKC_shE_A_S.gse (180) - mean of 466 events

M186___NKC_shN_A_S.gse (108) - mean of 65 events

M253___NKC_shN_A_S.gse (180) - mean of 466 events

M634___NKC_shE_A_S.gse (513) - 106 events

M669___SBC_shE_A_S.gse (555) - 24 events

M634___NKC_shN_A_S.gse (513) - 106 events

M669___SBC_shN_A_S.gse (555) - 24 events

M634___NKC_shE_A_S.gse (513) - mean of 106 events

M669___SBC_shE_A_S.gse (555) - mean of 24 events

M634___NKC_shN_A_S.gse (513) - mean of 106 events

M669___SBC_shN_A_S.gse (555) - mean of 24 events

Figure C.6: Automatic picks for S-phase (4 of 7)

M718___SBC_shE_A_S.gse (607) - 49 events

M769___SBC_shE_A_S.gse (655) - 50 events

M718___SBC_shN_A_S.gse (607) - 49 events

M769___SBC_shN_A_S.gse (655) - 50 events

M718___SBC_shE_A_S.gse (607) - mean of 49 events

M769___SBC_shE_A_S.gse (655) - mean of 50 events

M718___SBC_shN_A_S.gse (607) - mean of 49 events

M769___SBC_shN_A_S.gse (655) - mean of 50 events

M337___SKC_shE_A_S.gse (254) - 93 events

M466___SKC_shE_A_S.gse (394) - 52 events

M337___SKC_shN_A_S.gse (254) - 93 events

M466___SKC_shN_A_S.gse (394) - 52 events

M337___SKC_shE_A_S.gse (254) - mean of 93 events

M466___SKC_shE_A_S.gse (394) - mean of 52 events

M337___SKC_shN_A_S.gse (254) - mean of 93 events

M466___SKC_shN_A_S.gse (394) - mean of 52 events

Figure C.7: Automatic picks for S-phase (5 of 7)

Figure C.8: Automatic picks for S-phase (6 of 7)

M810___TRC_shE_A_S.gse (697) - 24 events

M470___ZHC_shE_A_S.gse (398) - 25 events

M810___TRC_shN_A_S.gse (697) - 24 events

M470___ZHC_shN_A_S.gse (398) - 25 events

M810___TRC_shE_A_S.gse (697) - mean of 24 events

M470___ZHC_shE_A_S.gse (398) - mean of 25 events

M810___TRC_shN_A_S.gse (697) - mean of 24 events

M470___ZHC_shN_A_S.gse (398) - mean of 25 events

M46___ZHC_shE_A_S.gse (9) - 54 events

M46___ZHC_shN_A_S.gse (9) - 54 events

M46___ZHC_shE_A_S.gse (9) - mean of 54 events

M46___ZHC_shN_A_S.gse (9) - mean of 54 events

Figure C.9: Automatic picks for S-phase (7 of 7)

Appendix D

Application of source volume segmentation

Five synthtetic tests to analyse the source volume segmentation technique are presented in section D.1. Section D.2 covers the inversion of the relative moment tensor data from section 3.1.3. Finally, focal mechanism data from the KTB hydraulic fracturing experiment, 2000 are analysed in section D.3 and D.4.

D.1 Synthetic tests

The stability of the source-volume-segmentation (SVS) technique has been tested in five synthetic scenarios that differ in the distribution of hypocentres, the orientation of fault planes, and the type of underlying stress field. The tests are set up as a series that become more complex until a scenario is described that approximates the Vogtland/NW-Bohemia swarm, 1997. The procedure begins with the random generation of fault planes. Then slip for the appropriate stress field is calculated in the form of a pure double-couple moment tensors by the forward method of Dahm and Plenefisch (2001). Last, the data is analysed by means of the SVS method with at least 10 events per box. Table D.1 shows the parameters of the tests and the results are shown in sections D.1.1 through D.1.4.

test name	hypocentre distribution	fault distribution	type of stress field
synth-0	equally	equally	homogeneous
synth-1	equally	gaussian around one major fault	homogeneous
synth-2	equally	equally	rotating with depth
synth-3	equally	gaussian around two major faults	rotating with depth

Table D.1: Synthetic test cases for SVS

D.1.1 Test 0
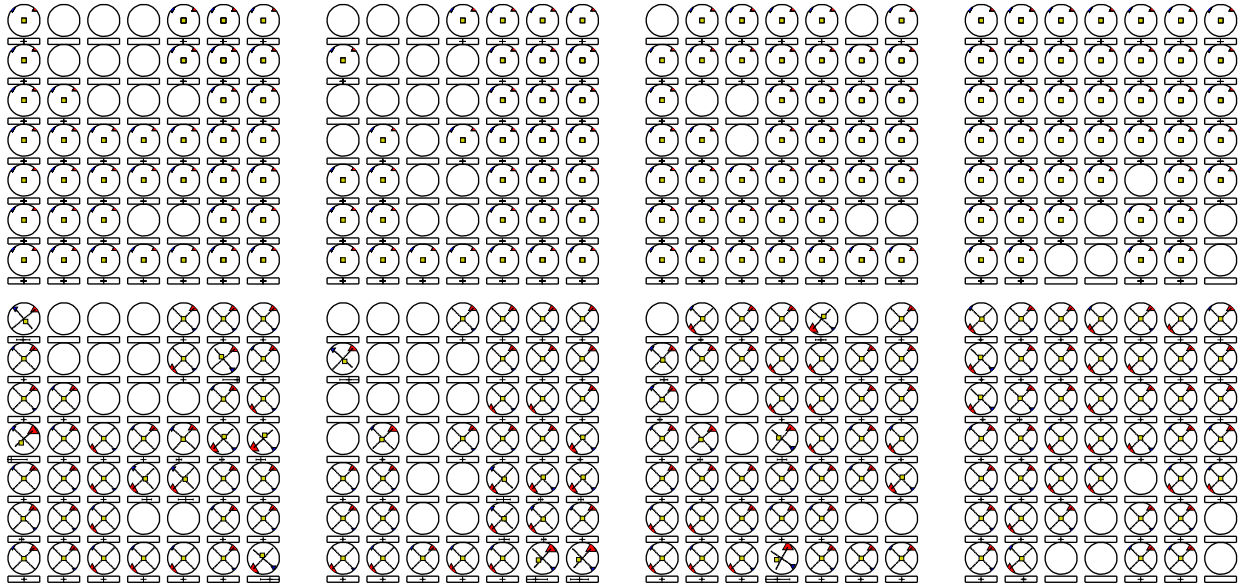
Figure D.1: synthetic test 0, 7 slices, z-slices 1, 2, 3, 4
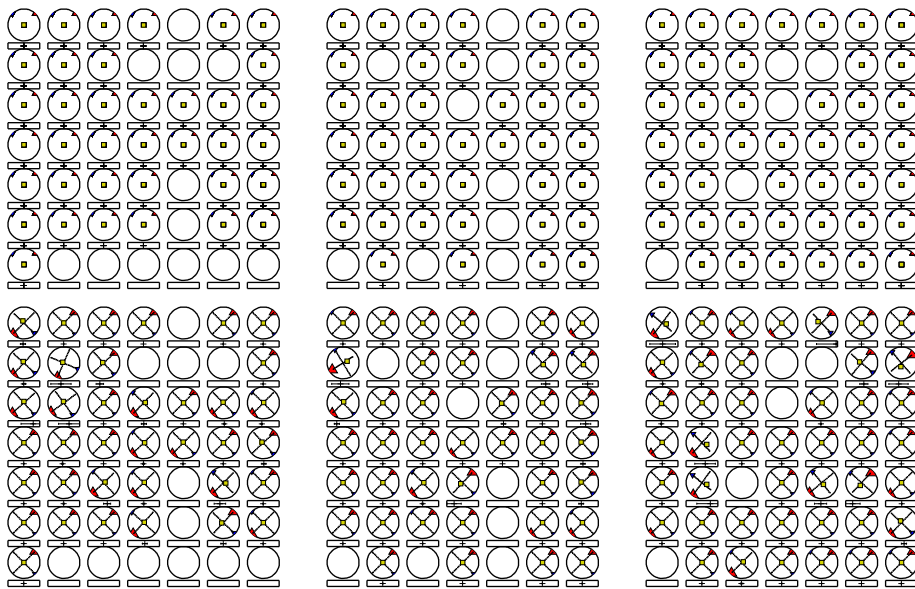
Figure D.2: synthetic test 0, 7 slices, z-slices 5, 6, 7

D.1.2 Test 1
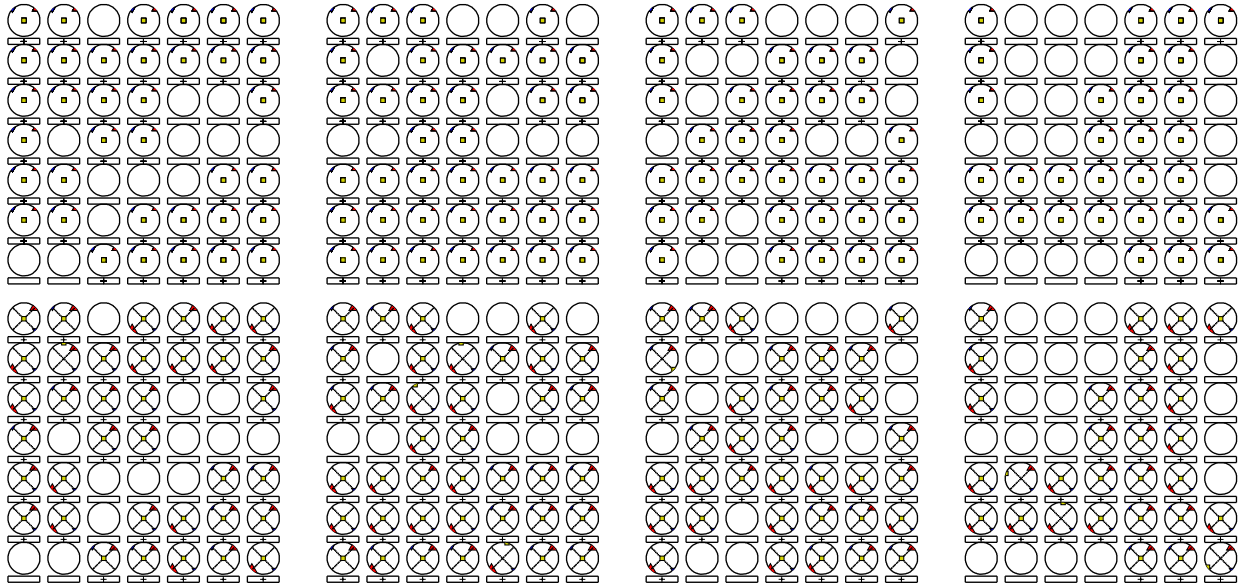
Figure D.3: synthetic test 1, 7 slices, z-slices 1, 2, 3, 4
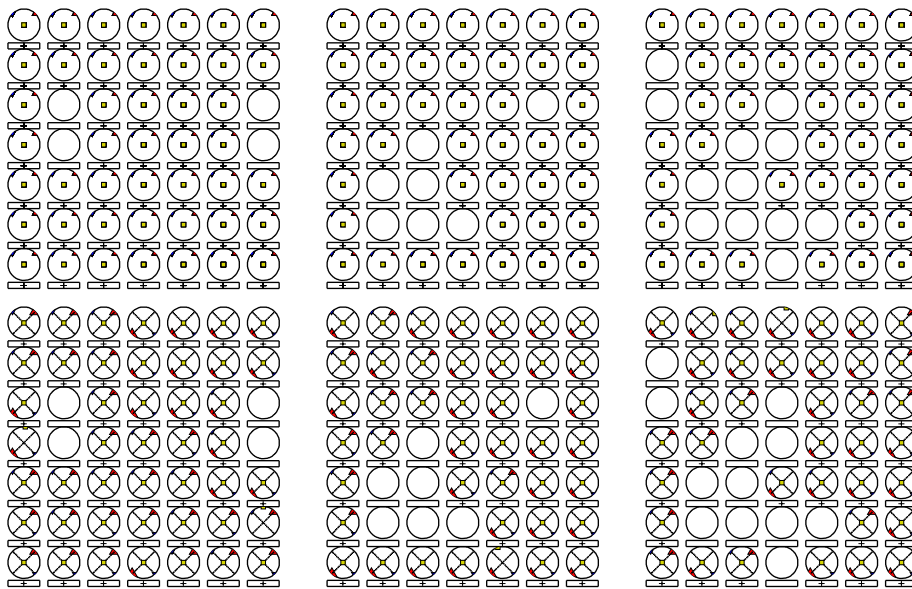
Figure D.4: synthetic test 1, 7 slices, z-slices 5, 6, 7

D.1.3 Test 2
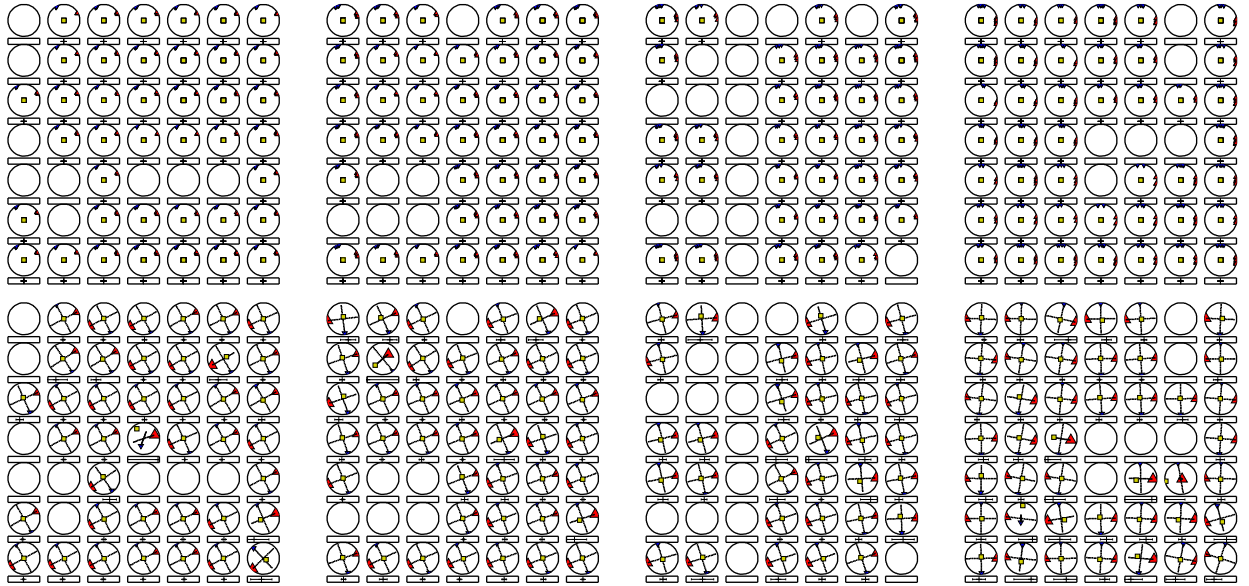
Figure D.5: synthetic test 2, 7 slices, z-slices 1, 2, 3, 4
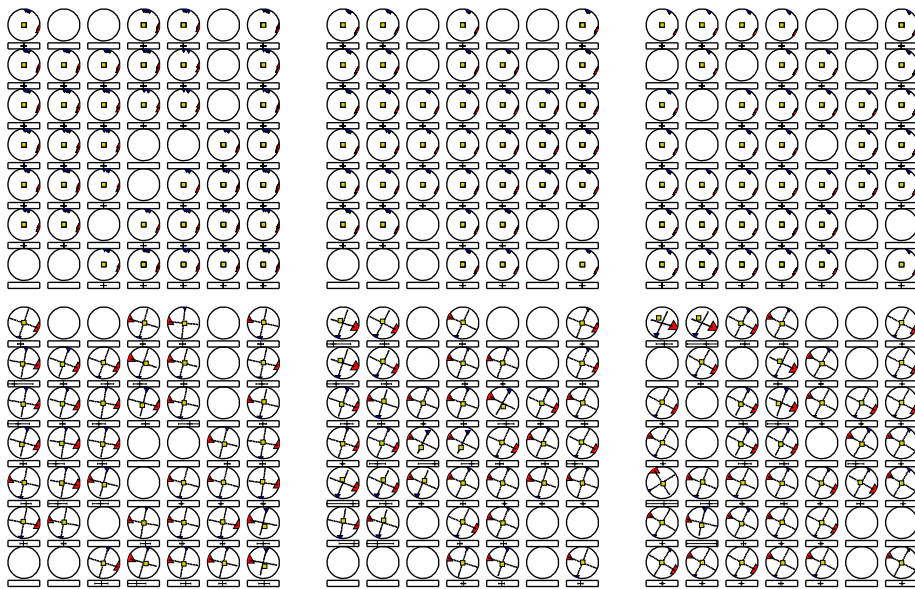
Figure D.6: synthetic test 2, 7 slices, z-slices 5, 6, 7

D.1.4   Test 3
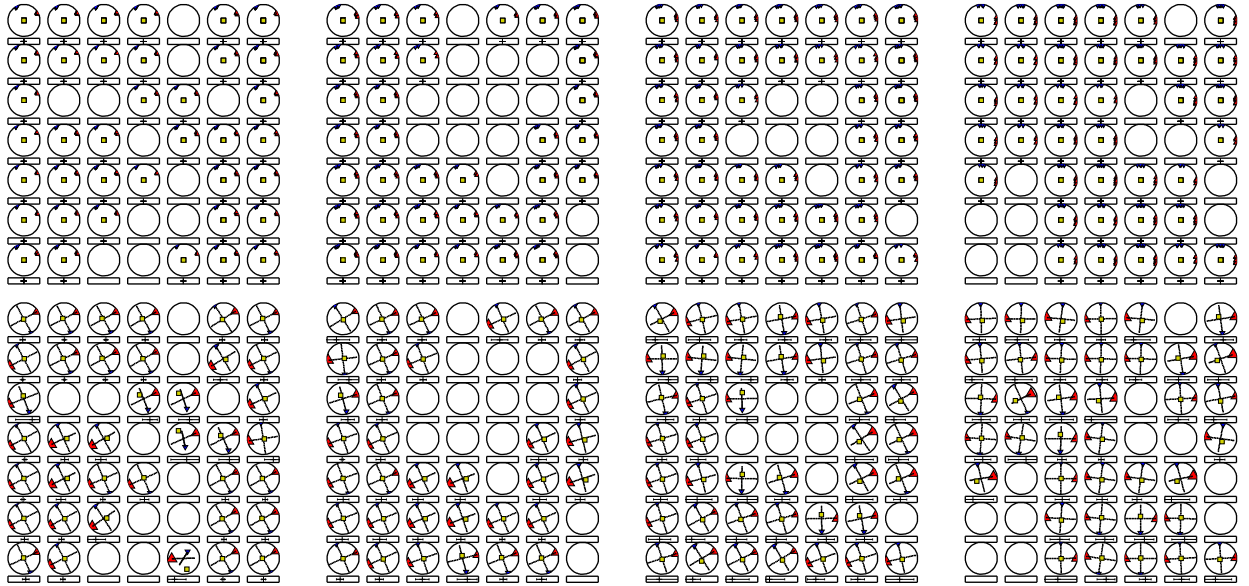
Figure D.7: synthetic test 3, 7 slices, z-slices 1, 2, 3, 4
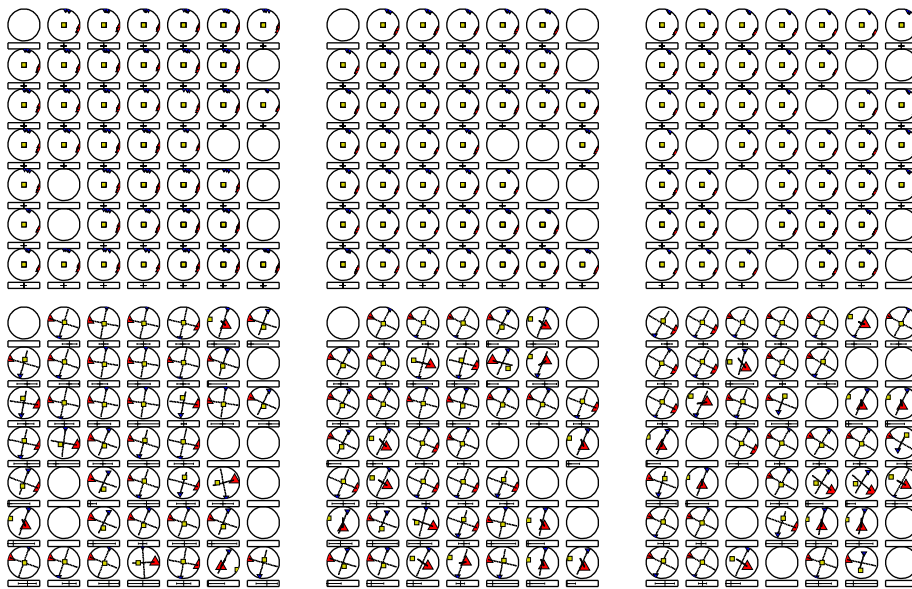
Figure D.8: synthetic test 3, 7 slices, z-slices 5, 6, 7

D.2   The 1997 swarm
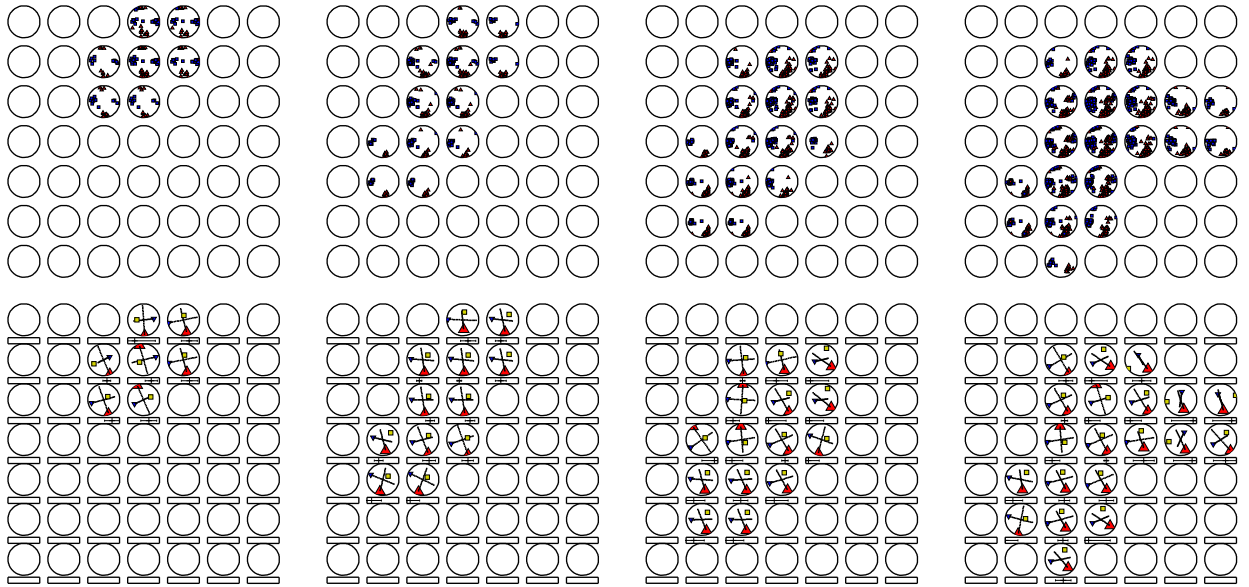
Figure D.9: 1997 swarm, 7 slices, z-slices 1, 2, 3, 4
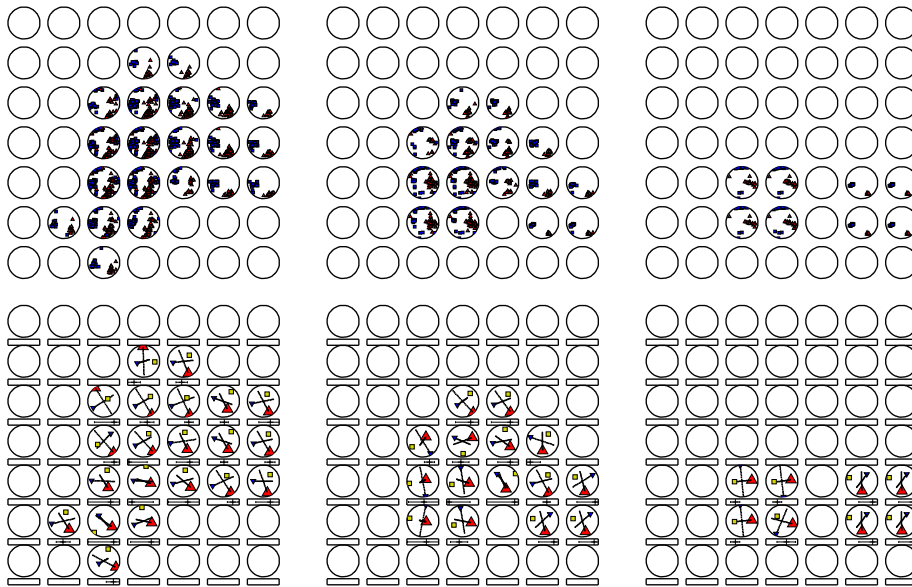
Figure D.10: 1997 swarm,7 slices, z-slices 5, 6, 7

D.3 KTB hydraulic fracturing experiment 2000, upper part ($z > -6000m$)
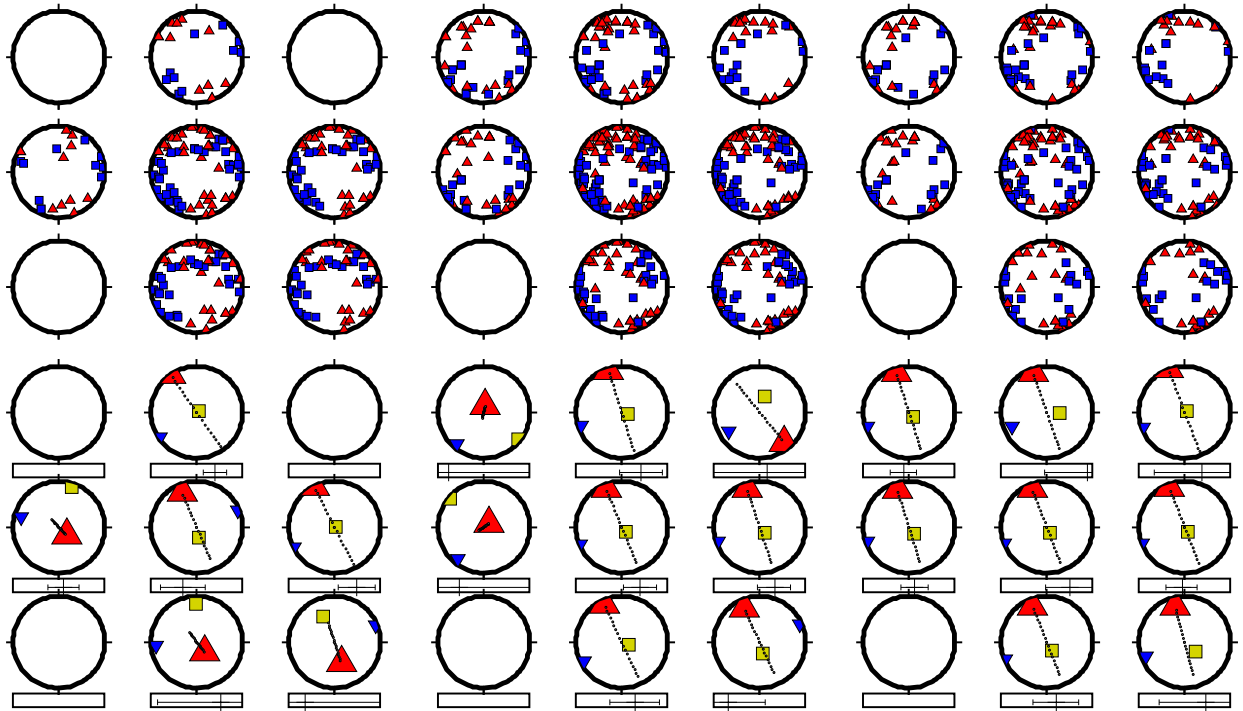
Figure D.11: dataset "KTB-hi", 3 slices, z-slices 1-3
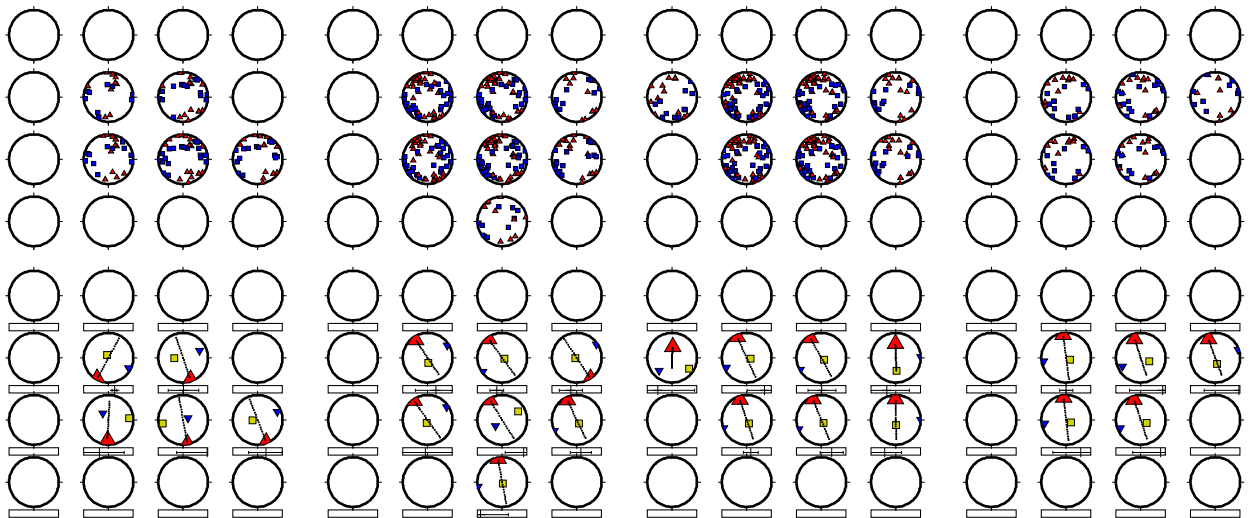
Figure D.12: dataset "KTB-hi", 4 slices, z-slices 1-4

D.4 KTB hydraulic fracturing experiment 2000, lower part ($z < -6000m$)
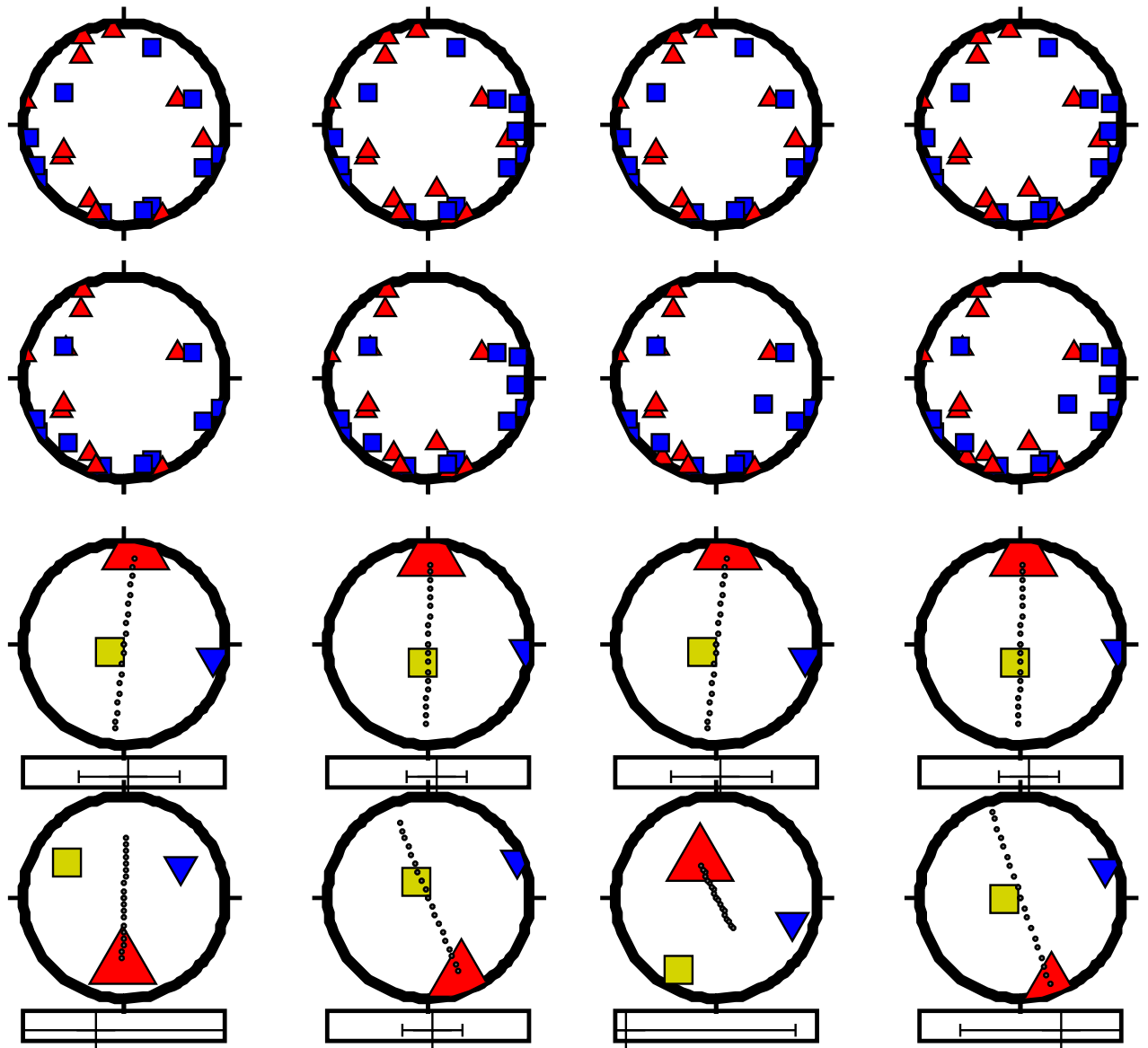
Figure D.13: dataset "KTB-lo", 2 slices, z-slice 1, 2

Appendix E

NURBS basics

E.1 B-spline curves

In graphics manipulation and painting programs, the standard method to create smooth curvatures is the use of Bézier curves. These are continuous functions which weight and sum a set of control points to define the shape of a curve. They have the very undesirable property to tend to polynomials of high degree if a curve needs to be bent strong locally. This is the motivation for the development of B-spline curves which are a generalisation of Bézier curves. One of the most important properties of B-spline curves is locality which means that control points affect only their local surroundings. Therefore the degree of a polynomial must not be very high to produce high curvatures.

$$N_{i,0}(u) = \begin{cases} 1 & \text{if } u_i \leq u < u_{i+1} \text{ and } u_i < u_{i+1} \\ 0 & \text{otherwise} \end{cases}$$

$$N_{i,p}(u) = \frac{u - u_i}{u_{i+p} - u_i} N_{i,p-1}(u) + \frac{u_{i+p+1} - u}{u_{i+p+1} - u_{i+1}} N_{i+1,p-1}(u)$$

(E.1)

The basic concept to accomplish locality is the use of basis functions, that are non-zero only on a certain interval. A given domain $[u_0, u_m]$ is subdivided into one or more intervals by a set of $m + 1$ non-decreasing numbers $u_0 \leq u_1 \leq \ldots \leq u_m$. The u_i are called knots, the ordered $m + 1$-tuple $U = (u_0, u_1, \ldots, u_m)$ is called the knot vector and the half-open interval $[u_i, u_{i+1})$ the i-th knot span. In the case that some u_i are equal, the appropriate knot spans may not exist. If a knot u_i appears k times (i.e., $u_i = u_{i+1} = \ldots = u_{i+k-1}$), where $k > 1$, u_i is a multiple knot of multiplicity k. Otherwise, if u_i appears only once, it is a simple knot. If the knots are equally spaced (i.e., $u_{i+1} - u_i$ is a constant for $0 \leq i \leq m - 1$), the knot vector or the knot sequence is said uniform; otherwise, it is non-uniform. The knots between the (usually multiple) knots u_0 and u_m are called internal knots. Eq. E.1 defines the B-spline basis functions where p is the degree and $0 \leq i \leq m - 1 - p$ denotes the i-th basis function. Figure E.1 shows basis functions for degrees $p = 0 \ldots 4$ and knot vectors defined in eq. E.2 with $m - 2(p + 1) + 1 = 5$ internal knots (the reason for selecting a multiplicity of $k = p + 1$ is given in the later in this section).

$$U = (\ \underbrace{0, \ldots, 0}_{p+1 \text{ times}}, u_{p+1}, \ldots, u_{m-p-1}, \underbrace{1, \ldots, 1}_{p+1 \text{ times}}\ )$$

(E.2)

Several important properties can be derived easily:
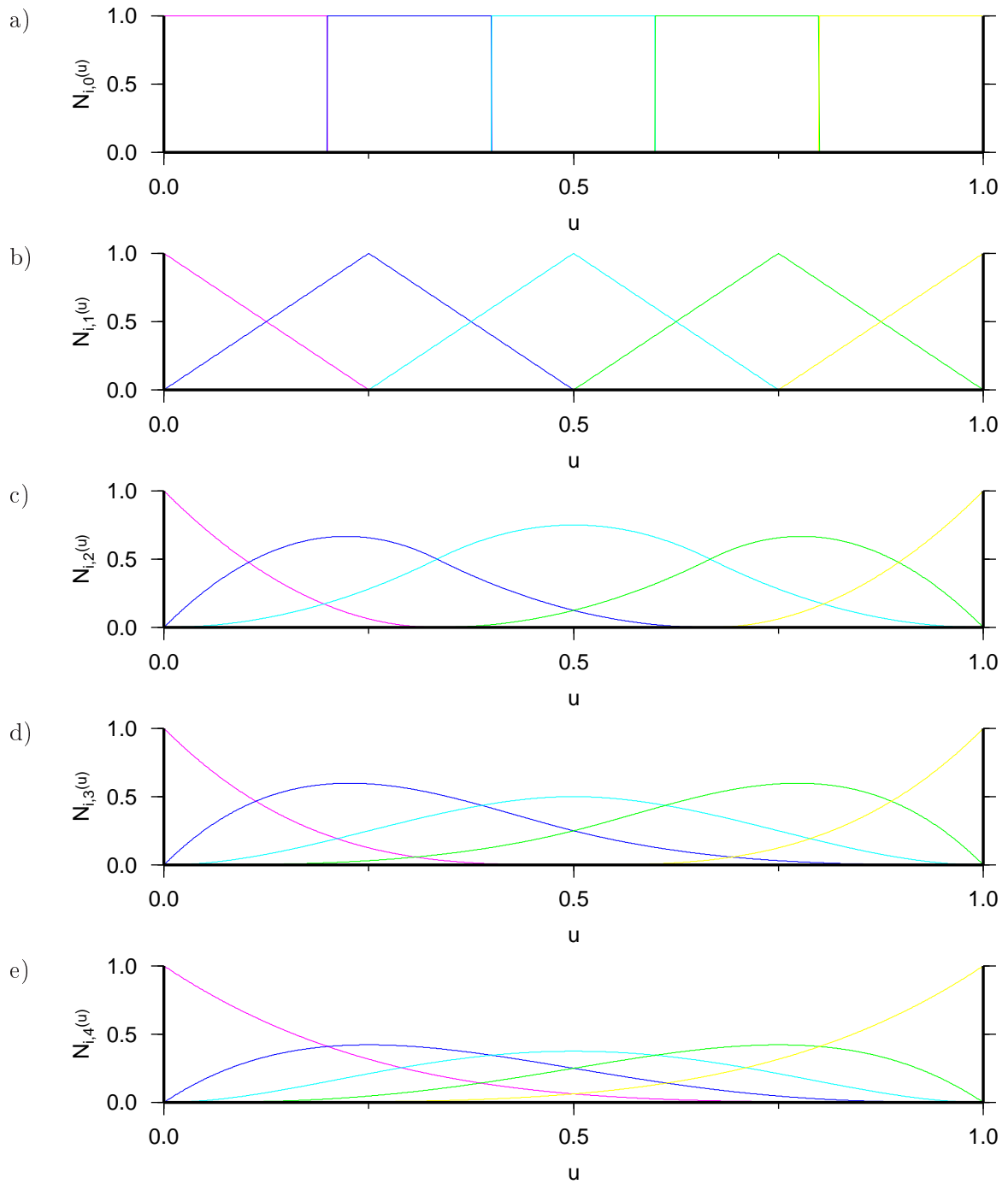
Figure E.1: B-spline basis functions for 5 control points defined on the interval $0 \leq u \leq 1$ marked by different colours; each control point's contribution to an interpolated value at a certain u is given by the value of the appropriate basis function, see text for detailed explanation; the degree p and last knot index m are a) $p = 0, m = 6$, b) $p = 1, m = 8$, c) $p = 2, m = 10$, d) $p = 3, m = 12$, e) $p = 4, m = 14$

1. $N_{i,p}(u)$ is a degree p polynomial in u

2. $N_{i,p}(u)$ is positive for all i, p, and u

3. $N_{i,p}(u)$ is is non-zero on the interval $[u_i, u_{i+p+1})$ (local support)

4. on any span $[u_i, u_{i+1})$, at most $p+1$ degree p basis functions are non-zero ($N_{i-p,p}(u)$, $N_{i-p+1,p}(u)$, ..., and $N_{i,p}(u)$)

5. $u \in [u_i, u_{i+1}) => \sum_{k=0}^{p} N_{i-k,p}(u) = 1$ (partition of unity)

6. if the number of knots is $m + 1$, the degree is p, and the number of degree p basis functions is $n + 1$, then $m + 1 = n + p + 2$

$$\mathbf{C}(u) = \sum_{i=0}^{n} N_{i,p}(u)\mathbf{P_i} \qquad (\text{E.3})$$

Equation E.3 gives the definition of the B-spline curve. Here u is the value in parameter space for which an interpolated value has to be calculated, n is the number of control points $\mathbf{P_i}$, and $N_{i,p}(u)$ is the corresponding B-spline basis function of degree p. In most applications the knot vector is uniform with respect to the internal knots while the edge knots are of multiplicity $k = p + 1$. The reason for selecting this specific value is that the curve is clamped, i.e. that it is a tangent to the legs of the control polyline (the line connecting the control points).

The control points normally contain the user data that should be interpolated but there are also applications that seek to fit the control points so that they interpolate a given set of data with minimum error in a least squares sense (see e.g. Lawson and Hanson, 1974, pp. 222).

E.2   NURBS curves

For most interpolation purposes, B-spline curves are completely sufficient. However, applications like the representation of conic sections, handling of different data quality, and interpolation of sparse datasets are simply not possible or at least extremely difficult to implement. A generalisation of B-splines with a weighting mechanism for the control points leads to the NURBS curves which are defined in equation E.4.

$$\mathbf{C}(u) = \frac{\sum_{i=0}^{n} N_{i,p}(u)w_i\mathbf{P_i}}{\sum_{i=0}^{n} N_{i,p}(u)w_i} \qquad (\text{E.4})$$

Here again, the $N_{i,p}$ are the B-spline basis functions, the $\mathbf{P_i}$ are the control points, and p is the degree. Newly introduced is the weight w_i for the corresponding control point. Rogers (2001) describes how to represent conic sections with the help of NURBS. The basic idea is to produce a polynomial that defines a conic section in parametric form (e.g. for an ellipse $x(t) = a\frac{1-t^2}{1+t^2}$, $y(t) = b\frac{2t}{1+t^2}$ for $-\infty < t < +\infty$). This is accomplished by weighting the control points appropriately. Another use of weights is to reflect different data quality. To illustrate this imagine the measurement of the direction of drilling induced fractures in a borehole. On some parts of the profile, the wall of the hole may show small zones of fractured material while on others the angle is very badly constrained. For the interpolation, the latter gets a smaller weight so that the impact on interpolated data in its vicinity is reduced. A third

application for weights is to use them for handling sparse datasets on regular grids. For those grid points where there is no data, a weight of $w = 0$ is introduced while all others get a weight of $w = 1$. That way data gaps affect their near vicinity.

E.3   NURBS surfaces

Definition NURBS-Volumen

$$\mathbf{V}(u,v,w) = \frac{\sum\limits_{i_u=0}^{n_u} \sum\limits_{i_v=0}^{n_v} N_{i_u,p_u}(u) N_{i_v,p_v}(v) w_{i_u i_v} \mathbf{P_{i_u i_v}}}{\sum\limits_{i_u=0}^{n_u} \sum\limits_{i_v=0}^{n_v} N_{i_u,p_u}(u) N_{i_v,p_v}(v) w_{i_u i_v}} \tag{E.5}$$

E.4   NURBS volumes

Definition NURBS-Volumen

$$\mathbf{V}(u,v,w) = \frac{\sum\limits_{i_u=0}^{n_u} \sum\limits_{i_v=0}^{n_v} \sum\limits_{i_w=0}^{n_w} N_{i_u,p_u}(u) N_{i_v,p_v}(v) N_{i_w,p_w}(w) w_{i_u i_v i_w} \mathbf{P_{i_u i_v i_w}}}{\sum\limits_{i_u=0}^{n_u} \sum\limits_{i_v=0}^{n_v} \sum\limits_{i_w=0}^{n_w} N_{i_u,p_u}(u) N_{i_v,p_v}(v) N_{i_w,p_w}(w) w_{i_u i_v i_w}} \tag{E.6}$$

E.5   NURBS with more parameters

The extension of the NURBS curve to a NURBS surface to a NURBS surface has been done by adding one dimension to the parameter space. Kesper (2001) suggests to add one more parameter for the time. There may also be applications where the parameter space doesn't represent euclidean space together with time, but totally different parameters like the number of people that pass a gate per time unit or something completely different. There is no limit for the dimension of the parameter space.

E.6   NURBS smoothing

Assuming a certain spatial distribution of n stress measurements $\underline{\sigma}(\mathbf{x}_i)$, $i = 1 \ldots n$ the maximum wavelength of stress change ν_{max} that can be resolved is given by half the minimum distance between the locations of the measurements $\nu_{max} = \frac{1}{2} min\{d_{ij} | d_{ij} = |\mathbf{x}_i - \mathbf{x}_j|, 1 \leq i, j \leq n\}$ which is a direct consequence of the Nyquist sampling theorem.

E.7   Miscellaneous definitions

The stress tensor is transformed into a vector as shown in eq. E.7 so that it can be used as input data to the NURBS smoothing.

$$\mathbf{P} = \{\tau_{xx}, \tau_{xy}, \tau_{yy}, \tau_{xz}, \tau_{yz}, \tau_{zz}\}^T \tag{E.7}$$

The quality of a given measurement is easily obtained through the basis functions and the weighting information as defined in eq. E.8.

$$0 \leq q(u,v,w) := \sum_{i_u=0}^{n_u} \sum_{i_v=0}^{n_v} \sum_{i_w=0}^{n_w} N_{i_u,p_u}(u) N_{i_v,p_v}(v) N_{i_w,p_w}(w) w_{i_u i_v i_w} \leq 1 \tag{E.8}$$

Appendix F

Selected fault planes from focal mechanisms

In section 3.1.3 different methods have been described that allow to distinguish between fault plane and auxiliary plane from the two nodal planes that are defined by a focal mechanism. Table F.1 through table F.6 summarise the result in the form of slip vectors together with the appropriate angular difference that lead to its selection.

ID	strike	dip	rake	angular error
3501	17.61	69.37	50.18	11.63
3701	231.27	75.07	-14.86	-37.35
4203	205.23	87.16	-57.28	-39.76
4601	208.86	80.99	-5.94	-41.51
4701	207.98	77.39	0.78	-44.81
5001	204.65	77.05	-1.74	-47.20
5201	200.36	75.14	4.70	-51.46
6001	194.21	80.78	-101.90	-52.29
6501	201.73	72.54	3.63	-52.43
6601	213.77	78.81	-7.34	-40.26
6701	201.68	75.61	1.27	-50.23

Table F.1: Selected slip vectors from focal mechanisms (1 of 6)

ID	strike	dip	rake	angular error
7201	208.68	79.32	-7.34	-42.89
7403	26.82	87.85	50.44	35.41
7702	208.05	77.41	-4.18	-44.75
8105	202.64	86.11	-64.76	-42.42
8301	207.43	82.77	-4.22	-41.16
8401	207.09	81.92	-8.43	-28.23
8901	203.44	89.86	-63.25	-39.49
9001	26.92	86.46	48.92	34.52
9301	28.10	83.99	38.40	32.17
9401	214.43	75.97	-4.41	-42.28
9502	206.48	75.50	3.17	-47.20
10605	39.49	16.88	-63.35	52.03
12102	22.69	87.37	76.24	38.53
12203	194.47	84.26	-77.29	-50.03
12401	192.22	87.74	-78.99	-50.00
12602	195.06	85.69	-77.23	-48.73
12801	222.68	87.37	-56.74	-28.33
13304	194.46	84.41	-78.28	-49.95
14004	214.10	84.78	-52.70	-35.27
14502	232.19	74.81	-14.75	-37.49
14602	201.00	72.81	27.30	-38.23
14902	199.21	79.42	-75.54	-49.35
15201	229.66	76.99	-10.37	-35.74
15901	225.74	81.56	-6.00	-32.39
16001	224.00	82.72	-51.72	-31.93
16401	226.63	77.48	-8.87	-35.99
16601	205.60	89.06	-60.35	-38.27
16801	56.29	83.30	27.85	-53.63
17201	228.35	77.93	-11.07	-35.11
17202	228.02	77.96	-10.75	-35.16
18202	220.02	86.95	-57.35	-25.06
18301	230.42	74.75	-13.77	-37.80
18402	225.97	77.05	-10.26	-36.59
18601	227.96	76.09	-11.91	-36.99
18701	225.68	78.93	-17.64	-34.69
18801	223.57	86.38	-42.25	-27.12
18902	198.37	89.28	-67.86	-43.98
19402	13.57	87.36	75.31	46.38
20001	223.11	83.04	-58.45	-32.00
20401	30.98	89.90	51.14	33.50
20802	218.95	89.29	-47.68	-22.49
20901	37.36	87.65	33.58	27.39
21002	201.30	86.95	-67.07	-42.95
21101	228.17	75.11	-13.23	-37.89
21601	226.92	78.09	-12.83	-35.32
22203	25.78	82.44	34.55	33.35
22401	220.68	81.26	-7.55	-34.66
22601	15.89	76.15	40.62	39.83

Table F.2: Selected slip vectors from focal mechanisms (2 of 6)

ID	strike	dip	rake	angular error
23602	225.25	76.15	-10.56	-37.66
24201	228.96	81.10	15.59	-34.40
24901	219.95	87.93	-57.12	-24.13
24902	220.47	87.85	-56.57	-29.05
25101	196.47	87.27	-77.33	-46.68
25401	14.51	85.87	77.68	44.85
27101	191.93	88.40	-83.96	-49.90
28905	199.28	89.53	-64.15	-43.09
29304	31.23	80.67	56.04	27.79
29601	220.31	88.36	-56.39	-23.89
29701	227.28	78.65	-9.30	-34.69
29702	227.29	74.65	-14.08	-38.54
29901	19.99	87.32	78.78	40.79
30101	224.33	77.36	-8.81	-36.80
30202	227.36	73.29	-6.29	-39.84
30301	31.84	86.09	39.74	30.37
30401	16.48	87.23	75.99	43.77
30801	215.56	79.04	-55.02	-39.10
31001	15.39	85.08	77.33	43.71
31302	94.47	2.77	13.64	65.81
31502	354.07	11.75	-113.40	48.67
31503	217.12	81.56	-54.79	-36.15
31802	204.77	82.99	-77.94	-42.88
31901	214.41	87.53	-62.58	-32.95
31903	305.62	47.16	135.49	36.49
32101	216.52	83.45	-54.43	-34.90
32601	216.35	81.38	-53.49	-36.71
33501	33.21	88.55	48.17	30.95
33901	15.35	85.50	78.73	43.94
34202	201.93	86.11	-71.58	-42.97
34301	203.06	88.44	-69.02	-40.65
34401	7.59	59.48	37.75	22.77
34704	219.24	80.18	-52.88	-36.28
35401	206.68	86.24	-63.53	-39.28
36201	222.44	77.12	-6.54	-37.69
36601	218.73	87.69	-56.76	-30.16
37001	223.62	81.68	-9.01	-33.04
37401	202.13	87.81	-65.13	-41.77
37801	18.62	89.85	71.95	43.30
38001	227.78	71.54	-7.07	-41.45
38101	37.83	88.24	38.56	27.52
38201	17.27	87.41	76.71	43.18
38303	200.46	89.07	-69.11	-42.37
38401	196.95	88.36	-73.99	-45.67
38402	197.76	87.65	-71.14	-45.40
39101	209.21	85.20	-55.32	-38.18
39301	20.32	82.02	81.85	37.96
39502	17.05	87.37	73.55	43.35

Table F.3: Selected slip vectors from focal mechanisms (3 of 6)

ID	strike	dip	rake	angular error
39702	228.48	81.10	14.03	-34.15
39901	199.27	54.40	-155.35	-56.52
40601	4.05	59.62	36.53	25.59
40701	219.67	89.44	-55.98	-22.64
40901	206.92	86.67	-57.65	-38.81
41101	227.35	74.81	-14.33	-38.37
41701	222.12	76.07	-1.98	-38.78
42001	202.92	88.71	-63.47	-40.60
42501	196.89	88.24	-77.79	-45.79
42701	203.19	86.83	-65.44	-41.54
42806	221.60	78.76	-8.52	-36.51
43704	217.58	89.72	-38.21	-29.24
44101	223.83	84.54	-35.58	-30.34
44202	193.75	88.41	-77.35	-48.34
44401	195.96	88.00	-74.00	-46.70
44702	199.50	79.83	-72.75	-48.86
44801	194.75	86.87	-77.43	-42.29
44803	202.82	86.07	-63.31	-42.31
44806	198.47	84.31	-72.20	-46.66
45102	37.66	89.59	41.08	28.66
45103	32.70	27.69	-68.55	43.58
45301	227.55	74.83	-14.04	-38.31
45401	224.97	75.21	-7.89	-38.63
45501	196.89	84.23	-75.17	-45.68
45901	16.53	88.03	79.91	39.80
45904	196.47	85.13	-83.99	-44.72
46102	194.81	87.41	-76.55	-41.92
46201	196.36	86.30	-77.52	-43.77
46404	215.15	79.23	-55.01	-39.16
46506	16.09	89.59	80.75	40.58
46601	199.42	86.45	-67.88	-44.75
47101	197.13	87.52	-76.00	-45.99
47201	17.34	87.86	80.15	40.27
47601	222.71	82.78	-49.98	-32.40
48001	201.40	85.84	-71.48	-47.57
48302	225.19	82.63	-55.51	-31.57
48501	201.46	88.68	-68.81	-45.64
48701	8.36	60.77	35.93	21.68
48801	17.70	89.69	78.96	41.79
48803	21.35	88.48	76.92	43.67
48902	17.11	88.78	79.78	40.74
49501	15.59	77.40	5.00	32.42
49601	36.08	65.47	-17.36	45.61
49802	17.86	87.22	76.39	42.57
56201	356.23	55.44	-152.18	33.14
57101	35.70	89.62	62.91	29.97
57201	27.99	89.17	71.51	35.29
57407	24.26	83.60	52.99	35.24

Table F.4: Selected slip vectors from focal mechanisms (4 of 6)

ID	strike	dip	rake	angular error
57701	44.22	85.75	50.47	21.64
57702	206.78	85.14	-62.20	-39.95
58401	9.63	68.93	25.20	23.40
58503	22.83	83.75	57.93	36.55
58601	11.72	84.35	-95.25	22.84
58701	24.42	34.45	-163.60	35.80
58901	194.85	85.14	-81.91	-49.22
59401	224.37	79.29	-12.25	-34.98
59807	208.59	78.56	-66.27	-43.53
59901	199.61	80.26	-78.54	-48.50
60501	221.78	84.88	-45.84	-30.94
61302	349.66	60.57	-149.33	37.64
62001	223.88	84.29	-43.66	-30.55
62501	20.36	79.59	45.09	36.93
63001	18.02	78.23	98.14	14.15
63101	213.36	89.28	-48.33	-32.37
63201	32.84	88.20	42.99	30.98
63602	356.21	43.50	-157.02	38.22
63801	31.19	68.73	-12.82	42.28
64401	8.54	60.71	35.25	21.55
64501	201.21	84.29	-67.89	-44.68
64601	203.24	83.80	-59.99	-43.46
64801	200.08	86.32	-71.68	-44.30
64901	19.86	89.23	76.19	41.92
65001	284.54	89.69	76.56	-75.60
65301	7.62	67.89	26.69	21.28
65501	12.05	70.26	23.54	26.01
65701	1.62	66.07	30.36	15.47
65801	15.82	67.96	19.51	28.48
65901	2.70	66.55	30.66	16.56
66001	8.73	70.92	23.37	23.46
66101	5.98	67.22	26.21	19.63
66102	2.74	67.06	29.88	16.78
66103	11.36	56.65	41.48	23.23
66201	9.76	70.70	23.43	24.23
66401	3.00	66.96	31.56	16.96
66801	4.17	66.10	34.90	17.70
67201	6.84	55.71	40.73	19.67
67502	96.79	57.74	68.53	60.28
67801	48.36	18.60	2.29	52.51
68401	209.09	79.74	-141.98	-30.27
68501	38.96	87.00	21.89	25.84
68801	210.26	87.79	-53.67	-35.61
68901	221.64	87.12	-43.88	-25.58
69001	221.38	83.69	-4.59	-32.18
69501	200.70	89.65	-72.30	-41.85
69601	22.75	84.43	42.49	36.95
69701	26.40	88.89	55.21	36.37

Table F.5: Selected slip vectors from focal mechanisms (5 of 6)

ID	strike	dip	rake	angular error
70801	311.22	13.91	-164.63	39.38
71001	313.95	10.78	-158.07	40.98
71101	22.94	84.33	44.64	42.33
71301	319.45	35.24	-162.79	41.81
71501	197.82	89.32	-76.70	-44.42
71701	14.18	77.00	91.20	16.69
72301	210.31	89.11	-49.16	-34.67
72501	228.39	77.79	-8.80	-35.24
72902	231.24	79.68	-41.75	-36.83
73701	216.56	76.44	-7.32	-40.82
74201	33.65	69.06	33.91	3.55
74301	29.24	87.19	63.89	33.09
74501	224.43	82.27	-50.99	-32.18
74601	229.73	80.26	14.88	-35.52
74701	315.88	25.81	-166.97	38.89
74801	312.43	50.68	138.21	42.60
75101	18.58	69.68	44.99	10.72
75301	214.86	82.02	-146.07	-28.39
75801	54.13	85.90	-57.28	28.38
76001	7.49	65.00	29.57	21.36
76201	5.36	70.64	26.55	20.51
76301	5.04	69.00	25.64	19.50
77301	7.86	58.70	36.99	22.87
78901	187.92	69.77	-148.63	-45.67
79104	47.22	64.92	-31.02	55.13
79202	308.35	19.53	-165.49	47.21
79707	4.53	67.24	33.54	18.38
80001	314.54	37.36	-169.30	33.38
80401	39.15	66.29	-16.58	48.53
80601	20.38	78.28	9.22	36.85
80702	22.22	82.95	27.56	40.94
80901	15.88	82.79	13.02	35.83
81003	178.74	62.95	-150.46	-56.61
81401	6.35	72.70	23.08	22.37
81501	11.57	71.86	40.20	17.51
82401	4.42	67.17	33.64	18.26
84701	224.43	83.68	-55.30	-30.88
84801	15.96	85.93	77.57	43.60
87301	353.10	66.59	-138.12	34.36

Table F.6: Selected slip vectors from focal mechanisms (6 of 6)

List of Figures

List of Tables